Title
Touring the Conformational Landscape of Proteins with High-Pressure SDSL EPR Spectroscopy

Author
Lerch, Michael

Publication Date
2015

Peer reviewed|Thesis/dissertation

UNIVERSITY OF CALIFORNIA

Los Angeles

Touring the Conformational Landscape of Proteins with High-Pressure SDSL EPR Spectroscopy

A dissertation submitted in partial satisfaction of the

requirements for the degree Doctor of Philosophy

in Chemistry

by

Michael Lerch

2015

ABSTRACT OF THE DISSERTATION

Touring the Conformational Landscape of Proteins with High-Pressure SDSL EPR Spectroscopy

by

Michael Lerch

Doctor of Philosophy in Chemistry

University of California, Los Angeles, 2015

Professor Wayne L. Hubbell, Chair

Proteins in solution are dynamic molecules that exhibit conformational flexibility across a range of time and length scales, and characterizing the functional role of protein motion is a primary goal in molecular biophysics. High hydrostatic pressure has emerged as a powerful probe of protein conformational flexibility. Development of instrumentation and methodologies that enable electron paramagnetic resonance (EPR) experiments on proteins at high pressure is the central aim of the work presented in this dissertation.

Pressurization of proteins reveals regions of elevated compressibility, and thus flexibility, within individual conformational states, but also shifts conformational equilibria such that "invisible" excited states become accessible for spectroscopic characterization. Current evidence indicates that pressure cleanly shifts the relative populations of states solely according to differences in partial molar volume without altering the shape of the conformational free energy landscape. Thus, variable pressure is a powerful tool for dissecting details of the landscape, and site-directed spin labeling coupled with electron paramagnetic resonance spectroscopy (SDSL

EPR) is an ideal strategy in terms of sensitivity and time scale to detect the effects of pressure and interpret them in terms of structure and dynamics. In this dissertation, newly developed high-pressure instrumentation for both variable-pressure continuous-wave EPR and pressure-resolve double electron-electron resonance (PR DEER) of proteins in aqueous solution is described. The applications presented illustrate the considerable potential of the methods to: (1) identify compressible (flexible) regions in a folded protein; (2) determine thermodynamic parameters that relate conformational states in equilibrium; (3) populate and characterize excited states of proteins undetected at atmospheric pressure; (4) reveal the structural heterogeneity of conformational ensembles and provide distance constraints on the global structure of pressure-populated states. The SDSL EPR results are complemented by global secondary structure information provided by high-pressure circular dichroism experiments.

This work lays the foundation for future developments in high-pressure SDSL EPR, including pressure-jump relaxation spectroscopy to determine the lifetime of conformational states in the millisecond range and high pressure saturation recovery exchange spectroscopy to enable measurement of lifetimes of states in the microsecond range. SDSL EPR has unique advantages for the study of membrane proteins in their native environment under physiological conditions, and applications of high-pressure SDSL EPR to explore the conformational equilibria and dynamics of integral membrane proteins is a high priority for future work.

The dissertation of Michael Lerch is approved

William M. Gelbart

Ernest M. Wright

Wayne L. Hubbell, Committee Chair

University of California, Los Angeles

2015

TABLE OF CONTENTS

LIST OF FIGURES

LIST OF TABLES

ACKNOWLEDGEMENTS

I would like to first express my gratitude to my loved ones, in particular Elizabeth Noey, for her love, patience, and for finding the best in me. I am also incredibly thankful to my parents and brothers, who have offered me love and encouragement throughout my life and career.

I would like to thank my advisor, Professor Wayne Hubbell, for his mentorship, guidance, and constant enthusiasm for the research we do. I am also grateful for the advice and support of Cherie Hubbell throughout my time at UCLA. I appreciate the time and effort given by the members of my graduate committee, and I am thankful to current and former members of the Hubbell group for their helpful discussions and the friendly working environment. I am grateful to all of the brilliant scientists I have collaborated with in and out of the group. Specifically, I would like to thank Dr. Zhongyu Yang, Dr. Carlos López, and Professor Joseph Horwitz, who selflessly spent so much of their time sharing their scientific expertise.

I am also grateful to the National Institutes of Health Chemistry-Biology Interface (CBI) Training Program for financial support (grant T32GM008496), and all those involved with CBI for insightful discussions on numerous topics on the frontiers of chemistry and biology. In particular, I would like to thank Professor Maynard, the current director of the CBI program at UCLA. I would like to thank the Gregory family for selecting me as a recipient of the George Gregory Award. I am grateful for the following funding sources that have supported the work presented in this dissertation: National Eye Institute training grant T32EY007026, grant R01EY05216, and core grant P30EY00331, the Jules Stein Professor Endowment, and a Research to Prevent Blindness unrestricted grant.

Chapter 2 is an extensively modified version of the publication "[2] High-pressure EPR and site-directed spin labeling for mapping molecular flexibility in EPR" Lerch MT, Yang Z, Altenbach C, Hubbell WL, *Electron Paramagnetic Resonance Investigations of Biological Systems by Using Spin Labels, Spin Probes, and Intrinsic Metal Ions Part A*, Methods in Enzymology, eds Qin PZ & Warncke K (Academic Press) Vol 563, **2015**, in press. I wrote this manuscript with Dr. Yang, Dr. Altenbach, and Professor Hubbell.

Chapter 3 is a modified version of the publication "Circular dichroism and site-directed spin labeling reveal structural and dynamical features of high-pressure states of myoglobin" Lerch MT, Horwitz J, McCoy J, Hubbell WL, *Proc Natl Acad Sci USA* **2013**, *110(49)*, E4714-22. DOI: 10.1073/pnas.1320124110. Dr. McCoy and Professor Horwitz developed the high-pressure circular dichroism instrumentation and performed most of the circular dichroism experiments. I performed some circular dichroism experiments and performed all EPR experiments and analysis under the guidance of Professor Hubbell. I wrote the manuscript with Professor Hubbell.

Chapter 4 is a modified version of the publication "Mapping protein conformational heterogeneity under pressure with site-directed spin labeling and double electron-electron resonance" Lerch MT, Yang Z, Brooks EK, Hubbell WL, *Proc Natl Acad Sci USA* **2014**, *111(13)*, E1201-10. DOI: 10.1073/pnas.1403179111. Evan Brooks generated new myoglobin mutants. I developed the pressure-resolved DEER methodology, performed DEER experiments, and analyzed the data in collaboration with Dr. Yang and under the guidance of Professor Hubbell. I wrote the manuscript with Professor Hubbell.

Chapter 5 is a modified version of the publication "Structure-relaxation mechanism for the response of T4 lysozyme cavity mutants to hydrostatic pressure" Lerch MT, López CJ, Yang Z, Kreitmam MJ, Horwitz J, Hubbell WL, *Proc Natl Acad Sci USA* **2015**, *112(19)*, E2437-46.

DOI: 10.1073/pnas.1506505112. I performed circular dichroism experiments with Professor Horwitz, and analyzed circular dichroism data with Dr. López under the guidance of Professor Horwitz. Dr. López and Margaux Kreitman prepared protein for all experiments. Dr. López performed atmospheric pressure EPR experiments and data analysis. I performed all variable-pressure CW EPR experiments and data analysis. I performed all pressure-resolved DEER experiments and data analysis in collaboration with Dr. Yang. I wrote the manuscript with Dr. López and Professor Hubbell. Professor Hubbell supervised the research.

VITA

EDUCATION

B.S. in Chemistry, University of San Francisco, Graduated First in Class (2009)

PUBLICATIONS

Johansen E, Schilling B, **Lerch M**, Niles RK, Liu H, Li B, Allen S, Hall SC, Witkowska HE, Regnier FE, Gibson BW, Fisher SJ, & Drake PM (2009) A lectin HPLC method to enrich selectively-glycosylated peptides from complex biological samples. *J Vis Exp* (32):e1398. DOI: 10.3791/1398

Drake PM, Schilling B, Niles RK, Braten M, Johansen E, Liu H, **Lerch M**, Sorensen DJ, Li B, Allen S, Hall SC, Witkowska HE, Regnier FE, Gibson BW, & Fisher SJ (2011) A lectin affinity workflow targeting glycosite-specific, cancer-related carbohydrate structures in trypsin-digested human plasma. Anal Biochem 408(1):71-85. DOI: 10.1016/j.ab.2010.08.010.

Lerch MT, Horwitz J, McCoy J, & Hubbell WL (2013) Circular dichroism and site-directed spin labeling reveal structural and dynamical features of high-pressure states of myoglobin. *Proc Natl Acad Sci USA* 110(49):E4714-22. DOI: 10.1073/pnas.1320124110.

Lerch MT, Yang Z, Brooks EK, & Hubbell WL (2014) Mapping protein conformational heterogeneity under pressure with site-directed spin labeling and double electron-electron resonance. Proc Natl Acad Sci USA 111(13): E1201-10. DOI: 10.1073/pnas.1403179111.

Lerch MT, López CJ, Yang Z, Kreitman MJ, Horwitz J, & Hubbell WL (2015) Structure-relaxation mechanism for the response of T4 lysozyme cavity mutants to hydrostatic pressure. *Proc Natl Acad Sci USA* 112(19):E2437-46. DOI: 10.1073/pnas.1506505112.

Manglik A, Kim TH, Masureel M, Altenbach C, Yang Z, Hilger D, **Lerch MT**, Kobilka TS, Thian FS, Hubbell WL, Prosser RS, & Kobilka BK (2015) Structural insights into the dynamic process of β2-adrenergic receptor signaling. *Cell* 161(5):1101-11. DOI: 10.1016.j.cell.2015.04.043.

Dror RO, Mildorf TJ, Hilger D, Manglik A, Borhani DW, Arlow DH, Philippsen A, Villanueva N, Yang Z, **Lerch MT**, Hubbell WL, Kobilka BK, Sunahara RK, & Shaw DE (2015) Structural basis for nucleotide exchange in heterotrimeric G proteins. *Science* 348(6241):1361-5. DOI: 10.1126/science.aaa5264.

Yang Z, Bridges MD, **Lerch MT**, Altenbach C, & Hubbell WL (2015) [1] Saturation recovery EPR and nitroxide spin labeling for exploring structure and dynamics in proteins. *Electron Paramagnetic Resonance Investigations of Biological Systems by Using Spin Labels, Spin Probes, and Intrinsic Metal Ions Part A,* Methods in Enyzmology, eds Qin PZ & Warncke K (Academic Press), Vol 563, in press.

Lerch MT, Yang Z, Altenbach C, & Hubbell WL (2015) [2] High-pressure EPR and site-directed spin labeling for mapping molecular flexibility in EPR. *Electron Paramagnetic Resonance Investigations of Biological Systems by Using Spin Labels, Spin Probes, and Intrinsic Metal Ions Part A,* Methods in Enzymology, eds Qin PZ & Warncke K (Academic Press), Vol 563, in press.

AWARDS

Undergraduate

University Scholar's Scholarship (2004-2009)
ACS Polymer Chemistry Award (2007)
Father Flynn Award: highest GPA in graduating class (2009)
Dr. Mel Gorman Award (co-recipient): outstanding senior Chemistry major (2009)

Graduate

NEI Vision Science Predoctoral Training Grant (2009-2010)
NIH Chemistry and Biology Interface Training Program at UCLA (2010-13)
George Gregory Award for graduate research in Physical Chemistry (2014)

TEACHING EXPERIENCE

TA for undergraduate Physical Biochemistry course (Fall 2013, Spring 2014)
TA for undergraduate Biochemistry course (Fall 2014)

Chapter 1: Introduction to electron paramagnetic resonance

1.1 Summary

This chapter contains a brief overview of electron paramagnetic resonance (EPR) theory. The contents are limited to the principles underlying EPR of nitroxides that have been attached to proteins *via* site-directed spin labeling (SDSL). For a more complete treatment of magnetic resonance theory, the reader is referred elsewhere (1-4). The present discussion begins with a description of the SDSL technique and the nitroxide-containing label R1 used in this dissertation, followed by examples from the literature that illustrate the ability of SDSL EPR to report local protein dynamics. Next, a description of the basic resonance condition and relaxation theory general to EPR spectroscopy is presented. The focus is then narrowed to nitroxides, in particular the structural aspects of nitroxides that influence the spectral lineshape. Then, a spectral simulation method for analyzing the motional dependence of the lineshape of nitroxide-labeled proteins in solution is described. Finally, the double electron-electron resonance (DEER) technique for determining inter-spin distances in doubly-labeled proteins is introduced.

1.2 Site-directed spin labeling

The concept of an environmentally sensitive “reporter” group targeted and covalently attached to a specific protein residue *via* a “positioning” group was introduced by Koshland for the purpose of monitoring functionally relevant changes in protein structure (5). This concept was extended to electron paramagnetic resonance (EPR) a year later by McConnell (6), where the idea of incorporating stable free radicals into proteins to serve as reporter groups for EPR was introduced in a method termed “spin labeling.” Nitroxide derivatives were the first spin labels used in EPR spectroscopy, and are still by far the most common, although other stable radicals have been used (7-10). Nitroxides are stable over a pH range of 3-10 and temperatures

up to 80^{o}C (11). Quaternary carbons at the neighboring bonds protect the radical from disproportionation reactions (12), and incorporation of the nitroxide group into a ring structure (six-membered piperidine or five-membered pyrrole) limits the flexibility of the nitroxide. One potential limitation is that nitroxide-containing spin labels are susceptible to reduction to the diamagnetic (EPR silent) form by mild reducing agents (13).

One option for spin-labeling the protein of interest is to label native residues. Functional groups with specific reactivity for a particular amino acid side chain allow covalent attachment of spin labels. Maleimide and methanethiosulfonate groups react with cysteine residues, while hydroxylsuccinimide reacts with lysines. Lysine residues are typically more abundant than cysteines, therefore cysteines are usually preferred in order to provide more specific, localized information in the EPR spectrum. Even though different positioning groups allow some versatility with respect to the incorporation of spin labels into proteins, the limitation to naturally occurring residues and the inability to select one site from among all cysteine or lysine locations was a significant limitation to early applications of EPR in proteins.

Development of site-directed mutagenesis and recombinant protein expression and purification techniques in the late 1980s provided the groundwork for a major advancement in biophysical EPR, wherein spin labels could be introduced site-specifically into any recombinant protein in a technique pioneered by Hubbell (14) known as site-directed spin labeling (SDSL). This is shown schematically in Figure 1.1A, where a native residue is mutated to a cysteine, which is then reacted with a nitroxide derivative to generate a nitroxide side chain.

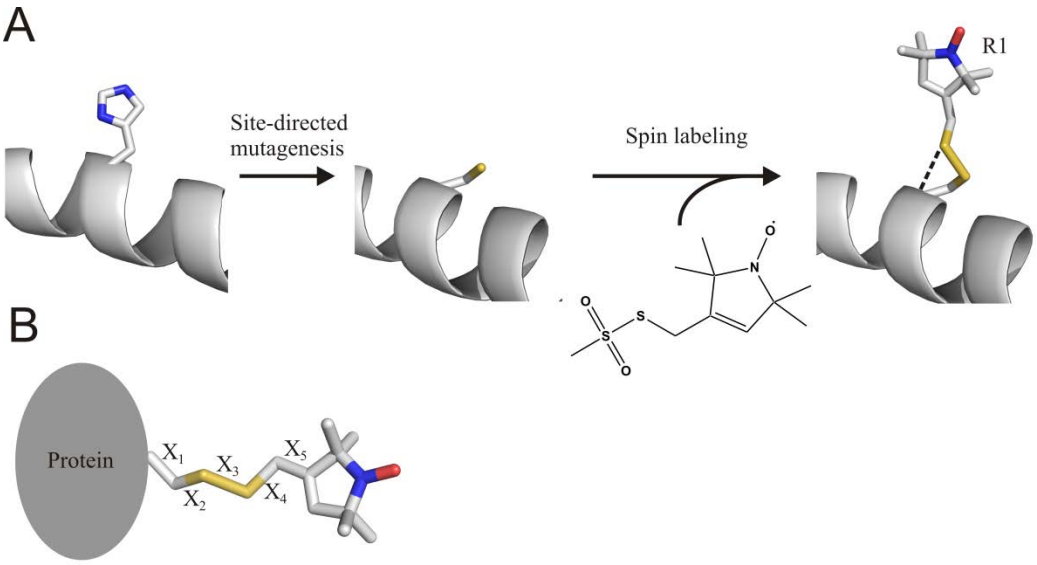

Figure 1.1 Site-directed spin labeling. (A) A native residue (left panel) is mutated to cysteine (center panel). The mutant is expressed and purified, and then a sulfhydryl-specific nitroxide-containing reagent is reacted with the protein to generate a spin label side chain (right panel). In the example shown here, a native histidine is mutated to a cysteine, and a methanethiosulfonate spin label reagent reacts with the cysteine to generate an R1 side chain linked to the protein through a disulfide bond. The dashed line indicates the intraresidue S_δ-HC_α bond that restricts rotation about the first two side chain bonds. (B) Designations of the five dihedral angles of R1 discussed in the text.

The nitroxide side chain used almost exclusively in the work presented in this dissertation is that designated R1 (Figure 1.1), utilized by reaction of 2,2,5,5-tetramethyl-pyrroline-1-oxyl methanethiosulfonate with the thiol of a cysteine to generate a nitroxide side chain covalently attached to the protein *via* a disulfide linkage. This commonly used spin label is well-characterized (15, 16) and advantages of the R1 label as a probe of protein dynamics include its relatively small size, with a molecular volume comparable to tryptophan, and its relatively flexible linker, which helps minimize perturbations to the protein structure and stability. The effect of R1 on protein structure and stability has been extensively studied and found to be minimal, particularly for solvent-exposed surface sites (7, 15) like those used in this dissertation. A potential disadvantage to thiol-reactive labels is the necessity for eliminating native cysteines by replacement with alanine or serine. This is not an issue for the two proteins studied in this

dissertation, but alternative strategies based on the incorporation of unnatural amino acids with bio-orthogonal groups for site-specific labeling are available (17, 18).

As discussed in the following sections of this chapter, the EPR spectrum is highly sensitive to motion of the nitroxide on the ns time scale, which contains contributions from protein rotary diffusion, local backbone fluctuations, and internal motion of the nitroxide side chain. In this dissertation, molecular motions are quantified in terms of a rotational correlation time τ unless specified otherwise. τ is related to the diffusion coefficient for molecular motion and indicates the characteristic time scale for fluctuations. Generally, a correlation time is the characteristic time for decay of an autocorrelation function. For isotropic rotational Brownian motion, τ is defined as 1/6D, where D is the spherical diffusion coefficient (4). The rotary diffusion of the protein makes a negligible contribution for membrane-bound proteins and soluble proteins with MW $\gtrsim$ 50 kDa, and may be minimized for smaller soluble proteins by increasing the effective viscosity of the solution or site-specific attachment to a solid support (19, 20).

The two remaining contributions to the motion of the nitroxide group are local backbone fluctuations and internal side chain motion. Ultimately the primary interest lies in local protein structure and dynamics, and interpretation of EPR spectra in terms of protein motion generally requires knowledge of the internal dynamics of the spin label side chain. In principle, internal motion of the spin label side chain may be reduced by developing more rigid and/or bulkier spin labels, but in practice a certain degree of flexibility in the spin label helps avoid distorting the native protein structure as mentioned above. The structural basis for spin label motion is best understood for R1 at solvent-exposed surface sites on helices and loops, wherein density functional calculations (16) and high-resolution crystal structures of spin-labeled T4 lysozyme

(15), Spa15 (21), CylR2 (22), KcsA (23), and LeuT (24) have demonstrated a ubiquitous intra-residue hydrogen bond (S_δ-HC_α) in R1 that restricts rotational motion about the first two bonds ($\mathbf{X}_1$ and $\mathbf{X}_2$, Figure 1.1). This, in combination with the restriction in $\mathbf{X}_3$ due to the rotational barrier common to disulfide bonds (25), results in anisotropic motion of the nitroxide due to rotation about $\mathbf{X}_4$ and $\mathbf{X}_5$. This "$\mathbf{X}_4/\mathbf{X}_5$ model" was originally proposed based on analysis of solution-based EPR measurements of T4 lysozyme using spin labels with various side chain structures (9), and is supported by earlier mutational analysis and side chain structure variation experiments (7, 8). Spin label dynamics in β structures are complicated by the increased propensity for interactions with neighboring residues, but progress has been made in the recent reporting of crystal structures of spin-labeled soluble (26) and membrane-bound (27) β proteins.

Non-interacting surface sites on helices/loops exhibit site-independent internal motion, therefore site-to-site variation in motion is due to contributions from local backbone motion. This is strongly supported by comparison of SDSL EPR data with results from previous studies employing other techniques. A detailed discussion of the motional dependence of the EPR spectral lineshape is presented later in the chapter. Next, illustrative examples of the sensitivity of EPR to local protein dynamics are briefly reviewed, wherein variation in ns timescale motion reported by lineshape analysis matched expectations for local motion based on published results.

In the case of the basic leucine zipper of yeast transcription factor GCN4 (GCN4-58 bZip), ^{15}N relaxation NMR experiments identified a gradient of motion along the DNA-binding region corresponding to relatively large backbone motions involving fluctuations between helical and non-helical conformations (28). A series of 27 singly spin-labeled mutants of this protein yielded spectra with sharp resonance lines in the DNA-binding region, consistent with the local disorder identified in this sequence by NMR. Spectral simulations (29) and a semi-quantitative

measure of motion based on the central linewidth, referred to as the scaled mobility parameter, revealed that the site-specific variation in EPR spectral lineshape captured the same motional gradient first identified by NMR (30). This was a landmark demonstration of the contribution of backbone motion to the spectral lineshape. However, the backbone motion was relatively high amplitude in the DNA-binding region in which the motional gradient was observed and measured. This leaves an open question as to the contribution of smaller amplitude backbone fluctuations, e.g. helical rocking motions.

Although contribution of local backbone fluctuations to the EPR lineshape was reported previously (7, 9, 30, 31), the study of myoglobin by López et al. (32) provided an extensive and thorough demonstration that even subtle variations in backbone fluctuations are reflected in the spectral lineshape. In this study, 29 non-interacting surface sites on holomyoglobin were labeled with R1, one at a time. As with the GCN4-58 bZip study, the EPR spectra were analyzed using the scaled mobility parameter and spectral simulations. Site-specific variation in these EPR-based measures of motion was compared to the local fractional buried surface area to determine whether local backbone fluctuations contributed significantly to the EPR lineshape. This comparison operates under the assumption that as the buried surface area increases, the greater number of atomic contacts made by the helix will decrease its mobility. Remarkably, the EPR-based measures of motion were found to correlate well with local packing.

Interestingly, the H-helix in holomyoglobin exhibits a gradient of motion, with motion increasing from the N- to C-terminal end of the helix, based on crystallographic B-factors. In analogy with the GCN4-58 bZip study, the EPR spectra of sites in the H-helix of myoglobin reflected a gradient of motion consistent with expectations, although in the case of

holomyoglobin the motions consisted of small-amplitude backbone fluctuations within an intact helix.

The model for R1 motion and experimental results discussed above pertain to non-interacting surface sites. Contact and buried sites exhibit spectra reflective of highly restrictive motion due to interaction of the nitroxide with the local protein environment, and therefore the motion no longer follows the model for non-interacting sites. However, the dramatically different spectral lineshape due to interaction with the local environment makes the EPR spectrum an exquisitely sensitive probe of protein conformational exchange for properly placed residues (30, 32, 33), as discussed in detail in chapter 2.

The information presented in this section served to introduce the technique of SDSL EPR and the specific nitroxide spin label used in the work presented in this dissertation. In the following sections, the basic resonance condition and relaxation processes common to all EPR experiments will be covered. Then, the focus will narrow to theoretical and experimental aspects of EPR of spin-labeled proteins.

1.3 The resonance condition

The electron is a fermion (spin quantum number s = ½) with an intrinsic angular momentum, or spin angular momentum, denoted by S with a value of

$$S = \hbar\sqrt{s(s+1)} = \frac{\sqrt{3}}{2}\hbar \qquad [1.1]$$

where $\hbar$ is the reduced Planck constant and is equal to the Planck constant h divided by 2π. Electrons are charged particles, therefore the angular momentum gives rise to an electronic magnetic moment given by

$$\boldsymbol{\mu_e} = -g\beta_e\mathbf{S} \qquad [1.2]$$

where the vectors **S** (in units of $\hbar$) and $\boldsymbol{\mu_e}$ represent the electron angular momentum and magnetic moment, respectively. In [1.2], g is the electronic g-factor (g ≈ 2.002319 for a free electron), and β_e is the Bohr magneton

$$\beta_e = \frac{e\hbar}{2m} \qquad [1.3]$$

The collection of constants that comprise β_e are the rest mass of an electron m, the elementary charge e, and $\hbar$, defined above. β_e is positive using this definition, but the electron is negatively charged, therefore expression [1.2] includes a negative sign to indicate that the vector $\boldsymbol{\mu_e}$ is anti-parallel to the vector **S** (Figure 1.2). The total magnetic moment of an electron bound to a nucleus contains contributions from the spin term defined in [1.2] and an analogous orbital angular momentum term, but for organic radicals such as nitroxides the orbital angular momentum is largely quenched (34). In such cases, $\boldsymbol{\mu_e}$ and **S** are anti-parallel as specified by [1.2] and deviations in the value of g from that of a free electron account for the contribution of the orbital angular momentum from spin-orbit coupling. An orbital magnetic moment that is not aligned perfectly with the spin magnetic moment generates g-anisotropy that is accounted for by employing a tensor representation for g, as described in section **1.5**.

The interaction energy E of a magnetic dipole moment $\boldsymbol{\mu}$ in a magnetic field $\mathbf{H_0}$ is given by the dot product of the two vectors

$$E = -\boldsymbol{\mu} \cdot \mathbf{H_0} \qquad [1.4]$$

Combining [1.2] and [1.3] yields the energy of the interaction between electron spin angular momentum and an external field, termed the Zeeman interaction.

$$E = g\beta_e \mathbf{S} \cdot \mathbf{H_0} \qquad [1.5]$$

If the applied field $\mathbf{H_0}$ is uniform and along a single axis defined as z, the interaction energy is then proportional to S_z, the projection of **S** along the z-axis and [1.5] becomes

$$E = \frac{g\beta_e}{\hbar} S_z H_z \quad [1.6]$$

where

$$S_z = m_s \hbar \quad [1.7]$$

The secondary spin quantum number m_s can take one of $2s + 1$ values ranging from $+s$ to $-s$ in increments of one. For an electron s = ½ and therefore m_s can take two values, +½ and –½, generating two possible energies in [1.6]. It should be noted that the magnitude of **S** is fixed, and is defined by the value of the spin angular momentum given by [1.1]. The vector **S** (and thus $\boldsymbol{\mu_e}$) is not directly aligned with the z-axis defined by $\mathbf{H_0}$. The two possible spin states restrict **S** to two possible angles with respect to the z-axis, and therefore the projection of **S** along the z-axis can take one of two values. In the m_s = +½ state, the projection of **S** along the z-axis runs in the +z direction; this is referred to as the spin +½ state or the spin-up state. In the m_s = –½ state, S_z is along the –z direction; this is the spin –½ state or the spin-down state.

According to [1.6], the energy of the spin +½ state will be positive and the energy of the spin –½ state will be negative, relative to zero field where the energy associated with both orientations is zero (Figure 1.2). The energies of spin states defined in [1.6] assume all orientations of **S** are iso-energetic (degenerate) in the absence of an external field. This is not strictly true for systems with total spin quantum number >½, including the nitroxides considered here wherein the unpaired electron is bound to a nucleus with spin = 1, and there is a splitting of energy levels even at zero field (i.e., zero field splitting). Additional contributions to spin state energies in the high-field limit will be considered in section **1.5**, but this section is limited to the interaction of an electron spin with an applied magnetic field.

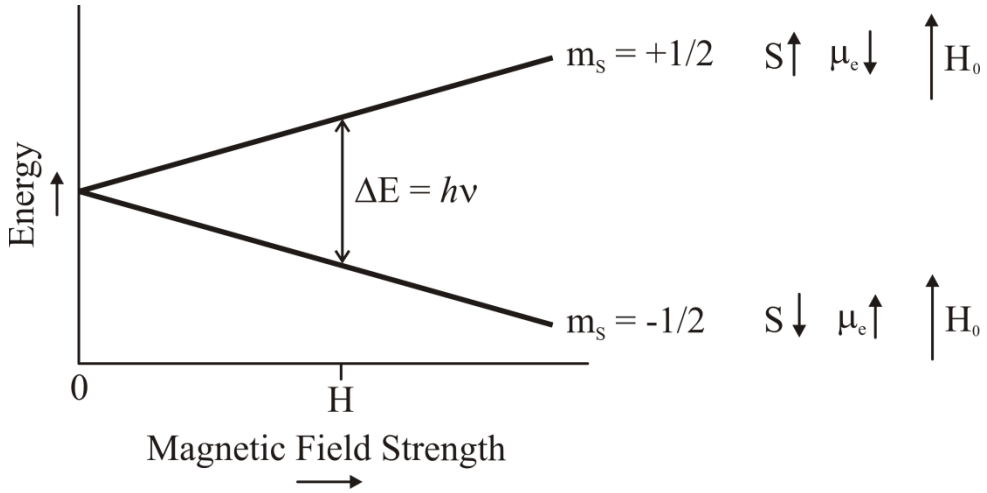

Figure 1.2 The basic resonance condition for an isolated electron spin. The energy separation between the two spin states increases linearly with magnetic field strength, and a transition between states may be stimulated if the indicated condition for radiation frequency and magnetic field is met (see [1.10]). On the right, arrows indicate the alignment of the projection of **S** and $\boldsymbol{\mu_e}$ on the axis of the external field $\mathbf{H_0}$ for each spin state.

Transitions between the spin +½ and spin –½ states can be induced by radiation of the proper frequency and polarization. The energy difference between the spin +½ and spin –½ states is

$$\Delta E = \mathrm{E}\left(S_z = +\frac{1}{2}\hbar\right) - \mathrm{E}\left(S_z = -\frac{1}{2}\hbar\right) = g\beta_e H_z \qquad [1.8]$$

The energy of radiation is proportional to its frequency according to the Planck relation

$$E = h\nu \qquad [1.9]$$

Therefore, the frequency of radiation required to excite a spin-state transition is given by

$$h\nu = g\beta_e H_z \qquad [1.10]$$

As indicated in [1.10], the frequency of radiation required to excite a transition is directly proportional to the magnitude of the applied field, illustrated graphically in Figure 1.2. The proportionality constants between field and frequency include h and β_e, which are invariant, and the g-factor, which depends on the particular system (see section **1.5**).

When the frequency and magnetic field are matched to induce a transition according to [1.10], time-dependent perturbation theory states that the radiation may be treated as a perturbation V(t) with the following probability of transition between states α and β:

$$P_{\alpha\beta} = \frac{2\pi}{\hbar}|\langle\beta|V|\alpha\rangle|^2\delta(\Delta E - h\nu) \qquad [1.11]$$

The Dirac delta $\delta(\Delta E - h\nu)$ serves to impose the requirement of [1.10] that the frequency of radiation match the energy difference between states, and $|\langle\beta|V|\alpha\rangle|^2$ represents the degree to which the states are mixed by the perturbation V(t) (4). The transition probability given by [1.11] is equivalent in either direction (i.e., $|\langle\beta|V|\alpha\rangle|^2 = |\langle\alpha|V|\beta\rangle|^2$), therefore for the two-state electron spin system under consideration here, the transition probability is equivalent for the transition from spin +½ to spin –½ and *vice versa*. A net absorption of radiation will therefore only occur if there is a difference in the population of spins in the two states.

A population difference is observed for an ensemble of spins in the presence of an applied field. The Boltzmann distribution law gives the relative population of spins in the +½ and –½ state at thermal equilibrium as a function of the energy separation between states,

$$\frac{N_+}{N_-} = e^{-\left(\Delta E/kT\right)} = e^{-\left(g\beta_e H_z/kT\right)} \qquad [1.12]$$

where N_+ is the number of spins in the +½ state, N_- is the number of spins in the –½ state, k is the Boltzmann constant, T is the temperature in Kelvin, and ΔE is the energy separation defined in [1.8]. As an example, consider the population difference anticipated at the commonly used X-band frequency, ≈ 9.5 GHz. This corresponds to a resonant field of ≈3400 Gauss, which yields a population ratio $\frac{N_+}{N_-}$ = 0.99847, or a difference of ≈0.08% in the equilibrium population of the two states at room temperature (298 K). As a side note, EPR uses radiation in the microwave frequency range and the different frequencies employed are often referred to using the frequency

band nomenclature originally developed during World War II. X-band is one commonly used frequency range; another is Q-band (≈35 GHz).

The transition between spin –½ and spin +½ states described above constitutes the fundamental spectroscopic transition measured in the EPR experiments reported in this dissertation. However, as implied by the introduction of [1.12], an ensemble of spins is monitored experimentally, and the description of this system developed by Bloch will be explored next.

1.4 The Bloch equations and magnetic relaxation

A phenomenological description of the behavior of an ensemble of spins in an applied field in terms of a single bulk magnetization vector **M** was developed by Felix Bloch in 1946 (1, 35). The time evolution of **M** is defined in the Bloch equations using the characteristic relaxation times T_1 and T_2. An abbreviated description of the Bloch equations is presented below, with the aim of illustrating two key results: the Lorentzian lineshape of the absorption spectrum, and the T_1 and T_2 dependence of the linewidth.

In classical electromagnetism, a magnetic dipole moment $\boldsymbol{\mu}$ in a magnetic field **H** experiences a torque given by $\boldsymbol{\mu} \times \mathbf{H}$, equal to the rate of change of its angular momentum $\frac{d\boldsymbol{\mu}}{dt}$. An electron possesses a magnetic moment proportional to its spin angular momentum as expressed in [1.2], and treating the electron magnetic moment classically yields

$$\frac{d\boldsymbol{\mu}_{\mathbf{e,i}}}{dt} = \gamma \boldsymbol{\mu}_{\mathbf{e,i}} \times \mathbf{H} \qquad [1.13]$$

where γ is the gyromagnetic ratio

$$\gamma = \frac{g\beta_e}{\hbar} \qquad [1.14]$$

The torque defined by [1.13] results in precession of $\boldsymbol{\mu}_{\mathbf{e,i}}$ about the axis of **H** with an angular frequency ω_0 known as the Larmor frequency, given by

$$\omega_0 = \gamma H \quad [1.15]$$

where H is the magnitude of the field. Expression [1.15] is equivalent to [1.10] with the ordinary frequency ν replaced by the angular frequency ω because the motion being described here is rotational. The two are related by

$$\omega = 2\pi\nu \quad [1.16]$$

where ν is in units of s^{-1} and ω is in units of rad* s^{-1}. Thus, the Larmor frequency is both the precession frequency of $\boldsymbol{\mu_{e,i}}$ and the angular frequency required to excite a transition for the energy level separation specified in [1.8]. The total electron magnetic moment, represented by the bulk magnetization vector **M**, is arrived at by a sum over all electrons in the ensemble.

$$\mathbf{M} = \sum \boldsymbol{\mu_{e,i}} \quad [1.17]$$

The motion of **M** in the presence of **H** is analogous to that of the individual $\boldsymbol{\mu_{e,i}}$.

$$\frac{d\mathbf{M}}{dt} = \gamma \mathbf{M} \times \mathbf{H} \quad [1.18]$$

H may be decomposed into two components,

$$\mathbf{H} = \mathbf{H_0} + \mathbf{H_1} \quad [1.19]$$

$\mathbf{H_0}$ is a large steady field applied along a single axis defined as z, and as discussed in section **1.2** it is responsible for splitting the energy levels of the spin states. $\mathbf{H_1}$ is an oscillatory field generated by microwave radiation with frequency defined in [1.8-10], and is usually weak for reasons presented below.

Expression [1.18] defines the rate of change of **M** due to the externally applied field **H**, but it doesn't account for relaxation processed due to internal fields within the sample. The contribution to the time evolution of **M** from relaxation may be defined with respect to the three principal axes x, y, and z using the following expressions:

$$\frac{dM_z}{dt} = -\frac{M_z - M_0}{T_1} \quad [1.20]$$

$$\frac{dM_y}{dt} = -\frac{M_y}{T_2} \quad [1.21]$$

$$\frac{dM_x}{dt} = -\frac{M_x}{T_2} \quad [1.22]$$

According to these expressions, magnetization along the z axis M_z will relax to its equilibrium value M_0 at a rate determined by the relaxation time constant T_1, and magnetization perpendicular to the large steady field $\mathbf{H_0}$ will relax to an equilibrium value of zero with the relaxation time constant T_2.

The time dependence of the bulk magnetization in the presence of the external fields $\mathbf{H_0}$ and $\mathbf{H_1}$ and relaxation mechanisms T_1 and T_2 is

$$\frac{d\mathbf{M}}{dt} = \gamma\mathbf{M} \times \mathbf{H_0} + \gamma\mathbf{M} \times \mathbf{H_1} - \frac{\mathbf{k}(M_z - M_0)}{T_1} - \frac{(\mathbf{i}M_x + \mathbf{j}M_y)}{T_2} \quad [1.23]$$

where **i**, **j**, and **k** are unit vectors in the x, y, and z direction. The torque imposed on **M** by the large uniform field $\mathbf{H_0}$ will result in clockwise precession about z when viewed along the positive z direction. In EPR experiments the $\mathbf{H_1}$ field oscillates with frequency ω_0 and is linearly polarized in a direction perpendicular to $\mathbf{H_0}$. $\mathbf{H_1}$ can be decomposed into two circularly polarized fields precessing in opposite directions, only one of which has a significant effect on the bulk electron magnetization because it precesses in the same direction and at the same frequency (i.e. is coherent). A solution to the Bloch equations is achieved using a transformation from a static frame of reference to a rotating frame defined by the circularly polarized component of $\mathbf{H_1}$ precessing in the clockwise direction, $\mathbf{H_1'}$. **M** is defined in the rotating coordinate system as

$$\mathbf{M} = \mathbf{i}'u + \mathbf{j}'v + \mathbf{k}'M_z \quad [1.24]$$

where $\mathbf{i}'$ is a unit vector in the same direction as $\mathbf{H_1'}$, $\mathbf{j}'$ is a unit vector in the xy-plane perpendicular to $\mathbf{i}'$, and $\mathbf{k}'$ is a unit vector pointing along the z-direction defined by $\mathbf{H_0}$ ($\mathbf{k}' = \mathbf{k}$) (Figure 1.3).

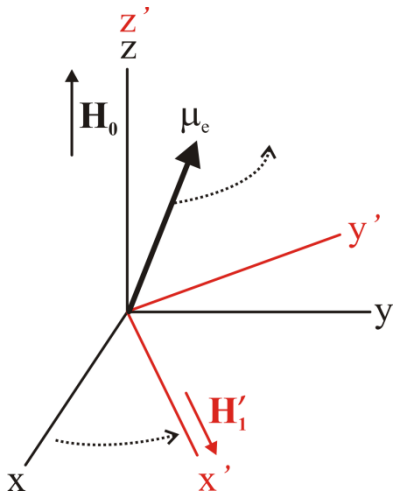

Figure 1.3 The static and rotating coordinate systems used in the Bloch relaxation equations. The static coordinate system is shown in black, with the z-axis defined by the direction of $\mathbf{H_0}$. The rotating coordinate system is shown in red, where the x' axis is defined by the direction of $\mathbf{H_1'}$ and the direction of precession is indicated by a dashed arrow. The magnitude of **M** projected along the x', y', and z' axes of the rotating system is u, v, and M_z, respectively. A magnetic moment vector $\boldsymbol{\mu_e}$ for a single electron spin is shown, and the dashed arrow indicates the precession direction. If the precession frequency of $\boldsymbol{\mu_e}$ matches that of $\mathbf{H_1'}$, a spin state transition may be induced.

The time evolution of u, v, and M_z is

$$\frac{du}{dt} = (\omega_0 - \omega)v - \frac{u}{T_2} \qquad [1.25]$$

$$\frac{dv}{dt} = -(\omega_0 - \omega)u + \gamma H_1 M_z - \frac{v}{T_2} \qquad [1.26]$$

$$\frac{dM_z}{dt} = -\gamma H_1 v - \frac{M_z - M_0}{T_1} \qquad [1.27]$$

The solution to these equations in the steady-state, where $\frac{du}{dt} = \frac{dv}{dt} = \frac{dM_z}{dt} = 0$, is

$$u = \frac{\gamma H_1 T_2^2 (\omega_0 - \omega) M_0}{1 + T_2^2(\omega_0 - \omega)^2 + \gamma^2 H_1^2 T_1 T_2} \qquad [1.28]$$

$$v = \frac{\gamma H_1 T_2 M_0}{1 + T_2^2(\omega_0 - \omega)^2 + \gamma^2 H_1^2 T_1 T_2} \qquad [1.29]$$

$$M_z = \frac{1 + T_2^2(\omega_0 - \omega)^2}{1 + T_2^2(\omega_0 - \omega)^2 + \gamma^2 H_1^2 T_1 T_2} \qquad [1.30]$$

The average power absorbed by the sample over one cycle of the $\mathbf{H_1'}$ field is

$$P(\omega) = \frac{\omega \gamma H_1^2 T_2 M_0}{1 + T_2^2(\omega_0 - \omega)^2 + \gamma^2 H_1^2 T_1 T_2} \qquad [1.31]$$

However, the recorded signal in most commercial EPR spectrometers is not the power absorbed by the sample, but rather the out-of-phase component of **M** in the rotating frame v. In the standard EPR experiment used to measure the resonance lineshape, $\mathbf{H_1'}$ is applied using

microwave radiation at a constant frequency and the large steady field $\mathbf{H_0}$ is slowly swept through the resonance line. This is referred to as a continuous-wave (CW) EPR spectrum, or simply an EPR spectrum. The signal v in terms of field-dependence is

$$v = \frac{\gamma H_1 \mathrm{T}_2 M_0}{1+\gamma^2 \mathrm{T}_2^2 (H_0 - H)^2 + \gamma^2 H_1^2 \mathrm{T}_1 \mathrm{T}_2} \quad [1.32]$$

where the signal maximum occurs when the applied field strength H matches the resonant field strength H_0. The absorption lineshape is Lorentzian (Figure 1.4A and B), and the full width at half-height $\Delta \mathrm{H}_{1/2}$ is

$$\Delta \mathrm{H}_{1/2} = \left[\frac{2}{\gamma \mathrm{T}_2}\right] \mathrm{s}^{-1/2} \quad [1.33]$$

where the saturation factor s is

$$\mathrm{s} = \frac{1}{1+\gamma^2 H_1^2 \mathrm{T}_1 \mathrm{T}_2} \quad [1.34]$$

Most EPR spectrometers employ field modulation (Figure 1.4A), therefore the signal recorded is the derivative $\frac{dv}{dH}$ where the peak-to-peak linewidth $\Delta \mathrm{H}_{\mathrm{pp}}$ is

$$\Delta \mathrm{H}_{\mathrm{pp}} = \left[\frac{2}{3^{1/2} \gamma \mathrm{T}_2}\right] \mathrm{s}^{-1/2} \quad [1.35]$$

The term $\gamma^2 H_1^2 \mathrm{T}_1 \mathrm{T}_2$ in [1.34] is small for weak H_1, and $\mathrm{s} \approx 1$ under these conditions. This is referred to as the non-saturating limit, and in this limit the linewidth given by [1.33] and [1.35] is dependent on T_2 but not T_1.

All CW EPR spectra reported in this dissertation were collected in the non-saturating limit. In this limit the signal is directly proportional to H_1 as indicated by [1.32]. Experimentally, it is the power of the microwave radiation used to generate H_1 that is controlled; the two are related by

$$H_1^2 = \mathrm{KP_w} \quad [1.36]$$

where K is a constant of order 1 and P_w is the microwave power (2). According to [1.36] and [1.32] the signal amplitude is directly proportional to $P_w^{1/2}$ in the non-saturating limit. At higher powers, the relaxation processes are not sufficiently fast to return the system to the equilibrium distribution of spins in the +½ and –½ state (as defined by the Boltzmann distribution [1.12]). When the power exceeds the non-saturating limit the saturation factor deviates from one, resulting in a non-linear dependence of the signal amplitude on $P_w^{1/2}$ and a dependence of the linewidth on T_1 and power instead of just T_2.

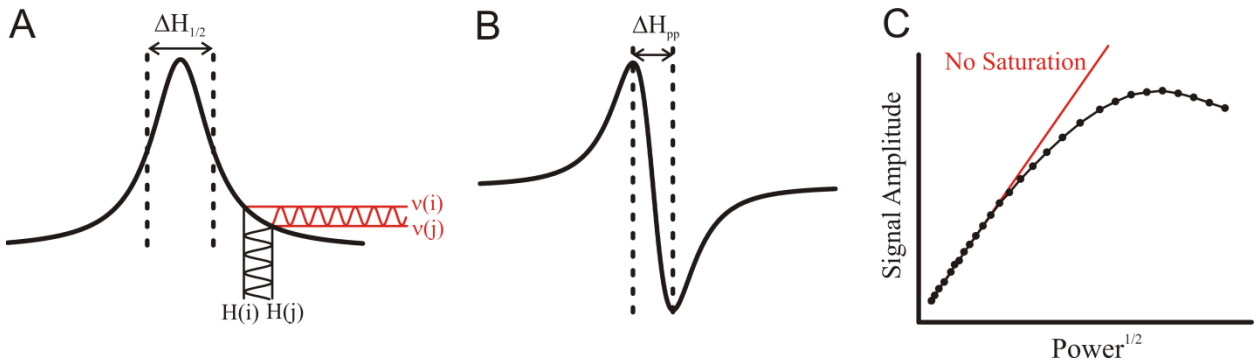

Figure 1.4 The Lorentzian lineshape, magnetic field modulation, and saturation effects. (A) The Lorentzian absorption lineshape is shown, with the full-width at half-height defined by [1.33] labeled. As the magnetic field strength is slowly swept through the resonance line, it is modulated at a fixed frequency with an amplitude given by H(j)-H(i). The amplitude of the signal v will oscillate between v(i) and v(j). (B) The detector monitors the signal at the frequency and phase set by the field modulation, resulting in the first-derivative lineshape shown. (C) Power saturation curve showing the behavior of the signal amplitude as power is increased, and the hypothetical signal amplitude in the absence of saturation (red).

A plot of signal amplitude vs. $P_w^{1/2}$ is called the power saturation curve (Figure 1.4C), and this illustrates the linear relationship at low powers and the reduction in signal amplitude at higher powers compared to the hypothetical non-saturated signal amplitude. A saturation curve may be used to determine the appropriate power range for measuring the CW EPR spectrum to avoid saturation. Alternatively, the saturation behavior may be utilized for determining T_1 and T_2 by measuring the signal amplitude and linewidth across a wide range of applied microwave

power, from the non-saturating to saturating regime (2). A direct measure of T_1 is possible using the saturation recovery method (36).

T_1 relaxation occurs through exchanges of energy between the spin and its surroundings that result in a transition from spin –½ to spin +½ or vice versa. As noted above, energy on the order of the separation between the two energy levels (i.e., radiation at the Larmor frequency) is required to induce such a transition. In early magnetic resonance experiments on crystalline solids, the degree to which the lattice thermal energy in the form of vibrations matched the energy of the spin transition was found to determine T_1 (1), thus this is often referred to as the spin-lattice relaxation time. Stronger coupling results in a more rapid return to equilibrium, therefore T_1 becomes shorter. In solution, mechanisms other than vibrational relaxation are known to be significant (37-41), but the relative contribution of the different mechanisms across different timescales of molecular motion, and a potential temperature-dependence separate from motional effects, is still unresolved.

In the non-saturating limit the Lorentzian linewidth is inversely proportional to T_2 according to [1.33] and [1.35], therefore identifying the factors contributing to T_2 relaxation is crucial for interpreting the spectral lineshape. Application of an oscillating field such as $\mathbf{H_1'}$ perpendicular to the z-axis can result in bulk magnetization vector components M_x and M_y having non-zero values, and the time constant for return of M_x and M_y to their equilibrium value of zero is T_2 as discussed above. Assume for the moment that a non-zero component of bulk magnetization is generated in the xy-plane, and then $\mathbf{H_1'}$ is no longer applied. If the only contribution to the magnetic field in the sample were the externally applied field $\mathbf{H_0}$ (and the field was perfectly homogeneous across the sample), all spins in the ensemble would then precess around the z-axis at exactly the same frequency, and the bulk magnetization component

in the xy-plane would precess about the z-axis indefinitely. However, variation in the local field at each spin causes the precession frequency to vary from spin-to-spin, and local field fluctuations will cause the precession frequency of each individual spin to vary as a function of time. Both effects will result in a loss of coherence (dephasing) of the precession about the z-axis and a return of M_x and M_y to their equilibrium values of zero. In addition to relaxation from local field fluctuations and/or variation, a T_2 relaxation can occur from direct spin-spin interactions *via* Heisenberg exchange, wherein two spins exchange magnetization during collision resulting in a loss of phase coherence (42).

Motional contributions dominate T_2 relaxation in solution, and originate from molecular tumbling that generates local field fluctuations. For example, in the spin-rotational mechanism molecular rotation results in a lag between the position of the electron and the nuclear framework to which it is attached, generating a magnetic moment that interacts with the electron spin through an intramolecular dipole-dipole interaction (43). The dipole-dipole (dipolar) interaction between the magnetic dipole moment of an electron and another dipole depends on the orientation of the vector joining the two with respect to the external field (44), therefore modulation of the dipolar interaction by molecular tumbling will generate local field fluctuations. Intermolecular dipolar interactions between electron spins and dipoles in surrounding solvent molecules may also contribute to T_2 relaxation. An additional mechanism related to orientation-dependence stems from anisotropy of the nitroxide g-factor and nitrogen hyperfine interaction (see section **1.5**). The orientation-dependence of these interactions means the electron spin will experience field fluctuations resulting from variation in these properties as the molecule tumbles in solution (4).

While T_1 and T_2 relaxation were introduced as distinct quantities representing separate processes, they are in fact related. Both T_1 and T_2 relaxation may be influenced by molecular motion, and Redfield theory provides a quantitative description of the dependence of T_1 and T_2 on the correlation time for isotropic rotational motion τ (3, 4, 45, 46). Redfield treated rotational tumbling using a random walk model, and derived the following expressions for T_1 and T_2 relaxation (3):

$$\frac{1}{T_1} = \gamma^2\left(\overline{H_x^2} + \overline{H_y^2}\right)\frac{\tau}{1+\omega_0^2\tau^2} \quad [1.37]$$

$$\frac{1}{T_2} = \gamma^2\left[\overline{H_z^2}\tau + \frac{1}{2}\left(\overline{H_x^2} + \overline{H_y^2}\right)\frac{\tau}{1+\omega_0^2\tau^2}\right] \quad [1.38]$$

According to these expressions, relaxation depends on γ, τ, the Larmor frequency ω_0, and the time-average squared fields $\overline{H_x^2}$, $\overline{H_y^2}$, and $\overline{H_z^2}$, which indicate the magnitude of the field fluctuations along the different axes of the static reference frame.

Field fluctuations along the x- and y-axis contribute to T_1 relaxation, and the magnitude of the contribution depends on the relative values of τ and ω_0 due to the $\omega_0^2\tau^2$ term in [1.37]. When rotational motion is much more rapid than Larmor precession (i.e. $\tau < \omega_0$) $1/T_1$ is proportional to τ, and when rotational motion is much slower than Larmor precession (i.e. $\tau > \omega_0$) $1/T_1$ is proportional to $1/\tau$. The right side of [1.37] is maximized when $\tau\omega_0 = 1$, meaning T_1 will reach a minimum when the inverse of the correlation time (i.e. rate of motion) is equivalent to the Larmor precession frequency. From a classical perspective, this result signifies that local field fluctuations which generate T_1 relaxation are those which induce a magnetic field in the xy-plane that precesses about the z-axis at the Larmor frequency. This is effectively a "static" field in the xy-plane from the perspective of a spin precessing about the z-axis at a matching frequency. As a result, precession is induced about the field in the xy-plane, changing

the net magnetization along z (T_1 relaxation); similar to $\mathbf{H_1'}$ defined above but highly localized (not uniform across the sample).

T_2 has a similar dependence to that of T_1 on fluctuating fields along the x- and y-axis, indicating that in addition to changing magnetization along the z-axis, these fluctuations cause dephasing of the precession about the z-axis (T_2 relaxation). In this respect, T_2 relaxation may be said to be influenced by T_1 relaxation. However, there is an additional term in expression [1.38] that indicates a dependence of T_2 on fluctuations along the z-axis. The z-axis contribution is influenced by τ but not ω_0, thus there is no minimum in T_2 predicted by Redfield theory. Instead, when $\tau > \omega_0$ the T_1-like term in [1.38] becomes negligible, T_2 relaxation is dominated by z-axis fluctuations, and $1/T_2$ is proportional to τ. Therefore, for rotational motion slower than the Larmor frequency, T_2 relaxation is not influenced by T_1 and the spectral linewidth defined by [1.33] and [1.35] is dependent on T_2 alone.

As mentioned above, Redfield theory uses a random-walk model for rotational motion, and field fluctuations due to the random walk cannot drive relaxation if relaxation occurs faster than a random-walk step. As τ increases, eventually it approaches equivalent values to T_2, and Redfield theory is no longer applicable. For nitroxide radicals in solution, Redfield theory is not applicable for τ longer than 1 ns, therefore it explains T_1 and T_2 relaxation for only a portion of the motional time window relevant to the EPR spectral lineshape as discussed in section **1.6**. At τ longer than the Redfield limit, other theoretical treatments and experimental observations have confirmed that T_1 remains much longer than T_2 (37, 38, 47-49). For nitroxide-labeled proteins in solution, T_1 ranges from ≈1-6 μs (36, 50) and T_2 ranges from ≈10-30 ns (2), such that T_1 makes only minimal contribution to the observed T_2.

1.5 The Spin Hamiltonian

In section **1.3**, the resonance condition for an isolated electron spin was discussed, and the resonant field position (i.e. magnetic field strength at which a spin transition will occur) was shown in [1.10] to be dependent on the frequency of radiation and the g-factor. The shape of the resonance line was described in section **1.4**, as well as the influence of relaxation on the linewidth. In both section **1.3** and **1.4**, the influence of attachment of the electron to a nucleus was not considered. For nitroxides the unpaired electron is bound to a nitrogen with spin quantum number $I = 1$ (^{14}N isotope, 99.6% natural abundance), the effects of which will be considered in this section.

As discussed in section **1.3**, the g-factor is a proportionality constant relating the frequency of radiation with the magnetic field of resonance for the Zeeman interaction between an electron spin and an applied magnetic field. For a free electron, the g-factor is ≈2.002319, but this value differs for electrons bound to a nucleus due to orbital angular momentum. The orbital angular momentum for nonlinear polyatomic free radicals like nitroxides is largely quenched (51), but spin-orbit coupling re-introduces a small orbital angular momentum (34), and the effect of the resulting magnetic moment is accounted for by variation in the g-factor. In this manner, the deviation of the g-factor from that of a free electron can be thought of as a measure of the degree of spin-orbit coupling. The orbital magnetic moment need not be aligned with the electron spin magnetic moment, therefore this interaction is anticipated to be anisotropic and the g-factor is represented as a symmetric 2^{nk} rank tensor **g**. The **g**-tensor is diagonalized by rotation to the principal axis system, reducing it to the three principal values g_{xx}, g_{yy}, and g_{zz}. The Hamiltonian defining the energy of the Zeeman interaction is then, using matrix formalism,

$$\hat{H}_g = \beta_e \mathbf{S} \cdot \mathbf{g} \cdot \mathbf{H} \qquad [1.39]$$

As mentioned above, in nitroxides the unpaired electron is bound to an ^{14}N nucleus with nuclear spin angular momentum $I = 1$. In addition to influencing the g-factor, nuclei with non-zero spin values such as this will have an interaction with the electron spin called the hyperfine interaction, resulting in splitting of the EPR resonance absorption lines referred to as hyperfine splitting. In essence, the nuclear magnetic moment alters the local field at the electron, resulting in either an increase or decrease in the external field strength required to excite a transition. Recall that for an electron, there are two possible quantum states in the presence of an applied field, the +½ and –½ state, with the relative energies shown schematically in Figure 1.2. The nuclear magnetic moment can have three possible orientations corresponding to the $m_I = +1$, 0, and -1 states, and thus each spin state of the electron is split into three energy levels The selection rules of quantum mechanics dictate that $\Delta m_S = \pm 1$, $\Delta m_I = 0$, resulting in the three allowed transitions illustrated in Figure 1.5. In the $m_I = +1$ state, the nuclear magnetic moment increases the effective local field at the electron, such that for a given applied field the magnitude of the electron spin energies is increased. In the $m_I = -1$ state, the nuclear magnetic moment decreases the effective local field at the electron, such that for a given applied field the magnitude of the electron spin energies is decreased. The nuclear magnetic moment is zero for the $m_I = 0$ state and will not influence the energy of the electron spin states. In EPR, a constant frequency of microwave radiation is applied and the magnetic field is swept, and thus the applied field at which the resonance condition is met is shifted. In comparison to the resonant field for the $m_I = 0$ state, the field shift is up in the case of the $m_I = -1$ state and down in the case of the $m_I = +1$ state.

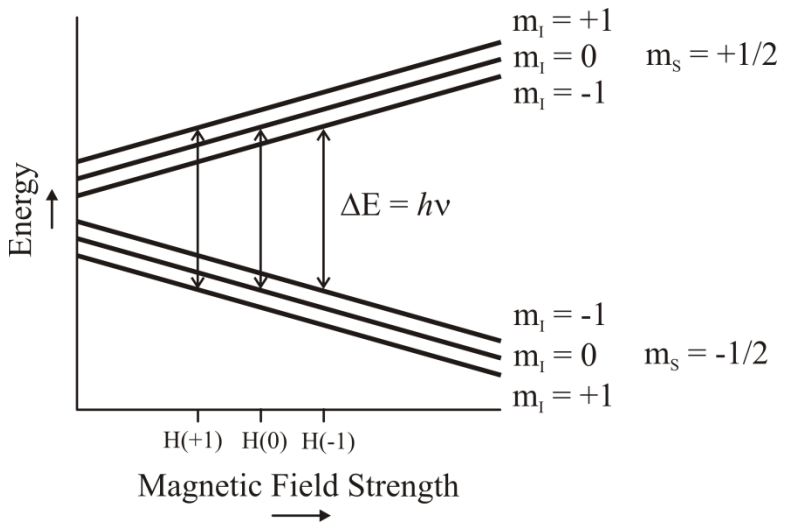

Figure 1.5 The resonance condition for an electron spin bound to a spin = 1 nucleus. The energy for each of the six states of the system is shown as a function of magnetic field strength. The three nuclear spin states result in three resonance lines, each corresponding to a transition between electron spin states stimulated when the indicated conditions for radiation frequency and magnetic field are met. The m_S and m_I values for each state are indicated on the right.

The hyperfine interaction has contributions from two sources: a dipolar interaction and Fermi contact interaction. The dipolar interaction between the nuclear and electron magnetic moments is a through space interaction with a Hamiltonian of the following form:

$$\widehat{H}_{A,dip} = g_0 \beta_e g_N \beta_N \left(\frac{\mathbf{I} \cdot \mathbf{S}}{r^3} - \frac{3(\mathbf{I} \cdot \mathbf{r})(\mathbf{S} \cdot \mathbf{r})}{r^5} \right) \quad [1.40]$$

where g_0 is the isotropic g-factor of the electron calculated by averaging the principal values of the **g**-tensor, g_N is the nuclear g-factor, β_N is the nuclear magneton, **I** is the nuclear angular momentum in units of $\hbar$, **r** is the interspin vector, and r is the distance between the electron and nucleus. The dot products of **I** and **S** with **r** are orientation-dependent, therefore the hyperfine interaction is anisotropic in non-spherical orbitals (e.g. p, d, f). The nitroxide nitrogen is sp^2 hybridized, and the unpaired electron occupies a 2p orbital highly localized to the nitrogen atom, giving it significant p_z character.

The Fermi contact interaction arises from direct electron contact with the nucleus, indicating that the electron has density at the nuclear center. Non-zero electron density at the

nucleus only occurs for s orbitals, therefore the electron has some sp^2 orbital occupancy. The Fermi contact interaction is isotropic and is represented with the Hamiltonian

$$\hat{H}_{A,\mathrm{Fermi}} = a\mathbf{I}\cdot\mathbf{S} \qquad [1.41]$$

where a is the isotropic hyperfine coupling constant

$$a = \frac{8\pi g_0 \beta_e g_N \beta_N}{3}|\psi(0)|^2 \qquad [1.42]$$

In [1.42], $|\psi(0)|^2$ is the electron wavefunction probability density at the origin of the nucleus. The total hyperfine interaction can be represented using matrix notation using the following Hamiltonian:

$$\hat{H}_A = \mathbf{S}\cdot\mathbf{A}\cdot\mathbf{I} \qquad [1.43]$$

A, like **g**, is a second rank tensor with the same principal axis sytem. **A** has principal values A_{xx}, A_{yy}, and A_{zz} and accounts for both the dipolar and Fermi contact interactions.

The polarity of the local environment is an additional factor that may influence the principal values of the **g** and **A** tensor (52). Although the electron primarily resides on the nitrogen atom in a 2p orbital, as mentioned above, it is somewhat delocalized along the NO bond, giving it some π-bond character. Spin labels at buried sites in globular proteins or along the transmembrane portion of membrane-bound proteins are in relatively apolar environments, causing electron delocalization along the NO bond to increase. Highly polar environments such as bulk water cause the electron density to become more concentrated to the nitrogen, increasing the density at the nitrogen nucleus and therefore increasing the isotropic hyperfine splitting and the g-factor deviation from the free electron value.

For nitroxides, ^{14}N provides the largest hyperfine splitting, but other nuclei on the nitroxide ring contribute to hyperfine structure. The twelve equivalent ^{1}H nuclei on the four methyl groups cause a splitting of ≈0.2 G, and the single ^{1}H on C4 of the ring causes a hyperfine

splitting of ≈0.5 G (53). This splitting is incredibly small compared to the ^{14}N hyperfine splitting, and is typically not observed in SDSL EPR due to any of a number of sources of linewidth broadening. One such source is a Heisenberg exchange contribution to T_2 relaxation caused by collision of the nitroxide with dissolved molecular oxygen. An investigation of oxygen Heisenberg exchange broadening found that at the physiological temperature of 37^{o}C, an oxygen concentration of ≈0.18 mM is sufficient to broaden the nitroxide linewidth of the $m_I = 0$ nitrogen line to the point where the proton hyperfine structure is no longer resolved (54). The concentration of oxygen in water at room temperature is ≈0.3 mM (55), and the proton hyperfine interaction leads to a peak-to-peak linewidth of ≈1 G (in the absence of further broadening from other sources). Even in the absence of dissolved oxygen, the typical values used for microwave power and field modulation amplitude are sufficient to broaden out the proton hyperfine structure such that the proton hyperfine interaction leads to an observed broadening of linewidths rather than splitting of resonance lines.

Combination of [1.39] and [1.43] yields the Hamiltonian defining the resonance energy of the nitroxide, referred to as the Spin Hamiltonian.

$$\hat{H} = \beta_e \mathbf{S} \cdot \mathbf{g} \cdot \mathbf{H} + h\mathbf{S} \cdot \mathbf{A} \cdot \mathbf{I} \qquad [1.44]$$

This Hamiltonian is sufficient to explain spectra of a single nitroxide spin label attached to a protein, although a complete Hamiltonian for this system includes additional terms that are omitted in [1.44] (2). For example, a Zeeman term for the interaction of the nuclear spin with the external field is negligible because the magnetic field experienced by the nuclear spin due to the field created by the electron is much larger in magnitude than the externally applied field. The nuclear contribution to the Hamiltonian is dominated by the hyperfine interaction rather than the nuclear Zeeman interaction, therefore only the former is included in [1.44].

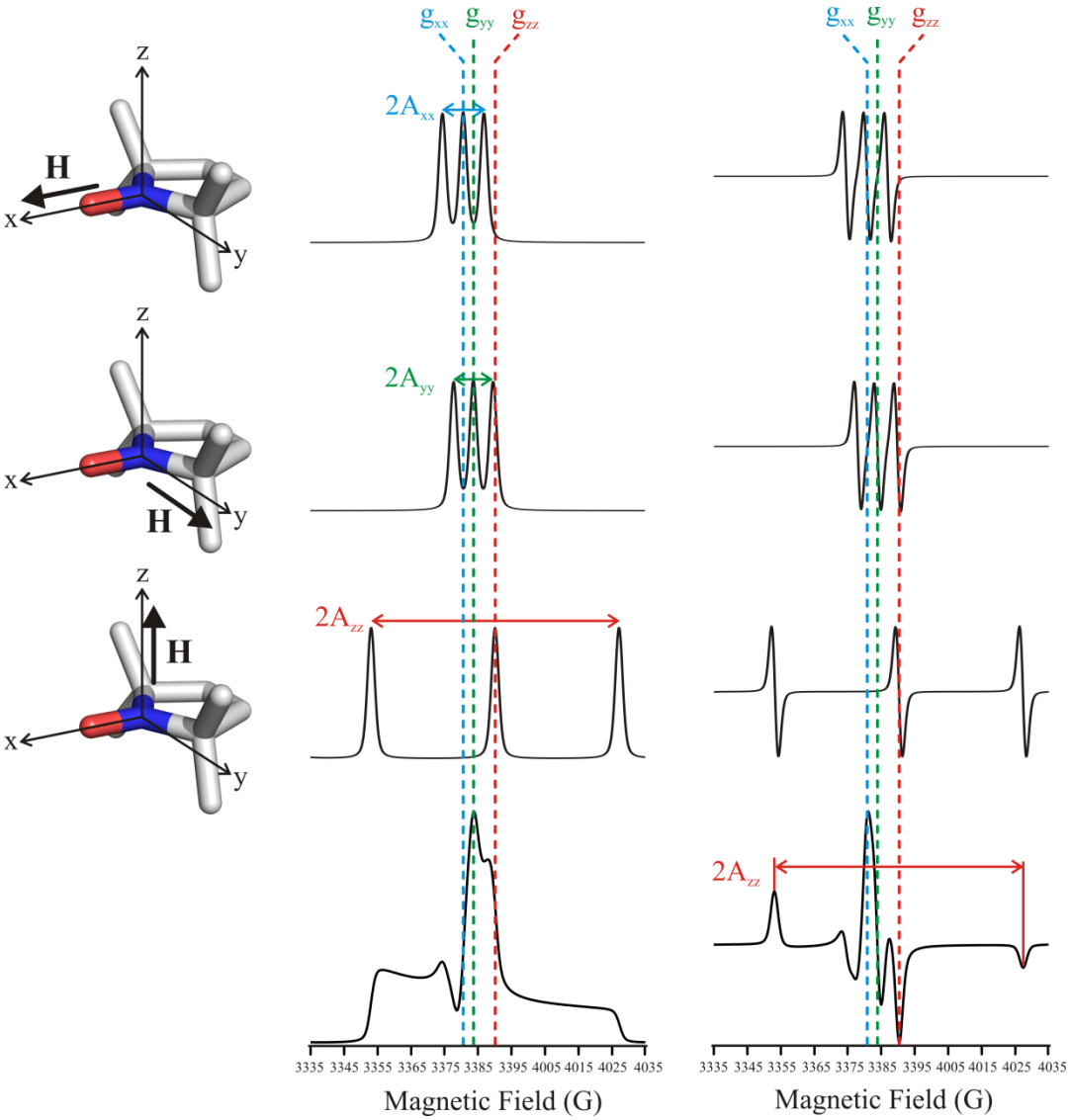

Figure 1.6 The rigid-limit spectrum of a nitroxide spin label. The absorption (center) and first-derivative (right) spectra of a single crystal doped with a nitroxide spin label reagent, where the crystal is oriented such that the external field **H** is aligned with the molecular principal axis system as indicated on the left. The molecular z-axis runs along the long axis of the nitrogen p orbital, the x-axis runs along the NO bond, the y-axis lies in the plane of the ring, perpendicular to x and z. If the crystal is crushed, the molecular orientations of the individual nitroxides are randomly distributed with respect to **H**, and the result is a powder spectrum shown at the bottom. The relationship of the principal A and g values to the spectral splitting and field position are indicated. Spectra were simulated at a frequency of 9.5 GHz using the principal values A_{xx} = 6.2 G, A_{yy} = 5.9 G, A_{zz} = 37 G, g_{xx} = 2.0078, g_{yy} = 2.0060, and g_{zz} = 2.0022.

As described above, both the Zeeman and hyperfine term in [1.44] are anisotropic, meaning the effective g-factor and hyperfine interaction energy depends on the relative orientation of the molecule with the external field. When the external field is aligned with one of

the three principal axes of the molecular frame, the principal values of the **g** and **A** tensors define the resonance position of the three hyperfine lines as shown in Figure 1.6. For the R1 side chain at solvent-exposed surface sites, the principal values A_{xx} = 6.2 G, A_{yy} = 5.9 G, A_{zz} = 37 G, g_{xx} = 2.0078, g_{yy} = 2.0060, and g_{zz} = 2.0022 were previously reported (56). The **g** tensor principal values determine the central field position, and the **A** values determine the splitting between the three resonance lines.

For an arbitrary orientation of the external field direction with respect to the molecular frame, defined by the polar and azimuthal angles θ and ϕ, the **g** and **A** tensors are reduced to the scalar values $g(\theta, \phi)$ and $A(\theta, \phi)$ and the resonance energy may be expressed as

$$\Delta E = h\nu = \beta_e g(\theta, \phi) H_{res} + hA(\theta, \phi) m_I \quad [1.45]$$

Rearranging [1.45] to solve for the magnetic field H_{res} yields

$$H_{res} = h\left(\frac{\nu - A(\theta,\phi) m_I}{\beta_e g(\theta,\phi)}\right) \quad [1.46]$$

which gives the three resonant field values for the three m_I values at a specific microwave frequency and orientation of the nitroxide. The EPR spectrum of a sample of nitroxides that are randomly oriented can be determined by a weighted sum over all angles. The spectrum thus calculated assumes a complete absence of motion.

In solution, the tumbling motion of the nitroxide results in an averaging of the anisotropy in the g-factor and hyperfine interaction (hereafter, together these are referred to as the magnetic anisotropies). The time scale of motion required to average the magnetic anisotropies can be understood in terms of a Bloch-McConnell multi-site exchange process (57-59). In this framework, states that give rise to distinct resonance positions exhibit broadening of the resonance line of each state and ultimately coalescence into a single resonance line as the rate of exchange increases. For the EPR spectrum of nitroxides, each orientation of the nitroxide with

respect to the external field corresponds to an individual state. Nitroxides with different orientations generate different resonance lines, as explained above, and exchange corresponds to reorientation resulting from molecular motion. The rate of motion required to average the different resonance lines such that they coalesce into a single line is approximately equal to the difference in the frequency of resonance, although other factors such as the intrinsic linewidth of each orientation and the relative populations in the absence of exchange also play a role. Thus, motional averaging of nitroxide magnetic anisotropies occurs with correlation times of

$$\tau \approx \frac{\hbar}{(A_{zz}-A_{xx})g_e\beta_e} \qquad [1.47]$$

and

$$\tau \approx \frac{\hbar}{(g_{xx}-g_{zz})\beta_e H} \qquad [1.48]$$

Inputting the principal A and g values given above for nitroxides attached to solvent-exposed sites on proteins, g_{xx}-g_{zz} ≈ 0.0056 and $A_{zz} - A_{xx}$ ≈ 31 G (9, 30), resulting in a correlation time of ≈6.9 ns and ≈1.8 ns, respectively. As correlation times become slower than the values given, the magnetic anisotropies are not averaged and the spectrum broadens, resulting in a spectrum approaching that given by a sum over [1.46] at sufficiently slow motion. As correlation times become faster than these values, the separate resonance lines for the different $g(\theta,\phi)$ and $A(\theta,\phi)$ merge and the spectrum exhibits three sharp resonance lines at positions given by the isotropic values of g and A: $\frac{1}{3}(g_{xx}+g_{yy}+g_{zz})$ and $\frac{1}{3}(A_{xx}+A_{yy}+A_{zz})$. It should be noted for the hyperfine anisotropy that complete motional averaging of the dipolar interaction results in zero splitting, but the Fermi contact interaction has no orientation-dependence and is therefore unaffected by molecular tumbling. Thus, the isotropic hyperfine splitting at very fast motions is due purely to Fermi contact.

The orientation-dependence of the EPR spectrum in combination with motional averaging is what gives it the structural and dynamical sensitivity discussed in the next section.

1.6 Lineshape analysis

The primary determinants of the CW EPR spectral lineshape for nitroxide-labeled proteins are anisotropy in the g-factor and hyperfine interaction (section **1.5**) and T_2 relaxation broadening (section **1.4**), both of which are sensitive to molecular motion. Internal spin label side chain motion as well as protein motion in the region local to the spin-labeled site contribute to the overall motion of the nitroxide; therefore local protein dynamics are encoded in the spectral lineshape. In this respect, CW EPR is a spectroscopy of motion, and a rigorous analysis of the spectral lineshape can provide quantitative information about the rate and angular amplitude (order) of nitroxide motion, as discussed below.

1.6.1 The intrinsic timescale of CW EPR. The time range typically specified as the region for sensitivity of the lineshape to molecular motion (specified in terms of correlation time) is 0.1-100 ns for X-band, because this is the timescale wherein motional contributions to T_2 relaxation broadening and averaging of magnetic anisotropies will significantly affect the spectral lineshape (Figure 1.7). The frequency difference of the anisotropies (splitting) determines the timescale of motion required to produce averaging of magnetic anisotropies (57-60), and since g-anisotropy is dependent on the microwave frequency, the time window for motional sensitivity of the lineshape can be shifted somewhat by operating at different EPR frequency bands.

When the motion is sufficiently fast to completely average out the magnetic anisotropies ($\tau < 0.1$ ns), referred to as the isotropic limit, the spectrum is becomes highly simplified to three sharp resonance lines of equivalent height and width. The resonance positions are specified by

the isotropic g-factor and hyperfine splitting values and may be calculated, for example, by the Breit-Rabi equation (1, 61-63). At the other end of the motional spectrum ($\tau > 100$ ns), the motion is too slow to produce averaging of magnetic anisotropy at X-band; this is referred to as the rigid limit. The spectral lineshape in this limit is relatively insensitive to motion and approaches that of a powder spectrum as correlation times approach infinity. Motional effects still contribute to T_2 relaxation until the true rigid limit (solid state) is reached, at which point T_2 relaxation contributions to the Lorentzian linewidth originate in solid-state spin-spin interactions such as proton (64, 65) and instantaneous diffusion (66). As such, there are small variations in lineshape in this motional regime due to differential T_2 broadening of homogeneous linewidths, but these are difficult to reliably measure experimentally. Proteins exhibit important functional motions on timescales slower than 100 ns. It is therefore important to be able to access motion on this timescale, which can be achieved using the EPR techniques of electron double resonance (17), saturation recovery (36), and saturation transfer spectroscopy (67-69).

1.6.2 Lineshape analysis in different motional regimes. Between the rigid and the isotropic limits ($\tau = 0.1 - 100$ ns), incomplete motional averaging of magnetic anisotropies and variation in T_2 relaxation broadening result in exquisite sensitivity of the spectral lineshape to both the rate and angular amplitude (order) of motion. In the fast motional regime ($\tau \approx 0.1 - 2$ ns), magnetic anisotropies are sufficiently averaged out such that three resonance lines are observed, similar to those predicted using the Breit-Rabi equation in the isotropic limit. However, the line heights and widths vary substantially for the different nuclear manifolds, indicating that the magnetic anisotropies are not fully averaged. Kivelson (70) and McConnell (6) developed expressions relating peak-to-peak linewidths and line heights to the rotational correlation time for isotropic motion, although the principal components of the **g** and **A** tensors

must be known (2, 71, 72). In the slow motional regime ($\tau \approx 10 - 100$ ns), Freed developed an empirical equation for determining the rotational correlation time from the effective A_{zz} splitting (A'_{zz}), which is the field separation of the low field peak and the high field trough (Figure 1.7) (49). These models provide quantitative measures of motion from directly measurable spectral quantities, but are unfortunately only applicable to a portion of the 0.1-100 ns time window and assume isotropic motion of the nitroxide, which is a limitation discussed next.

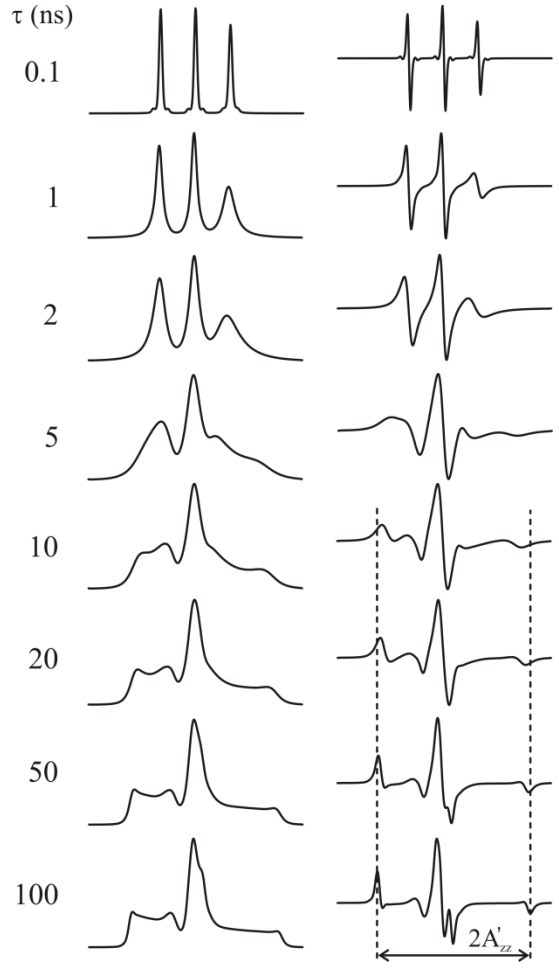

Figure 1.7 The effect of isotropic motion on the EPR spectral lineshape. Absorption (left) and first-derivative (right) spectra were simulated using the isotropic rotational correlation times indicated. The effective A_{zz} splitting (A'_{zz}) becomes resolved for τ longer than ≈10 ns. Spectra were simulated at a frequency of 9.5 GHz using the principal values A_{xx} = 6.2 G, A_{yy} = 5.9 G, A_{zz} = 37 G, g_{xx} = 2.0078, g_{yy} = 2.0060, and g_{zz} = 2.0022.

In the analyses of motional averaging discussed to this point, it is assumed that the nitroxide is tumbling isotropically in solution. However, in SDSL the nitroxide is covalently attached to a macromolecule, and the effective nitroxide τ is related to the correlation times for

protein rotary diffusion, local backbone fluctuations, and internal motion of the nitroxide side chain according to

$$\frac{1}{\tau} = \frac{1}{\tau_{\text{protein,rotary}}} + \frac{1}{\tau_{\text{protein,local}}} + \frac{1}{\tau_{\text{side chain}}} \qquad [1.49]$$

It is important to note that [1.49] is strictly valid only when the motional modes are independent and isotropic. According to [1.49], the rates (i.e. inverse correlation times) of the different motions are additive, and therefore the fastest motion will be the dominant factor in determining the spectral lineshape. For the CW EPR experiments reported in this dissertation, the contribution from protein rotary diffusion was minimized by the addition of the macroscopic viscogen Ficoll-70. This viscogen has negligible osmolytic effect (20) and therefore will not exert an osmotic pressure that may complicate the interpretation of high hydrostatic pressure effects that are the focus of this dissertation. The addition of the viscogen results in tumbling of the protein that is so slow that it can be approximated to be stationary, but does not influence internal motion of the spin label side chain (19, 20). The two important sources of motion are then rotameric motion of the spin label side chain and local backbone motion of the protein. Rotational motion from these sources is frequently restricted about the principal axes to differing degrees, resulting in differential averaging of the x, y, and z components of the magnetic anisotropies. In such cases, a more complex model is needed that can account for variations in both the rate and amplitude of motion. For the lineshape analysis presented in this dissertation, spectra are simulated according to a theoretical treatment of nitroxide motion developed by Freed and co-workers (29, 49) that can model isotropic and anisotropic motion across the entire relevant motional range of 0.1-100 ns.

1.6.3 The stochastic Liouville equation and microscopic order macroscopic disorder model. In the theory developed by Freed (49), the spectrum is calculated using a stochastic

Liouville equation (SLE), which is a semiclassical master diffusion equation in which the spins are treated quantum mechanically but the motional effects are treated as classical rotational diffusion. This approach allows calculation of spectra across the entire relevant motional range. The calculated spectrum is fit to the experimental one by least-squares minimization of the model parameters.

The microscopic order macroscopic disorder (MOMD) model is a motional model that may be implemented in simulations that use the SLE, and applies to spin-labeled lipid membranes and proteins. In this model, protein tumbling is assumed to be sufficiently slow that it is in the rigid limit, and the proteins are assumed to be randomly oriented with respect to the external field (macroscopic disorder). Tethering of the spin label to the protein results in restricted (anisotropic) motion of the label with respect to the protein (microscopic ordering). The parameters of primary importance in the determination of the spectral lineshape are discussed below, although a full description of all parameters in the MOMD model are discussed in detail in (29) for interested readers.

1.6.3.1 Coordinate frames. Three coordinate frames are typically employed in MOMD modeling of nitroxide motion (Figure 1.8). The magnetic frame (x_m, y_m, z_m) axes align with the principal axis system of the tensors **g** and **A**, which are coincident for R1 and its derivatives. This frame is fixed with respect to the structure of the nitroxide. The rotational diffusion frame (x_R, y_R, z_R) is principal axis system for the rotational diffusion tensor. Rotation about each axis is defined by an independent diffusion constant based on a Brownian model for rotation. The orientation of the three axes depends on the geometry of the label and its attachment to the protein backbone, and is generally not coincident with the magnetic frame. The diffusion frame

is related to the magnetic frame through the diffusion tilt angles α_D, β_D, and γ_D. As such, the diffusion frame is fixed with respect to the structure of the nitroxide.

The rotational diffusion axes will move as the nitroxide position fluctuates due to internal bond rotations of the R1 side chain and local protein backbone motion, but the attachment to the protein will generally result in partial ordering of this motion (anisotropy). For modeling motion of spin labels attached to proteins, this ordering is described with respect to a uniaxial director frame z_D, which is fixed with respect to the global protein structure. This is the only frame not fixed with respect to the nitroxide structure. z_D serves as the symmetry axis of the ordering potential employed in the MOMD model (see below) to constrain the extent of the spatial reorientation of the nitroxide.

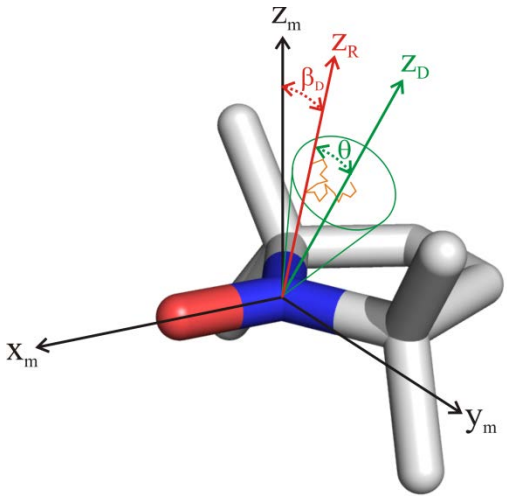

Figure 1.8 Principal frames employed in the MOMD model. The magnetic frame (x_m, y_m, z_m) is coincident with the molecular frame of the nitroxide. The z-axis of the diffusion frame (z_R) is fixed with respect to the magnetic frame at a position defined by the angle β_D. The uniaxial director frame (z_D) is fixed to the protein. z_R reorients with respect to z_D over time (orange line), and θ is the instantaneous angle between z_R and z_D. The average θ is used to calculate the order parameter S.

1.6.3.2 Magnetic parameters. These are the **g** and **A** tensor principal values (g_{xx}, g_{yy}, g_{zz}, A_{xx}, A_{yy}, A_{zz}) of the Spin Hamiltonian. They are typically determined experimentally using spectra of crystals at different orientations (73), fitting rigid limit spectra (56), or fitting spectra collected at multiple frequencies (74, 75). As mentioned in section **1.5**, local polarity can alter the **g** and **A** tensor values, so these values vary between solvent exposed surface sites and buried sites on globular proteins or transmembrane sites on membrane proteins. However, the values are

dictated primarily by the structure of the nitroxide ring and substituents, and typically are allowed to vary only slightly during fitting.

1.6.3.3 Rate. The rotational diffusion constants R_{xx}, R_{yy}, and R_{zz} define the rate of rotation about the principle axes of the diffusion frame x_R, y_R, and z_R, respectively. The values of these parameters are specified in the fitting program as $\log_{10}$ of the actual principal component values to make them the same order of magnitude as the non-dynamical fitting parameters. In the case of isotropic motion, these three constants will be equivalent and the x, y, and z components of the magnetic anisotropies will be averaged to the same degree (Figure 1.7). As discussed above, the nitroxide motion may be anisotropic, and in this case the values of R_{xx}, R_{yy}, and R_{zz} will not be the same and averaging of the x, y, and z components of the magnetic anisotropies will vary. An effective rotational correlation time can be calculated using

$$\tau = \frac{1}{6\times 10^{\bar{R}}} \qquad [1.50]$$

where $\bar{R}$ is the geometric mean of R_{xx}, R_{yy}, and R_{zz},

$$\bar{R} = \left(R_{xx}R_{yy}R_{zz}\right)^{1/3} \qquad [1.51]$$

In many cases spectra are well-characterized using an "axially symmetric" model for rotational diffusion, meaning rotation about two of the three principle diffusion axes is equivalent and slower than rotation about the third axis. The extreme case of this is shown in Figure 1.9 to illustrate what is commonly referred to as x-, y-, and z-anisotropy. To generate the spectra in this figure, the diffusion frame was taken to be equivalent to the magnetic frame ($\alpha_D = \beta_D = \gamma_D = 0$). Rotation about one axis is sufficiently fast to fully average the magnetic anisotropy of the other two, but rotation about the other two is sufficiently slow such that no averaging of the magnetic anisotropies occurs for the first axis (e.g. in Figure 1.9A, rotation about x is fast, and rotation about y and z is slow). Interestingly, the spectrum resulting from z-anisotropy is very similar to a

rigid limit spectrum (compare Figures 1.9C and 1.6). This illustrates the fact that averaging of x and y components of the magnetic anisotropies has little effect on the spectral lineshape, because the x and y magnetic parameter values are so similar. It is averaging of the x and y components with the z component of the magnetic anisotropies that leads to significant spectral changes.

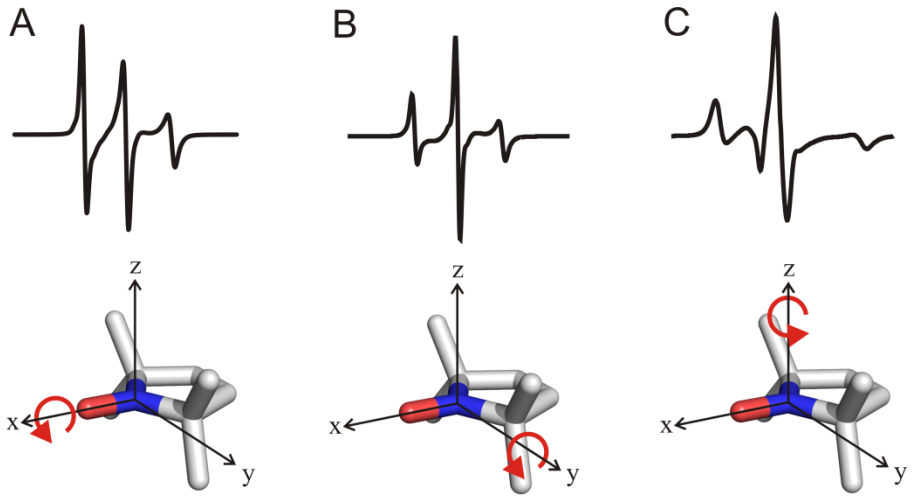

Figure 1.9 Principal axis anisotropies. Simulated spectra for rapid motion ($\tau = 0.1$ ns) about the (A) x-axis, (B) y-axis, and (C) z-axis of the molecular frame. To simulate the spectra, τ was set to 0.1 ns for the axis indicated by the red curved arrow, and 20 ns for the other two axes. A frequency of 9.5 GHz was used, and the principal magnetic values were $A_{xx} = 6.2$ G, $A_{yy} = 5.9$ G, $A_{zz} = 37$ G, $g_{xx} = 2.0078$, $g_{yy} = 2.0060$, and $g_{zz} = 2.0022$.

It should be noted that in this discussion of x-, y-, and z-anisotropy and in Figure 1.9, the diffusion tilt angles were taken to be zero, so that the diffusion frame and magnetic frame are coincident. Thus, the values of R_{xx}, R_{yy}, and R_{zz} correspond to rotational rates about the x, y, and z axes of the magnetic frame (x_m, y_m, z_m), respectively. However, non-zero values of these angles can rotate the diffusion frame to change how the magnetic parameters are mixed. For example, $\alpha_D = 0$, $\beta_D = 90^o$, $\gamma_D = 0$ causes rotation of the z_R axis to align it with x_m, resulting in averaging of z and y components of the magnetic anisotropies as a function of R_{zz}. $\alpha_D = 90^o$, $\beta_D = 90^o$, $\gamma_D = 0$ causes rotation of the z_R axis to align it with y_m, resulting in increased averaging of z and x components of the magnetic anisotropies as R_{zz} increases.

1.6.3.4 Order. The motional anisotropy associated with different rates of rotation about the principal axes of the diffusion frame was described above. An additional consideration is that the spin label will likely not freely rotate about each principal axis, due primarily to the attachment of the label to the protein. The restriction in the range of orientations of the spin label about one or more of these axes functions as an additional source of anisotropy. This restriction in motion is accounted for using a restoring (ordering) potential:

$$U(\Omega) = -kT \sum_{L,K} c_K^L D_{0K}^L(\Omega) \qquad [1.52]$$

The ordering potential $U(\Omega)$ is a function of the Euler angles relating the diffusion frame to the director frame, $D_{0K}^L(\Omega)$ are a restricted set of spherical harmonics, and the weighting coefficients c_K^L are the parameters fitted in the simulation. The uniaxial director frame z_D serves as the symmetry axis for the restoring potential, and the Euler angles Ω define the instantaneous position of the z_D axis with respect to the diffusion frame. There are five terms in this potential, although in most simulations only the first term is required to achieve a good fit. In this case, the potential becomes

$$U(\theta) = -\frac{1}{2} kT c_0^2 (3\cos^2\theta - 1) \qquad [1.53]$$

where θ is the angle between z_D and z_R. Expression [1.53] defines an energetic cost or gain as θ increases from 0^o to 90^o, depending on the sign and magnitude of the coefficient c_0^2. If c_0^2 is positive, the shape swept out by the z_D axis is approximately conical, where the size of the cone decreases as c_0^2 increases.

It is important to recall that the director frame is fixed with respect to the macromolecule, and therefore it will vary in position with respect to the nitroxide (i.e. the diffusion and magnetic frames). This description of a director frame that varies in position with respect to the diffusion frame is suggestive of a moving macromolecule and a static nitroxide, but an equivalent and

more appropriate perspective is to view the motion of the nitroxide with respect to a fixed macromolecule. In this perspective, the ordering potential describes the anisotropic distribution of nitroxide (diffusion frame) orientations with respect to the macromolecule (director frame), and the conical area swept out is that of the z_R axis with z_D serving as the center. The conical distribution of z_R axis orientations shown in Figure 1.8 is an illustration, and there is no rigid boundary for the possible orientations as a result of the ordering potential. This potential results in a probability distribution where the smaller θ angles are favored to an extent determined by the magnitude of c_0^2.

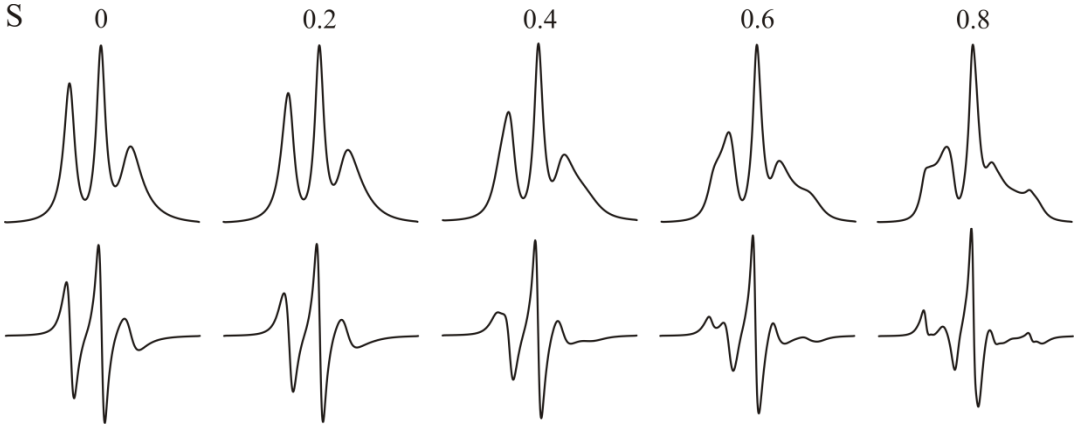

Figure 1.10 Order parameter dependence of the EPR spectral lineshape. Absorption (top) and first-derivative (bottom) spectra were simulated using the order parameter values indicated. An isotropic rotational correlation time of 2 ns and diffusion tilt angles $\alpha_D = 0$, $\beta_D = 36^o$, $\gamma_D = 0$ were used in all simulations. Spectra were simulated at a frequency of 9.5 GHz using the principal values $A_{xx} = 6.2$ G, $A_{yy} = 5.9$ G, $A_{zz} = 37$ G, $g_{xx} = 2.0078$, $g_{yy} = 2.0060$, and $g_{zz} = 2.0022$.

This ordering effect of the restoring potential is typically reported as an order parameter (S) defined as

$$S = \frac{1}{2}\langle(3\cos^2\theta - 1)\rangle \qquad [1.54]$$

where the brackets indicate a spatial average. The spectral lineshape dependence on S is illustrated in Figure 1.10. It should be noted that the order parameter denoted by S is unrelated to the spin angular momentum **S** discussed earlier in this chapter. In a few cases in this dissertation,

a second term for the restoring potential, with L=K=2, was used in spectral simulations. In these cases, c_0^2 and c_2^2 were positive, and the effect of the second term on the shape of the potential was the elongate the cone along one axis to generate an elliptic cone.

1.6.4 Limitations of spectral simulation with the SLE. It is important to emphasize that although spectral simulations are an important analytical tool for determining motional information from spectral lineshapes, there are practical issues that limit the application of this approach. The primary issue is that the SLE simulations use a large number of parameters that are often correlated, leading to the possibility of more than one equally-good fit (i.e. degeneracy of the fits). Additionally, simulations are generally time-consuming and are therefore not ideal for analyzing large datasets. These problems are compounded in the case of conformational exchange that generates a multicomponent spectrum, because the number of parameters is increased and the components are not fully resolved (at X-band).

1.7 Double electron-electron resonance (DEER)

The addition of a second spin label into the protein introduces the possibility for measuring distances between them *via* the dipolar interaction, which is proportional to $1/r^3$, where r is the interspin distance. When the two spin labels are close ($\lesssim 30$ Å), the dipolar interaction reduces the T_2 relaxation time sufficiently to determine the interspin distance based on broadening of the EPR spectrum (76, 77). Alternatively, saturation recovery can measure T_1 relaxation-enhancement to determine distances between spins (78). CW EPR and relaxation-based measurements have the advantage that they can be measured at room temperature, whereas DEER currently requires cryogenic temperatures (see below). The disadvantage to the CW and relaxation enhancement methods is that they are limited to shorter distances for spin-labeled proteins (≈30 Å for CW, ≈40 Å for relaxation at room temperature), and in the case of relaxation,

provide only an average distance and not a distribution. Due to these limitations, DEER is by far the most commonly used technique for measuring interspin distance distributions (79) and is employed in this dissertation. DEER is an increasingly popular technique (79, 80) that can measure distances in the range of ≈20-80 Å. The principal advantage of DEER is that it provides the full distribution of interspin distances including their relative probability. For a doubly-labeled protein, the discrete distances report each structural state in the ensemble, and the widths indicate the heterogeneity of each state. In this manner, DEER measures structure and structural heterogeneity of the conformational ensemble. Double quantum coherence is an alternative pulsed experiment that can measure distance distributions comparable to DEER (81-83), but current commercially-available instrumentation is better suited to DEER. This section provides an overview of the basic principles of the DEER experiment; more detailed descriptions of the theory and practical implementation of DEER are available elsewhere (84-87).

1.7.1 Hamiltonian for the electron-electron dipolar interaction. The additional electron spin requires modification of the Spin Hamiltonian described in section **1.5**. In the high field limit, this interaction is small compared to the Zeeman interaction and may therefore be treated using perturbation theory as a separate, additive term to the Spin Hamiltonian. This term, for two free electron spins A and B, may be represented analogously to the hyperfine dipolar interaction expression ([1.40]) as follows:

$$\widehat{H}_{dd} = c\frac{1}{r_{AB}^3}\left[\mathbf{S}_A \cdot \mathbf{S}_B - \frac{3}{r_{AB}^2}(\mathbf{S}_A \cdot \mathbf{r}_{AB})(\mathbf{S}_B \cdot \mathbf{r}_{AB})\right] \quad [1.55]$$

where r_{AB} is the distance between the two spins, $\mathbf{r}$ is the interspin vector, $\mathbf{S}_A$ and $\mathbf{S}_B$ are the spin angular momenta vector operators, and

$$c = \frac{\mu_0}{4\pi\hbar} g_A g_B \beta_e^2 \quad [1.56]$$

where μ_0 is the vacuum permeability, and g_A and g_B are the isotropic g-factors for each spin. The dipolar interaction Hamiltonian term can be expanded into six terms, and all but one are negligible in the high field limit and when the difference in resonant frequency between the two spins is greater than the dipolar frequency (1, 83), leaving

$$\hat{H}_{dd} = c\frac{1}{r_{AB}^3}(3\cos^2\theta - 1)S_{z,A}S_{z,B} \quad [1.57]$$

where θ is the angle between the interspin vector and the external field. The dipolar coupling frequency is given by $\omega_{AB} = c\frac{1}{r_{AB}^3}(3\cos^2\theta - 1)$. The fundamental aim of the DEER measurement is to isolate and measure the dipolar coupling frequency ω_{AB} to determine r_{AB}.

1.7.2 DEER pulse sequence and signal. Different pulse sequences may be used for the DEER experiment, including a 3-pulse (87), 4-pulse (86), and 5-pulse sequence (88); the 4-pulse sequence shown in Figure 1.11 was used in all DEER experiments reported in this dissertation. In 4-pulse DEER, a refocused primary echo pulse sequence (i.e. observe sequence) is used to populate an echo for a subset of spins in the sample (i.e. observe spins or A spins). Using the bulk magnetization framework of Bloch (section **1.4**), the $\pi/2$ pulse along the x-axis aligns the bulk magnetization vector along the negative y-axis, and afterwards the individual spins precess about the z-axis at slightly different frequencies due to local field inhomogeneities in the sample, causing a loss of magnetization in the xy-plane. The initial π pulse of the observe sequence inverts the precession direction, and the magnetization will realign in the xy-plane at a time τ_1 after the π pulse equal to the separation of the $\pi/2$ and π pulses, forming the primary echo. After another fixed time interval τ_2, a second π pulse inverts the precession direction again, resulting in a secondary (i.e. refocused) echo at a time τ_2 after the second π pulse. The intensity of this echo, V, is the signal measured in the DEER experiment.

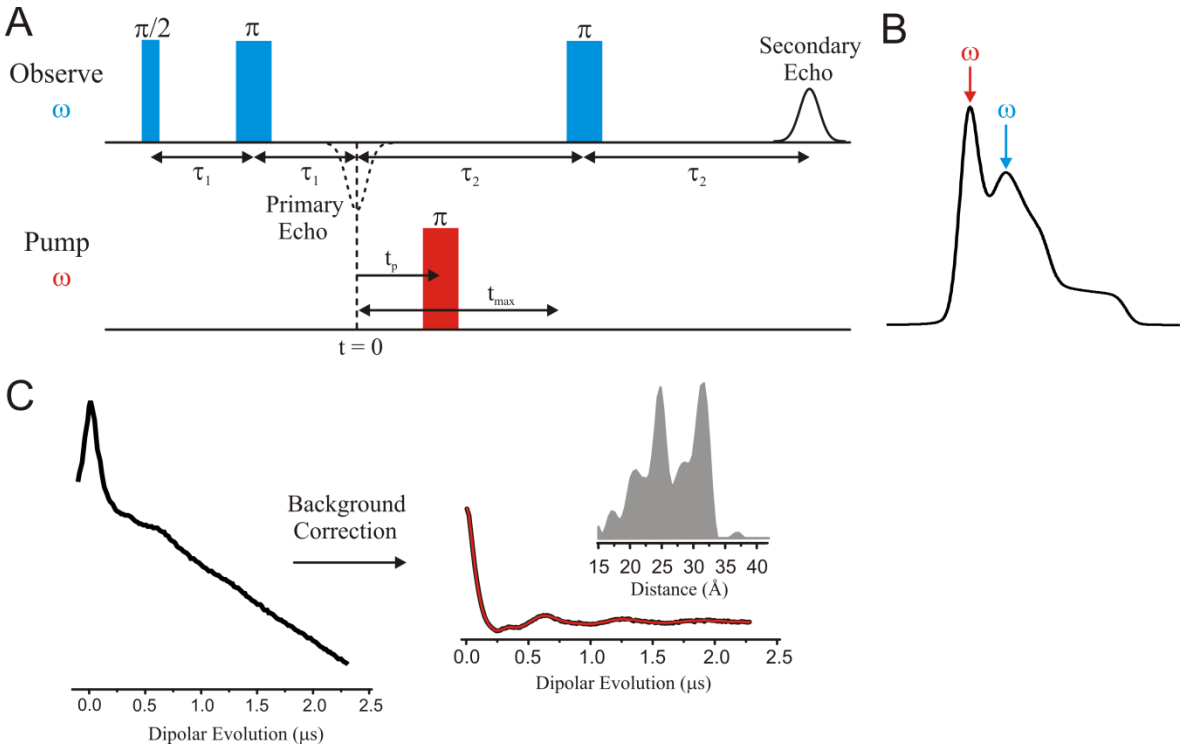

Figure 1.11 The DEER experiment. (A) The four-pulse DEER sequence described in the text employs pulses of microwave radiation at two different frequencies (blue and red) to induce transitions in two different populations of spins. (B) The angular frequencies ω for the observe (blue) and pump (red) sequence correspond to different positions in the spectral lineshape, thus exciting separate spin populations. The absorption spectrum shown is a simulated rigid limit spectrum of a nitroxide at 33.5 GHz (Q-band), which is the frequency employed for DEER experiments reported in this dissertation. (C) The raw DEER data shown on the left is background-corrected to remove the intermolecular contribution to the signal, and the intramolecular form factor is then fit (red trace) to determine the distance distribution (in grey) for the spin pair.

In the time between the first and second observe π pulses, an inversion of magnetization for a second population of spins (i.e. pump spins or B spins) is triggered using a π pulse at a different frequency (i.e. pump frequency). This changes the local field at the observe spins, which introduces a phase gain of $\omega_{AB}t_p$ to these spins, where the time t_p gives the pump pulse position with respect to the primary echo position and ω_{AB} is the dipolar coupling frequency described in section **1.7.1**. The pump pulse position is varied, modulating V with a period equal to $1/\omega_{AB}$; therefore $V(t_p)$ is proportional to $\cos(\omega_{AB}t_p)$.

It should be noted that, even in the absence of the pump pulse, the echo intensity V decays exponentially as a function of the pulse separation times τ_1 and τ_2,

$$V \propto exp\left[-\left(\frac{1}{T_2} + k_{ID,A}\right)(\tau_1 + \tau_2)\right] \quad [1.58]$$

where the decay rate constant is proportional to the instantaneous diffusion rate $k_{ID,A}$ and inversely proportional to the spin-spin relaxation time T_2 (66). The instantaneous diffusion rate $k_{ID,A}$ is proportional to the concentration of A spins, therefore the signal loss will occur as sample concentration increases. The pulse separation times are critical parameters in the DEER experiment, because they determine the maximum t_p for which data may be collected (t_{max}) (Figure 1.11). The time domain over which V is measured must be sufficiently long that the oscillation period and thus ω_{AB} may be accurately determined. The maximum reliable distance $r_{max,\langle r\rangle}$ that may be determined is

$$r_{max,\langle r\rangle} \approx 5\sqrt[3]{t_{max}/2\mu s} \quad [1.59]$$

The maximum distance for which the width of the distribution is reliable, $r_{max,\langle\sigma\rangle}$, is

$$r_{max,\langle\sigma\rangle} \approx 4\sqrt[3]{t_{max}/2\mu s} \quad [1.60]$$

Thus, a t_{max} of ≈6.5 μs is required for reliable distances and widths to be determined to 60 Å. For nitroxides, T_2 is prohibitively short at room temperature (≈10-30 ns), therefore samples are cooled to cryogenic temperatures to lengthen relaxation times. In addition to freezing, buffer deuteration can further lengthen T_2 to allow access to longer distances (89). Freezing samples serves a second purpose, namely to avoid molecular tumbling that would result in motional averaging of the dipolar interaction as described in section **1.5**.

In the frozen sample, the interspin vectors are randomly distributed in terms of orientation with respect to the external field, defined by θ in [1.57]. The relative population for each angle follows a sin(θ) distribution, indicating that perpendicular orientations are more likely than parallel orientations. Assuming equivalent excitation of each orientation, a distribution of

dipolar frequencies will be observed for a particular interspin distance, representative of the different angles of the interspin vectors. The DEER signal $V(t_p)$ for a spin pair at a fixed distance, but with random orientation with respect to the external field, can be analytically calculated by integrating over all possible θ angles (90)

$$V(t_p) = 1 - \lambda + \lambda \int_0^{\pi/2} \xi(\theta) \cos(\omega_{AB} t_p) \sin(\theta) d\theta \quad [1.61]$$

where the modulation depth λ reflects the fraction of spins coupled to A spins that are inverted by the pump pulse and $\xi(\theta)$ is an excitation function that defines the relative excitation as a function of the interspin vector orientation; $\xi(\theta)$ is ≈1 for nitroxides. Expression [1.61] ignores any contribution from orientation selection, which refers to the dependence of the dipolar frequency on the relative orientation of the molecular frames of the two spin labels (91). Orientation selection effects arise for rigidly oriented samples where the excitation coverage is incomplete across all θ values, but are rarely observed for nitroxide-labeled proteins due to the inherent flexibility of both the protein and the spin label side chain (79)**.**

Up to this point, the DEER signal has been described for two spins in a protein with a fixed distance between them. In reality, the flexibility of proteins results in a distribution of distances, and calculation of the DEER signal requires summation over all interspin distances weighted by their probabilities:

$$V(t_p) = \left[1 - \lambda + \lambda \int_{r_{min}}^{r_{max}} \int_0^{\pi/2} \xi(\theta) \cos(\omega_{AB} t_p) P(r) \sin(\theta) d\theta dr\right] B(t_p) \quad [1.62]$$

where P(r) is the distance distribution function and $B(t_p)$ is the background function describing the echo attenuation due to interactions between spins on different proteins. The intermolecular interaction contribution to the echo intensity has the form

$$B(t_p) = exp\left[k_{ID,B} t_p^{D/3}\right] \quad [1.63]$$

where $k_{ID,B}$ is the instantaneous diffusion rate for B spins and D is the fractional dimension, or dimensionality (92). For a random distribution of globular proteins in solution D is expected to be ≈3, and for membrane proteins in a bilayer D is expected to be ≈2. The background may be determined experimentally using singly-labeled mutants where the intramolecular interaction is eliminated, and it is apparent from experiments of this kind that the observed $B(t_p)$ may have non-ideal values of D (93). Typically, $B(t_p)$ is fitted using the raw DEER data of the doubly-labeled mutant under investigation.

To solve for the distance distribution function, the background is removed and the remaining time domain data (referred to as the dipolar evolution function or form factor) is discretized and converted into a system of linear algebraic functions of the form:

$$\mathbf{F}(t_p) = \mathbf{K}(r, t_p) \cdot \mathbf{P}(r) \qquad [1.64]$$

F is a vector containing the background-corrected data, **P** is the probability distribution, and **K** is a kernel function that is equivalent to the integral [1.61]. For a given **P**, a kernel function may be readily constructed to solve for **F**. However, the inverse problem of solving for a **P** which fits a given **F** is ill-posed (94). Tikhonov regularization is the most commonly employed method for solving this equation for the distance distribution **P** and has been implemented in DEERAnalysis (95), a Matlab-based software package that may be downloaded at: http://www.epr.ethz.ch/software. Alternative methods have been employed for the analysis of DEER data, including a maximum entropy modification to suppress negative probabilities in the distance distribution function (96). In this dissertation, all DEER data were analyzed using the program LongDistances, which employs a modified regression analysis. This program was written by Dr. Christian Altenbach in LabVIEW and is available online at: http://www.biochemistry.ucla.edu/biochem/Faculty/Hubbell/.

1.8 References

1. Abragam A (1961) *The Principles of Nuclear Magnetism* (University Press, Oxford).
2. Poole J, Charles P. (1983) *Electron Spin Resonance: A Comprehensive Treatise on Experimental Techniques* (John Wiley & Sons, Inc., USA).
3. Slichter CP (1963) *Principles of Magnetic Resonance, with Examples from Solid State Physics* (Harper & Row, New York).
4. Carrington A & McLachlan AD (1967) *Introduction to Magnetic Resonance with Applications to Chemistry and Chemical Physics* (Harper & Row, New York,).
5. Burr M & Koshland DE, Jr. (1964) Use of "reporter groups" in structure-function studies of proteins. *Proc Natl Acad Sci USA* 52:1017-1024.
6. Stone TJ, Buckman T, Nordio PL, & McConnell HM (1965) Spin-labeled biomolecules. *Proc Natl Acad Sci USA* 54(4):1010-1017.
7. Mchaourab HS, Lietzow MA, Hideg K, & Hubbell WL (1996) Motion of spin-labeled side chains in T4 Lysozyme. Correlation with protein structure and dynamics. *Biochemistry* 35(24):7692-7704.
8. Mchaourab HS, Kálai T, Hideg K, & Hubbell WL (1999) Motion of spin-labeled side chains in T4 Lysozyme: effect of side chain structure. *Biochemistry* 38(10):2947-2955.
9. Columbus L, Kálai T, Jekö J, Hideg K, & Hubbell WL (2001) Molecular motion of spin labeled side chains in α-helices: analysis by variation of side chain structure. *Biochemistry* 40(13):3828-3846.
10. Hubbell WL, López CJ, Altenbach C, & Yang Z (2013) Technological advances in site-directed spin labeling of proteins. *Curr Opin Struct Biol* 23(5):725-733.

11. Campbell ID & Dwek RA (1984) *Biological Spectroscopy* (Benjamin-Cummings Publishing Co., Menlo Park, CA).

12. Dupeyre R-M & Rassa A (1966) Nitroxides. XIX. Norpseudopelletierine-N-oxyl, a new, stable, unhindered free radical. *J Am Chem Soc* 88(13):3180-3181.

13. Getz EB, Xiao M, Chakrabarty T, Cooke R, & Selvin PR (1999) A comparison between the sulfhydryl reductants tris(2-carboxyethyl)phosphine and dithiothreitol for use in protein biochemistry. *Anal Biochem* 273(1):73-80.

14. Todd AP, Cong J, Levinthal F, Levinthal C, & Hubbell WL (1989) Site-directed mutagenesis of colicin E1 provides specific attachment sites for spin labels whose spectra are sensitive to local conformation. *Proteins: Struct, Funct, Bioinf* 6(3):294-305.

15. Fleissner MR, Cascio D, & Hubbell WL (2009) Structural origin of weakly ordered nitroxide motion in spin-labeled proteins. *Protein Sci* 18(5):893-908.

16. Warshaviak DT, Serbulea L, Houk KN, & Hubbell WL (2011) Conformational analysis of a nitroxide side chain in an α-helix with density functional theory. *J Phys Chem B* 115(2):397-405.

17. Fleissner MR, *et al.* (2011) Structure and dynamics of a conformationally constrained nitroxide side chain and applications in EPR spectroscopy. *Proc Natl Acad Sci USA* 108(39):16241-16246.

18. Schmidt MJ, Borbas J, Drescher M, & Summerer D (2014) A genetically encoded spin label for electron paramagnetic resonance distance measurements. *J Am Chem Soc* 136(4):1238-1241.

19. López CJ, Fleissner MR, Brooks EK, & Hubbell WL (2014) Stationary-phase EPR for exploring protein structure, conformation, and dynamics in spin-labeled proteins. *Biochemistry* 53(45):7067-7075.

20. López CJ, Fleissner MR, Guo Z, Kusnetzow AK, & Hubbell WL (2009) Osmolyte perturbation reveals conformational equilibria in spin-labeled proteins. *Protein Sci* 18(8):1637-1652.

21. Lillington JED, *et al.* (2011) Shigella flexneri Spa15 crystal structure verified in solution by double electron electron resonance. *J Mol Biol* 405(2):427-435.

22. Gruene T, *et al.* (2011) Integrated analysis of the conformation of a protein-linked spin label by crystallography, EPR and NMR spectroscopy. *J Biomol NMR* 49(2):111-119.

23. Raghuraman H, *et al.* (2012) Mechanism of Cd^{2+} coordination during slow inactivation in potassium channels. *Structure* 20(8):1332-1342.

24. Kroncke BM, Horanyi PS, & Columbus L (2010) Structural origins of nitroxide side chain dynamics on membrane protein α-helical sites. *Biochemistry* 49(47):10045-10060.

25. Fraser RR, Boussard G, Saunders JK, Lambert JB, & Mixan CE (1971) Barriers to rotation about the sulfur-sulfur bond in acyclic disulfides. *J Am Chem Soc* 93(15):3822-3823.

26. Cunningham TF, *et al.* (2012) High-resolution structure of a protein spin-label in a solvent-exposed β-sheet and comparison with DEER spectroscopy. *Biochemistry* 51(32):6350-6359.

27. Freed DM, Khan AK, Horanyi PS, & Cafiso DS (2011) Molecular origin of electron paramagnetic resonance line shapes on β-barrel membrane proteins: the local solvation environment modulates spin-label configuration. *Biochemistry* 50(41):8792-8803.

28. Bracken C, Carr PA, Cavanagh J, & Palmer III AG (1999) Temperature dependence of intramolecular dynamics of the basic leucine zipper of GCN4: implications for the entropy of association with DNA1. *J Mol Biol* 285(5):2133-2146.

29. Budil DE, Lee S, Saxena S, & Freed JH (1996) Nonlinear-least-squares analysis of slow-motion EPR spectra in one and two dimensions using a modified Levenberg–Marquardt algorithm. *J Magn Reson, Ser A* 120(2):155-189.

30. Columbus L & Hubbell WL (2004) Mapping backbone dynamics in solution with site-directed spin labeling: GCN4−58 bZip free and bound to DNA. *Biochemistry* 43(23):7273-7287.

31. Isas JM, Langen R, Haigler HT, & Hubbell WL (2002) Structure and dynamics of a helical hairpin and loop region in annexin 12: a site-directed spin labeling study. *Biochemistry* 41(5):1464-1473.

32. López CJ, Oga S, & Hubbell WL (2012) Mapping molecular flexibility of proteins with site directed spin labeling: a case study of myoglobin. *Biochemistry* 51(33):6568-6583.

33. López CJ, Yang Z, Altenbach C, & Hubbell WL (2013) Conformational selection and adaptation to ligand binding in T4 lysozyme cavity mutants. *Proc Natl Acad Sci USA* 110(46):E4306-E4315.

34. Humphries GMK & McConnell HM (1982) Nitroxide spin labels. *Methods in Experimental Physics*, eds Gerald E & Harold L (Academic Press), Vol 20, pp 53-122.

35. Bloch F (1946) Nuclear induction. *Phys Rev* 70(7-8):460-474.

36. Bridges MD, Hideg K, & Hubbell WL (2010) Resolving conformational and rotameric exchange in spin-labeled proteins using saturation recovery EPR. *Appl Magn Reson* 37(1-4):363-363.

37. Sato H, *et al.* (2008) Electron spin–lattice relaxation of nitroxyl radicals in temperature ranges that span glassy solutions to low-viscosity liquids. *J Magn Reson* 191(1):66-77.

38. Robinson BH, Haas DA, & Mailer C (1994) Molecular dynamics in liquids: spin-lattice relaxation of nitroxide spin labels. *Science* 263(5146):490-493.

39. Eaton S & Eaton G (2002) Relaxation times of organic radicals and transition metal ions. *Distance Measurements in Biological Systems by EPR,* Biological Magnetic Resonance, eds Berliner L, Eaton G, & Eaton S (Springer, US), Vol 19, pp 29-154.

40. Owenius R, Terry GE, Williams MJ, Eaton SS, & Eaton GR (2004) Frequency dependence of electron spin relaxation of nitroxyl radicals in fluid solution. *J Phys Chem B* 108(27):9475-9481.

41. Sato H, *et al.* (2008) Impact of electron−electron spin interaction on electron spin relaxation of nitroxide diradicals and tetraradical in glassy solvents between 10 and 300 K. *J Phys Chem B* 112(10):2818-2828.

42. Griffiths DJ (2005) *Introduction to quantum mechanics* (Pearson Prentice Hall, Upper Saddle River, NJ) 2nd edition.

43. Atkins PW & Kivelson D (1966) ESR linewidths in solution. II. Analysis of spin—rotational relaxation data. *J Chem Phys* 44(1):169-174.

44. Eaton G & Eaton S (1989) Resolved electron-electron spin-spin splittings in EPR spectra. *Spin Labeling,* Biological Magnetic Resonance, eds Berliner L & Reuben J (Springer US), Vol 8, pp 339-397.

45. Redfield AG (1957) On the theory of relaxation processes. *IBM J Res Dev* 1(1):19-31.

46. Redfield AG (1965) The theory of relaxation processes. *Advances in Magnetic and Optical Resonance*, ed John SW (Academic Press), Vol 1, pp 1-32.

47. Millhauser GL & Freed JH (1984) Two-dimensional electron spin echo spectroscopy and slow motions. *J Chem Phys* 81(1):37-48.

48. Stillman AE, Schwartz LJ, & Freed JH (1980) Direct determination of rotational correlation time by electron-spin echoes. *J Chem Phys* 73(7):3502-3503.

49. Freed JH (1976) Theory of slow tumbling ESR spectra for nitroxides. *Spin Labeling Theory and Applications*, ed Berliner LJ (Academic Press, New York, NY), pp 53-132.

50. Altenbach C, Froncisz W, Hyde JS, & Hubbell WL (1989) Conformation of spin-labeled melittin at membrane surfaces investigated by pulse saturation recovery and continuous wave power saturation electron paramagnetic resonance. *Biophys J* 56(6):1183-1191.

51. Likhtenshtein GI, Yamauchi J, Nakatsuji Si, Smirnov AI, & Tamura R (2008) Fundamentals of magnetism. *Nitroxides* (Wiley-VCH Verlag GmbH & Co. KGaA), pp 1-45.

52. Shimshick EJ & McConnell HM (1973) Lateral phase separation in phospholipid membranes. *Biochemistry* 12(12):2351-2360.

53. Robinson BH, Mailer C, & Reese AW (1999) Linewidth analysis of spin labels in liquids: I. Theory and data analysis. *J Magn Reson* 138(2):199-209.

54. Hyde JS & Subczynski WK (1984) Simulation of ESR spectra of the oxygen-sensitive spin-label probe CTPO. *J Magn Reson* 56(1):125-130.

55. Wilhelm E, Battino R, & Wilcock RJ (1977) Low-pressure solubility of gases in liquid water. *Chem Rev* 77(2):219-262.

56. Kusnetzow AK, Altenbach C, & Hubbell WL (2006) Conformational states and dynamics of rhodopsin in micelles and bilayers. *Biochemistry* 45(17):5538-5550.

57. McConnell HM (1958) Reaction rates by nuclear magnetic resonance. *J Chem Phys* 28(3):430-431.

58. Abergel D & Palmer AG (2004) Approximate solutions of the Bloch–McConnell equations for two-site chemical exchange. *ChemPhysChem* 5(6):787-793.

59. Palmer III AG (2004) NMR characterization of the dynamics of biomacromolecules. *Chem Rev* 104(8):3623-3640.

60. Marsh D (1989) Experimental methods in spin-label spectral analysis. *Spin Labeling Theory and Applications*, Biological Magnetic Resonance, eds Berliner L & Reuben J (Springer, US), Vol 8, pp 255-303.

61. Weil JA (1971) The analysis of large hyperfine splitting in paramagnetic resonance spectroscopy. *J Magn Reson* 4(3):394-399.

62. Stoll S & Schweiger A (2007) Easyspin: simulating CW ESR spectra. *Biol Magn Reson* 27:299-321.

63. Breit G & Rabi II (1931) Measurement of nuclear spin. *Phys Rev* 38(11):2082-2083.

64. Bloembergen N (1949) On the interaction of nuclear spins in a crystalline lattice. *Physica* 15(3–4):386-426.

65. Kevan L & Schwartz RN (1979) *Time domain electron spin resonance* (Wiley, New York).

66. Schweiger A & Jeschke G (2001) *Principles of pulse electron paramagnetic resonance* (Oxford University Press, Oxford, UK; New York).

67. Hyde JS (1978) Saturation-transfer spectroscopy. *Enzyme Structure, Part G*, Methods in Enzymology, eds Hirs CHW & Timasheff SN (Academic Press), Vol 49, pp 480-511.

68. Thomas DD (1978) Large-scale rotational motions of proteins detected by electron paramagnetic resonance and fluorescence. *Biophys J* 24(2):439-462.

69. Dalton LR, Robinson BH, Dalton LA, & Coffey P (1976) Saturation transfer spectroscopy. *Advances in Magnetic and Optical Resonance*, ed Waugh JS (Academic Press), Vol 8, pp 149-259.

70. Kivelson D (1960) Theory of ESR linewidths of free radicals. *J Chem Phys* 33(4):1094-1106.

71. Schreier S, Polnaszek CF, & Smith ICP (1978) Spin labels in membranes problems in practice. *Biochim Biophys Acta, Rev Biomembr* 515(4):395-436.

72. Knowles PF, Marsh D, & Rattle HWE (1976) *Magnetic resonance of biomolecules: an introduction to the theory and practice of NMR and ESR in biological systems* (Wiley, London; New York).

73. Griffith OH, Cornell DW, & McConnell HM (1965) Nitrogen hyperfine tensor and g tensor of nitroxide radicals. *J Chem Phys* 43(8):2909-2910.

74. Liang Z, Lou Y, Freed JH, Columbus L, & Hubbell WL (2004) A multifrequency electron spin resonance study of T4 lysozyme dynamics using the slowly relaxing local structure model. *J Phys Chem B* 108(45):17649-17659.

75. Barnes JP, Liang Z, Mchaourab HS, Freed JH, & Hubbell WL (1999) A multifrequency electron spin resonance study of T4 lysozyme dynamics. *Biophys J* 76(6):3298-3306.

76. Altenbach C, Oh K-J, Trabanino RJ, Hideg K, & Hubbell WL (2001) Estimation of inter-residue distances in spin labeled proteins at physiological temperatures: experimental strategies and practical limitations. *Biochemistry* 40(51):15471-15482.

77. Kittell AW, Hustedt EJ, & Hyde JS (2012) Inter-spin distance determination using L-band (1-2 GHz) non-adiabatic rapid sweep electron paramagnetic resonance (NARS EPR). *J Magn Reson* 221:51-56.

78. Yang Z, *et al.* (2014) Long-range distance measurements in proteins at physiological temperatures using saturation recovery EPR spectroscopy. *J Amer Chem Soc* 136(43):15356-15365.

79. Jeschke G (2012) DEER distance measurements on proteins. *Ann Rev Phys Chem* 63(1):419-446.

80. Mchaourab Hassane S, Steed PR, & Kazmier K (2011) Toward the fourth dimension of membrane protein structure: insight into dynamics from spin-labeling EPR spectroscopy. *Structure* 19(11):1549-1561.

81. Borbat PP & Freed JH (1999) Multiple-quantum ESR and distance measurements. *Chem Phys Lett* 313(1–2):145-154.

82. Borbat PP & Freed JH (2000) Double-quantum ESR and distanct measurements. *Distance measurements in biological systems by EPR*, Biological Magnetic Resonance, (Academic/Plenum, New York), Vol 19, pp 385-459.

83. Borbat PP & Freed JH (2013) Pulse dipolar electron spin resonance: distance measurements. *Structural Information from Spin-Labels and Intrinsic Paramagnetic Centres in the Biosciences*, Structure and Bonding, eds Timmel CR & Harmer JR (Springer Berlin Heidelberg), Vol 152, pp 1-82.

84. Jeschke G, Panek G, Godt A, Bender A, & Paulsen H (2004) Data analysis procedures for pulse ELDOR measurements of broad distance distributions. *Appl Magn Reson* 26(1-2):223-244.

85. Salikhov KM, Dzuba SA, & Raitsimring AM (1981) The theory of electron spin-echo signal decay resulting from dipole-dipole interactions between paramagnetic centers in solids. *J Magn Reson* 42(2):255-276.

86. Pannier M, Veit S, Godt A, Jeschke G, & Spiess HW (2000) Dead-time free measurement of dipole-dipole interactions between electron spins. *J Magn Reson* 142(2):331-340.

87. Milov AD, Ponomarev AB, & Tsvetkov YD (1984) Electron-electron double resonance in electron spin echo: model biradical systems and the sensitized photolysis of decalin. *Chem Phys Lett* 110(1):67-72.

88. Borbat PP, Georgieva ER, & Freed JH (2012) Improved sensitivity for long-distance measurements in biomolecules: five-pulse double electron–electron resonance. *J Phys Chem Lett* 4(1):170-175.

89. Jeschke G, Bender A, Paulsen H, Zimmermann H, & Godt A (2004) Sensitivity enhancement in pulse EPR distance measurements. *J Magn Reson* 169(1):1-12.

90. Bode BE, *et al.* (2007) Counting the monomers in nanometer-sized oligomers by pulsed electron−electron double resonance. *J Amer Chem Soc* 129(21):6736-6745.

91. Endeward B, Butterwick JA, MacKinnon R, & Prisner TF (2009) Pulsed electron−electron double-resonance determination of spin-label distances and orientations on the tetrameric potassium ion channel KcsA. *J Amer Chem Soc* 131(42):15246-15250.

92. Milov AD & Tsvetkov YD (1997) Double electron-electron resonance in electron spin echo: conformations of spin-labeled poly-4-vinilpyridine in glassy solutions. *Appl Magn Reson* 12(4):495-504.

93. Manglik A, *et al.* (2015) Structural insights into the dynamic process of β2-adrenergic receptor signaling. *Cell* 161(5):1101-1111.

94. Chiang Y-W, Borbat PP, & Freed JH (2005) The determination of pair distance distributions by pulsed ESR using Tikhonov regularization. *J Magn Reson* 172(2):279-295.

95. Jeschke G, *et al.* (2006) DeerAnalysis2006-a comprehensive software package for analyzing pulsed ELDOR data. *Appl Magn Reson* 30(3-4):473-498.

96. Chiang Y-W, Borbat PP, & Freed JH (2005) Maximum entropy: a complement to Tikhonov regularization for determination of pair distance distributions by pulsed ESR. *J Magn Reson* 177(2):184-196.

Chapter 2: Introduction to high-pressure EPR and site-directed spin labeling for mapping conformational flexibility in proteins

2.1 Summary

Proteins in solution are dynamic molecules, exhibiting conformational fluctuations across a range of time and length scales (1). High hydrostatic pressure is a powerful probe of protein conformational flexibility, revealing regions of elevated compressibility and thus flexibility within individual conformational states, but in addition shifting conformational equilibria such that “invisible” excited states become accessible for spectroscopic characterization. The central aim of this chapter is to describe the thermodynamic and mechanistic basis for the pressure response, and describe the motivation for and information content of high-pressure site-directed spin labeling electron paramagnetic resonance (SDSL EPR) experiments. Following a brief introduction to functional protein dynamics and the types of flexibility revealed by pressure, the thermodynamics of proteins under pressure is considered. Then, the mechanism of the pressure response is reviewed. Finally, a discussion of the principles underlying the detection of pressure effects in proteins using SDSL EPR is presented.

2.2 Insight into protein flexibility and function using high hydrostatic pressure

Proteins in solution exist in conformational equilibria that cannot be appreciated from structures observed in crystal lattices (2-6). While a well-ordered native state typically predominates under physiological conditions, excursions to higher-energy (excited) states may be required for function (1, 7). For example, on a funnel-shaped energy landscape (8, 9) excited states have increased configurational entropy that may give rise to the promiscuous protein-protein interactions that define a protein interactome (10, 11). The transition from native to excited state may involve local unfolding (12, 13) or rigid-body motions of intact secondary structural elements (6, 14), and both the structural changes and the time scale of exchange may

contribute to protein function (15). Functional excited states are often only a few kcal/mol higher in energy than the native state, yet this difference results in excited state populations that are inaccessible to traditional spectroscopic detection. Excited states with populations below the detection limit are often referred to as “invisible” states (7).

For a complete understanding of molecular mechanisms underlying function, characterization of functionally relevant conformational states is required. However, in the case of excited states, low populations and short lifetimes present a challenge for biophysical characterization. One solution to this problem is the application of high hydrostatic pressure, which induces compression of individual states, but also shifts conformational equilibria towards excited states, allowing for their spectroscopic characterization (16, 17). Compression under pressure is often heterogeneous across the structure (18), and may help identify flexible regions in an otherwise rigid protein; such regions are often of functional significance (19). With high hydrostatic pressure, both folding intermediates (20) and low-lying excited states with functional roles (21) have been investigated. Even when protein conformations are of similar energy and the populations are readily observable, pressure-induced shifts in the populations can be used to confirm an equilibrium, extract thermodynamic properties, and define mechanistic roles of known states (22). In addition, the kinetics of conformational exchange may be determined from the relaxation time following a pressure-jump (23).

2.3 The thermodynamics of proteins under pressure

2.3.1 Pressure effects on protein conformational equilibria. The pressures used to study biomacromolecules typically range from 1 bar to 10 kbar. Covalent bond lengths and angles are not significantly affected at these pressures, and the predominant effects are on intramolecular conformation and intermolecular interaction (24). The focus of this dissertation is

on intramolecular effects of pressure, namely the structure and dynamics of monomeric proteins under pressure. As described above, protein structure fluctuates within an ensemble of conformations. For an equilibrium between two conformations in the ensemble, A ↔ B, the free energy difference (ΔG) between the conformational states as a function of pressure (P) and temperature (T) can be obtained from a Taylor's expansion of ΔG in P and T (assuming constant solution conditions, e.g. pH, ionic strength) (16),

$$\Delta G = G_B - G_A = \Delta G^o - \Delta S^o(T - T_0) - \frac{\Delta C_P}{2T_0}(T - T_0)^2 + \Delta \bar{V}^o(P - P_0) - \frac{\Delta \bar{\beta}_T}{2}(P - P_0)^2 + \Delta\alpha(P - P_0)(T - T_0) \quad [2.1]$$

where ΔS^o is the entropy, ΔC_P is the heat capacity, $\Delta \bar{V}^o$ is the partial molar volume, $\Delta \bar{\beta}_T$ is the isothermal compressibility, and $\Delta\alpha$ is the thermal expansion coefficient difference between states A and B. In this expression ΔC_P, $\Delta \bar{\beta}_T$, and $\Delta\alpha$ are assumed to be constant, thus third-order terms and higher are ignored. The equilibrium constant K between the states is related to ΔG according to the expression

$$K = \frac{[B]}{[A]} = \exp\left(\frac{\Delta G}{RT}\right) \quad [2.2]$$

Application of pressure at a constant temperature allows elimination of the temperature-dependent terms on the right side of [2.1]. Combining this simplified expression with [2.2] yields

$$\ln\left(\frac{K}{K(0)}\right) = -\frac{\Delta \bar{V}^o}{RT}(P) + \frac{\Delta \bar{\beta}_T}{2RT}(P)^2 \quad [2.3]$$

where K and K(0) are the equilibrium constants at applied (gauge) pressure P and at atmospheric pressure (P_0=0), respectively, and

$$\Delta \bar{V}^o = \bar{V}_B^o - \bar{V}_A^o \quad [2.4]$$

$$\Delta \bar{\beta}_T = \bar{\beta}_{T,B} - \bar{\beta}_{T,A} \quad [2.5]$$

where the partial molar volume, $\bar{V}_i^o$, and isothermal compressibility, $\bar{\beta}_{T,i}$, are defined as follows:

$$\bar{V}_i^o = \left(\frac{\partial V}{\partial n_i}\right)_{T,P,n_{j\neq i}} \quad [2.6]$$

$$\bar{\beta}_{T,i} = -\left(\frac{\partial \bar{V}_i^o}{\partial P}\right)_T \quad [2.7]$$

It is important to note that the volume of the protein defined in [2.6] is the partial molar volume, which is the change in volume of the system per mole of protein added. The system in this case is the protein plus hydration water, therefore $\bar{V}_i^o$ includes the difference in the volume of bulk and hydration water and is intimately related to the solvation of the protein.

The first term in [2.3] typically dominates at low pressures due to the relative magnitudes of $\Delta\bar{V}^o$ and $\Delta\bar{\beta}_T$, but compressibility differences between states becomes important at higher pressures due to the quadratic pressure dependence of the second term. In many studies, $\Delta\bar{\beta}_T$ is assumed to be negligible based on limiting analysis to moderate pressures or to simplify interpretation of results, but unless confirmed this assumption may lead to errors in other thermodynamic parameters ($\Delta\bar{V}^o$ and ΔG^o) determined from experimentally measured K(P) and [2.3] (25). Typically, high-pressure studies of protein conformational exchange use pressures in the range of 1-4 kbar and the reported values of $\Delta\bar{V}^o$ range from ≈-10 to -100 mL/mol (17, 26). As an example of the potential shift in K at elevated pressures, consider a conformational exchange between a ground state that is 98% populated and an excited state that is 2% populated, with a $\Delta\bar{V}^o$ = -50 mL/mol and $\Delta\bar{\beta}_T$ = 0. Pressurization to 2 kbar provides 2.4 kcal/mol in $P\Delta\bar{V}^o$ stabilization energy, which is sufficient to equalize the populations of the two states.

It is important to note that a prerequisite for meaningful interpretation of changes observed with pressure application is a demonstration of reversibility, i.e., the system must return to its original state following depressurization. Only with reversibility can one guarantee thermodynamic equilibrium between states observed under pressure, and that states populated by

pressure are part of the protein conformational ensemble even at ambient conditions, although perhaps at a level below the detection limit.

2.3.2 The volume rule. In the equilibrium described above, it was shown that pressure will increase the population of the conformational state with lower volume, but there was no discussion of the structure of the states involved in the equilibrium. The volume rule, proposed by Akasaka (17), establishes a correlation between partial molar volume and conformational order.

The first observation of pressure influencing protein conformation was the complete coagulation of egg white at 7 kbar observed by Bridgman in 1914 (27); this also serves as the first demonstration of pressure-populated denaturation of a protein. Experimental investigation of pressure effects on a multitude of proteins in the years since confirm the generality of this early result (26). As a result of these studies, the application of sufficiently high pressure is expected to increase the population of the denatured state at the expense of the native (ground) state.

For the study of protein dynamics as it relates to function, the primary interest is in functional excited states rather than the pressure-denatured state. With the development in the late 1990s of an on-line high-pressure cell enabling multi-dimensional NMR, Akasaka and coworkers (16) found that pressure-denaturation of proteins is often sequential, with low-lying excited states populated at intermediate pressures. The results from these studies were synthesized by Akasaka into the empirical “volume rule,” which states that partial molar volume parallels conformational order (17, 29). For a given protein in solution the volume rule predicts that the random coil conformation at the top of the conformational free energy landscape will have the lowest volume. Assuming a funnel-shaped landscape (Figure 2.1) (30), conformational

order increases as the protein adopts conformations further down the funnel, and generation of small packing imperfections or defects results in an increase in volume. The native ground state, which is the most highly ordered state in the conformational ensemble, will have the largest volume. According to the volume rule, the application of pressure essentially reverses this process.

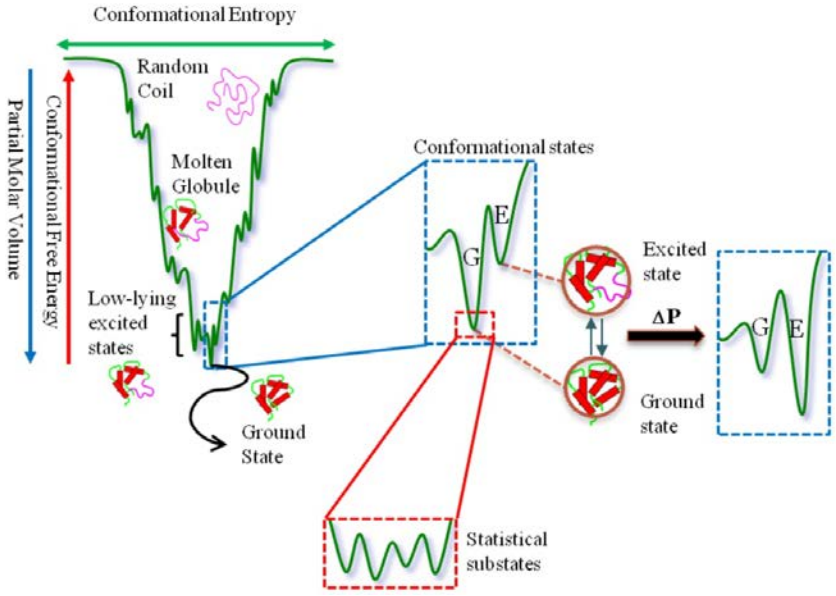

Figure 2.1 The pressure response of protein conformational equilibria. In a conformational equilibrium between an excited state (E) and ground state (G), the volume rule predicts that the E state will have a lower volume and is therefore favored upon pressurization (ΔP). Within the energy well of each conformer lies a large number of substates that are nearly iso-energetic and have lifetimes that are much shorter than those of conformational states (28). Compression of an individual conformational state corresponds to a shift in the population of substates.

2.3.3 Compressibility. In addition to shifting populations of conformational states, pressure will compress the individual conformations at the same time. Compressibility is defined in [2.7] as the change in volume of a particular state as a function of pressure. As shown in Figure 2.1, within the energy well of each conformational state exists a large number of statistical substates (28), and the volume change associated with compression thus corresponds to a shift in the relative population of substates of a given conformation.

A statistical mechanical treatment of a solvent-impenetrable particle, including a folded protein, reveals that compressibility is related to the mean-squared volume fluctuations according to the following expression (31):

$$\langle(\delta V)^2\rangle = \beta_T kT \qquad [2.8]$$

where k is the Boltzmann constant. According to this expression, compressibility of a conformation is the variance of its volume (Figure 2.2). Each of the substates for a particular conformational state will have a slightly different volume, therefore the volume of an individual protein molecule will vary as it exchanges between substates. The compressibility of a particular conformation may be viewed from this perspective as originating from the magnitude of fluctuations in volume associated with the exchange between statistical substates within a single conformational well (Figure 2.1).

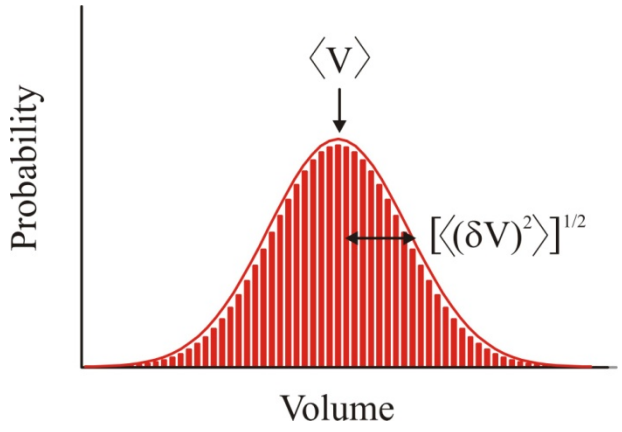

Figure 2.2 Graphic representation of the relationship between compressibility and volume fluctuations. The volume probability distribution for a single conformation is shown. The mean volume ⟨V⟩ is equivalent to the partial molar volume, but the instantaneous volume will vary as an individual protein molecule fluctuates between different substates within a particular conformation. The standard deviation of the distribution is equal to the root-mean-squared volume fluctuations, illustrating the relationship between compressibility as defined in [2.8] and the volume fluctuations.

2.4 Mechanism of the pressure response

The volume change associated with pressure-populated conformational exchange is a result of the difference in molecular volumes of the conformers (i.e., the sum of atomic and

solvent-inaccessible cavity volumes) and differences in the volume of solvation water. In this section, the relative magnitude of these contributions is considered, beginning with the minor role of solvation revealed through studies of both model compounds and proteins. Then, packing imperfections (cavities) are shown to play a dominant role in the pressure response, largely based on results from investigations of cavity-creating mutants of proteins.

In early studies, the role of solvation in the volumetric properties of protein unfolding was investigated using small molecule analogues of protein backbone and side chain groups. Volume changes were measured for the transfer of these compounds from a hydrophobic to aqueous environment. In this approach, unfolding of a protein is modeled as the transfer of moieties from the hydrophobic protein interior to the aqueous bulk water environment. The results predicted that protein unfolding will coincide with a large and negative volume change. This is inconsistent with experimental volume changes for pressure-denaturation of proteins, which are found to be small and negative (26, 32).

An alternative model treats solvation of the protein upon denaturation as solvent penetration into the protein interior. This model is based on results from energetic calculations of solvent-separated hydrophobic interactions as a function of pressure (33). In addition to predicting reasonable values for the volume change for denaturation, this model is more consistent with the available structural information for the pressure-denatured state, which indicates that this state is relatively compact and retains significant secondary structure in the absence of denaturants such as urea (34-37). This suggests that solvation of buried hydrophobic groups is responsible for the volume change upon pressure-denaturation, rather than hydrophilic groups such as backbone amides and polar side chains. Indeed, studies of the helix-coil transition

of isolated peptides have found that pressure stabilizes the helical conformation rather than a random-coil state (38-40), indicating that solvation of the backbone is not favored by pressure.

Although the solvent-separated hydrophobic interaction calculations gave reasonable thermodynamic values for pressure-denaturation of proteins, experimental results on proteins suggest a minor role for solvation effects. For example, the volume change for pressure-denaturation was found to be uncorrelated to the size of the surface area exposed (41, 42). This and other evidence (43) suggests that the role of solvation is small, and that elimination of cavities is the driving force for pressure effects.

The packing density of globular proteins is high (44), yet native packing defects ranging from a few to a few hundred cubic angstroms in size are typical (45, 46). Small-to-large residue mutations that fill native cavities can increase the stability of a protein (47), but result in a loss of function (48, 49). Thus, although cavities can be destabilizing (50, 51), by increasing flexibility (2) they may play an important functional role. Filling active site cavities *via* mutation (52) or ligand binding (53, 54) dramatically stabilizes proteins against pressure denaturation, demonstrating the importance of cavities in the pressure response. Additionally, NMR studies have found that the regions of a protein most sensitive to pressure are localized to cavities (55-57). In the most direct demonstration of the dominant role of cavities in the pressure response, the magnitude of the volume change for pressure-denaturation was found to increase as a result of cavity-creating and cavity-enlarging mutations in T4 lysozyme (T4L) and staphylococcal nuclease (58, 59).

Cavity elimination upon pressurization is commonly attributed to hydration, although direct observation of hydration is rare. Two such cases of experimentally observed water penetration of internal cavities at high pressure were reported for the L99A cavity-enlarging

mutant of T4L; an NMR study employing a reverse-micelle environment (60) and a crystallographic study (61). However, it is possible that the highly restricted environments used in these studies influenced the protein's response to pressure, and typically only indirect evidence is available for hydration of cavities under pressure. For example, in the studies of Roche et al. on cavity mutants of staphylococcal nuclease (59) in solution, chemical denaturants were employed to destabilize the protein sufficiently that experimentally accessible pressures led to unfolding. In this case, it is safe to assume that the pressure-denatured state is sufficiently unfolded that the cavity void is eliminated by occupancy with solvent.

Most investigations of the mechanism of the pressure response have focused on the equilibrium between native and pressure-denatured states, but in the equilibrium between two folded conformations alternative mechanisms for cavity elimination may contribute. One such possibility is a "structure-relaxation" mechanism that has been observed in cavity mutants at atmospheric pressure (2, 6), and may play a role in the pressure response. In this model, voids are eliminated by pressure due to an increase in the population of an alternative packing arrangement of the core in which cavities are filled with native side chains rather than solvent. This model has been suggested to play a role in certain proteins at high pressure (2, 62, 63), although the first direct experimental evidence for a structure-relaxation response to pressure is presented in chapter 5 of this dissertation using technologies reported in chapters 3 and 4.

2.5 The principles of SDSL EPR detection of pressure effects on proteins

SDSL EPR is a powerful spectroscopic tool for exploring both structure and dynamics in proteins. Most applications have employed the extensively characterized nitroxide side chain designated R1 (inset, Figure 2.3A) (64), and the present considerations will be restricted to use of R1 at helical sites where most information is available. Continuous wave (CW) spectral analysis

and saturation recovery (SR) of single R1 residues introduced site-specifically reveal local structural and dynamical features of the protein fold (65, 66), while pairs of R1 spin labels are employed to provide information on global structure *via* interspin distance measurements using CW EPR (67-70) or the time domain methods of double electron-electron resonance (DEER) (69, 71) or double quantum coherence (DQC) (72). There is no inherent size restriction on the systems that may be studied by SDSL EPR, making it particularly attractive for studying integral membrane proteins and large protein complexes. As reported in the following chapters, CW spectral analysis and DEER methodologies have been developed to explore the effects of pressure on spin-labeled proteins.

The CW spectrum of R1 in a protein encodes information on dynamic modes of the structure, and the way in which they are revealed is determined by the relative time scales of the EPR experiment and protein motions. For X-band EPR spectroscopy (≈9.5 GHz) the spectral lineshape of a nitroxide is modulated by rotational correlation times (τ) and/or lifetimes for exchange between different states (τ_{ex}) in the range of ≈0.1-100 ns, thus defining the time window through which CW EPR views protein motions. This time window conveniently overlaps that for fast backbone fluctuations that occur on the ns time scale, and sequence-specific variations in CW lineshape of R1 can provide a map of the relative amplitude and rate of fast backbone motions throughout a protein (66, 73) (Figure 2.3A). On the other hand, fluctuations between different conformations of a protein (conformational exchange) generally occur with τ_{ex} in the μs-ms range and are too slow to produce lineshape effects. However, if an R1 residue is placed at a site in the protein where the motion of the nitroxide is differentially modulated due to interactions with the protein, the EPR spectrum will have two resolved components, thus revealing the presence of conformational exchange but without information on τ_{ex} (66).

Essentially, the CW spectrum represents a snapshot of the conformational equilibrium frozen on the EPR time scale, as illustrated in Figure 2.3B.

The dynamical modes illustrated in Figure 2.3 are pressure sensitive and serve to define the information content derived from high-pressure SDSL EPR at the present stage of development. Consider first the influence of pressure on the ns time scale backbone motions illustrated in Figure 2.3A. For an R1 residue on the solvent accessible surface of a helix or structured loop, where the nitroxide does not make contact with the surrounding structure, the EPR spectrum consists of a single component that reflects an anisotropic motion of the nitroxide with effective rotational correlation time on the order of 1-2 ns (74). Such sites are generally abundant in relatively rigid helical proteins (66), and the overall nitroxide motion has contributions from internal fluctuations in the R1 side chain itself and fast backbone fluctuations (73, 74). To analyze the pressure dependence of the overall motion, McCoy and Hubbell adopted a simple model wherein the R1 side chain and protein segment to which it is attached were considered to move as a single kinetic unit (75). In chapter 3, this model is compared with one in which R1 and protein motions are considered as independent. Using these models, site-to-site variation in the pressure dependence of CW spectra of R1 at non-interacting helix surface sites may be viewed in the context of the relative compressibility of different regions, and can be used to define a site-specific map of relative molecular compressibility correlated with motions on the ns time scale.

Next consider the conformational equilibrium of Figure 2.3B, where R1 has a different mobility, and hence EPR spectrum, in each conformation due to differential interactions of the nitroxide with the protein. For conformational exchange that is slow on the CW EPR time scale, the spectrum of an equilibrium mixture of states is the sum of spectra corresponding to the

individual states weighted by their population (Figure 2.3B) (65, 66). The populations of the individual components can be extracted from such composite spectra (75) and the apparent equilibrium constant thus determined. In general, equilibrium constants are pressure-dependent and fitting data for the equilibrium constants as a function of pressure to [2.3] can provide the thermodynamic parameters that relate the conformational states. In situations where the equilibrium involves an excited state, one expects new spectral components to appear with applied pressure.

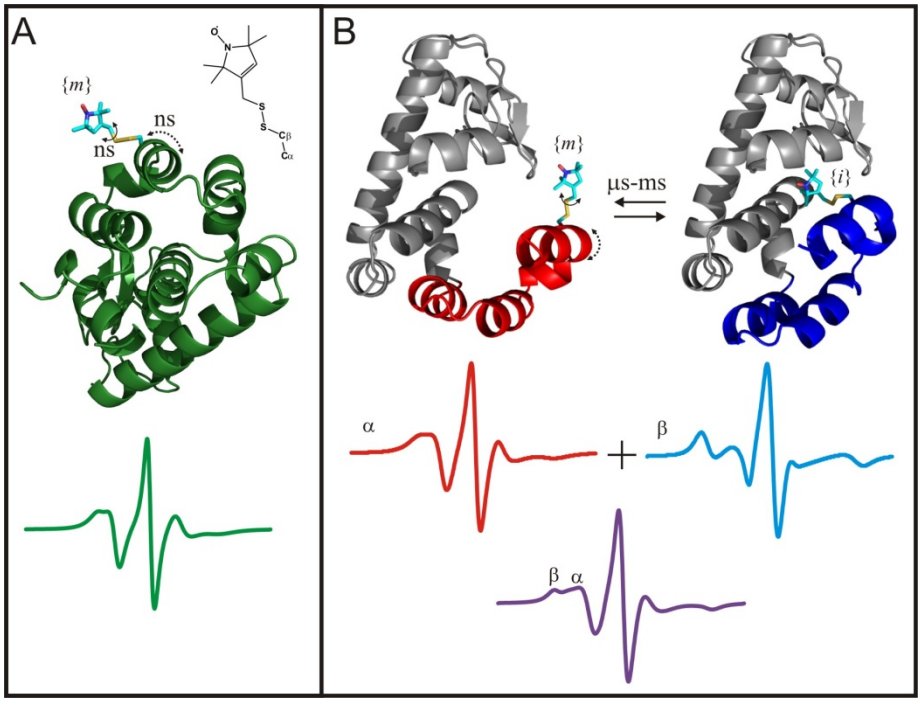

Figure 2.3 Protein dynamical modes and their manifestation in SDSL EPR. (A) In a well-ordered protein with a single dominant conformational state (green ribbon), the CW spectral lineshape for R1 at non-interacting surface sites reflects weakly anisotropic motion of the nitroxide (green spectrum), which varies from site-to-site due to variations in local backbone motion (66). The structure of R1 is shown in an inset, and the side chain is shown in stick representation attached to the protein model. The nitroxide motion is directly influenced by backbone fluctuations, here illustrated by a helix rocking mode (dashed curved arrow) and internal R1 motions (solid curved arrow) on the nanosecond time scale. (B) Equilibrium exchange between conformations α and β on the microsecond and longer time scale. Provided that R1 is placed such that it has distinct motions and spectra in α and β, the spectrum of the equilibrium mixture is the weighted sum (purple spectrum) of the spectra reflecting each state. In this example, the nitroxide exhibits a weakly anisotropic motion in α (red), and is immobilized due to interaction with the local protein environment in β (blue). The contributions from α and β in the low-field resonance line of the composite spectrum are indicated.

However, in general the EPR spectrum of each conformational state may have multiple and overlapping components due to μs exchange between substates within a given conformational well on the energy landscape. Moreover, *a priori* the population of each conformation is in general unknown at any pressure, therefore the spectra of the "pure" states are unknown. In such cases, analysis by spectral simulation is impractical and singular value decomposition (SVD) may be a viable alternative strategy for providing theremodynamic parameters that describe the conformational equilibrium, and is evaluated for this purpose in chapter 3. SVD is commonly used in analysis of time-dependent changes in spectroscopic data (76), and has been implemented in EPR (77, 78).

The distinction between "backbone fluctuations" and "conformational exchange" made in Figure 2.3 is based on the EPR time scale. Fluctuations of sufficiently high frequency to directly influence spectral lineshapes and to produce spectral averaging of distinct states ($\gtrsim 10^7$ sec^{-1}) are classified as fast backbone motions within a given conformational state. On the other hand, fluctuations that are slow on the EPR time scale (frequency $< 10^7$ sec^{-1}) are indicated as multiple components in the spectrum of R1, and are assigned as fluctuations between resolved protein states. These states could be two different conformations, as shown in Figure 2.3B, but could also be two substates of similar energy within a particular conformation. For example, the simple helical rocking motion illustrated in Figure 2.3A could in principle occur on a μs rather than a ns time scale and a properly placed nitroxide would sense different rotational states of the helix through local interactions, resulting in a multicomponent spectrum (66). In this case, due to the EPR time scale even low-amplitude helix rocking would be classified as an exchange event between substates rather than fast backbone fluctuation.

A priori, distinguishing exchange between substates in a single global conformation from exchange between distinct conformations cannot be made on the basis of a single multicomponent CW EPR spectrum. However, the dependence of the CW spectra on pressure aids in this distinction, as will be discussed in chapter 3. Structural fluctuations between substates are expected to be of small amplitude compared to those that transition one conformation into another, and intramolecular distance measurements between pairs of R1 residues with DEER spectroscopy (69) may distinguish the two. The unique strength of DEER is that it provides a distance distribution, revealing each structure present at equilibrium along with its probability. With pressure-resolved DEER (PR DEER), it becomes possible to track the population shifts and the magnitude of structural transitions as a function of pressure.

The above discussion provides the motivation for high-pressure SDSL EPR. Although high-pressure EPR has been extensively used in solid-state physics since its introduction in 1957 (79), biophysical studies utilizing spin labels have been much more limited, and have mostly focused on spin labeled lipids (80-91) or spin labeled proteins studied at atmospheric pressure to identify irreversible changes in protein structure caused by pressure (92-98). Early studies of spin labeled proteins at high pressure were limited to relatively low pressures (99) or were of limited scope (100), and in this dissertation technological and methodological developments in high-pressure SDSL EPR and their application to the study of spin-labeled proteins are presented.

2.6 Appendix

Proper buffer selection is an important practical consideration in any high pressure experiment because buffer ionization is accompanied by volume changes due to electrostriction of water, giving rise to pressure-dependent changes in pH. Moreover, for conformational changes accompanied by protonation or deprotonation of titratable residues, the buffer ionization

volume will directly contribute to the overall volume change (101-103). Thus, buffers with strongly pressure-dependent properties will invalidate the underlying assumption of constant solvent conditions in the thermodynamic treatment presented in section **2.3.1**, and buffers with small ionization volumes and minimal pH shifts with pressure are desired. Both the volume change of ionization and the associated pressure-dependent change in pH have been reported for many buffers, based on different theoretical and experimental approaches (104-107), including recent measurements using a pH meter (108) capable of operation at high pressures. These latter measurements revealed smaller pH changes than those calculated using experimental volume changes for buffer ionization, indicating non-negligible contributions from pressure-dependent changes in the dissociation constants of water and dissolved gases, particularly carbon dioxide. Some buffers useful with high pressure along with their corresponding properties are provided in Table 2.1.

Table 2.1 Examples of suitable buffers for use under high pressure (104, 105, 108)

Buffer	**pH range**	**ΔV^o(ionization) mL*mol^{-1}**	**ΔpH/ΔP kbar^{-1}**
2-Amino-2-(hydroxymethyl)-1,3-propanediol (TRIS)	7.0 – 9.0	+4.3	-0.03
2-(N-morpholino) ethanesulfonic acid (MES)	5.5 - 6.7	+3.9	-0.06
Sodium Acetate	3.6 – 5.6	-11	-0.03

2.7 References

1. Henzler-Wildman K & Kern D (2007) Dynamic personalities of proteins. *Nature* 450(7172):964-972.
2. López CJ, Yang Z, Altenbach C, & Hubbell WL (2013) Conformational selection and adaptation to ligand binding in T4 lysozyme cavity mutants. *Proc Natl Acad Sci USA* 110(46):E4306-4315.

3. Fanucci GE, Lee JY, & Cafiso DS (2003) Spectroscopic evidence that osmolytes used in crystallization buffers inhibit a conformation change in a membrane protein. *Biochemistry* 42(45):13106-13112.

4. Cafiso DS (2014) Identifying and quantitating conformational exchange in membrane proteins using site-directed spin labeling. *Acc Chem Res* 47(10):3102-3109.

5. Mulder FA, Hon B, Muhandiram DR, Dahlquist FW, & Kay LE (2000) Flexibility and ligand exchange in a buried cavity mutant of T4 lysozyme studied by multinuclear NMR. *Biochemistry* 39(41):12614-12622.

6. Bouvignies G, *et al.* (2011) Solution structure of a minor and transiently formed state of a T4 lysozyme mutant. *Nature* 477(7362):111-114.

7. Baldwin AJ & Kay LE (2009) NMR spectroscopy brings invisible protein states into focus. *Nat Chem Biol* 5(11):808-814.

8. Leopold PE, Montal M, & Onuchic JN (1992) Protein folding funnels: a kinetic approach to the sequence-structure relationship. *Proc Natl Acad Sci USA* 89(18):8721-8725.

9. Onuchic JN, Luthey-Schulten Z, & Wolynes PG (1997) Theory of protein folding: the energy landscape perspective. *Ann Rev Phys Chem* 48:545-600.

10. Boehr DD, Nussinov R, & Wright PE (2009) The role of dynamic conformational ensembles in biomolecular recognition. *Nat Chem Biol* 5(11):789-796.

11. Ma B, Shatsky M, Wolfson HJ, & Nussinov R (2002) Multiple diverse ligands binding at a single protein site: a matter of pre-existing populations. *Protein Sci* 11(2):184-197.

12. Kitahara R, *et al.* (2012) A delicate interplay of structure, dynamics, and thermodynamics for function: a high pressure nmr study of outer surface protein A. *Biophys J* 102(4):916-926.

13. Neudecker P, *et al.* (2012) Structure of an intermediate state in protein folding and aggregation. *Science* 336(6079):362-366.

14. Korzhnev DM, Religa TL, Banachewicz W, Fersht AR, & Kay LE (2010) A transient and low-populated protein-folding intermediate at atomic resolution. *Science* 329(5997):1312-1316.

15. Manglik A, *et al.* (2015) Structural insights into the dynamic process of β2-adrenergic receptor signaling. *Cell* 161(5):1101-1111.

16. Akasaka K (2006) Probing conformational fluctuation of proteins by pressure perturbation. *Chem Rev* 106(5):1814-1835.

17. Fourme R, Girard E, & Akasaka K (2012) High-pressure macromolecular crystallography and NMR: status, achievements and prospects. *Curr Opin Struct Biol* 22(5):636-642.

18. Wilton DJ, Kitahara R, Akasaka K, Pandya MJ, & Williamson MP (2009) Pressure-dependent structure changes in barnase on ligand binding reveal intermediate rate fluctuations. *Biophys J* 97(5):1482-1490.

19. Berlow RB, Dyson HJ, & Wright PE (2015) Functional advantages of dynamic protein disorder. *FEBS Lett* in press.

20. Kuwata K, *et al.* (2001) High pressure NMR reveals a variety of fluctuating conformers in β-lactoglobulin. *J Mol Biol* 305(5):1073-1083.

21. Kitahara R, Yokoyama S, & Akasaka K (2005) NMR snapshots of a fluctuating protein structure: ubiquitin at 30 bar–3 kbar. *J Mol Biol* 347(2):277-285.

22. Kitahara R, *et al.* (2000) High pressure NMR reveals active-site hinge motion of folate-bound Escherichia coli dihydrofolate reductase. *Biochemistry* 39(42):12789-12795.

23. Torrent J, *et al.* (2006) The use of pressure-jump relaxation kinetics to study protein folding landscapes. *Biochim Biophys Acta, Proteins Proteomics* 1764(3):489-496.

24. Winter R & Dzwolak W (2005) Exploring the temperature–pressure configurational landscape of biomolecules: from lipid membranes to proteins. *Philos Trans R Soc, A* 363(1827):537-563.

25. Prehoda KE, Mooberry ES, & Markley JL (1998) Pressure denaturation of proteins: evaluation of compressibility effects. *Biochemistry* 37(17):5785-5790.

26. Royer CA (2002) Revisiting volume changes in pressure-induced protein unfolding. *Biochim Biophys Acta, Protein Struct Mol Enzymol* 1595(1–2):201-209.

27. Bridgman PW (1914) The coagulation of albumen by pressure. *J Biol Chem* 19(4):511-512.

28. Frauenfelder H, Sligar SG, & Wolynes PG (1991) The energy landscapes and motions of proteins. *Science* 254(5038):1598-1603.

29. Kitahara R, Yamada H, Akasaka K, & Wright PE (2002) High pressure NMR reveals that apomyoglobin is an equilibrium mixture from the native to the unfolded. *J Mol Biol* 320(2):311-319.

30. Onuchic JN & Wolynes PG (2004) Theory of protein folding. *Curr Opin Struct Biol* 14(1):70-75.

31. Cooper A (1984) Protein fluctuations and the thermodynamic uncertainty principle. *Prog Biophys Mol Biol* 44(3):181-214.

32. Chalikian TV & Breslauer KJ (1996) On volume changes accompanying conformational transitions of biopolymers. *Biopolymers* 39(5):619-626.

33. Hummer G, Garde S, García AE, Paulaitis ME, & Pratt LR (1998) The pressure dependence of hydrophobic interactions is consistent with the observed pressure denaturation of proteins. *Proc Natl Acad Sci USA* 95(4):1552-1555.

34. Chalikian TV & Macgregor Jr RB (2009) Origins of pressure-induced protein transitions. *J Mol Biol* 394(5):834-842.

35. Meersman F, Smeller L, & Heremans K (2002) Comparative fourier transform infrared spectroscopy study of cold-, pressure-, and heat-induced unfolding and aggregation of myoglobin. *Biophys J* 82(5):2635-2644.

36. Chryssomallis GS, Torgerson PM, Drickamer HG, & Weber G (1981) Effect of hydrostatic pressure on lysozyme and chymotrypsinogen detected by fluorescence polarization. *Biochemistry* 20(14):3955-3959.

37. Zhang J, Peng X, Jonas A, & Jonas J (1995) NMR study of the cold, heat, and pressure unfolding of ribonuclease A. *Biochemistry* 34(27):8631-8641.

38. Imamura H & Kato M (2009) Effect of pressure on helix-coil transition of an alanine-based peptide: an FTIR study. *Proteins* 75(4):911-918.

39. Neumaier S, Buttner M, Bachmann A, & Kiefhaber T (2013) Transition state and ground state properties of the helix-coil transition in peptides deduced from high-pressure studies. *Proc Natl Acad Sci USA* 110(52):20988-20993.

40. Iwadate M, *et al.* (2001) Pressure-dependent changes in the structure of the melittin α-helix determined by NMR. *J Biomol NMR* 19(2):115-124.

41. Frye KJ, Perman CS, & Royer CA (1996) Testing the correlation between ΔA and ΔV of protein unfolding using m value mutants of staphylococcal nuclease. *Biochemistry* 35(31):10234-10239.

42. Rouget J-B, *et al.* (2011) Size and sequence and the volume change of protein folding. *J Amer Chem Soc* 133(15):6020-6027.

43. Voloshin VP, Medvedev NN, Smolin N, Geiger A, & Winter R (2015) Exploring volume, compressibility and hydration changes of folded proteins upon compression. *Phys Chem Chem Phys* 17:8499-8508.

44. Richards FM (1974) The interpretation of protein structures: total volume, group volume distributions and packing density. *J Mol Biol* 82(1):1-14.

45. Liang J & Dill KA (2001) Are proteins well-packed? *Biophys J* 81(2):751-766.

46. Hildebrand PW, Rother K, Goede A, Preissner R, & Frommel C (2005) Molecular packing and packing defects in helical membrane proteins. *Biophys J* 88(3):1970-1977.

47. Munson M, *et al.* (1996) What makes a protein a protein? Hydrophobic core designs that specify stability and structural properties. *Protein Sci* 5(8):1584-1593.

48. Lee C, Maeng JS, Kocher JP, Lee B, & Yu MH (2001) Cavities of a_1-antitrypsin that play structural and functional roles. *Protein Sci* 10(7):1446-1453.

49. Ogata K, *et al.* (1996) The cavity in the hydrophobic core of Myb DNA-binding domain is reserved for DNA recognition and trans-activation. *Nat Struct Biol* 3(2):178-187.

50. Eriksson AE, *et al.* (1992) Response of a protein structure to cavity-creating mutations and its relation to the hydrophobic effect. *Science* 255(5041):178-183.

51. Vlassi M, Cesareni G, & Kokkinidis M (1999) A correlation between the loss of hydrophobic core packing interactions and protein stability. *J Mol Biol* 285(2):817-827.

52. Lassalle MW, *et al.* (2001) Filling a cavity dramatically increases pressure stability of the c-Myb R2 subdomain. *Proteins: Struct, Funct, Bioinf* 45(1):96-101.

53. Toleikis Z, Cimmperman P, Petrauskas V, & Matulis D (2011) Determination of the volume changes induced by ligand binding to heat shock protein 90 using high-pressure denaturation. *Anal Biochem* 413(2):171-178.

54. Toleikis Z, Cimmperman P, Petrauskas V, & Matulis D (2012) Serum albumin ligand binding volumes using high pressure denaturation. *J Chem Thermodyn* 52(0):24-29.

55. Inoue K, *et al.* (2000) Pressure-induced local unfolding of the Ras binding domain of RalGDS. *Nat Struct Mol Biol* 7(7):547-550.

56. Kamatari YO, Smith LJ, Dobson CM, & Akasaka K (2011) Cavity hydration as a gateway to unfolding: an NMR study of hen lysozyme at high pressure and low temperature. *Biophys Chem* 156(1):24-30.

57. Kitahara R, *et al.* (2011) Structural plasticity of staphylococcal nuclease probed by perturbation with pressure and pH. *Proteins: Struct, Funct, Bioinf* 79(4):1293-1305.

58. Ando N, *et al.* (2008) Structural and thermodynamic characterization of T4 lysozyme mutants and the contribution of internal cavities to pressure denaturation. *Biochemistry* 47(42):11097-11109.

59. Roche J, *et al.* (2012) Cavities determine the pressure unfolding of proteins. *Proc Natl Acad Sci USA* 109(18):6945-6950.

60. Nucci NV, Fuglestad B, Athanasoula EA, & Wand AJ (2014) Role of cavities and hydration in the pressure unfolding of T4 lysozyme. *Proc Natl Acad Sci USA* 111(38):13846-13851.

61. Collins MD, Hummer G, Quillin ML, Matthews BW, & Gruner SM (2005) Cooperative water filling of a nonpolar protein cavity observed by high-pressure crystallography and simulation. *Proc Natl Acad Sci USA* 102(46):16668-16671.

62. Vidugiris GJA, Truckses DM, Markley JL, & Royer CA (1996) High-pressure denaturation of staphylococcal nuclease proline-to-glycine substitution mutants. *Biochemistry* 35(12):3857-3864.

63. Maeno A, *et al.* (2015) Cavity as a source of conformational fluctuation and high-energy state: high-pressure NMR study of a cavity-enlarged mutant of T4Lysozyme. *Biophys J* 108(1):133-145.

64. Fleissner MR, Cascio D, & Hubbell WL (2009) Structural origin of weakly ordered nitroxide motion in spin-labeled proteins. *Protein Sci* 18(5):893-908.

65. Bridges MD, Hideg K, & Hubbell WL (2010) Resolving conformational and rotameric exchange in spin-labeled proteins using saturation recovery EPR. *Appl Magn Reson* 37(1-4):363-363.

66. López CJ, Oga S, & Hubbell WL (2012) Mapping molecular flexibility of proteins with site directed spin labeling: a case study of myoglobin. *Biochemistry* 51(33):6568-6583.

67. Altenbach C, Oh K-J, Trabanino RJ, Hideg K, & Hubbell WL (2001) Estimation of inter-residue distances in spin labeled proteins at physiological temperatures: experimental strategies and practical limitations. *Biochemistry* 40(51):15471-15482.

68. Rabenstein MD & Shin YK (1995) Determination of the distance between two spin labels attached to a macromolecule. *Proc Natl Acad Sci USA* 92(18):8239-8243.

69. Jeschke G (2012) DEER distance measurements on proteins. *Annu Rev Phys Chem* 63:419-446.

70. Mchaourab Hassane S, Steed PR, & Kazmier K (2011) Toward the fourth dimension of membrane protein structure: insight into dynamics from spin-labeling EPR spectroscopy. *Structure* 19(11):1549-1561.

71. Pannier M, Veit S, Godt A, Jeschke G, & Spiess HW (2000) Dead-time free measurement of dipole-dipole interactions between electron spins. *J Magn Reson* 142(2):331-340.

72. Borbat PP & Freed JH (2013) Pulse dipolar electron spin resonance: distance measurements. *Structural Information from Spin-Labels and Intrinsic Paramagnetic Centres in the Biosciences,* Structure and Bonding, eds Timmel CR & Harmer JR (Springer, Berlin; Heidelberg), Vol 152, pp 1-82.

73. Columbus L & Hubbell WL (2004) Mapping backbone dynamics in solution with site-directed spin labeling: GCN4−58 bZip free and bound to DNA. *Biochemistry* 43(23):7273-7287.

74. Columbus L, Kálai T, Jekö J, Hideg K, & Hubbell WL (2001) Molecular motion of spin labeled side chains in α-helices: analysis by variation of side chain structure. *Biochemistry* 40(13):3828-3846.

75. McCoy J & Hubbell WL (2011) High-pressure EPR reveals conformational equilibria and volumetric properties of spin-labeled proteins. *Proc Natl Acad Sci USA* 108(4):1331-1336.

76. Henry ER & Hofrichter J (1992) Singular value decomposition: application to analysis of experimental data. *Numerical Computer Methods,* Methods in Enzymology, eds Brand L & Johnson ML (Academic Press), Vol 210, pp 129-192.

77. Keszler A, Kalyanaraman B, & Hogg N (2003) Comparative investigation of superoxide trapping by cyclic nitrone spin traps: the use of singular value decomposition and multiple linear regression analysis. *Free Radical Biol Med* 35(9):1149-1157.

78. Lauricella R, Allouch A, Roubaud V, Bouteiller J-C, & Tuccio B (2004) A new kinetic approach to the evaluation of rate constants for the spin trapping of superoxide/hydroperoxyl radical by nitrones in aqueous media. *Org Biomol Chem* 2(9):1304-1309.

79. Walsh WM & Bloembergen N (1957) Paramagnetic resonance of nickel fluosilicate under high hydrostatic pressure. *Phys Rev* 107(3):904-905.

80. Hsia JC & Boggs JM (1973) Pressure effect on the membrane action of a nerve-blocking spin label. *Proc Natl Acad Sci USA* 70(11):3179-3183.

81. Trudell JR, Hubbell WL, & Cohen EN (1973) Electron spin resonance studies with the volatile anesthetics on phospholipid model membranes. *Ann N Y Acad Sci* 222(1):530-538.

82. Trudell JR, Hubbell WL, & Cohen EN (1973) Pressure reversal of inhilation anesthetic-induced disorder in spin-labeled phospholipid vesicles. *Biochim Biophys Acta, Biomembr* 291(2):328-334.

83. Trudell JR, Hubbell WL, Cohen EN, & Kendig JJ (1973) Pressure reversal of anesthesia - extent of small-molecule exclusion from spin-labeled phospholipid model membranes. *Anesthesiology* 38(3):207-211.

84. Trudell JR, Payan DG, Chin JH, & Cohen EN (1974) Pressure-induced elevation of phase transition temperature in dipalmitoylphosphatidylcholine bilayers: an electron spin resonance measurement of the enthalpy of phase transition. *Biochim Biophys Acta, Biomembr* 373(3):436-443.

85. Kendig JJ, Trudell JR, & Cohen EN (1975) Effects of pressure and anesthetics on conduction and synaptic transmission. *J Pharmacol Exp Ther* 195(2):216-224.

86. Trudell JR, Payan DG, Chin JH, & Cohen EN (1975) Antagonistic effect of an inhalation anesthetic and high-pressure on phase-diagram of mixed dipalmitoyl-dimyristoylphosphatidylcholine bilayers. *Proc Natl Acad Sci USA* 72(1):210-213.

87. Chin JH, Trudell JR, & Cohen EN (1976) The compression-ordering and solubility-disordering effects of high pressure gases on phospholipid bilayers. *Life Sci* 18(5):489-497.

88. Mastrangelo CJ, Kendig JJ, Trudell JR, & Cohen EN (1979) Nerve membrane lipid fluidity - opposing effects of high-pressure and ethanol. *Undersea Biomed Res* 6(1):47-53.

89. Hwang JS, Rao KVS, & Freed JH (1976) An electron spin resonance study of the pressure dependence of ordering and spin relaxation in a liquid crystalline solvent. *J Phys Chem* 80(13):1490-1501.

90. Iwamoto S, Yoshioka D, & Sueishi Y (2006) Distinctive pressure effects on partitioning and rotational motions of nitroxide spin probes in dispersions of a triglyceride membrane. *Chem Phys Lett* 430(4–6):314-318.

91. Sueishi Y, Iwamoto S, Miyazono K, Nakatani S, & Nakagawa K (2012) Macroscopic characterization of bilayer membranes composed of triglyceride and phosphatidylcholine investigated using high-pressure ESR spin probe technique. *Colloids Surf A* 415(0):262-267.

92. Yamaguchi T, Kawamura H, Kimoto E, & Tanaka M (1989) Effects of temperature and pH on hemoglobin release from hydrostatic pressure-treated erythrocytes. *J Biochem* 106(6):1080-1085.

93. Kaneshiro SM & Clark DS (1995) Pressure effects on the composition and thermal behavior of lipids from the deep-sea thermophile Methanococcus jannaschii. *J Bacteriol* 177(13):3668-3672.

94. Yuasa M, Ono T-a, & Inoue Y (1995) Effects of hydrostatic pressure on photosynthetic systems. I. Preferential destruction of the O_2-evolving center. *Plant Cell Physiol* 36(6):1081-1088.

95. Martinis SA, *et al.* (1996) Probing the heme iron coordination structure of pressure-induced cytochrome P420cam. *Biochemistry* 35(46):14530-14536.

96. Schulze H, Hui Bon Hoa G, Helms V, Wade RC, & Jung C (1996) Structural changes in cytochrome P-450cam effected by the binding of the enantiomers (1R)-camphor and (1S)-camphor. *Biochemistry* 35(45):14127-14138.

97. Yamaguchi T, Yamamoto M, & Kimoto E (1996) Release of spectrin-containing vesicles from human erythrocyte ghosts by dimyristoylphosphatidylcholine. *J Biochem* 119(1):95-99.

98. Yamaguchi T, Nakano T, Matsumoto M, & Terada S (1998) Effects of chemical modification of cysteines 201 and 317 of band 3 on hemolytic properties of human erythrocytes under hydrostatic pressure. *Jpn J Physiol* 48(3):205-210.

99. Affleck R, Clark DS, Kamat S, & Russell AJ (1994) High pressure EPR studies of protein mobility in reversed micelles. *Biotechnol Bioeng* 43(4):342-348.

100. von Goldammer E, Paul J, & Wenzel HR (1992) Applications of spin-label techniques at high pressures. *Bioactive Spin Labels*, ed Zhdanov R (Springer Berlin; Heidelberg), pp 611-629.

101. Lee S, Heerklotz H, & Chalikian TV (2010) Effects of buffer ionization in protein transition volumes. *Biophys Chem* 148(1–3):144-147.

102. Rasper J & Kauzmann W (1962) Volume changes in protein reactions. I. Ionization reactions of proteins. *J Amer Chem Soc* 84(10):1771-1777.

103. Zipp A & Kauzmann W (1973) Pressure denaturation of metmyoglobin. *Biochemistry* 12(21):4217-4228.

104. Neuman RC, Kauzmann W, & Zipp A (1973) Pressure dependence of weak acid ionization in aqueous buffers. *J Phys Chem* 77(22):2687-2691.

105. Kitamura Y & Itoh T (1987) Reaction volume of protonic ionization for buffering agents. Prediction of pressure dependence of pH and pOH. *J Solution Chem* 16(9):715-725.

106. El'yanov BS & Hamann SD (1975) Some quantitative relationships for ionization reactions at high pressures. *Aust J Chem* 28(5):945-954.

107. Min SK, Samaranayake CP, & Sastry SK (2011) In situ measurement of reaction volume and calculation of pH of weak acid buffer solutions under high pressure. *J Phys Chem B* 115(20):6564-6571.

108. Samaranayake CP & Sastry SK (2010) In situ measurement of pH under high pressure. *J Phys Chem B* 114(42):13326-13332.

Chapter 3: Site-directed spin labeling and circular dichroism reveal structural and dynamical features of high-pressure states of myoglobin

3.1 Summary

In this chapter, high-pressure instrumentation for circular dichroism and developments in high-pressure site-directed spin labeling EPR are reported, and a combination of EPR and circular dichroism is used to map pressure-populated structural changes in various states of myoglobin. To monitor global secondary structure content by circular dichroism (CD) at high pressure, a modified optical cell using a custom MgF_2 window with a reduced aperture is introduced. A high-pressure EPR system based on a commercially available pressure intensifier and ceramic sample cell is described, and methods for quantitative spectral analysis are evaluated. A combination of SDSL EPR and CD is employed to map reversible structural transitions in holomyoglobin (holoMb) and apomyoglobin (apoMb) as a function of applied pressure up to 2 kbar. CD shows that the high-pressure excited state of apoMb at pH 6 has helical content identical to that of native apoMb, but reversible changes reflecting the appearance of a conformational ensemble are observed by SDSL EPR, suggesting a helical topology that fluctuates slowly on the EPR time scale. Although the high-pressure state of apoMb at pH 6 has been referred to as a molten globule (MG), the data presented here reveal significant differences from the well-characterized pH 4.1 MG of apoMb. Pressure-populated states of both holo- and apoMb at pH 4.1 have significantly less helical structure. The data reveal that a MG state of holomyoglobin populated at pH 4.1 and high-pressure retains ligand-binding capacity, and under the same equilibrium conditions a state of apomyoglobin is populated that is structurally similar to a transient folding intermediate.

3.2 Introduction

Proteins in solution are dynamic molecules, exhibiting conformational flexibility across a range of time and length scales (1). In addition to a well-ordered native state, conformational excursions to low-lying "excited states" may be required in protein function (2). Despite their functional relevance, excited states are sparsely populated and may escape detection by standard spectroscopic techniques. As discussed in detail in chapter 2, hydrostatic pressure apparently offers a solution to this problem by reversibly populating excited states of proteins, allowing for spectroscopic characterization (3-8).

Assuming that pressure can populate excited states for study, the increased configurational entropy of such states presents a challenge to spectroscopic methods that aim to describe structure; depending on the intrinsic time scale of the method either a population-weighted average structure or a heterogeneous ensemble is observed. The intrinsic time scale of continuous wave (CW) EPR spectroscopy (0.1 – 100 ns) is fast compared to protein conformational fluctuations (typically μs-ms), and site-directed spin labeling EPR (SDSL EPR) can provide a snap-shot of a conformational equilibrium frozen in time (9-11). The EPR spectrum of the commonly implemented R1 spin label (12) in a protein encodes information on local structure (13-15), topology (16), and ps - ns backbone dynamics (11, 17), and can thereby serve to identify conformational heterogeneity in equilibrium states (11), including those populated by pressure. Recently, an EPR system capable of pressures up to 4 kbar and optimized for SDSL was reported, making it possible to explore the structure and dynamics of high-pressure states of proteins using SDSL EPR (18). An improved system with a programmable pressure intensifier and ceramic sample cell is introduced here.

Conformational exchange that is slow on the EPR time scale results in a spectrum that is the sum of spectra corresponding to the individual states weighted by their population (11). In the simple case of a conformational equilibrium wherein each conformation generates a single, distinct spectral component, spectral simulation (19) allows the populations of the individual components to be readily extracted from such composite spectra and the apparent equilibrium constant thus determined. In general, equilibrium constants are pressure-dependent and fitting data for the equilibrium constants as a function of pressure to [3.1] can provide the thermodynamic parameters that relate the conformational states for a two-state equilibrium.

$$\ln\left(\frac{K}{K(0)}\right) = -\frac{\Delta\bar{V}^o}{RT}(P) + \frac{\Delta\beta_T}{2RT}(P)^2 \qquad [3.1]$$

K and K(0) are the equilibrium constants at applied (gauge) pressure P and at atmospheric pressure (P=0), respectively, and $\Delta\bar{V}^o$ and $\Delta\bar{\beta}_T$ are the partial molar volume and isothermal compressibility differences, respectively, between states. In more complex cases, the spectral lineshape corresponding to each thermodynamic state may be complex (multi-component), and the spectra of the "pure" states may not be known. Thus, alternative methods for identifying and characterizing conformational exchange from EPR spectral changes are desired. Singular value decomposition (SVD) is an attractive potential alternative to spectral simulations (see section **3.4**). SVD is commonly used in analysis of time-dependent changes in spectroscopic data (20), and has been implemented in EPR (21, 22); in this chapter, SVD is evaluated for analysis of pressure-dependent changes in EPR spectra.

For sites on the surface of a helix or structured loop, the EPR spectrum of an R1 residue consists of a single component that reflects an anisotropic motion of the nitroxide with effective rotational correlation time on the order of 1-2 ns (11), provided that the nitroxide does not make contact with the surrounding structure. Pressure generally causes changes in the single

component lineshape without populating new spectral components for such sites in relatively rigid helical proteins or protein segments, as shown in this chapter. The effective nitroxide motion has contributions from fast backbone fluctuations of the protein in addition to internal fluctuations in the R1 side chain itself (17, 23). In earlier work the pressure dependence of the nitroxide motion (18) was treated using a model wherein the R1 side chain and protein segment to which it is attached were considered to move as a single kinetic unit. In this chapter, this model is compared to one described below in which R1 and protein motions are considered as independent.

The EPR spectrum of R1 in a stable helix is primarily sensitive to rocking motions of the segment to which it is attached (24). Such motion adds to the internal motion of R1 so that the observed effective correlation time of R1 on a helical segment (τ_e) is approximately related to the correlations times for R1 internal (τ_i) and protein (τ_p) motions by

$$\frac{1}{\tau_e} = \frac{1}{\tau_i} + \frac{1}{\tau_p} \qquad [3.2]$$

Each reciprocal correlation time (rate) in [3.2] can be related to pressure through a volume of activation, $\Delta V^{\ddagger}$, according to (18), by

$$\frac{1}{\tau(P)} = \frac{1}{\tau(0)} e^{\frac{-P\Delta V^{\ddagger}}{RT}} \approx \frac{1}{\tau(0)}\left(1 - \frac{P\Delta V^{\ddagger}}{RT}\right) \qquad [3.3]$$

where $\tau(0)$ is a correlation time at P = 0 and the linearized approximate form is obtained by expansion of the exponential about P = 0 and truncating higher-order terms based on the typically small $\Delta V^{\ddagger}$ encountered ($\lesssim$5 mL/mol) and limiting analysis to moderate pressures ($\lesssim$2 kbar). In the simpler model used by McCoy and Hubbell (18), the natural log of the exponential form of [3.2] is taken, and

$$\ln\left(\frac{\tau_e(P)}{\tau_e(0)}\right) = \frac{\Delta V_e^{\ddagger} P}{RT} \qquad [3.4]$$

where the effective activation volume $\Delta V_e^{\ddagger}$ is determined from a linear fit of $\ln\left(\frac{\tau_e(P)}{\tau_e(0)}\right)$ vs. P. To separate contributions from protein and nitroxide motion, [3.2] is combined with the linearized form of [3.3] for each correlation time to yield

$$\frac{1}{\tau_o(P)} = \frac{1}{\tau_o(0)} - \frac{P}{RT}\left(\frac{\Delta V_i^{\ddagger}}{\tau_i(0)} + \frac{\Delta V_p^{\ddagger}}{\tau_p(0)}\right) \qquad [3.5]$$

For the non-interacting solvent exposed surface sites being considered here, the internal motion of R1 has a rate $1/\tau_i(0) \approx 5x10^8$ sec^{-1} that is expected to be site-independent (17, 24). Values for $1/\tau_p(0)$ can be determined from equation [3.2] using experimental values of $1/\tau_e(0)$ determined from spectral simulation together with $1/\tau_i(0) = 5x10^8$ sec^{-1}. For the backbone motions that strongly influence the EPR lineshape, $\tau_p(0)$ must be on the order of $\tau_i(0)$ and experimental data suggest that in many cases they are essentially the same.

The activation volume for nitroxide motion, $\Delta V_i^{\ddagger}$, likely has its origin in fluctuations of the solvent cage around the nitroxide (18) and, like $\tau_i(0)$, is expected to be approximately site-independent. Thus, variations of the slope from site-to-site are taken to reflect differences in $\Delta V_p^{\ddagger}$, which in this model corresponds to local volume fluctuations at frequency near $1/\tau_p(0) \approx 5x10^8$ sec^{-1}.

Mean-squared volume fluctuations of a solvent-impenetrable particle, including a folded protein, are related to the compressibility according to (25)

$$\langle(\delta V)^2\rangle = \beta_T kT \qquad [3.6]$$

where k is the Boltzmann constant. Thus, activation volumes from variable-pressure EPR spectra of R1 at non-interacting helix surface sites may be viewed in the context of the relative compressibility of different regions, and can be used to define a site-specific map of relative molecular compressibility correlated with motions on the ns time scale.

While SDSL EPR provides site-specific information on tertiary contact sites and topology in a protein, it does not provide global information on secondary structure that is needed to reliably interpret SDSL EPR data in terms of conformational changes due to pressure application. Far-UV circular dichroism (CD) spectroscopy can provide the required information on secondary structure (26, 27), but high-pressure CD spectroscopy has not been developed due to the lack of a viable window material for a high-pressure sample cell (28); materials used in other optical spectroscopies for high-pressure experiments (quartz and sapphire) are unsuitable for use with circularly polarized light (see section **3.7**). As a result, CD studies have been limited to low pressures (0.2 kbar) (29), or for measuring pressure-populated changes after pressure has been released (30-35). Here a high-pressure optical cell for CD studies up to 2.4 kbar is introduced, using a custom MgF_2 window with a reduced aperture. Design and evaluation of the modified optical cell is presented in section **3.7**. This development sets the stage for combined application of SDSL EPR and CD to explore the structure of pressure-populated excited states of proteins.

An example of an excited protein state is the molten globule (MG), a compact but dynamic state with native-like secondary structure but without close side chain packing in the core that is typical of the native state (36). MGs are typically stabilized at low pH or in the presence of denaturants and are believed to represent intermediates in protein folding (37, 38) and in some cases may mediate protein function (39). The MG of apomyoglobin (apoMb) stabilized at pH 4.1 is an ideal subject for exploring the structure and dynamics of such states because it can be populated under conditions suitable for study by high-resolution NMR (40). At pH 4.1, NMR $^{13}C\alpha$ chemical shift data showed that the native A, G, and H helices are largely retained in the MG state, but reduced values of the chemical shift relative to the native state of

apoMb suggest that non-helical states are sampled. Moreover, heteronuclear NOE data reveal gradients of fast backbone fluctuations in these helices not observed in native apoMb (41). Relaxation dispersion NMR showed the MG to be in pH-dependent equilibrium with other partially folded forms, indicating that the MG state will also be present in an equilibrium mixture at neutral pH, although with a small population relative to the native structure (i.e., an excited state) (38). Furthermore, this equilibrium MG was found to be structurally similar to the second of two intermediates identified during kinetic refolding by ultra-fast H/D exchange coupled with 2D NMR (42).

Application of pressure is expected to increase the equilibrium population of a MG state at neutral pH to levels that can be observed spectroscopically (43). Indeed, a state of apoMb, populated at 2 kbar, pH 6, was designated as a MG based on the similarity of its intrinsic fluorescence properties with that of the pH 4.1 state of apoMb (44), although it does not bind the dye ANS as is typical of MG states in general (45, 46). This pressure-populated state has been examined with high-resolution NMR (47, 48), where the integral intensities of most cross-peaks in the ^{1}H-^{15}N HSQC spectrum disappear due to broadening, suggesting that the entire polypeptide chain is transformed into a heterogeneously disordered conformation fluctuating on the ms time scale (48). Based on this behavior, the high pressure state was also designated as a MG, but the lack of spectral information precluded any information regarding details of the structures present. Clearly, this high-pressure MG state differs in detail from the pH 4.1 MG, for which high resolution information was obtained (41). Limited proteolysis and H/D exchange experiments in the same pressure range also reported increased flexibility, particularly in the B and E helices (49), and fluorescence and absorption spectroscopy revealed pressure-dependent

changes in both apoMb and holomyoglobin (holoMb), but again without specific information regarding the structures present (44-46, 50).

Thus, there is little information on the secondary or tertiary structure of the pressure-populated MG and how it compares to the well-characterized pH 4.1 MG. In the present study, high-pressure CD and SDSL EPR are used to explore the secondary structure and tertiary fold of high-pressure states of both apo- and holo-Mb. Results show that unlike the pH 4.1 MG of apoMb, the high-pressure state formed at pH 6 at 2 kbar retains the full secondary structure content of native apoMb, despite a heterogeneous tertiary fold revealed by SDSL EPR. At pH 4.1, a MG-like state of holoMb is reversibly populated at 2 kbar but with a reduced helical content. Finally, at pH 4.1 and 2 kbar, a state of apoMb is formed that retains a significant population of secondary structure and may correspond to a transient folding intermediate. In each case, EPR provides site-specific information regarding the location and local dynamics associated with the transition to these states.

3.3 Results

At pH 6.0 and atmospheric pressure, apoMb retains a structure largely similar to the holo protein except for local unfolding in the region of helix F that caps the heme pocket (51, 52); at pH 4.1, the well-characterized MG state is populated (41). In contrast, holoMb retains the WT structure under the same conditions (53). In the present study, far-UV CD spectra were acquired on holoMb and apoMb at pH 6.0 and pH 4.1 in the pressure range 0 to 2.4 kbar (Figure 3.1 and 2). These data were analyzed to determine the changes in secondary structural content as a function of pressure in each state (Table 3.1), and the apparent change in partial molar volume ($\Delta\overline{V}^{o}$) and free energy (ΔG^{o}) for transitions observed in the low pH states (insets, Figure 3.1 and 2). UV-Vis spectra were acquired on holoMb at pH 6.0 and pH 4.1 to monitor the Soret band as

an indicator of structural changes in the heme-binding pocket in the pressure range 0 to 2 kbar (Figure 3.A1). The reversibility of all pressure-populated changes in CD and UV-Vis spectra was verified by acquiring spectra at 0 bar after maximum pressurization; these were universally superimposable upon pre-pressurization spectra taken at 0 bar, and are not included for clarity of presentation.

Table 3.1 Pressure-dependent secondary structure content estimation from far-UV circular dichroism.

	pH	Pressure (kbar)	α-helix[a]	β-Sheet	Turn	Unordered
HoloMb	6.0	0	0.67	0.02	0.13	0.18
		2	0.67	0.02	0.10	0.21
		2.4	0.68	0.01	0.11	0.20
	4.1	0	0.72	0.01	0.10	0.17
		2	0.43	0.05	0.22	0.30
		2.4	0.42	0.06	0.22	0.30
ApoMb	6.0	0	0.57	0.02	0.20	0.21
		2	0.56	0.02	0.19	0.23
		2.4	0.56	0.02	0.19	0.23
	4.1	0	0.48	0.08	0.22	0.22
		2	0.28	0.19	0.22	0.31
		2.4	0.26	0.23	0.22	0.29

[a] the content of secondary structure calculated using the Contin algorithm (26, 27) are given as fractional populations.

To monitor site-specific changes in structure and dynamics due to pressure in holoMb and apoMb, a single R1 residue was introduced in each of the 8 native helices, one at a time, at the sites shown in Figure 3.3 and the EPR spectra were recorded for each state investigated at 0 and 2 kbar (Figure 3.4A). Although this is a sparse sampling of the structure, the data serve to illustrate the capability of the combined CD/SDSL approach and to identify salient features of each of the myoglobin states under pressure. To further characterize the pressure-populated changes in apoMb and holoMb at pH 6.0, variable-pressure EPR spectra were collected from 0 to 2 kbar in 250 bar increments for 19 residues in holoMb (Figure 3.5 and 3.A2) and a single R1 residue in apoMb for more comprehensive spectral analysis.

Atmospheric pressure EPR spectra for each of these mutants were previously reported for holoMb and apoMb at pH 6.0 and for apoMb at pH 4.1 (11); these spectra are reproduced here for comparative purposes. The atmospheric pressure EPR spectra of holoMb at pH 4.1 are new, as are the high-pressure EPR spectra for all states. As for the CD and UV-Vis data, EPR spectral changes at high pressure are reversible (Figure 3.A3), ensuring thermodynamic equilibrium between the conformational states observed over the pressure range investigated.

3.3.1 HoloMb at pH 6.0 is relatively rigid and pressure insensitive to 2 kbar. Analysis of the far-UV CD spectrum of holoMb (Figure 3.1A) using the Contin algorithm (26) estimates 67% helical content at 0 bar (gauge pressure; equivalent to atmospheric pressure), consistent with previously reported CD measurements of holoMb under similar conditions (54). Upon pressurization, there is little change in the fractional helicity, with a final value of 68% at 2 kbar. The Soret band intensity remains constant from 0 to 2 kbar, with only a small shift in the wavelength of maximum intensity from 409 to 408 nm (Figure 3.A1), suggesting little change in the structure surrounding the heme-binding pocket.

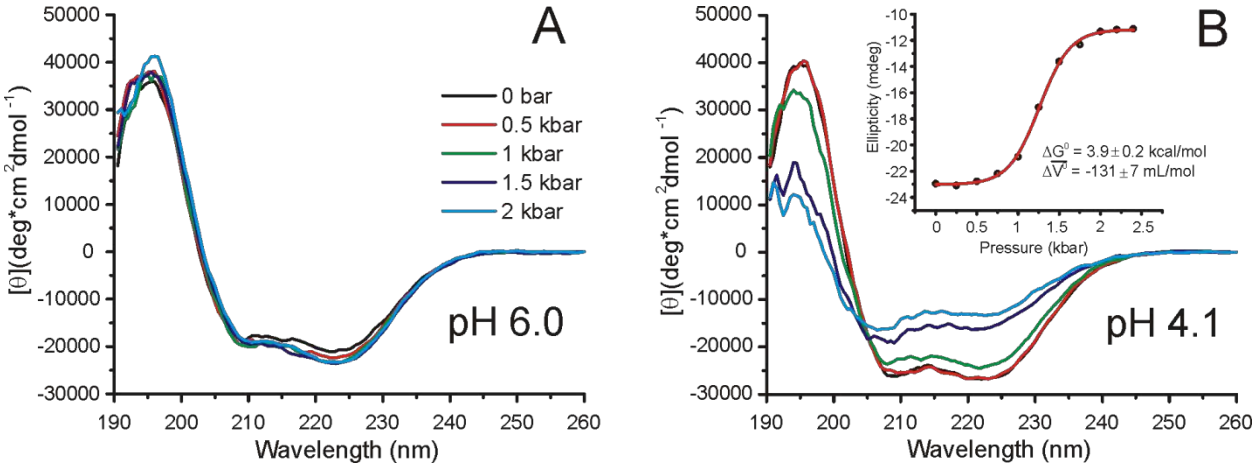

Figure 3.1 Variable-pressure CD spectra of holoMb. Each spectrum is the average of 9 scans. (A) Far-UV CD spectra of 14.1 μM holoMb in 5 mM MES at pH 6.0, without salts, from 0 to 2 kbar in 0.5 kbar increments. (B) Far-UV CD spectra of 11.2 μM holoMb in 5 mM sodium acetate at pH 4.1, without salts. Inset: a plot of ellipticity vs. pressure and the best-fit to a two-state model (red trace) to give the indicated ΔG^o and $\Delta \overline{V}^o$ of transition (see section **3.6**).

Most of the EPR spectra for holoMb at 0 bar (black traces, column 1, Figure 3.4A) have a single component reflecting a weakly anisotropic motion of the nitroxide, typical of non-interacting helix surface residues (23). The lineshape variation among these spectra reflects, in part, residue-to-residue differences in the ns time scale dynamics of the backbone (11). Exceptions are residues 87R1 and 106R1 which have two resolved components, one of which corresponds to a small population of an immobilized state of the nitroxide (arrows, column 1, Figure 3.4A). In the case of 87R1 it was previously shown that the origin of the immobile state was flexibility of the F helix, in which the residue is located, where some conformations allow contact of the nitroxide with the nearby protein environment (11). Flexibility in the adjacent C helix (11, 55) may similarly account for the immobile state in residue 106R1, although this remains to be established.

Upon pressurization, two classes of behavior are observed. In most residues, there are only small lineshape changes arising from a decrease in the nitroxide mobility; this is evidenced by the reduction in intensity of the central line (compare black and green traces, column 1, Figure 3.4A). A similar effect was observed for R1 at sites in T4 lysozyme under pressure and was interpreted in terms of an activation volume for rotational diffusion of the nitroxide (18). The second behavior exhibited is a shift in the relative population of spectral components toward the more immobile component, illustrated in Figure 3.4B (center panel), and observed on a smaller scale for 87R1 and 106R1. This pressure-dependent shift in population for 87R1 and 106R1 is presumably a reflection of local compressibility of the protein. For 87R1, this interpretation is consistent with crystallographic and near-IR/Raman spectroscopic studies of holoMb at high pressure which revealed flexibility in helix F (56, 57).

To quantitatively examine the subtle lineshape changes observed for the majority of residues in Figure 3.4, spectra were collected for a larger set of residues from 0 to 2 kbar in 250 bar increments (Figure 3.A2). Spectral simulations were performed according to the microscopic order macroscopic disorder (MOMD) model (19) to determine τ_e for nitroxide motion as a function of pressure (see section **3.6**). The fitted order parameters (S) and τ_e for each residue at 0 bar are shown in Table 3.2. All sites were well-fit to a model wherein S is constant and τ_e varies as a function of pressure, except for 66R1. For this residue, the simulations were improved by allowing S to vary, and the fits show a decrease in order as pressure is increased. As an example of the general quality of the fits, Figure 3.A4 shows variable-pressure EPR spectra with fits overlaid for 22R1 and 42R1.

The pressure-dependent τ_e for each of the 19 residues was fit to [3.4] to determine $\Delta V_e^{\ddagger}$ (Table 3.2). As anticipated, there is site-to-site variation in $\Delta V_e^{\ddagger}$, although most residues exhibit values of ≈2-3 mL/mol. In order to decompose the activation volume into protein and nitroxide components using [3.5], a residue with approximately zero contribution from protein motion is desired. Residue 22R1 was selected for this purpose; variable-pressure EPR spectra for this residue are shown in Figure 3.6A and B, and Figure 3.A2A. Residue 22 is located in the core B helix, one of the most rigid regions of the sequence based on crystallographic thermal factors (Figure 3.6C) and NMR data (41). For this residue, $1/\tau_e$ vs. pressure was plotted according to [3.5], and a linear fit with $\tau_e = \tau_i$ and $\Delta V_p^{\ddagger} = 0$ yielded a volume of activation for internal R1 motion $\Delta V_i^{\ddagger} = 2.27$ mL/mol (Figure 3.6D). With this value for $\Delta V_i^{\ddagger}$ the pressure dependence of R1 at other sites can be used to estimate $\Delta V_p^{\ddagger}$ and gauge the relative flexibility of the sequences to which R1 is attached.

Table 3.2 Variable-pressure EPR spectral simulation parameters and activation volumes for holoMb at pH 6.0

Spin-labeled residue	$\tau_o(0)$ (ns)	S	Effective Activation Volume (mL/mol)	Protein Activation Volume (mL/mol)
5	1.50	0.27	1.57±0.04	-1.2±0.2
12	1.79	0.26	3.22±0.04	
19	1.11	0.35	2.24±0.03	2.1±0.1
22	2.03	0.31	2.48 ± 0.03	
23	2.35	0.20	2.18 ± 0.06	
35	2.03	0.30	3.0 ± 0.1	
38	1.99	0.50	3.08 ± 0.05	
41	1.56	0.32	3.1 ± 0.1	4.9±0.7
42	1.01	0.47	5.81 ± 0.09	7.1±0.4
54	1.22	0.26	2.34 ± 0.03	2.17±0.09
57	1.12	0.40	2.38 ± 0.06	2.1±0.2
66	1.69	0.42-0.36	1.16 ± 0.02	
70	1.79	0.63	3.8 ± 0.1	
78	1.52	0.40	3.22 ± 0.04	4.9±0.2
96	1.63	0.37	2.84 ± 0.03	4.0±0.2
105	5.14	0.37	2.47 ± 0.09	
126	1.07	0.20	2.79 ± 0.07	2.4±0.2
132	3.50	0.58	1.3 ± 0.1	
147	1.56	0.21	2.03± 0.04	-0.03±0.3

As an example, spectra, simulations, and a plot of $1/\tau_e$ vs. pressure for 42R1 are shown in Figure 3.6. For this residue $\tau_e(0)$ = 1.01 ns, therefore $\tau_P(0)$ = 2.04 ns from [3.2]. The $\Delta V_p^{\ddagger}$ for this site is 7.1 mL/mol (using a value of $\Delta V_i^{\ddagger}$ = 2.27 mL/mol from 22R1). In two cases, 5R1 and 147R1, negative values of $\Delta V_p^{\ddagger}$ were calculated according to this analysis. Negative activation volumes are not physically reasonable, and observation of small negative activation volumes for these residues highlights that the $\Delta V_i^{\ddagger}$ from 22R1 is an approximation and may be improved upon in future studies. For residues where $\tau_e(0)$ is greater than 1.5 ns, $\tau_P(0)$ is over 6 ns according to [3.2], assuming $\tau_i(0)$ = 2 ns. Thus, as $\tau_e(0)$ approaches and exceeds 2 ns, one can no longer assume that internal nitroxide motion and protein backbone motion occur on roughly the same

timescale ($\tau_i(0) \neq \tau_P(0)$). Therefore, $\Delta V_p^{\ddagger}$ was calculated for residues with a $\tau_e(0) \lesssim 1.6$ ns (Table 3.2).

3.3.2 ApoMb at pH 6.0 retains the full complement of helical structure to 2 kbar, but adopts a heterogeneous tertiary fold. ApoMb is 57% helical at 0 bar according to the far-UV CD spectrum. This is approximately 10% less than that for holoMb at pH 6.0 and 0 bar (Table 3.1), in agreement with previously published values from CD (52, 54). $^{13}C\alpha$ and ^{1}H-^{15}N HSQC NMR have shown this loss is due to conformational exchange involving non-helical states primarily in the F helix, the N-terminal end of the G helix, and the C-terminal end of helix H (51). Upon pressurization of apoMb, there is very little change in the far-UV CD spectrum (Figure 3.2). Remarkably, at 2 kbar, where apoMb is known to form a MG-like state, the total helicity is 56%, essentially the same as that at 0 bar.

EPR spectra of spin-labeled residues 12R1, 54R1, and 132R1 in apoMb at pH 6.0 and 0 bar are identical to their holoMb counterparts, indicating that the structure and backbone dynamics are unchanged at these locations upon removal of the heme group (compare black traces, columns 1 and 3, Figure 3.4A). The spectrum of 66R1 is single-component, and the change in the lineshape between the holo- and apo-Mb states reflects differences in the local dynamics of helix E. On the other hand, residues 35R1, 42R1, 87R1, and 106R1 have well-resolved two-component spectra. For residues 42R1, 87R1, and 106R1 the two-component spectra were previously shown to arise from conformational exchange involving helices C, F, and G, respectively; conformational exchange was also identified at the N-terminus of E and the C-terminal of H (11).

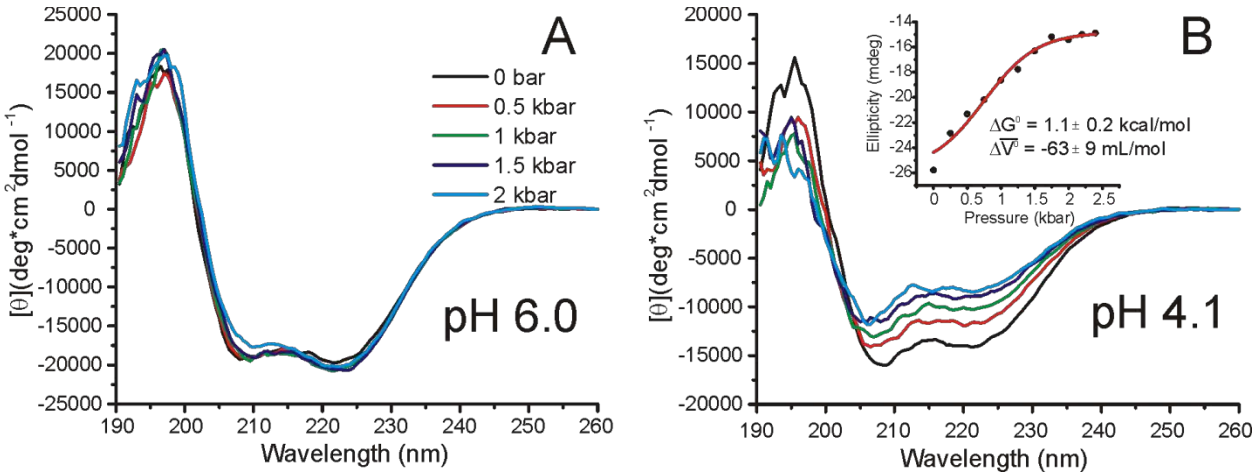

Figure 3.2 Variable-pressure CD spectra of apoMb. Each spectrum is the average of 9 scans. (A) Far-UV CD spectra of 24 μM apoMb in 5 mM MES at pH 6.0, without salts, from 0 to 2 kbar in 0.5 kbar increments. (B) Far-UV CD spectra of 24 μM apoMb in 5 mM sodium acetate at pH 4.1, without salts. Inset: a plot of ellipticity vs. pressure and the best-fit (red trace) to a two-state model of the transition to give the indicated ΔG^o and $\Delta \bar{V}^o$ (see section **3.6**).

Pressurization to 2 kbar, where the putative MG state is essentially completely populated (44, 48), results in well-resolved spectral changes in most residues, unlike the holoMb samples at pH 6.0 (Figure 3.4A). For 54R1 and 66R1 in the D and E helices, respectively, the single component spectra at 0 bar give rise to two-component spectra signaling the presence of new conformations of the protein; one component closely resembles that of the 0 bar state and the other reflects immobilization due to tertiary contact with the protein. For 12R1, 35R1, 42R1, and 106R1 in the A, B, C, and G helices, respectively, pressure induces a strong shift towards a more immobile state. For 87R1 and 132R1, the changes are relatively small and indicate a general decrease in mobility as would be expected from local compression. The two-component EPR spectra found throughout the protein at 2 kbar are consistent with widespread conformational exchange slow compared with intrinsic time scale of EPR, involving at least two states (see section **3.4**). Based on the CD data, the conformational sub-states must differ in the relative positions of helical segments.

MOMD simulations have been used previously to identify and characterize pressure-dependent conformational equilibria (18), but this approach has drawbacks that could limit its

application to the analysis of conformational exchange reported by variable-pressure EPR EPR (see section **3.4**). To evaluate the potential of singular value decomposition (SVD) as an alternative to MOMD simulations, SVD of variable-pressure EPR spectra of the 12R1 mutant of holoMb and apoMb at pH 6 was performed as described in section **3.6** and illustrated in Figure 3.A5; the results of this analysis are shown in Figure 3.7. The SVD component amplitudes for apoMb 12R1 have a sigmoidal pressure dependence that is well-fit using the two-state equilibrium model for [3.1], with $\Delta\bar{\beta}_T = 0$. The values of $\Delta\bar{V}^o$ and ΔG^o indicated in Figure 3.7A predict the native state to be ≈96% populated at 0 bar and the MG state to be ≈86% populated at 2 kbar. The SVD amplitudes of holoMb 12R1 are almost perfectly linear and thus do not indicate the presence of a pressure-dependent conformational exchange, consistent with expectations for holoMb at pH 6 in the pressure range of 0 to 2 kbar.

3.3.3 HoloMb reversibly loses helicity upon pressurization at pH 4.1. HoloMb has 72% helical content at 0 bar (Table 3.1), and the Soret band intensity is similar to that at pH 6.0 and atmospheric pressure (Figure 3.A1). This agrees with previously reported data and indicates a native-like conformation at pH 4.1 and 0 bar (50, 53, 58). The helical content drops as a function of pressure, beginning at 0.5 kbar and leveling off at 43% at 2 kbar. The Soret band intensity showed significant pressure dependence as well, in agreement with previous high-pressure UV-Vis absorbance measurements (50). The ellipticity at 222 nm was used to monitor the fractional helicity during the pressure-populated transition observed in this state. The sigmoidal character of the pressure dependence of the ellipticity is well-fit using a two-state model to give a ΔG^o and $\Delta\bar{V}^o$ of 3.9 ± 0.2 kcal/mol and -131 ± 7 mL/mol, respectively, for the pressure-populated transition (Figure 3.1B).

At 0 bar, all holoMb EPR spectra at pH 4.1 are similar to their pH 6.0 counterparts, indicating that the backbone dynamics are largely unchanged, and no new spectral components are detected (compare black traces, columns 1 and 2, Figure 3.4A). Specifically, residues 12R1, 42R1, 54R1, 66R1, 106R1, and 132R1 have EPR spectra that are nearly superimposable on the pH 6.0 spectra, while 35R1 contains a new small population of a component corresponding to an immobilized state of the nitroxide. Both 35R1 and 87R1 exhibit slight sharpening of the mobile spectral components, indicating a small increase in the rate of motion at these sites. These results are consistent with the CD and Soret band data at 0 bar, which indicate the protein has a similar global secondary structure composition and local tertiary structure in the heme pocket, respectively.

Pressure application causes changes in the EPR spectra of most residues, unlike the case for the pH 6.0 state. For 12R1, 35R1, 42R1, 54R1, and 106R1 the spectra transition from single- to two-component at 2 kbar, consistent with the presence of new conformations involving helices A, B, C, D, and G. For 132R1 the small lineshape change with pressure results from changes in nitroxide mobility, and is similar to that observed for most residues at pH 6.0; such small changes indicate rigidity (incompressibility) of the protein at the corresponding site. The most interesting responses are for 66R1 and 87R1, where pressure produces a new component with a sharp resonance line corresponding to a rapid isotropic motion of the nitroxide (arrows, column 2, Figure 3.4A and shown in expanded view in the lower panel, Figure 3.4B). Such lineshapes are characteristic of dynamically disordered states (11, 59, 60), suggesting that the loss of helicity detected by CD under pressure can be attributed in part to regions involving helices E and F. This is in contrast to apoMb at pH 4.1, 2 kbar (see below), where sharp isotropic

resonance lines are observed for residues 42R1 and 54R1 as well, indicating loss of helical content in the C and D helices (compare colored spectra in columns 2 and 4, Figure 3.4A).

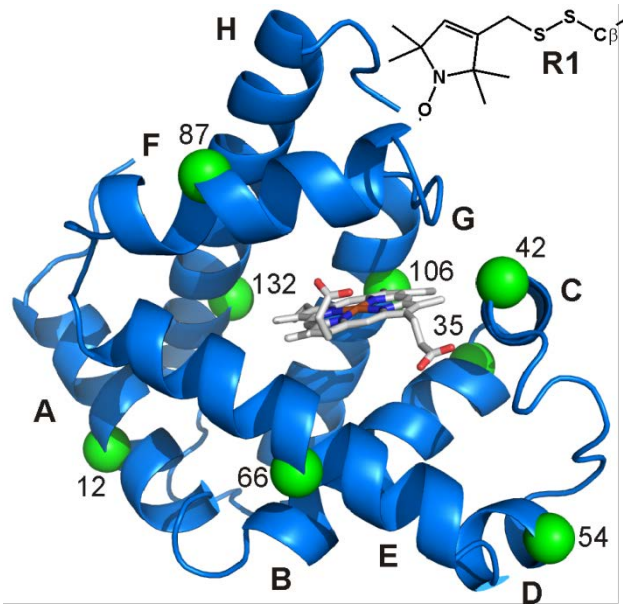

Figure 3.3 Spin-labeled residues for EPR experiments on holoMb and apoMb at pH 6.0 and 4.1. A ribbon model of the holoMb structure (PDB ID code 2MBW (61)) is shown, with green spheres at Cα positions identifying the residues where the R1 side chain was introduced, one at a time. The heme group is shown in stick representation. An inset shows the structure of R1.

3.3.4 The high-pressure 'unfolded' state of apoMb at pH 4.1 retains significant secondary structure. At pH 4.1 and 0 bar, apoMb forms a MG state that is 48% helical according to the far-UV CD spectrum (Table 3.1). In relation to native apoMb and holoMb at pH 6.0 this is a roughly 10% and 20% reduction of helicity, respectively. A combination of $^{13}C\alpha$, ^{1}H-^{15}N HSQC, $\{^{1}H\}$-^{15}N heteronuclear NOE, and H/D exchange NMR experiments have shown that the "core" helices A, G, and H remain intact in the pH 4.1 MG state, while helices C, D, E and F are partially or completely unfolded; the N-terminal half of helix B is largely disordered, while the C-terminal half is helical (41, 42, 52).

Pressurization of apoMb to 2 kbar at pH 4.1 reduced the helical content from 48% to 28%, at which point the drop in helicity levels off, for a final helical content of 26% at 2.4 kbar. Additionally, there is an increase in β-sheet population to ≈23% at 2.4 kbar, although the relative uncertainty in β-sheet estimation is higher than that for helical content. The ellipticity at 222 nm

was used to obtain a ΔG^o of 1.1 ± 0.2 kcal/mol and $\Delta \overline{V}^o$ of -63 ± 9 mL/mol for the transition (Figure 3.2B), in good agreement with earlier tryptophan fluorescence measurements (44). The pressure-dependence of ellipticity at low pressures (0 – 0.75 kbar) is non-sigmoidal, indicating that a mixture of states is present at 0 bar, perhaps including a small population of a partially folded state that is distinct from the MG state known to be predominant at pH 4.1 and 0 bar (38, 41). However, the MG state is approximated to be fully populated at 0 bar for the purpose of fitting the data, as described in section **3.6**. As a result, the estimates for ΔG^o and $\Delta \overline{V}^o$ are a rough approximation, and provide an upper limit for the transition.

All spin-labeled residues in the pH 4.1 MG state of apoMb exhibit two-component EPR spectra at 0 bar (Figure 3.4A), consistent with the widespread conformational exchange known to exist in this state. Detailed interpretations of the 0 bar spectra in terms of structure and dynamics have been recently published (11). Briefly, the sharp spectral components of residues 54R1, 66R1, and 87R1 reflect essentially isotropic motion of the nitroxide, consistent with dynamically disordered states in the D, E, and F helices, respectively. Residues 12R1, 35R1, 42R1, 106R1 and 132R1 have two-component spectra consistent with conformational exchange in a partially folded state. Upon pressurization, the dominant spectral change observed is an increase in the relative population of sharp spectral components reflecting dynamically disordered conformational states (column 4, Figure 3.4A). This is most prominent in residues 54R1, 66R1, and 87R1, which already exhibit isotropic mobile components at 0 bar; a small population of a component corresponding to high mobility appears at high pressure for 42R1. Residues 12R1, 35R1, 106R1, and 132R1 show only minor changes in mobility due to pressure. Based on these results, the loss of helicity detected by CD apparently has significant

contributions from unfolding in the helical sequences around residues 54R1, 66R1, and 87R1 in helices D, E, and F.

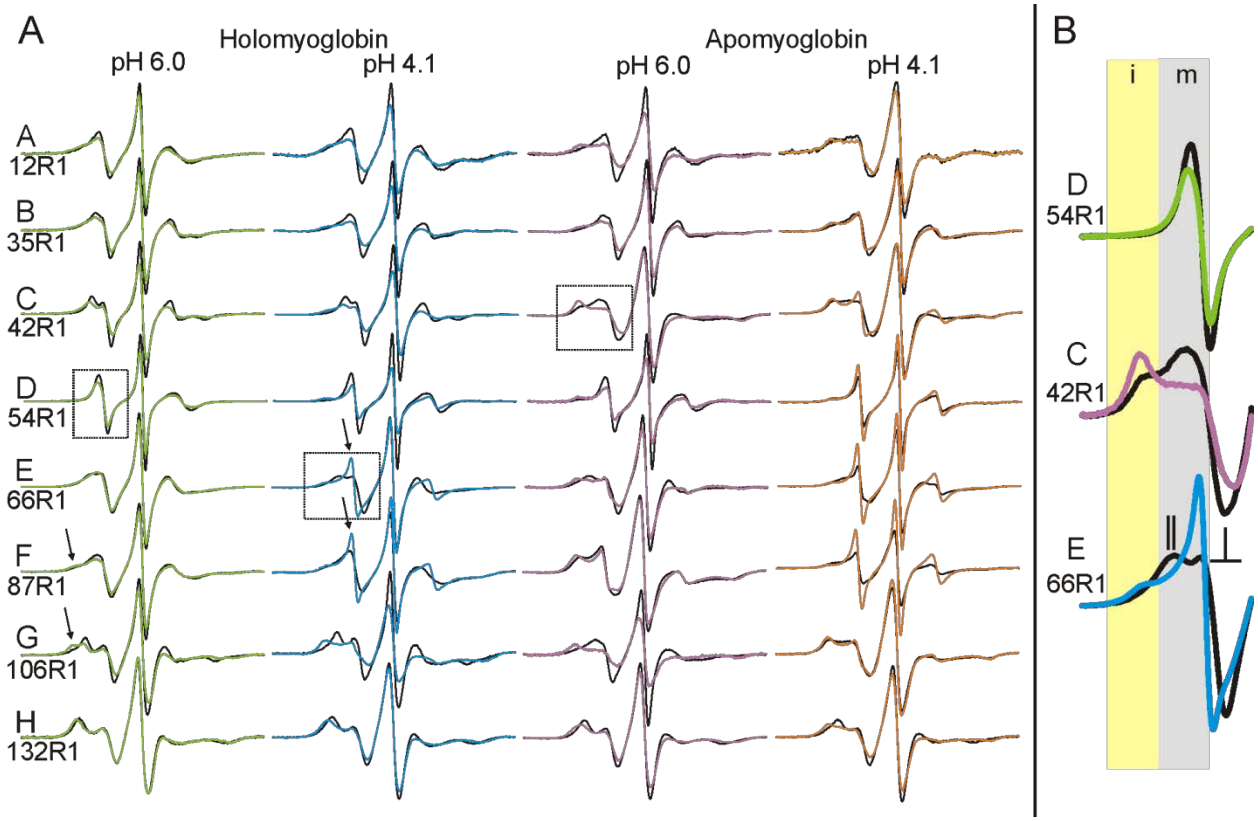

Figure 3.4 EPR spectra of R1 in the various states of myoglobin as a function of pressure. (A) EPR spectra at 0 bar (black trace) and 2 kbar (colored trace) are shown for R1 at the indicated sites and states of myoglobin. The arrows highlight examples of spectral components corresponding to immobilization of the nitroxide in the holoMb pH 6.0 state, and to rapid isotropic motion of the nitroxide in the holo pH 4.1 state. (B) The different classes of pressure-dependent spectral change are illustrated using enlargements of the low-field regions of the spectra identified by the dotted boxes. Shaded areas indicate the portions of the spectra that display intensity corresponding to mobile (m, grey) and immobile (i, yellow) motional states of the nitroxide. In response to an increase in pressure, the spectrum of residue 54R1 (top panel) exhibits only subtle changes in the single spectral component; the spectrum of 42R1 (center panel) exhibits a shift in the population toward the component corresponding to an immobilized state, while that for 66R1 (lower panel) exhibits a shift toward a spectral component representing rapid isotropic motion of the nitroxide. The 0 bar spectrum of 66R1 (black trace) illustrates the characteristic lineshape for a nitroxide undergoing rapid anisotropic motion, where parallel and perpendicular hyperfine components are resolved (17), as indicated. This feature can be recognized in several of the spectra for holoMb in column 1, A. The component corresponding to the more mobile state of 54R1 and 42R1 (black traces) also reflects anisotropic motion, but the order is too weak to resolve the parallel and perpendicular components.

3.3.5 Horse heart myoglobin is less stable than sperm whale myoglobin. All of the CD and EPR results presented above are for sperm whale myoglobin. Identical high-pressure CD experiments were performed on horse heart myoglobin in the same four states, and the results are

qualitatively similar to those for sperm whale myoglobin (Table 3.A1). In agreement with previous comparisons of these two variants (62, 63), horse heart myoglobin is slightly less stable. This is particularly apparent in horse heart apoMb at pH 6.0, in which there is a 17% drop in helicity upon pressurization to 2 kbar (from 60% to 43%; Table 3.A1), compared to almost no change for sperm whale myoglobin under the same conditions (Table 3.1). SDSL EPR studies were not done on the horse heart protein.

3.4 Discussion

One aim of this study was methodology development, i.e. to use myoglobin as a well-studied model system to provide an empirical foundation for interpretation of high-pressure SDSL EPR and CD data in terms of structure and dynamics. To the extent that they can be compared, the data obtained in this study are consistent with existing information from other established methods (44-48, 50, 64), an outcome that provides some level of validation for the approach. Additionally, because the time scale of the SDSL EPR experiment provides an instantaneous sampling of an ensemble of structures fluctuating in the time scale of μs-ms, the data offer a unique view of the conformationally flexible states populated by pressure, the highlights of which are summarized below.

3.4.1 The pressure response of holo- and apo-Mb at pH 6.0: the high-pressure MG state of apoMb and local compressibility in the native state of holoMb. HoloMb at pH 6.0 was explored as a well-ordered reference state. At neutral pH and atmospheric pressure in solution, the protein is well-ordered and devoid of high-amplitude conformational fluctuations (41, 65). The UV-Vis (Soret band), CD, and EPR data are generally consistent with this picture of a rigid, relatively incompressible structure at pH 6.0 in the pressure range investigated. However, the EPR spectrum of residue 87R1 in the F helix shows the appearance of an immobile

component at 2 kbar, reflecting the onset of localized conformational exchange. This result is consistent with previous studies that identified rearrangements in the heme group upon pressurization that are transmitted to the F helix through the coordinating His93 (56, 57). In addition, the pressure-sensitivity of 106R1 in helix G reveals a small and highly localized compressibility that may occur in an otherwise rigid structure.

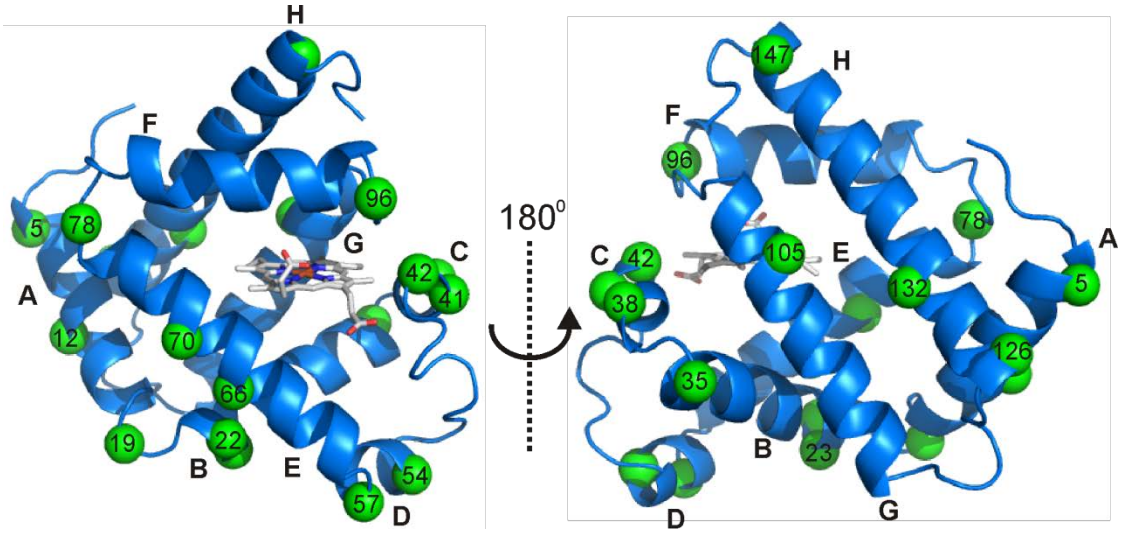

Figure 3.5 Spin-labeled residues for EPR experiments on holoMb at pH 6.0. A ribbon model of the holoMb structure (PDB ID code 2MBW (61)) is shown, with green spheres at Cα positions identifying the residues where the R1 side chain was introduced, one at a time. The heme group is shown in stick representation.

As outlined in section **3.2**, variable-pressure EPR promises to be an important tool to identify regions of elevated protein backbone fluctuations by monitoring the pressure dependence of the nitroxide correlation time (τ_e) for R1 at non-interacting helix surface sites (Figure 3.5) where the spectra correspond to a simple anisotropic motion (Figure 3.A2). Values of the correlation time are readily extracted at each pressure by spectral simulations using the macroscopic-order-microscopic-disorder (MOMD) model of Freed and coworkers (19). The pressure dependence of τ_e can be analyzed to give a total volume of activation, from which $\Delta V_p^{\ddagger}$ can be determined using [3.5] if a value of $\Delta V_i^{\ddagger}$ is known. $\Delta V_p^{\ddagger}$ is of particular interest because it reflects the volume fluctuations and thus compressibility of the protein segment to which R1 is

attached. An estimate of $\Delta V_i^{\ddagger}$ was calculated from the the pressure dependence of holoMb 22R1 at pH 6.0. This is a non-interacting site on the solvent-exposed surface of the rigid B helix, where the pressure dependence may be assigned exclusively to R1 internal motion. With this value for $\Delta V_i^{\ddagger}$, the pressure dependence of R1 at other sites was used to estimate $\Delta V_p^{\ddagger}$ and gauge the relative flexibility of the sequences to which R1 is attached.

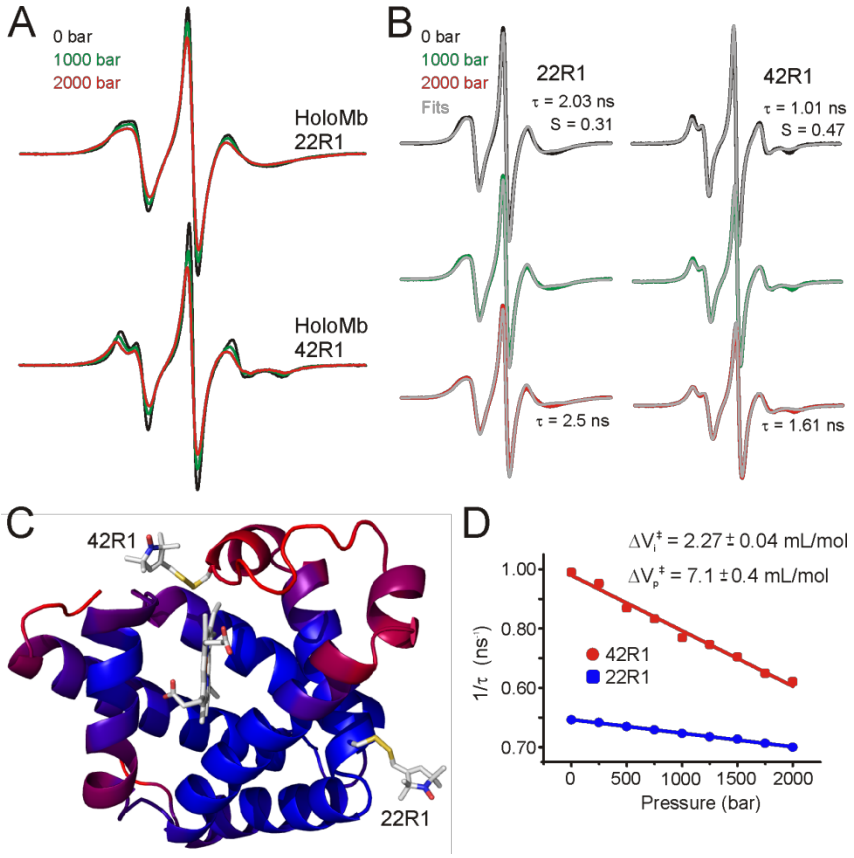

Figure 3.6 Protein backbone dynamics revealed in variable-pressure CW EPR. (A) Variable-pressure EPR spectra of holoMb 22R1 (top) and 42R1 (bottom) at pH 6, normalized to the same number of spins. (B) Pressure-dependence of the nitroxide τ_e was determined from fits to the spectra. (C) Models of the R1 side chain are shown at residue 22 and 42 of holoMb (PDB ID code 2MBW (61)) in stick representation. (D) A plot of $1/\tau_e$ vs. pressure for 22R1 was fit to extract the indicated $\Delta V_i^{\ddagger}$. A plot of $1/\tau_e$ vs. pressure for 42R1 was fit, and using $\Delta V_i^{\ddagger}$ from the analysis of 22R1 the indicated value of $\Delta V_p^{\ddagger}$ was determined for 42R1. Spectra are color coded as indicated.

As an example, Figure 3.6 shows the pressure dependence of holoMb 42R1, located in the short C helix which has been identified to having significant flexibility on the basis of crystallographic thermal factors (Figure 3.6C) and other studies (11, 55, 66). The pressure

dependence of the spectra is clearly greater than that for holoMb 22R1. Analysis of the 42R1 data using the $\Delta V_i^{\ddagger}$ determined from analysis of 22R1 leads to an observed $\Delta V_p^{\ddagger}$ = 7.1 mL/mol, indicating that the short C helix is a region of elevated compressibility. The E-F and F-G loops (78R1 and 96R1) are two other "hot spots" of backbone flexibility within the otherwise rigid structure of holoMb identified by this analysis.

In contrast to the relatively pressure-insensitive holoMb, apoMb at pH 6.0 undergoes a transition to a pressure-populated MG state around 1.5 kbar with a $\Delta\bar{V}^o \approx$-70 mL/mol detected by both tryptophan fluorescence (44) and NMR (48). In principle, NMR is capable of providing atomic level information on the pressure-populated MG structure, but the loss of nearly all cross peak intensity in the HSQC spectrum was observed at 2 kbar, with less than 20% of the atmospheric pressure signal intensity remaining at random coil positions. The significant loss of signal intensity due to line broadening only allowed the conclusion that the entire polypeptide chain had lost the native fold and was disordered to form a heterogeneous state exchanging just slowly enough to cause the observed broadening (48). The EPR spectra of apoMb at 2 kbar clearly reveal the heterogeneity *via* multicomponent EPR spectra, one component of which is very similar to apoMb at atmospheric pressure.

In addition to providing a window into the local dynamic modes of the protein in the native and MG states, it should be possible to quantitatively characterize the conformational exchange using variable-pressure EPR spectra of apoMb. In the case of a two-state conformational equilibrium, where each state is characterized by a unique spectral component, spectral simulations using a two-component MOMD model can provide the relative population of each state as a function of pressure, thereby providing the pressure-dependent equilibrium constant (K) for determination of $\Delta\bar{V}^o$ and $\Delta\bar{\beta}_T$ using [3.1] (18). However, in general the EPR

spectrum of each conformational state may have multiple and overlapping components due to μs exchange between sub-states within a given conformational well on the energy landscape. Moreover, the population of each conformation is in general unknown at any pressure, and the spectra of the "pure" states are unknown. In such cases, analysis by spectral simulation is impractical and SVD may be a viable alternative strategy.

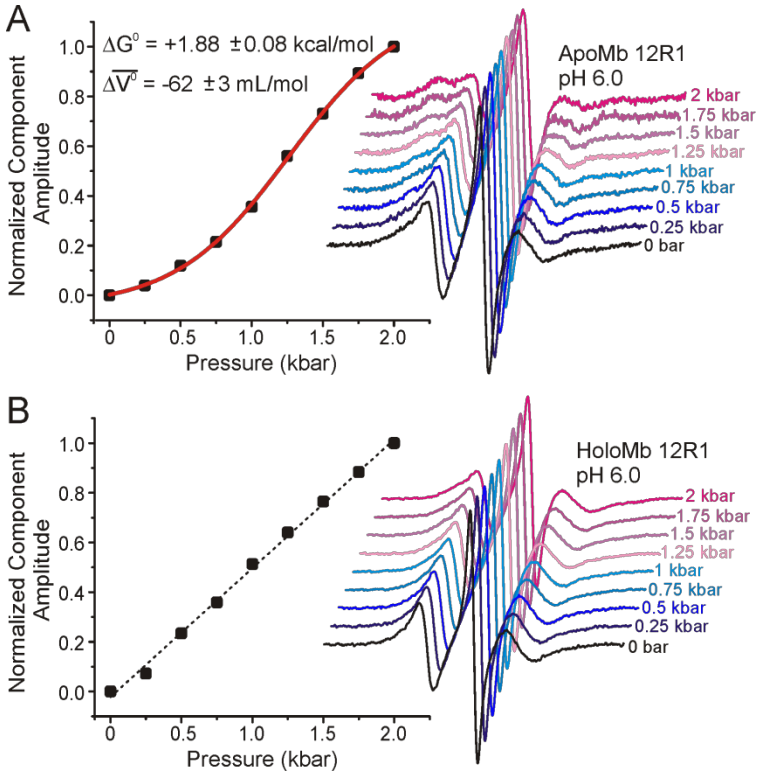

Figure 3.7 Identification and characterization of protein conformational exchange with SVD of variable-pressure EPR. Variable-pressure EPR spectra (right) of (A) apoMb and (B) holoMb 12R1 at pH 6.0. The normalized amplitudes from SVD of the spectra are plotted vs. pressure (left). For apoMb, a fit (red trace) to this plot yielded the indicated values of ΔG^{o} and $\Delta \bar{V}^{o}$. For holoMb, a dashed black line indicates the linearity of the plot, confirming the lack of a conformational transition in this state in the pressure range investigated. EPR spectra are normalized to the same number of spins for each pressure series. Spectra are color coded as indicated.

The MG state of apoMb populated at pH 6.0 and 2 kbar provides just such a situation. Despite the preponderance of a single state of the protein, the CW spectrum of every R1 residue studied here has two components, and in many cases one of the components is very similar to a spectral component present at 0 bar where the native state is predominant. The component

amplitudes from SVD analysis of apoMb 12R1 spectra reflect the shift in population from the native to MG state and the data are well-fit using the two-state equilibrium model of [1] (Figure 3.7A) with thermodynamic parameters close to those reported based on high-pressure fluorescence and NMR measurements (48, 67). The results from SVD of holoMb 12R1 spectra (Figure 7B) verify the ability of SVD to distinguish spectral changes due to conformational exchange from those due to compression of an individual state. The SVD analysis presented here strongly support future use of this methodology to rapidly identify and characterize conformational exchange in complex EPR spectra.

Taken alone, the EPR data do not define the structures present, except that the heterogeneous population includes a conformation much like native apoMb. However, together with CD data that show no change in secondary structure in the MG relative to native apoMb, and the NMR data that reveal ms exchange between populations, a working model can be constructed. With the assumption that a defined thermodynamic state is present at 2 kbar, as concluded from the SVD of apoMb 12R1 as well as intrinsic fluorescence and NMR studies (44, 48), it is proposed here that the high-pressure MG state consists of a native-like population with the helical segments fluctuating on the ms time scale. In some positions of the helices, the R1 side chain makes contact with neighboring structures giving rise to the immobile component. The resolution of X-band EPR to discern different motions in the slow motion regime is not sufficiently high to conclude that the immobile state is a single dynamic mode of the nitroxide, so the immobile state itself could be heterogeneous and represent an ensemble. In future studies, this could be resolved by high-field EPR (68).

It is of interest to compare the high-pressure MG of apoMb with that produced at pH 4.1, atmospheric pressure. The HSQC spectrum of the pH-populated MG did not show the extensive

cross-peak broadening observed at 2 kbar, pH 6.0; the difference was attributed to a presumed sensitivity of the MG state to details of experimental conditions, which included a difference in temperature (48). The results from the current work suggest that the discrepancies in the NMR spectra may instead be due to structural and dynamical differences between the two states. In the present study, the MG states were compared with respect to helical content and EPR spectral signatures at the same temperature. The data reveal a difference in helical content of ≈10%, lower in the pH 4.1 MG, and the presence of sharp isotropic components in the spectra of R1 in helices D, E, and F (11) that are not observed in the pressure-populated MG state. Together, these results suggest local unfolding in these helices in the pH-populated MG but not in the pressure-populated MG. A working model summarizing the main features of the high-pressure MG in comparison to the pH 4.1 MG and native apoMb is shown in Figure 3.8.

Specific details of the pressure-dependent changes in apoMb warrant comment. At first glance, the lack of change in 87R1 in helix F upon pressurization is perhaps unexpected. Numerous solution NMR studies have shown helix F to be conformationally disordered in the native state of apoMb (38, 41, 51), therefore one might anticipate 87R1 to be mobile and malleable under pressure. However, the spectrum reveals a dominant immobile state in apoMb with only a minor change at 2 kbar. The difference can be attributed to the different time scales of EPR and NMR. For NMR, high flexibility would correspond to μs-ms motions, which are frozen on the EPR time scale. Earlier SDSL EPR (11) and NMR (38) studies suggested that helix F sequence might be tucked into the heme pocket in native apoMb where it could undergo motions on the NMR but not EPR time scales.

3.4.2 The pressure response of holoMb at pH 4.1: a holoMb MG state. HoloMb was investigated at pH 4.1 at high pressure. Earlier crystallographic (53), UV-Vis absorbance (50),

and CD (58) measurements all indicate that the secondary and tertiary structure of holoMb is invariant between pH 4.1 and 6.0 at atmospheric pressure, and the data presented here support this view (Figure 3.4, Table 3.1). However, at pH 4.1 increasing pressure from 0 to 2 kbar results in a reversible loss of the Soret band and reversible loss of ≈29% helical content (Table 3.1) that accompany a structural transition with $\Delta\overline{V}^o$ of -131 ± 7 mL/mol and ΔG^o of 3.9 ± 0.2 kcal/mol (Figure 3.1B). This implies an atmospheric pressure population of ≈0.1% for the excited state, illustrating the ability of pressure to make extremely rare states accessible for study. SAXS studies at pH 4.5 identified a compact state at 2 kbar that was attributed to a MG state (64), and the large $\Delta\overline{V}^o$ and pattern of EPR spectral changes (appearance of two-component spectra at most sites) is generally consistent with this idea (Figure 3.4A). However, there are clear differences between the pressure-populated MGs of holoMb at pH 4.1 and apoMb at pH 6.0. In the holoMb MG, EPR spectral components corresponding to dynamically disordered states appear for R1 residues in the E and F helices; in the apoMb MG state, R1 residues in these helices become more immobilized. As suggested above, the F helix may occupy the empty heme pocket in the apoMb MG state. If so, this pocket is not available in the holo protein, and the response to pressure is instead unfolding that apparently involves at least part of the contiguous E helix, contributing to the observed loss in helicity. In addition, an unfolding of helices E and F would move the heme ligands His93 and His64, resulting in the loss of the Soret band under pressure. A schematic representation comparing the proposed model for the holoMb MG state and other states of apoMb is given in Figure 3.8.

Recently it has been reported that MG states can retain the ability to bind native ligands, implying that close-packing is not a requirement for this function (36). A comparison of the high-pressure EPR spectra of holoMb at pH 4.1 with that of apoMb under the same conditions

reveals partial stabilization of the C and D helices by the heme group (Figure 3.8). Furthermore, the rapid reversibility of all pressure related changes in this state implies that the heme ligand remains bound to the protein. Thus, this system adds to existing examples of MG states that retain ligand binding capability, albeit not in the native binding conformation.

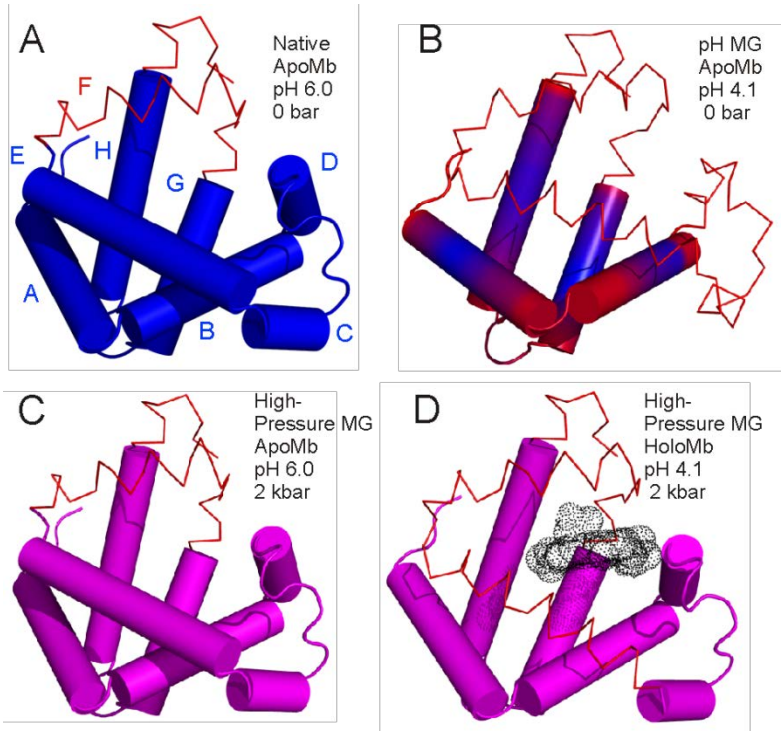

Figure 3.8 Models for the structure and dynamics of partially-folded states of myoglobin. Each model is based on the crystal structure of holoMb; sequences that retain helical content are shown as cylinders; segments that have some fraction unfolded are shown in wire representation. (A) and (B) are models of native apoMb and the pH 4.1 MG state, respectively, based on solution NMR (41, 51). Regions undergoing conformational exchange are colored red, and more rigid regions colored blue. The structure of native apoMb is similar to that of holoMb, but with localized unfolding in the F helix and portions of the G and H helices. In (B), the conformational exchange implied by the gradient of color in the helices represents a gradient in the population of non-helical states, increasing toward the helix termini, as inferred from $^{13}C\alpha$ chemical shifts (41). (C) and (D) are models of the high-pressure MG of apoMb and holoMb, based on SDSL, CD, and NMR. Helices with a fluctuating tertiary structure are colored magenta. (C) The pressure-populated MG of apoMb at pH 6.0, 2 kbar, contains the full complement of native state secondary structure according to CD, but line broadening in NMR and the spectral shifts in EPR indicate a fluctuating tertiary fold. (D) The pressure-populated MG of holoMb at pH 4.1 and 2 kbar experiences dynamic disorder in some fraction of the E and F helices, and a fluctuating tertiary fold in the remaining helices.

3.4.3 The pressure response of apoMb at pH 4.1: the pressure 'unfolded' state.

Earlier tryptophan fluorescence studies of the pH-populated MG state of apoMb at high pressure

reported that the protein undergoes a transition to an unfolded state, with a $\Delta\overline{V}^{o}$ of -61 mL/mol (44). A similar value for $\Delta\overline{V}^{o}$ was found in this study using CD as a monitor (Figure 3.2B). However, the CD data also show that pressure causes only a partial loss of helical structure, resulting in a final value of 28% at 2 kbar with a concurrent appearance of ≈19% β-sheet. While it cannot be ruled out that the reversible formation of β-sheet is due to intermolecular interactions in small soluble aggregates, large-scale aggregation would cause scattering not detected in the CD data. Thus, the population existing at 2 kbar is not unfolded in the literal sense, and certainly retains a higher fraction of secondary structure than that produced by chemical perturbation techniques, including GdnHCl (≈5%), Urea (≈7%), and pH (≈13%) (69, 70). Although EPR spectral changes at high pressure confirm the appearance of a dynamically disordered population in the non-core helices C, D, E, and F, the spectra at all sites retain two components, indicating the retention of a tertiary fold.

Kinetic studies of apoMb folding near neutral pH suggested the mechanism U ↔ Ia ↔ Ib ↔ N, where U is the unfolded state and Ia and Ib are transient intermediates (42, 71). The intermediate Ia is formed within 0.4 ms after initiation of folding from an acid denatured state, and relaxes to form Ib within 6 ms (43). In principle, these states are in equilibrium under all conditions, but at pH 4.1 and atmospheric pressure where the acid MG is formed, the dominant species is Ib (38, 71). Interestingly, the equilibrium CD and EPR data collected at pH 4.1 and 2 kbar are consistent with the Ia rather than the Ib intermediate. For example, the Ia intermediate has a stable core consisting of helices A, G and H, giving a total helical content of about 30%, the same as that found by CD for the pH 4.1, 2 kbar state within experimental error. Moreover, the EPR results under these conditions reveal an increase in the population of disordered states for R1 residues in non-core helices, consistent with the lower protection factors for hydrogen

exchange in these helices in Ia compared to Ib (42). Note that the Ib intermediate is distinct from Ia in having greater helical content (48%) due to partial folding of the non-core B, C, and E helices (41). Thus, pressure may cause a shift in the Ia ↔ Ib equilibrium toward the Ia state. The ability to populate a transiently-formed kinetic intermediate under equilibrium conditions highlights the utility of the application of pressure for exploring the conformational ensemble of proteins.

3.5 Conclusions

Pressure reversibly shifts protein conformational equilibria in a direction to lower the total volume of the system (Le Chatelier's principle), and excited states populated by pressure apparently have a smaller partial molar volume than the ground (native) state (8). The major contribution to the smaller molar volume for excited states is believed to be hydration of internal cavities (packing defects) enabled by conformational changes relative to the native state (72, 73). In the case of apoMb, the data presented here argue that at high pressure hydration of internal cavities, either native or resulting from heme removal, occurs *via* population of an ensemble of conformations in which there is a global disruption of close packing without secondary structure change, perhaps involving solvent-separated hydrophobic interactions (74) that effectively lubricate transitions between members of the ensemble.

An alternative to the cavity hydration model is a structure-relaxation model in which excited states represent alternative packing modes of higher energy that reduce the size of internal cavities with concomitant reduction in the overall protein molecular volume. Indeed, it is observed in crystal structures of cavity-creating mutants that the protein generally responds by shifts in atomic positions in a direction to substantially reduce the cavity volume (75, 76). Recent NMR and modeling studies of the T4 lysozyme L99A cavity-creating mutation showed that the

protein responds to the mutation with a backbone structural rearrangement that allowed Phe114 to move into and fill the cavity; this alternative structure is poorly populated due to strain (77). Whether pressure favors hydration or filling the cavity with Phe114 is a matter currently debated in the literature (78, 79); resolving this issue with high-pressure EPR is a central goal of the work presented in chapter 5. High-pressure is expected to favor alternative packing modes of lower volume, and the fluctuating helix model for the pressure-populated MG state of apoMb can be understood in terms of an ensemble of alternative packing modes that reduce cavity volumes at the expense of strain. It remains to be elucidated whether one of these models dominate, or whether both play a role.

3.6 Methods

3.6.1 Myoglobin cloning, expression, purification, and spin-labeling. All single cysteine mutants of sperm whale myoglobin and their spin labeled derivatives in both the apo- and holo-state have been previously reported and were prepared following the procedures described (11). The purified protein was transferred to the appropriate buffer and concentrated to ≈500 μM for EPR experiments or ≈10 μM for CD experiments using an Amicon ultra concentrator (10 kDa MWCO; Millipore). ApoMb and holoMb samples were prepared in either 20 mM MES buffer at pH 6.0 or 10 mM sodium acetate at pH 4.1 for EPR experiments. For CD experiments, the same conditions were used, except the concentration of MES or sodium acetate was reduced to 5 mM. HoloMb samples prepared as described in (11) auto-oxidize to the aquomet form (Fe^{3+}-H_2O), confirmed by the ratio of the Soret band maxima at 409 nm to the absorption at 280 nm (ε_{280} = 31,000 L*mol^{-1}*cm^{-1}, ε_{409} = 157,000 L*mol^{-1}*cm^{-1}) (80). Protein concentration was measured *via* absorption spectroscopy at 280 nm for apoMb (ε_{280} = 15,400 L*mol^{-1}*cm^{-1}) and 409 nm for holoMb. Samples for EPR were diluted in a 1:1 ratio with 50%

wt/wt Ficoll-70 (Sigma) in the appropriate buffer in order to reduce the effect of protein rotational diffusion on the EPR spectral lineshape (10, 18, 68); the final protein concentrations for EPR were ≈250 μM.

Horse heart holoMb (Sigma) was solubilized in buffer and used without further purification. ApoMb was prepared by the standard butanone extraction method (81). Briefly, 100 mg of holoMb was dissolved in water. The pH of the solution was adjusted to 1.5 with concentrated HCl over ice. The solution was then mixed with two volumes of 2-butanone, and the upper organic layer was decanted. The extraction procedure was repeated twice. The aqueous phase was than dialyzed at 4°C for 2 days against 10 mM Tris buffer at pH 8, and then concentrated at 4°C to ≈10 μM for CD experiments. Protein concentration was measured *via* absorption at 280 nm for apoMb (ε_{280} = 14,300 $L*mol^{-1}*cm^{-1}$) and 408 nm for holoMb (ε_{408} = 188,000 $L*mol^{-1}*cm^{-1}$) (82).

3.6.2 High-pressure circular dichroism and UV-Vis spectroscopy. Far-UV circular dichroism was performed on a Jasco 810 spectropolarimeter using a modified high-pressure optical cell (ISS Model HP-200). Briefly, the standard windows were replaced with MgF_2 windows (Karl Lambrecht Corporation) and the unsupported aperture was reduced to 3 mm, resulting in a cell capable of withstanding pressures up to 2.5 kbar. Details of the modifications to the high-pressure cell and evaluation of performance are provided in section **3.7**. Pressure was produced with a manually operated piston screw pump generator (High Pressure Equipment Company Model 37-5.75-60) rated at 4.14 kbar, and monitored with a pressure gauge (Enerpac Model T6010L) mounted in-line with the sample cell. Each far-UV CD spectrum is the average of 9 scans, acquired after a 3 minute equilibration at each pressure. The pressure was increased in steps of 0.5 kbar from 0 to 2 kbar, and then in 0.2 kbar steps up to 2.4 kbar. For the

thermodynamic analysis, the pressure was increased in steps of 0.2 kbar from 0 to 2.4 kbar. UV-Vis spectra were acquired using the same high-pressure cell with the absorption channel of the spectrometer. Reversibility was verified for each sample by collecting a spectrum at 0 bar befor and after pressurization. For all the experiments the sample cell optical pathlength was 0.5 mm. The secondary structure parameters were estimated using the Contin algorithm (26, 27).

3.6.3 Thermodynamic analysis of CD spectra. CD experiments detected a significant loss of helicity the pH 4.1 states of both apoMb and holoMb due to pressure. In both cases presented here, the data were fit using a two state model, $1 \leftrightarrow 2$, where the equilibrium constant is given by [3.7], and the f_i are the fractions of the respective states.

$$K = f_2/f_1 \qquad [3.7]$$

Structural changes were followed using CD ellipticity (θ) at 222 nm, which is related to the fraction of protein in state 2 (f_2) by [3.8].

$$f_{2,p} = (\theta_P - \theta_1)/(\theta_2 - \theta_1) \qquad [3.8]$$

In [3.8], θ_1 and θ_2 are the ellipticity of state 1 and 2, respectively, and θ_p is the ellipticity at pressure P. The free energy difference (ΔG) in a two state system at equilibrium is given by [3.9], and [3.10] is a first order approximation of the pressure dependence of ΔG.

$$\Delta G = -RT\ln(f_2/f_1) \qquad [3.9]$$

$$\Delta G = \Delta G^o + \Delta\bar{V}^o(P) \qquad [3.10]$$

Combining [3.8], [3.9], and [3.10] and solving for θ_P yields [3.11].

$$\theta_p = \theta_1 + [\theta_2 - \theta_1]/[1 + \exp([\Delta G^o + \Delta\bar{V}^o(P)]/RT)] \qquad [3.11]$$

Plots of θ_P vs. P were fit using [3.11] to solve for free energy and partial molar volume differences at atmospheric pressure (ΔG^o and $\Delta\bar{V}^o$, respectively). In the pressure-populated transition of holoMb at pH 4.1, the fitted values for θ_1 and θ_2 were very similar to the θ at 0 and

2 kbar, respectively. This supports the two-state model for this transition, and indicates that state 1 is fully populated at 0 bar and state 2 is fully populated at 2 kbar. The data for apoMb at pH 4.1 suggest that a mixture of states is populated at 0 bar, as reported previously (44), and as such the two-state model for this transition is an approximation. The low pH MG of apoMb is known to be populated at pH 4.1 and 0 bar, therefore state 1 is taken to be the low pH MG and θ_1 was set to equal θ at 0 bar in order to generate a reasonable fit.

3.6.4 Variable-pressure EPR spectroscopy. A computer-controlled pressure intensifier rated at 4 kbar and ceramic samples cells rated to 3 kbar were jointly developed with Pressure Biosciences, Inc (PBI). The intensifier, now commercially available from PBI (Model HUB440), is feed-back regulated to maintain constant pressure even in the presence of small leaks, and can be programmed to provide automated changes in pressure with various profiles in time. The ceramic cells, also now commercially available (HUB440-Cer), were fabricated for use in a 5-loop 4-gap resonator operating at X-band microwave frequency (83). The ceramic cell has a pressure-independent EPR signal that was subtracted from all spectra after data acquisition. The pressurization fluid was either water or buffer, and pressure was monitored with two separate transducers (Kistler Model 6229A and Precise Sensors Model 5550) connected in-line with the sample cell. Additional details of the instrumentation used for variable-pressure EPR experiments in this dissertation are given in section **3.7**. Pressure values given in this dissertation are gauge pressure, i.e, 0 bar is equivalent to atmospheric pressure.

EPR spectra were acquired on either a Bruker ELEXSYS 580 or Varian E-109 spectrometer fitted with the above mentioned 5-loop 4-gap resonator operating with 5 mW incident power and at a temperature of 298 K. The sweep width for all spectra was 100 G. Atmospheric pressure spectra were acquired before and after pressurization to ensure

reversibility. Figure 3.A3 shows reversibility for the spectral changes shown in Figure 3.4A; all pressure effects reported in this dissertation were reversible.

3.6.5 Singular value decomposition (SVD) of variable-pressure EPR spectra. SVD of holoMb and apoMb 12R1 variable-pressure EPR spectra was performed using the standard SVD function in LabVIEW. SVD of a matrix **A** generates three matrices **U**, **S**, and **V**. **U** and **V** are comprised of orthonormal eigenvectors of $\mathbf{AA^T}$ and $\mathbf{A^TA}$, respectively, and **S** is a diagonal matrix containing the eigenvalues of $\mathbf{AA^T}$ and $\mathbf{A^TA}$ (the eigenvalues of these two matrices are equivalent) (20). The input matrix **A** was generated by subtracting an average of all spectra in the pressure series from the spectrum collected at each pressure. The resulting difference spectra comprise the columns of **A**, and each column corresponds to a different pressure (Figure 3.A5). **U** contains the basis spectra (components) and **V** contains the amplitude vectors (amplitudes) at each pressure. The singular values in the diagonal matrix **S** are the weights of each component. **US** then contains the weighted components in columns, and each row of $\mathbf{V^T}$ contains the amplitude of a particular component as a function of pressure. **A** can be reconstructed by multiplying **U**, **S**, and $\mathbf{V^T}$ ($\mathbf{A}=\mathbf{USV^T}$).

As may be seen in Figure 3.A5, only the first few components are significant, and subsequent components have low weighting factors (singular values) and few defining features in the lineshape, such that they contribute only noise. Indeed, noise reduction is a common application of SVD (20). Two components were significant for apoMb 12R1 (Figure 3.A5) and only the first component was significant for holoMb 12R1; other components had singular values <10% of the first component singular value.

The amplitudes for a particular component reflect the pressure-dependence of the spectral change reflected in that component. If these changes result from pressure-populated shifts in

conformational equilibria, the amplitudes (here designated A_P) may be treated in an equivalent way to the CD spectroscopic observable θ_P, and for a two-state exchange

$$A_p = A_1 + [A_2 - A_1]/[1 + \exp([\Delta G^o + \Delta\bar{V}^o(P)]/RT)] \quad [3.12]$$

For apoMb 12R1, the amplitudes of the first two components ($\mathbf{V}_1$ and $\mathbf{V}_2$, Figure 3.A10) were linearly combined using their singular values as coefficients and normalized to generate A_P, based on the assumption that the pressure-populated spectral changes reflect a single process (transition). A plot of A_P vs. P revealed a clear sigmoidal transition that was well fit using [3.12], and the resulting values for ΔG^o and $\Delta\bar{V}^o$ are consistent with those previously reported (see section **3.3**), supporting the two-state model [3.1] used to fit the SVD amplitudes.

For holoMb 12R1 only the first component was significant, therefore the normalized amplitudes of the first component were taken as A_P. As anticipated, a plot of A_P vs. P was linear, indicating the absence of a conformational transition in holoMb at pH 6.0 between 0 and 2 kbar.

3.6.6 MOMD simulations of variable-pressure EPR spectra. Spectral simulations of variable-pressure EPR spectra for 19 singly-labeled mutants of holoMb were performed according to established procedures for fitting EPR spectra of R1-labeled proteins (11, 18) using the program MultiComponent, written in LabVIEW and available at www.chemistry.ucla.edu/directory/hubbell-wayne-l. This employs the non-linear least squares stochastic Liouville (NLSL) fitting program developed by Freed and coworkers (19) as a kernel. Details of the MOMD model and parameters are given in Chapter 1 of this dissertation and references therein.

Initial values of the A and g tensor principal components were A_{xx} = 6.2, A_{yy} = 5.9, A_{zz} = 37, g_{xx} = 2.0078, g_{yy} = 2.0060, and g_{zz} = 2.0022, previously reported for a nitroxide in an aqueous environment (84). Although all spin-labeled mutants used here are surface sites, the

polarity of the local environment could vary slightly from site-to-site, thus A and g principal component values were allowed to vary slightly during fitting due to their known dependence on polarity (85).

The principal components of the rotational diffusion tensor are given in a modified spherical form $\bar{R} = \frac{1}{3}(R_x + R_y + R_z)$, $N = R_z - \frac{1}{2}(R_x + R_y)$, and $N_{xy} = R_x - R_y$, where R_x, R_y, and R_z are the principal components in Cartesian form, and $\bar{R}$, N, and N_{xy} are the isotropic, axial, and rhombic components, respectively, of the tensor in spherical form. The values of these parameters are specified in the fitting program as $\log_{10}$ of the actual principal component values to make them the same order of magnitude as the non-dynamical fitting parameters. This improves convergence of the fitting algorithm. The reported effective correlation times (t) were calculated using the isotropic component of the diffusion tensor ($\bar{R}$) according to

$$\tau = \left[6 * 10^{\bar{R}}\right]^{-1} \qquad [3.13]$$

All spectra were fit using z-axis anisotropic motion (diffusion tensor tilt angles $\alpha_D = 0^0$, $\beta_D = 36^0$, and $\gamma_D = 0^0$) and axial symmetry ($N_{xy} = 0$), except for 105R1 for which a non-zero value of N_{xy} was required to achieve a good fit.

A restoring potential defined by the following expression was used to model the local ordering of the nitroxide motion due to attachment to the protein:

$$U(\Omega) = -kT \sum_{L,K} c_K^L D_{0K}^L(\Omega) \qquad [3.14]$$

The ordering potential (U) is a function of the angles relating the principal axes of the diffusion tensor to the director frame (Ω), and $D_{0K}^L(\Omega)$ are a restricted set of spherical harmonics. The coefficients c_K^L are the parameters allowed to vary in the simulation. Typically only the first coefficient c_0^2 is required to achieve a good fit, resulting in a model for angular motion of the diffusion tensor z-axis about the director z-axis that traces out a roughly conical trajectory. For a

few residues (5R1, 12R1, 19R1, and 22R1) the second coefficient c_2^2 was required. Moderate values of this coefficient modify the motion of the diffusion z-axis to an elliptic cone. Values for the order parameter S were calculated from the fitted c_0^2 and c_2^2 parameters (19).

In addition to the parameters listed above, the inhomogeneous linewidth tensor W was allowed to vary slightly in order to improve the fit quality. Inhomogeneous broadening due to the proton and ^{13}C hyperfine interactions and field modulation are explicitly included in the MultiComponent implementation of the NLSL program. Other parameters available in the program were not used in the simulations reported here.

The 19 spin-labeled holoMb mutants for which MOMD simulations were performed are solvent-exposed surface sites that exhibited single component spectra across the full pressure range. These residues were fit according to a previously reported model for pressure dependence. In this model, after achieving a parameter set that accurately fit the spectrum collected at atmospheric pressure, only $\overline{R}$ and N were allowed to vary as a function of pressure (18). This model accurately represents the pressure dependence for all residues except 66R1, for which an improved fit was achieved by allowing the order parameter S to vary as well.

3.7 Appendix

3.7.1 The high-pressure circular dichroism (CD) system. The high-pressure unit is an ISS model HP-200 with three optical windows for absorption, fluorescence, and Raman spectroscopy. The windows are mounted in a Poulter-type configuration using highly polished metal plugs with a 10 mm aperture (Figure 3.A6). The whole unit is mounted on a platform built in-house that fits inside the Jasco 810 spectropolarimeter sample compartment such that center of the polarized light is centered on the window of the high-pressure unit. The original windows in the high-pressure unit are UV-grade quartz that can withstand pressures up to 3 kbar, or sapphire

windows that can withstand pressures up to 4 kbar. Neither quartz nor sapphire is suitable for CD measurements at high-pressure. While quartz is an isotopic material with no crystal orientations, under high hydrostatic pressure these windows produce major artifacts and loss of CD signal below 250 nm. Sapphire windows are birefringent and pressure induces significant depolarization (Figure 3.A7A). Magnesium fluoride (MgF_2) windows are found to be suitable for high-pressure CD measurements (Figure 3.A7B and 3.A8). MgF_2 windows have excellent transmission properties in the UV-visible range, even at high pressures. However, MgF_2 windows do not have the same strength of quartz or sapphire windows, and will fracture at relatively low pressures using the standard window configuration of the HP-200. By reducing the unsupported aperture diameter from 10 mm to 3 mm, MgF_2 windows will retain their optical properties up to pressures of 2.5 kbar without fracturing. Custom-made high-pressure side plugs with a 3 mm aperture were obtained from ISS. The custom made MgF_2 windows (Karl Lambrecht Corporation) have the optical axis perpendicular to the circular polished face, and the same dimensions as the standard windows for easy interchangeability (Figure 3.A6). To be able to perform measurements in the far-UV region water is used as the pressure transmitting fluid. The pressure is produced by a model 37-5.75-6 High-pressure Generator from High Pressure Equipment Company.

3.7.2 CD sample cells. Various quartz sample cells can be fitted into the high-pressure unit. For measurements in the far-UV region, custom made cells with path lengths of 0.2, 0.5, and 1 mm were obtained from NSG Precision Cells. The cells were completely filled with buffered sample to avoid trapping of air and then sealed with a flexible material such as parafilm because the liquid inside the cells will compress as the pressure is increased. The cells are inserted into the high-pressure unit and immersed in water, which serves as a pressure-

transmitting fluid around the sample cell. These quartz cells are not subjected to the differential pressure due to the flexible parafilm seal, and thus do not produce any pressure artifacts in CD spectra.

3.7.3 Interference from leakage. When using the high-pressure unit for absorption and fluorescence measurements with the standard quartz or sapphire windows and the 10 mm aperture, there are generally no leakage problems. However, minor leaks of the pressurization fluid (water) are common with the 3.0 mm aperture side plug at pressures above 1.5 kbar. Even minor leaks (< 1 μL) will coat the outer surface of the aperture and interfere with CD measurements. This can be easily detected by the large sudden changes in the CD signal as well as changes in the photomultiplier dynode voltage. This problem is solved by continuously flowing a stream of nitrogen gas on the side windows to keep the apertures dry (Figure 3.A6).

3.7.4 Baseline pressure dependence. Buffer ellipticity is generally pressure-dependent. A typical buffer baseline is shown in Figure 3.A8B for 5 mM Tris at pH 7.2 from 0 to 2 kbar. As shown, at 200 nm the maximum change is on the order of ≈1.5 mdeg, and the changes are completely reversible. It was found that the baselines are reproducible during a day's operation. However, baselines have to be obtained daily.

3.7.5 Calibration of the CD spectropolarimeter. Camphor sulfonic acid is commonly used to calibrate the CD spectropolarimeter. Spectra of camphor sulfonic acid as a function of pressure from 0 to 2 kbar (Figure 3.A7B) reveal minimal changes in the peak intensity at 290 nm. Pantolactone was chosen as an additional calibration standard (86) because it has a well-defined signal peak at 219 nm (Figure 3.A8A), and monitoring the secondary structure of proteins in the regions of 190 to 260 nm is the principle interest here. The variation in signal intensity as a function of pressure between 0 and 2 kbar is on the order of ±3.0%. Because water

or buffer will compress as the pressure is raised, the concentration of the sample will increase and the CD signal is expected to increase accordingly. However, inspection of the pressure-dependent spectra of camphor sulfonic acid and pantolactone shows that this is not the case. The reason for this discrepancy is that as the pressure is increased, the MgF_2 windows in the high-pressure cell partially depolarize the circular polarized light, thereby reducing the CD signal. Interestingly, the amount of depolarization as a function of pressure compensates for the concomitant increase in sample concentration. This is proved by placing the sample cell in the light pathway outside the high-pressure cell and recording the CD spectra as the pressure is increased. The concentration increase as a function of pressure can be easily monitored using the absorption channel in the CD spectropolarimeter, where the peak absorbance of the sample increases with pressure. The insertion of the high-pressure unit in the light path adds two additional windows causing a 7 ± 0.5% loss of CD signal at atmospheric pressure. This 7% loss is independent of the material being measured or the wavelength used.

3.7.6 High-pressure ceramic cell for SDSL EPR. Two types of high-pressure sample cells have been developed and implemented in X-band SDSL EPR experiments. The first is fabricated from PTFE-coated fused silica capillary as described by (18). An alternative high-pressure cell for X-band SDSL EPR is the commercially available yttria-stabilized zirconia ceramic cell (HUB440-Cer; Pressure BioSciences, Inc.) shown in Figure 3.A9A. This cell was used for all variable-pressure EPR experiments reported in this dissertation. The total sample volume of the cell is 19 μL, with ≈5 μL in the ≈1 cm active region of a resonator; sample concentrations of ≈200 μM give satisfactory signal-to-noise. The typical maximum operating pressure of these cells is 2.4 kbar, although pressures up to 3 kbar are achievable with select cells.

The ceramic cell exhibits a broad EPR signal due to paramagnetic inclusions (87-91). While this signal overlaps that of nitroxides in EPR spectra, it is pressure-independent and is readily removed by subtraction after data collection (Figure 3.A9B). The larger inner diameter of the ceramic cells compared to the previously used capillary bundle cell makes it more amenable to studies of proteins immobilized on solid support (92).

Water compresses by ≈12% at 4 kbar (93), and the increased water content in the active volume of an EPR resonator under pressure causes a shift in the resonant frequency due to the high dielectric constant of water. As a result, adjustments in the frequency and/or coupling may be required. In experiments presented here, manual frequency adjustments were required with every ≈1 kbar change in pressure, although this will depend on the EPR instrumentation used. Water compression also increases the effective concentration of spin in the sample, which is not an issue for line shape analysis such as MOMD simulations. However, in analysis where accurate normalization is critical, minor inaccuracies in subtraction of the ceramic cell background signal make normalization using double-integration of CW spectra unreliable. An effective alternative normalization strategy is to scale spectra by a correction factor based on the compression of water (93); this strategy was implemented for data analyzed by SVD.

3.7.7 Pressure generation and regulation. Air-operated pressure intensifiers from PBI are employed for pressure generation in all experiments reported here. These intensifiers are particularly attractive for on-line operation because they are self-regulating and maintain a set pressure even in the presence of small leaks. The PBI HUB440 pressure intensifier has a maximum operating pressure of 4 kbar and is suitable for use with the ceramic cells from the same company. The PBI HUB880 has a maximum operating pressure of 6.2 kbar and is employed in PR DEER experiments described in chapters 4 and 5 of this dissertation. Water can

be used as a pressurization fluid in these systems, and sample diffusion is sufficiently limited to eliminate the need for a separator between the sample and pressurization fluid. Both the HUB440 and HUB880 can operate under external computer control, enabling time-varying pressure profiles of arbitrary shape to be implemented.

Although solely static high-pressure experiments are reported here, a high-pressure system was developed for both static and time-varying experiments. A schematic of the system, including pressure-jump experiments, is given in Figure 3.A10A along with suppliers and part numbers for key items. For static and slowly varying pressure operation both valves are open and the pressure is controlled by the intensifier. For pressure-jump experiments the following sequence is used: the sample cell is pressurized to pressure P_1 with both valves open, valve 2 is closed, the reservoir is pressurized to P_2, valve 1 is closed, and finally a pressure jump is initiated by opening valve 2, which connects the sample and reservoir thus triggering a rapid equilibration to an intermediate pressure. The final pressure is determined by P_1, P_2, and the relative volumes of sample and reservoir. The system is capable of kbar-magnitude pressure jumps and drops with a 10-90% rise time of ≈1.5 ms (Figure 3.A10B). With computer control of the valves and pressure intensifier, the system can be reset to initial or other selected conditions and the cycle repeated with full automation. As indicated with part numbers, the pressure intensifier, solenoid operated. The high-pressure ceramic cell introduced above may be used in pressure-jump EPR experiments without further modification. The primary future use of the pressure-jump mode of operation will be to determine the relaxation time for conformational exchange on the time scale of ms.

Table 3.A1 Pressure-dependent secondary structure content of horse heart myoglobin estimated from circular dichroism.

Horse Heart	pH	Pressure (kbar)	α-Helix[a]	β-Sheet	Turn	Unordered
Holomyoglobin	6.0	0	0.73	0.01	0.09	0.17
		2	0.80	0.01	0.06	0.13
	4.1	0	0.78	0.00	0.08	0.14
		2	0.40	0.05	0.24	0.31
Apomyoglobin	6.0	0	0.60	0.03	0.14	0.23
		2	0.43	0.08	0.19	0.30
	4.1	0	0.51	0.05	0.19	0.25
		2	0.21	0.22	0.22	0.35

[a]the content of secondary structure estimated using the Contin algorithm (26, 27)are given as fractional populations.

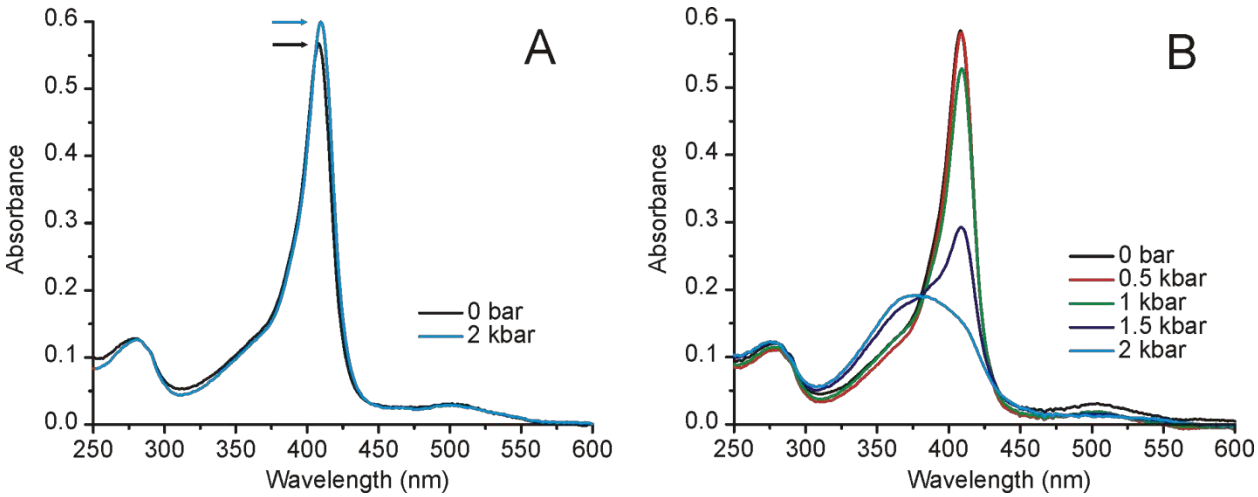

Figure 3.A1 Soret band of holoMb as a function of pressure. (A) The absorption spectrum is pressure insensitive at pH 6.0. The intensity of the Soret peak at 409 nm increases by ≈7% at 2 kbar as a result of the compression of the sample. The lack of change of the absorption spectrum reflects the maintenance of native tertiary structure in the heme pocket at high-pressure. (B) At pH 4.1, the Soret peak intensity begins to drop above 0.5 kbar, and is lost entirely at 2 kbar, indicating loss of native tertiary structure in the heme pocket; this change is reversible. Protein concentration was 68 μM and pathlength was 0.5 mm.

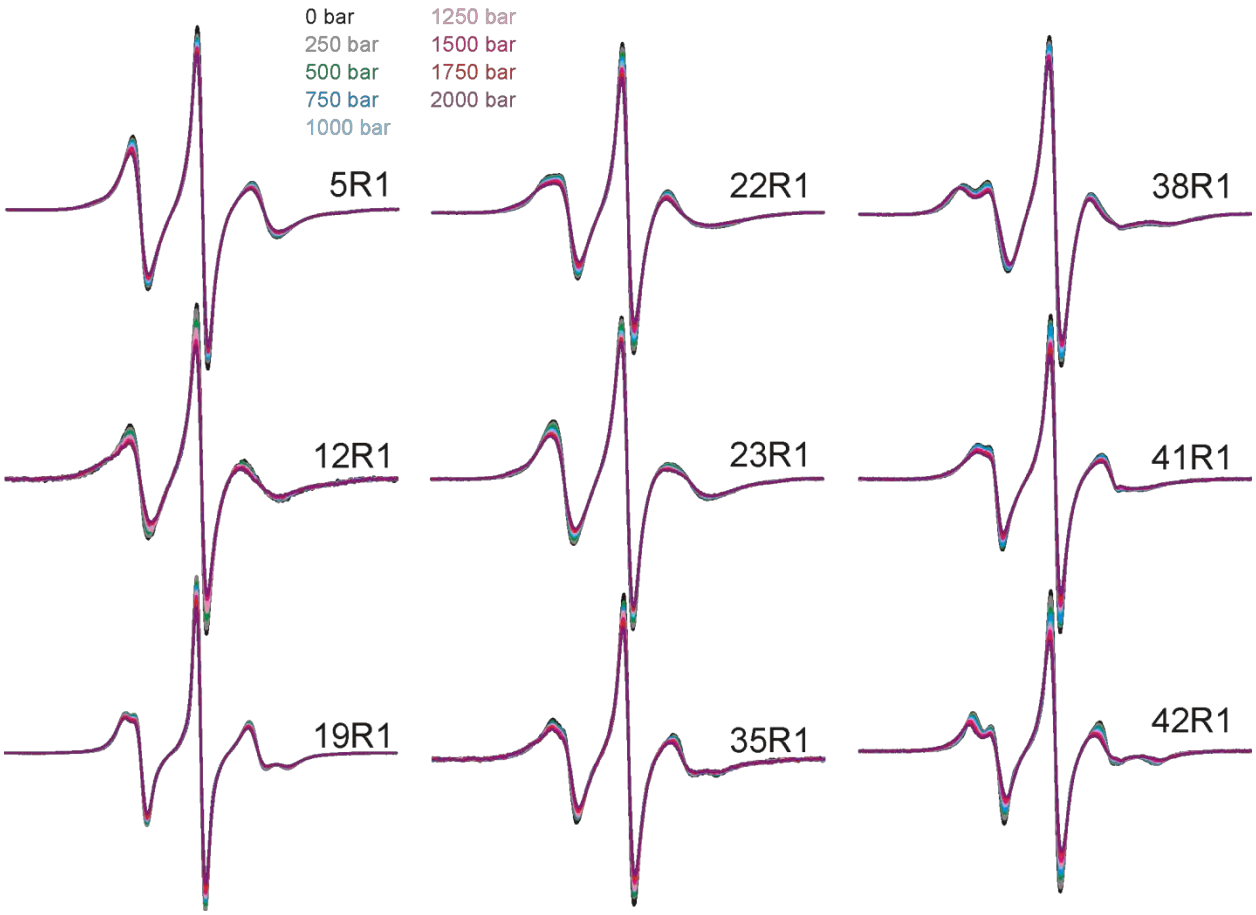

Figure 3.A2A Variable-pressure EPR spectra of holoMb mutants at pH 6.0. Variable-pressure EPR spectra of each residue are normalized to the same number of spins, and are color-coded as indicated.

Figure 3.A2B Variable-pressure EPR spectra of holoMb mutants at pH 6.0. Variable-pressure EPR spectra of each residue are normalized to the same number of spins, and are color-coded as indicated.

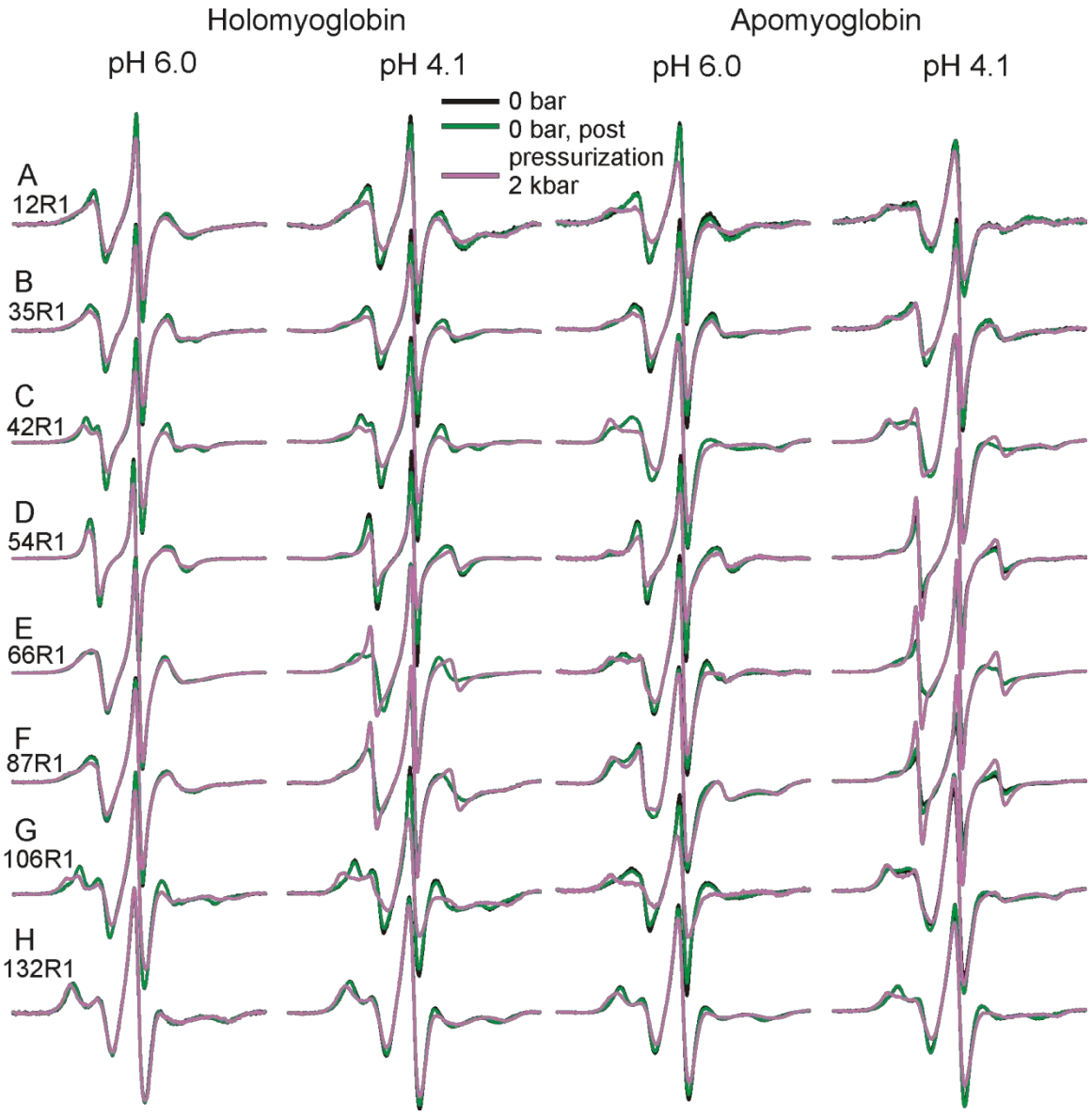

Figure 3.A3 Reversibility of pressure-populated EPR spectral changes. EPR spectra taken at atmospheric pressure before and after pressurization are shown for the indicated residues in each state of myoglobin. Spectra taken at 2 kbar are shown as a reference for comparing the magnitude of pressure effects vs. reversibility for each state.

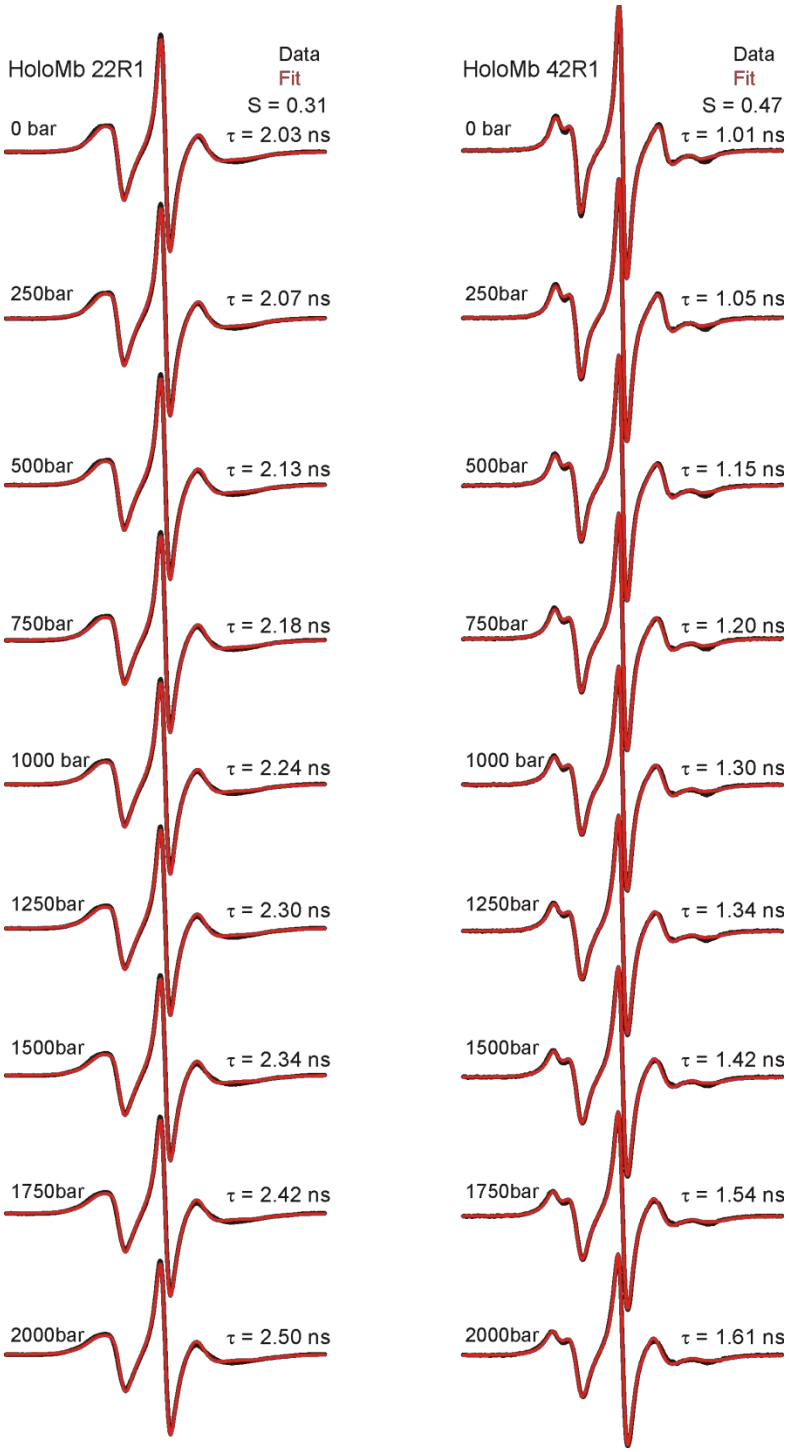

Figure 3.A4 MOMD simulations of variable-pressure EPR spectra. Spectra of holoMb 22R1 (left) and 42R1 (right) at pH 6 are shown at the indicated pressures with fits from MOMD simulations overlaid. In the model used to generate the fits, the order parameter is invariant while the correlation time is allowed to vary as a function of pressure.

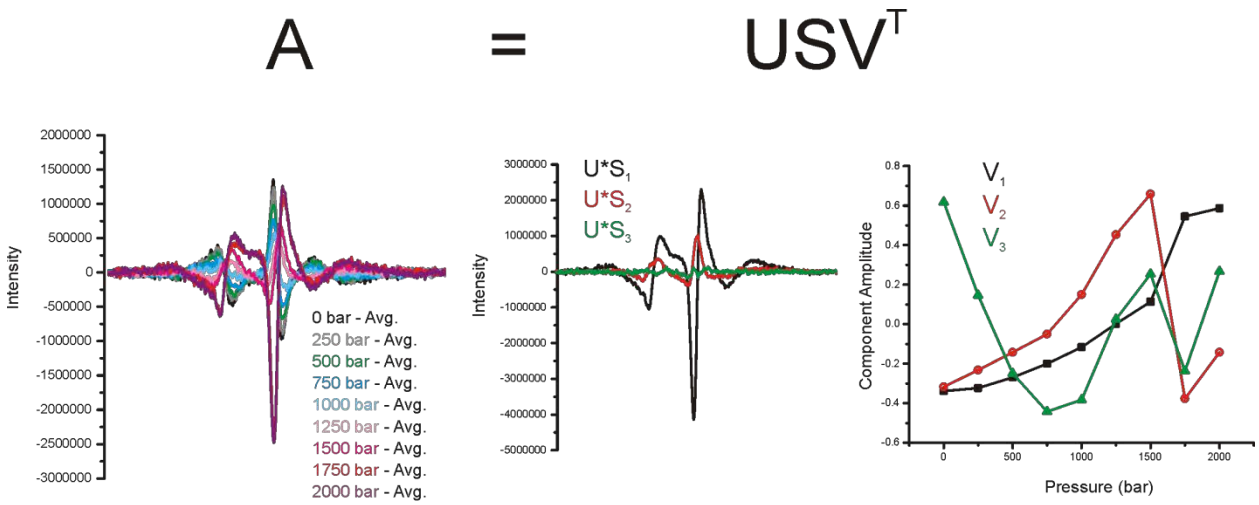

Figure 3.A5 Singular value decomposition (SVD) of variable-pressure EPR spectra for apoMb 12R1 at pH 6.0. An average of all spectra in the pressure series is subtracted from the spectrum collected at each pressure, and the resulting difference spectra (left panel) comprise the columns of the matrix **A**, where each column corresponds to a different pressure. The matrix **US** contains the weighted components in columns, and the first three weighted components are shown in the center panel. Each row of $\mathbf{V}^{\mathbf{T}}$ contains the amplitude of a particular component as a function of pressure, and the first three component amplitudes are shown in the right panel. For apoMb 12R1, only the first two components are significant.

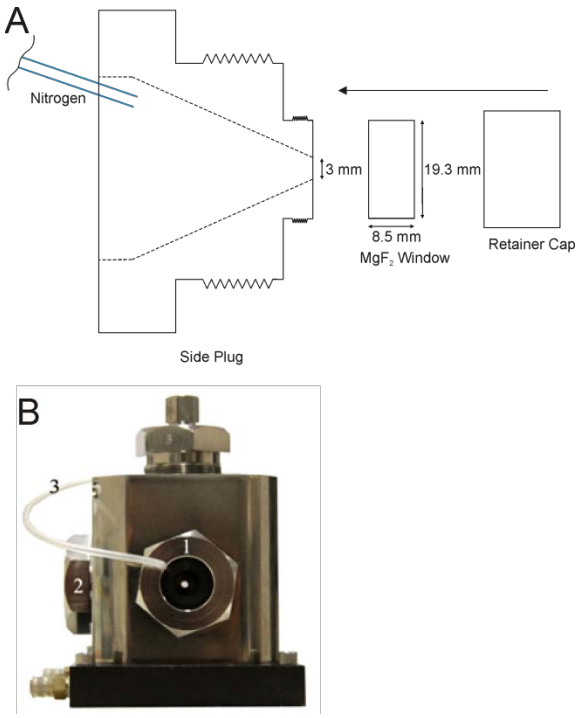

Figure 3.A6 High-pressure optical cell modified for CD. (A) Schematic of the side plug and window assembly. Nitrogen gas (blue) is flowed continuously over the external face of the MgF_2 window to keep it dry. (B) Picture of the high-pressure unit, showing the side plug with MgF_2 window for high-pressure CD, 1, side plug at 90^o for fluorescence, 2, and nitrogen gas line for maintaining a dry aperture, 3.

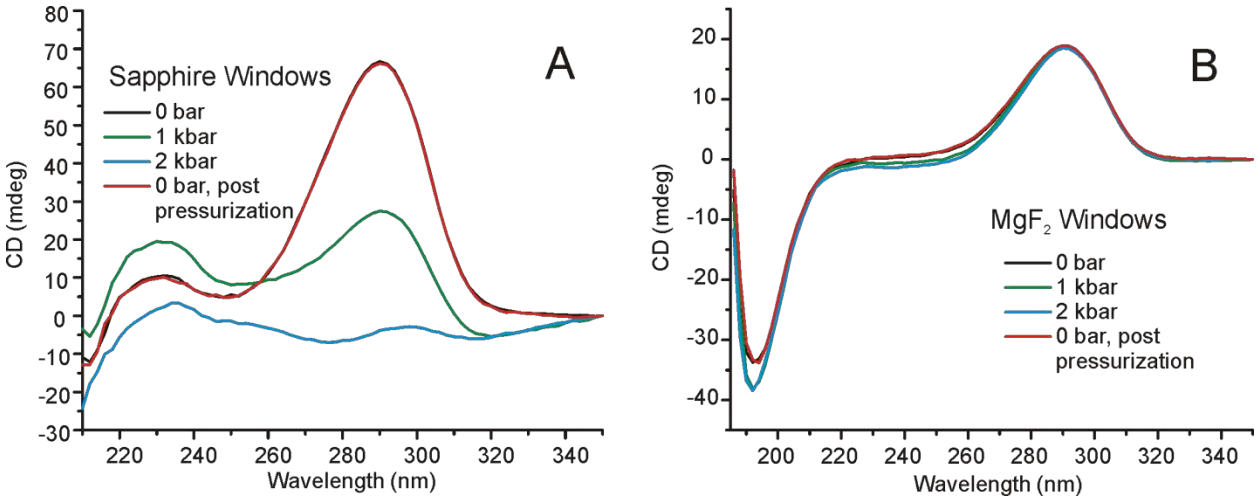

Figure 3.A7 High-pressure CD spectra of camphor sulfonic acid. (A) Sapphire windows result in significant, although reversible, pressure-populated spectral changes. (B) MgF_2 windows result in minimal changes as a function of pressure.

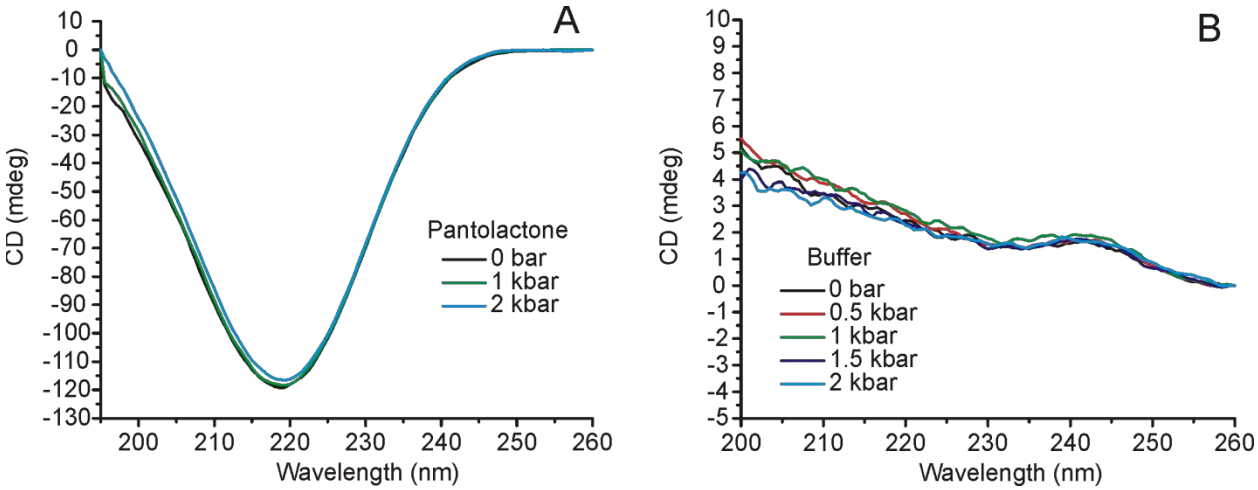

Figure 3.A8 High-pressure CD spectra using MgF_2 windows. (A) Pantolactone has a peak at ≈220 nm, which perfectly overlaps with important far-UV CD spectral features of proteins. This peak is nearly pressure-independent, indicating the suitability of MgF_2 windows for protein studies. (B) 5 mM Tris, pH 7.2 baseline as a function of pressure. The signal is expected to increase with pressure due to compression, but distortion of the MgF_2 windows at high pressure results in depolarization that decreases the buffer signal. Interestingly, these two effects nearly perfectly compensate for one another, resulting in a constant baseline.

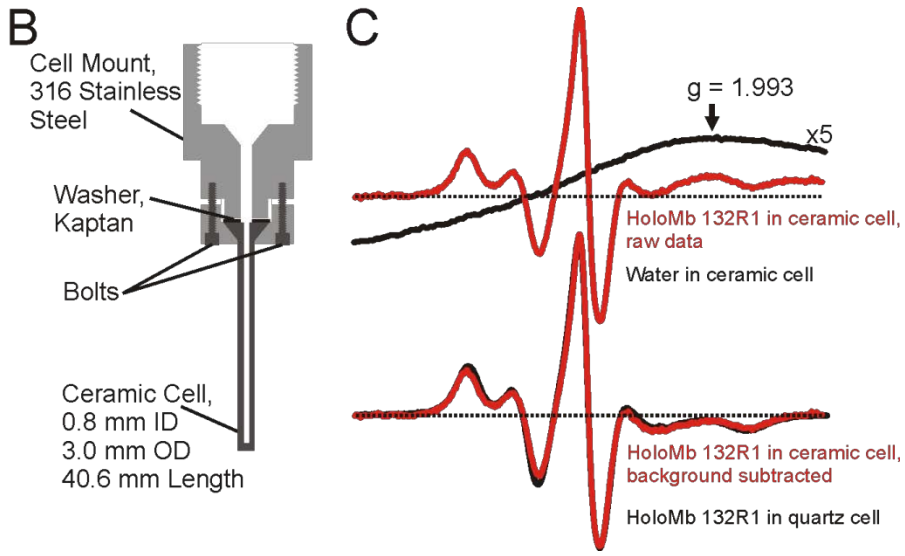

Figure 3.A9 Ceramic cell used for variable-pressure CW EPR. (Left) Details of the ceramic cell assembly. (Right) The spectrum of holomyoglobin (holoMb) 132R1 at atmospheric pressure in the ceramic cell before subtraction of the background signal (red, upper panel). The ceramic EPR signal (black, upper panel) is amplified five times with respect to the magnitude of the background signal in the holoMb 132R1 spectrum; the g-factor corresponding to the signal maximum is ≈1.993. The holoMb 132R1 spectrum after subtraction of the ceramic background signal (red, lower panel) is superimposed on the spectrum collected in quartz (black, lower panel), where there is no background signal, to illustrate the accuracy of the background subtraction. The horizontal dashed line is added to indicate the magnitude of the baseline artifact before and after subtraction of the ceramic signal. The holoMb 132R1 spectrum in quartz was previously reported in (11).

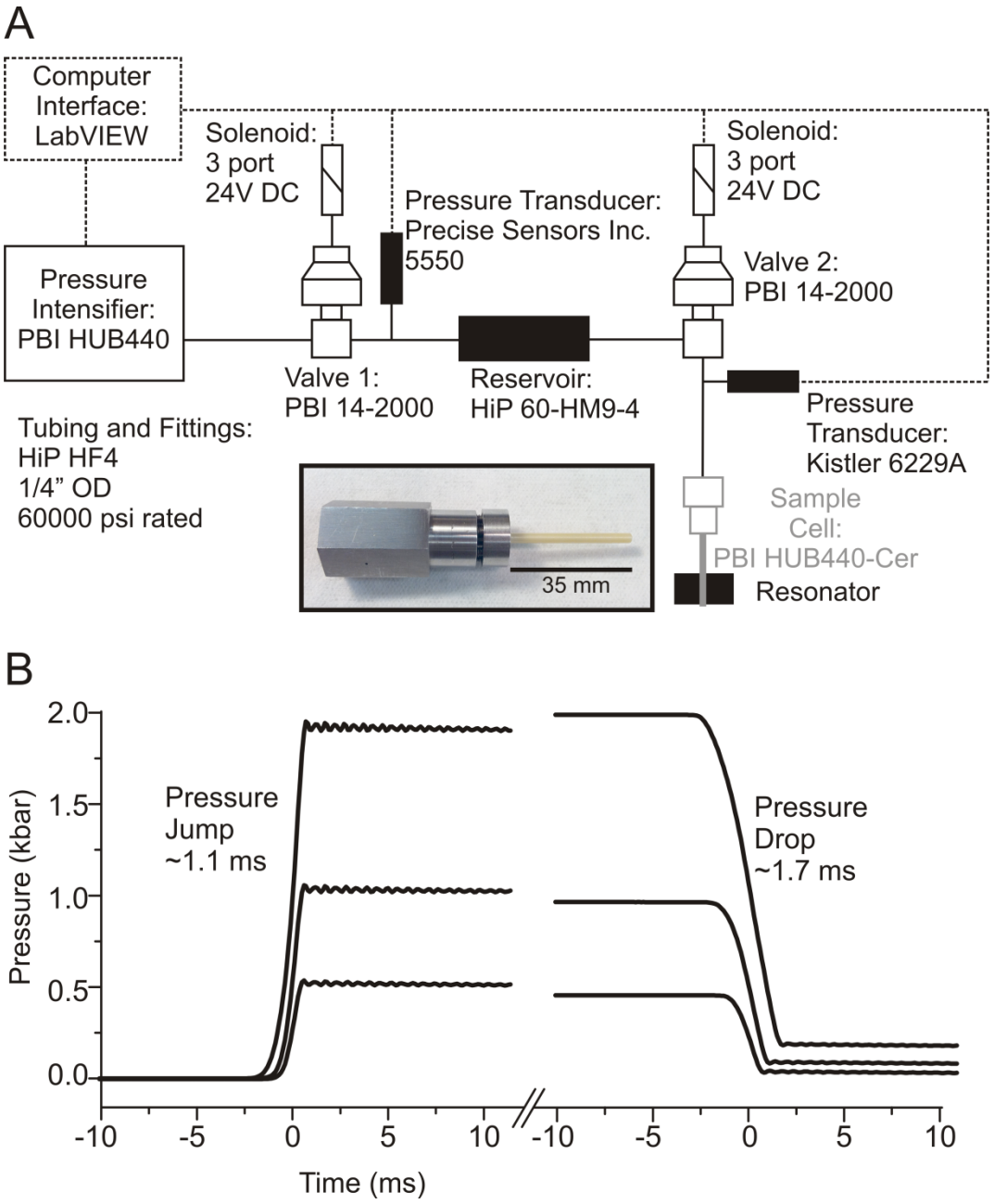

Figure 3.A10 A high-pressure EPR system for static and pressure-jump experiments. (A) Schematic of the high-pressure system. A picture of the HUB440-Cer ceramic cell is shown in an inset for reference. (B) The time dependence of the system pressure monitored by the Kistler transducer following pressure-jumps induced by opening of valve 2 with various pressures of the reservoir and sample; the pressure-jump is ≈1.5 ms, and is relatively independent of the jump magnitude and direction.

3.8 References

1. Henzler-Wildman K & Kern D (2007) Dynamic personalities of proteins. *Nature* 450(7172):964-972.
2. Baldwin AJ & Kay LE (2009) NMR spectroscopy brings invisible protein states into focus. *Nat Chem Biol* 5(11):808-814.
3. Kitahara R, *et al.* (2000) High pressure NMR reveals active-site hinge motion of folate-bound Escherichia coli dihydrofolate reductase. *Biochemistry* 39(42):12789-12795.
4. Kitahara R, Yokoyama S, & Akasaka K (2005) NMR snapshots of a fluctuating protein structure: ubiquitin at 30 bar-3 kbar. *J Mol Biol* 347(2):277-285.
5. Girard E, *et al.* (2010) Structure-function perturbation and dissociation of tetrameric urate oxidase by high hydrostatic pressure. *Biophys J* 98(10):2365-2373.
6. Dellarole M, Roumestand C, Royer C, & Lecomte JT (2013) Volumetric properties underlying ligand binding in a monomeric hemoglobin: a high-pressure NMR study. *Biochim Biophys Acta* 1834(9):1910-1922.
7. Kapoor S, *et al.* (2012) Revealing conformational substates of lipidated N-Ras protein by pressure modulation. *Proc Natl Acad Sci USA* 109(2):460-465.
8. Fourme R, Girard E, & Akasaka K (2012) High-pressure macromolecular crystallography and NMR: status, achievements and prospects. *Curr Opin Struct Biol* 22(5):636-642.
9. Bridges MD, Hideg K, & Hubbell WL (2010) Resolving conformational and rotameric exchange in spin-labeled proteins using saturation recovery EPR. *Appl Magn Reson* 37(1-4):363.

10. López CJ, Fleissner MR, Guo Z, Kusnetzow AK, & Hubbell WL (2009) Osmolyte perturbation reveals conformational equilibria in spin-labeled proteins. *Protein Sci* 18(8):1637-1652.

11. López CJ, Oga S, & Hubbell WL (2012) Mapping molecular flexibility of proteins with site-directed spin labeling: a case study of myoglobin. *Biochemistry* 51(33):6568-6583.

12. Hubbell WL, López CJ, Altenbach C, & Yang Z (2013) Technological advances in site-directed spin labeling of proteins. *Curr Opin Struct Biol* 23(5):725-733.

13. Guo Z, Cascio D, Hideg K, Kalai T, & Hubbell WL (2007) Structural determinants of nitroxide motion in spin-labeled proteins: tertiary contact and solvent-inaccessible sites in helix G of T4 lysozyme. *Protein Sci* 16(6):1069-1086.

14. Mchaourab HS, Lietzow MA, Hideg K, & Hubbell WL (1996) Motion of spin-labeled side chains in T4 lysozyme. Correlation with protein structure and dynamics. *Biochemistry* 35(24):7692-7704.

15. Hubbell WL, Cafiso DS, & Altenbach C (2000) Identifying conformational changes with site-directed spin labeling. *Nat Struct Biol* 7(9):735-739.

16. Hubbell WL, Gross A, Langen R, & Lietzow MA (1998) Recent advances in site-directed spin labeling of proteins. *Curr Opin Struct Biol* 8(5):649-656.

17. Columbus L & Hubbell WL (2004) Mapping backbone dynamics in solution with site-directed spin labeling: GCN4-58 bZip free and bound to DNA. *Biochemistry* 43(23):7273-7287.

18. McCoy J & Hubbell WL (2011) High-pressure EPR reveals conformational equilibria and volumetric properties of spin-labeled proteins. *Proc Natl Acad Sci USA* 108(4):1331-1336.

19. Budil DE, Lee S, Saxena S, & Freed JH (1996) Nonlinear-least-squares analysis of slow-motion epr spectra in one and two dimensions using a modified Levenberg–Marquardt algorithm. *J Magn Reson* 120(2):155-189.

20. Henry ER & Hofrichter J (1992) Singular value decomposition: application to analysis of experimental data. *Methods in Enzymology*, ed Ludwig Brand MLJ (Academic Press), Vol 210, pp 129-192.

21. Keszler A, Kalyanaraman B, & Hogg N (2003) Comparative investigation of superoxide trapping by cyclic nitrone spin traps: the use of singular value decomposition and multiple linear regression analysis. *Free Radical Biol Med* 35(9):1149-1157.

22. Lauricella R, Allouch A, Roubaud V, Bouteiller J-C, & Tuccio B (2004) A new kinetic approach to the evaluation of rate constants for the spin trapping of superoxide/hydroperoxyl radical by nitrones in aqueous media. *Org Biomol Chem* 2(9):1304-1309.

23. Columbus L, Kálai T, Jekö J, Hideg K, & Hubbell WL (2001) Molecular motion of spin labeled side chains in α-helices: analysis by variation of side chain structure. *Biochemistry* 40(13):3828-3846.

24. Columbus L & Hubbell WL (2002) A new spin on protein dynamics. *Trends Biochem Sci* 27(6):288-295.

25. Cooper A (1984) Protein fluctuations and the thermodynamic uncertainty principle. *Prog Biophys Mol Biol* 44(3):181-214.

26. Sreerama N & Woody RW (2000) Estimation of protein secondary structure from circular dichroism spectra: comparison of CONTIN, SELCON, and CDSSTR methods with an expanded reference set. *Anal Biochem* 287(2):252-260.

27. Fasman GD (1996) *Circular dichroism and the conformational analysis of biomolecules* (Plenum, New York, NY).

28. Akasaka K (2006) Probing conformational fluctuation of proteins by pressure perturbation. *Chem Rev* 106(5):1814-1835.

29. Harris RD, Jacobs M, Long MM, & Urry DW (1976) A high-pressure sample cell for circular dichroism studies. *Anal Biochem* 73(2):363-368.

30. Di Venere A, *et al.* (2011) Characterization of monomeric substates of ascorbate oxidase. *FEBS J* 278(9):1585-1593.

31. Fraga TR, *et al.* (2010) Refolding of the recombinant protein OmpA70 from Leptospira interrogans from inclusion bodies using high hydrostatic pressure and partial characterization of its immunological properties. *J Biotechnol* 148(2-3):156-162.

32. Gonçalves RB, Sanches D, Souza TL, Silva JL, & Oliveira AC (2008) The proapoptotic protein Smac/DIABLO dimer has the highest stability as measured by pressure and urea denaturation. *Biochemistry* 47(12):3832-3841.

33. Menéndez O, Rawel H, Schwarzenbolz U, & Henle T (2006) Structural changes of microbial transglutaminase during thermal and high-pressure treatment. *J Agric Food Chem* 54(5):1716-1721.

34. Ikeuchi Y, *et al.* (2001) Pressure-induced denaturation of monomer beta-lactoglobulin is partially irreversible: comparison of monomer form (highly acidic pH) with dimer form (neutral pH). *J Agric Food Chem* 49(8):4052-4059.

35. Yang J, Dunker AK, Powers JR, Clark S, & Swanson BG (2001) Beta-lactoglobulin molten globule induced by high pressure. *J Agric Food Chem* 49(7):3236-3243.

36. Baldwin RL & Rose GD (2013) Molten globules, entropy-driven conformational change and protein folding. *Curr Opin Struct Biol* 23(1):4-10.

37. Ptitsyn OB, Pain RH, Semisotnov GV, Zerovnik E, & Razgulyaev OI (1990) Evidence for a molten globule state as a general intermediate in protein folding. *FEBS Lett* 262(1):20-24.

38. Meinhold DW & Wright PE (2011) Measurement of protein unfolding/refolding kinetics and structural characterization of hidden intermediates by NMR relaxation dispersion. *Proc Natl Acad Sci USA* 108(22):9078-9083.

39. Bhattacharyya S & Varadarajan R (2013) Packing in molten globules and native states. *Curr Opin Struct Biol* 23(1):11-21.

40. Eliezer D, Jennings PA, Dyson HJ, & Wright PE (1997) Populating the equilibrium molten globule state of apomyoglobin under conditions suitable for structural characterization by NMR. *FEBS Lett* 417(1):92-96.

41. Eliezer D, Yao J, Dyson HJ, & Wright PE (1998) Structural and dynamic characterization of partially folded states of apomyoglobin and implications for protein folding. *Nat Struct Biol* 5(2):148-155.

42. Uzawa T, *et al.* (2008) Hierarchical folding mechanism of apomyoglobin revealed by ultra-fast H/D exchange coupled with 2D NMR. *Proc Natl Acad Sci USA* 105(37):13859-13864.

43. Akasaka K, Kitahara R, & Kamatari YO (2013) Exploring the folding energy landscape with pressure. *Arch Biochem Biophys* 531(1-2):110-115.

44. Vidugiris GJ & Royer CA (1998) Determination of the volume changes for pressure-induced transitions of apomyoglobin between the native, molten globule, and unfolded states. *Biophys J* 75(1):463-470.

45. Bismuto E, Irace G, Sirangelo I, & Gratton E (1996) Pressure-induced perturbation of ANS-apomyoglobin complex: frequency domain fluorescence studies on native and acidic compact states. *Protein Sci* 5(1):121-126.

46. Bismuto E, Sirangelo I, Irace G, & Gratton E (1996) Pressure-induced perturbation of apomyoglobin structure: fluorescence studies on native and acidic compact forms. *Biochemistry* 35(4):1173-1178.

47. Bondos SE, Sligar S, & Jonas J (2000) High-pressure denaturation of apomyoglobin. *Biochim Biophys Acta* 1480(1-2):353-364.

48. Kitahara R, Yamada H, Akasaka K, & Wright PE (2002) High pressure NMR reveals that apomyoglobin is an equilibrium mixture from the native to the unfolded. *J Mol Biol* 320(2):311-319.

49. Tanaka N, *et al.* (2000) Pressure effect on the conformational fluctuation of apomyoglobin in the native state. *Biochemistry* 39(39):12063-12068.

50. Zipp A & Kauzmann W (1973) Pressure denaturation of metmyoglobin. *Biochemistry* 12(21):4217-4228.

51. Eliezer D & Wright PE (1996) Is apomyoglobin a molten globule? Structural characterization by NMR. *J Mol Biol* 263(4):531-538.

52. Hughson FM, Wright PE, & Baldwin RL (1990) Structural characterization of a partly folded apomyoglobin intermediate. *Science* 249(4976):1544-1548.

53. Yang F & Phillips GN, Jr. (1996) Crystal structures of CO-, deoxy- and met-myoglobins at various pH values. *J Mol Biol* 256(4):762-774.

54. Nishii I, Kataoka M, Tokunaga F, & Goto Y (1994) Cold denaturation of the molten globule states of apomyoglobin and a profile for protein folding. *Biochemistry* 33(16):4903-4909.

55. Frauenfelder H, *et al.* (1987) Thermal expansion of a protein. *Biochemistry* 26(1):254-261.

56. Galkin O, Buchter S, Tabirian A, & Schulte A (1997) Pressure effects on the proximal heme pocket in myoglobin probed by Raman and near-infrared absorption spectroscopy. *Biophys J* 73(5):2752-2763.

57. Urayama P, Phillips GN, Jr., & Gruner SM (2002) Probing substates in sperm whale myoglobin using high-pressure crystallography. *Structure* 10(1):51-60.

58. Goto Y & Fink AL (1994) Acid-induced folding of heme proteins. *Hemoglobins, Part C, Biophysical Methods*, Methods in Enzymology, eds Everse J, Vandegriff KD, & Winslow RM (Academic Press), Vol 232, pp 3-15.

59. Morin B, *et al.* (2006) Assessing induced folding of an intrinsically disordered protein by site-directed spin-labeling electron paramagnetic resonance spectroscopy. *J Phys Chem B* 110(41):20596-20608.

60. Belle V, *et al.* (2008) Mapping α-helical induced folding within the intrinsically disordered C-terminal domain of the measles virus nucleoprotein by site-directed spin-labeling EPR spectroscopy. *Proteins* 73(4):973-988.

61. Brucker EA, Olson JS, Phillips GN, Jr., Dou Y, & Ikeda-Saito M (1996) High resolution crystal structures of the deoxy, oxy, and aquomet forms of cobalt myoglobin. *J Biol Chem* 271(41):25419-25422.

62. Regis WC, Fattori J, Santoro MM, Jamin M, & Ramos CH (2005) On the difference in stability between horse and sperm whale myoglobins. *Arch Biochem Biophys* 436(1):168-177.

63. Puett D (1973) The equilibrium unfolding parameters of horse and sperm whale myoglobin. Effects of guanidine hydrochloride, urea, and acid. *J Biol Chem* 248(13):4623-4634.

64. Spinozzi F, *et al.* (2007) Met-myoglobin association in dilute solution during pressure-induced denaturation: an analysis at pH 4.5 by high-pressure small-angle X-ray scattering. *J Phys Chem B* 111(14):3822-3830.

65. Jennings PA, Stone MJ, & Wright PE (1995) Overexpression of myoglobin and assignment of its amide, C^{α} and C^{β} resonances. *J Biomol NMR* 6(3):271-276.

66. Phillips GN, Jr. (1990) Comparison of the dynamics of myoglobin in different crystal forms. *Biophys J* 57(2):381-383.

67. Ando N, *et al.* (2008) Structural and thermodynamic characterization of T4 lysozyme mutants and the contribution of internal cavities to pressure denaturation. *Biochemistry* 47(42):11097-11109.

68. Zhang Z, *et al.* (2010) Multifrequency electron spin resonance study of the dynamics of spin labeled T4 lysozyme. *J Phys Chem B* 114(16):5503-5521.

69. Goto Y, Calciano LJ, & Fink AL (1990) Acid-induced folding of proteins. *Proc Natl Acad Sci USA* 87(2):573-577.

70. Barrick D & Baldwin RL (1993) Three-state analysis of sperm whale apomyoglobin folding. *Biochemistry* 32(14):3790-3796.

71. Jamin M & Baldwin RL (1998) Two forms of the pH 4 folding intermediate of apomyoglobin. *J Mol Biol* 276(2):491-504.

72. Roche J, *et al.* (2012) Cavities determine the pressure unfolding of proteins. *Proc Natl Acad Sci USA* 109(18):6945-6950.

73. Kamatari YO, Smith LJ, Dobson CM, & Akasaka K (2011) Cavity hydration as a gateway to unfolding: an NMR study of hen lysozyme at high pressure and low temperature. *Biophys Chem* 156(1):24-30.

74. Hummer G, Garde S, Garcia AE, Paulaitis ME, & Pratt LR (1998) The pressure dependence of hydrophobic interactions is consistent with the observed pressure denaturation of proteins. *Proc Natl Acad Sci USA* 95(4):1552-1555.

75. Buckle AM, Cramer P, & Fersht AR (1996) Structural and energetic responses to cavity-creating mutations in hydrophobic cores: observation of a buried water molecule and the hydrophilic nature of such hydrophobic cavities. *Biochemistry* 35(14):4298-4305.

76. Xu J, Baase WA, Baldwin E, & Matthews BW (1998) The response of T4 lysozyme to large-to-small substitutions within the core and its relation to the hydrophobic effect. *Protein Sci* 7(1):158-177.

77. Bouvignies G, *et al.* (2011) Solution structure of a minor and transiently formed state of a T4 lysozyme mutant. *Nature* 477(7362):111-114.

78. Wand AJ & Nucci NV (2015) Reply to Kitahara and Mulder: an ensemble view of protein stability best explains pressure effects in a T4 lysozyme cavity mutant. *Proc Natl Acad Sci USA* 112(9):E924.

79. Kitahara R & Mulder FAA (2015) Is pressure-induced signal loss in NMR spectra for the Leu99Ala cavity mutant of T4 lysozyme due to unfolding? *Proc Natl Acad Sci USA* 112(9):E923.

80. Fasman GD (1992) *Practical Handbook of Biochemistry and Molecular Biology* (CRC Press, USA) p 601.

81. Teale FW (1959) Cleavage of the haem-protein link by acid methylethylketone. *Biochim Biophys Acta* 35:543.

82. Crumpton MJ & Polson A (1965) A comparison of the conformation of sperm whale metmyoglobin with that of apomyoglobin. *J Mol Biol* 11:722-729.

83. Eaton SR, Eaton GR, & Berliner LJ (2005) *Biomedical EPR, Part B: Methodology, Instrumentation, and Dynamics* (Springer, New York, NY) p 470.

84. Kusnetzow AK, Altenbach C, & Hubbell WL (2006) Conformational states and dynamics of rhodopsin in micelles and bilayers. *Biochemistry* 45(17):5538-5550.

85. Shimshick EJ & McConnell HM (1973) Lateral phase separation in phospholipid membranes. *Biochemistry* 12(12):2351-2360.

86. Konno T, Meguro H, & Tuzimura K (1975) D-pantolactone as a circular dichromism (CD) calibration. *Anal Biochem* 67(1):226-232.

87. Swider KE & Worrell WL (1995) Electron paramagnetic resonance of titanium impurities in reduced yttria-stabilized zirconia. *J Amer Ceram Soc* 78(4):961-964.

88. Thorp JS, Aypar A, & Ross JS (1972) Electron spin resonance in single crystal yttria stabilized zirconia. *J Mater Sci* 7(7):729-734.

89. Slipenyuk AM, *et al.* (2004) ESR investigation of yttria stabilized zirconia powders with nanosize particles. *Ferroelectrics* 298(1):289-296.

90. Bykov IP, *et al.* (2008) Variation in the EPR characteristics of nanosized zirconia particles under exposure to X-ray radiation and annealing in hydrogen. *Phys Solid State* 50(12):2311-2316.

91. Sasaki K & Maier J (2000) Re-analysis of defect equilibria and transport parameters in Y_2O_3-stabilized ZrO_2 using EPR and optical relaxation. *Solid State Ionics* 134(3–4):303-321.

92. López CJ, Fleissner MR, Brooks EK, & Hubbell WL (2014) Stationary-phase EPR for exploring protein structure, conformation, and dynamics in spin-labeled proteins. *Biochemistry* 53(45):7067-7075.

93. Chen CT, Fine RA, & Millero FJ (1977) The equation of state of pure water determined from sound speeds. *J Chem Phys* 66(5):2142-2144.

Chapter 4: Mapping protein conformational heterogeneity under pressure with site-directed spin labeling and double electron-electron resonance

4.1 Summary

In the previous chapter, high-pressure circular dichroism and continuous-wave EPR spectroscopy were used to characterize conformational flexibility in various states of myoglobin, but the true amplitude of the structural fluctuations in the pressure-populated states remains to be determined. Site-directed spin labeling (SDSL) in combination with double electron-electron resonance (DEER) provides long range (20-80 Å) distance distributions with angstrom-level resolution and is thus ideally suited to resolve conformational heterogeneity in an excited state populated with high pressure. DEER is currently performed at cryogenic temperatures. Therefore, a method was developed for rapidly freezing spin labeled proteins under pressure to kinetically trap the high-pressure conformational ensemble for subsequent DEER data collection at atmospheric pressure (pressure-resolved, or PR DEER). The methodology was evaluated using seven doubly-labeled mutants of myoglobin designed to monitor selected inter-helical distances. For holomyoglobin, the distance distributions are narrow and relatively insensitive to pressure. On the other hand, in apomyoglobin, the distributions reveal a striking conformational heterogeneity involving specific helices in the pressure range of 0-3 kbar, where a molten globule state is formed. The data directly reveal the amplitude of helical fluctuations; information unique to the DEER method that complements information from the techniques introduced in chapter 3. Comparison of the distance distributions for pressure- and pH-populated molten globules shows them to be remarkably similar despite a lower helical content in the latter.

4.2 Introduction

As reported in chapter 3 for various states of myoglobin, the pressures required to populate low-lying excited states are typically a few kbar, corresponding to perturbation energies

of a few kilocalories per mole. At these low energies, pressure should not strongly remodel the energy landscape itself, but simply shift the relative population of pre-existing conformers (1), allowing for the study of functional excited states at equilibrium (2).

With a funnel-shaped model for the energy landscape (3, 4), an excited state populated by pressure will have a greater configurational entropy than the native state and is expected to consist of an ensemble of conformations in exchange on a time scale that can in principle span from ns to ms and beyond (5, 6). Structural characterization of the excited state is thus complicated by conformational heterogeneity, and how the ensemble is viewed depends on the intrinsic time scale of the experimental method employed relative to the protein dynamics. High-pressure crystallography cannot directly reveal conformational equilibria due to lattice interactions that select a particular conformation, but it has been used to monitor compressibility in the crystal environment (2). Solution NMR has played a central role in illustrating the utility of high pressure in the study of the excited state conformational ensemble, both in elucidating the physical basis for pressure effects and revealing the structure and dynamics of excited states in small soluble proteins (7, 8). However, due to the time scale of the NMR experiment, conformational exchange on the μs time scale can limit information to average structures, while relaxation effects due to exchange on the ms time scale can cause extreme broadening and loss of peaks in the commonly employed ^{1}H-^{15}N heteronuclear single quantum coherence (HSQC) spectrum (9). Moreover, application of these methods to the interesting case of high molecular mass membrane proteins in a native environment is challenging.

Conformational exchange is slow on the time scale of SDSL EPR, and continuous wave (CW) EPR spectra can provide a view of conformational equilibria frozen in time (10, 11), but the spectral resolution is insufficient to resolve all states present and there is no information on

the scale of structural differences between various conformations. However, DEER spectroscopy (12, 13) in combination with SDSL can identify the individual states with high resolution and provide a length scale to compare structural differences. DEER spectroscopy determines long-range distance distributions (20-80 Å) between pairs of spin labeled side chains selectively introduced in proteins. With a judiciously selected set of spin labeled pairs, structural models can be checked and conformational changes detected with angstrom level resolution (14). In the DEER experiment, the sample is flash-frozen, and data are acquired at cryogenic temperatures (50-80 K) (13, 15, 16). If different conformations are present in the sample, DEER will resolve each distinct distance and its probability distribution, thereby revealing the presence of heterogeneity, the magnitude of structural differences between members of the ensemble, and the inherent spatial order of each from the distribution width. Thus, SDSL DEER is an ideal and unique spectroscopic technique for exploring the excited state ensemble of proteins populated at high pressure. In order to use DEER with high pressure, an approach is introduced herein whereby the high-pressure equilibrium is kinetically trapped by flash-freezing samples under pressure followed by de-pressurization and subsequent data acquisition at 80 K.

In the present work, the above strategy is applied to the well-studied protein myoglobin (Mb) to both validate the methodology and to provide new information on the nature of pressure-populated species, particularly regarding structural heterogeneity and the amplitude of structural rearrangements relative to the native state. Apomyoglobin (apoMb) has an excited state (the molten globule, MG) that can be populated at atmospheric pressure at pH 4.1, enabling structure determination by solution NMR (17). The pH 4.1 MG appears to be a folding intermediate of apoMb (18) and a true equilibrium state of the system, although it is present at very low concentrations at neutral pH (i.e., an excited state) (19). The NMR data show that the MG retains

much of the helical structure of the native state of apoMb populated at pH 6 but with fluctuations to non-helical states in particular regions (20). However, the NMR methods provided no information on the amplitude of the fluctuations, i.e., whether the non-helical states involve large scale unfolding or localized distortions.

If pressure does not substantially alter the energy landscape, the same MG state should also be populated at pH 6 with the application of high pressure. Indeed, solution NMR showed that pressurizing apoMb to 2 kbar at pH 6 produced a state accompanied by a loss of most cross-peak intensities in the ^{1}H-^{15}N HSQC spectrum, presumably due to the onset of global conformational exchange on the ms time scale. The state produced at 2 kbar was assumed to be a MG, but no information on the secondary or tertiary structure could be obtained due to the loss of cross peak intensity (9). In chapter 3, high-pressure circular dichroism (CD) and SDSL together revealed that the MG state populated at 2 kbar, pH 6, has in fact the same helical content as the native state despite a tertiary fold that fluctuates on the ms time scale. The fact that the pressure-populated MG (2 kbar, pH 6) has a higher helical content than the pH-populated MG (0 bar, pH 4.1), and that a loss of peak intensities in the HSQC was observed in the former but not the latter (9, 20), raises a question as to the similarity of the pH- and pressure-populated species.

In the present chapter, distance distributions were determined for pairs of spin labels in Mb selected to monitor motions of the helical segments as a function of pressure. In holomyoglobin (holoMb) at pH 6, there is little pressure dependence. For apoMb at pH 6, the inter-spin distance distributions are relatively narrow at atmospheric pressure (≈5-10 Å width), but broad distributions implying large scale collective motions (>25 Å) of particular helices are seen at 2 kbar. Remarkably, the distinctive distance distributions of the pressure-populated MG are very similar to those in the pH-populated MG, despite the differences between them noted

above. It is concluded that the global topology of the folds is similar in the MG states, although there are clear differences in the local dynamics likely related to the compressibility of the excited state.

4.3 Results

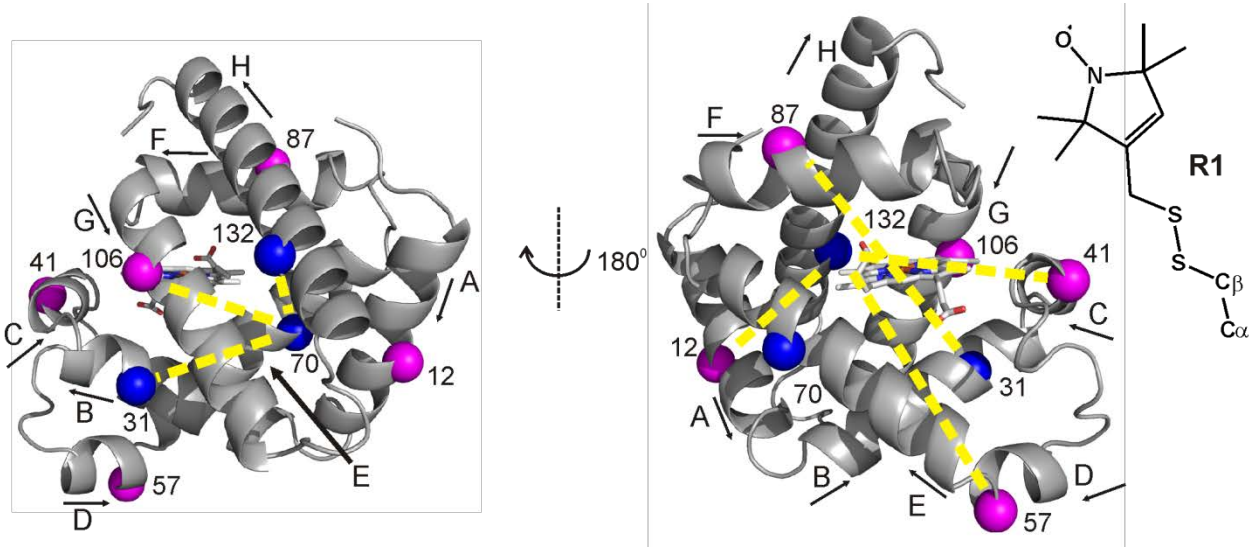

Figure 4.1 Ribbon model of holoMb with spin-labeled sites used in DEER measurements (PDB ID code 2MBW (21)). The spheres indicate the Cα of sites where the nitroxide spin label R1 (inset) was introduced pairwise to measure the corresponding inter-nitroxide distances (yellow dashed lines). Blue spheres indicate reference sites (see section **4.3**). The heme group is shown in stick representation. Arrows next to helix labels indicate the N- to C-terminus direction of each helix.

4.3.1 Trapping high-pressure equilibria for DEER spectroscopy. For DEER distance mapping of high-pressure states of Mb, seven doubly-labeled mutants were prepared containing the nitroxide side chain R1 (Figure 4.1). Solvent-exposed sites for R1 were selected in each helix to monitor distance distributions relative to a selected reference site. The reference sites are those in helices whose positions in the structure are apparently pressure independent; as shown below in Figure 4.1, these are selected as 31, 70, and 132 in helices B, E, and H, respectively.

Standard DEER methodology requires flash-freezing of a sample, typically in liquid nitrogen, and data acquisition at 50-80 K (14, 15, 22, 23). For the application of DEER to monitoring the structure of high-pressure states, a procedure is introduced here in which the

pressurized sample is rapidly frozen in a dry ice/ethanol bath to 200 K. The frozen sample is then depressurized and cooled further to 77 K in liquid nitrogen for subsequent data acquisition at atmospheric pressure. This methodology is shown schematically in Figure 4.2, and the details are provided in section **4.6**. The freezing rate in dry ice/ethanol is in fact more rapid to ≈223 K than that in liquid nitrogen (Figure 4.A1) because liquid nitrogen boils when the borosilicate sample tube is initially submerged in the bath, resulting in the formation of an insulating gas sheath around the tube.

The evidence reported to date indicates that the effects of flash-freezing in liquid nitrogen on R1 rotameric equilibria are minimal (22) and that conformational equilibria are effectively trapped (14, 24-31). To compare the efficacy of rapid freezing in dry ice/ethanol with that in liquid nitrogen, DEER distance distributions at atmospheric pressure for each doubly-labeled mutant of apoMb and holoMb were compared using the two freezing methods (Figure 4.A2). The distance distributions are nearly identical, indicating the equivalence of the methods with respect to both protein conformational equilibria and rotameric equilibria of the R1 side chain.

The glass transition temperature of the glycerol/water mixture used here is ≈150 K (32). Thus, it is possible that above this temperature at 200 K, the conformational ensemble could relax after depressurization and before cooling to 77 K. Complete relaxation at 200 K during the time between depressurization and cooling to 77 K, approximately 3 min, is ruled out by the observation of distinct distance distributions for individual spin pairs held at different pressures prior to freezing to 200 K. However, to check for partial relaxation at 200 K, samples of 57R1/132R1 were pressurized to 2 kbar, frozen in dry ice/ethanol as described above, and depressurized. Then, the samples were held at 200 K for either 3, 10, or 120 minutes prior to cooling further to 77 K in liquid nitrogen for data acquisition. The resulting distance distributions

are similar (Figure 4.A3A), indicating that conformational relaxation does not occur at 200 K on the experimental time scale employed here.

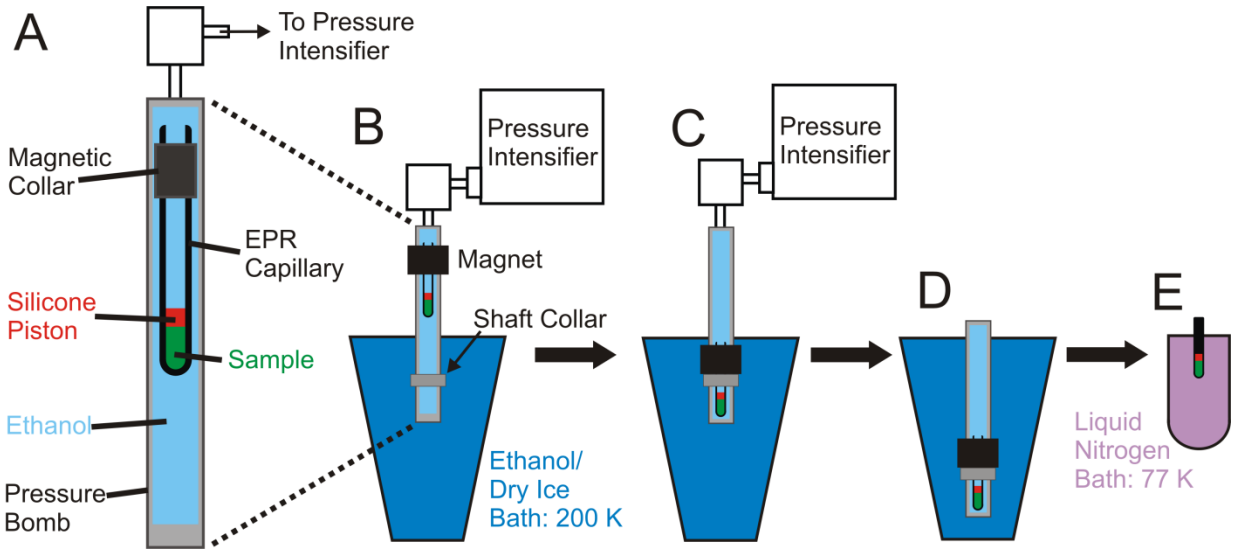

Figure 4.2 Methodology for freezing under pressure. (A) Detail of sample in the pressure bomb. A borosilicate capillary is modified by the addition of a magnetic collar near the top. A silicone piston (red) separates the sample (green) from the ethanol pressurization fluid (light blue) that fills the pressure bomb. (B) The bomb is connected to the pressure intensifier with the lower portion immersed in dry ice/ethanol (dark blue) at 200 K. The sample is held at the top of the bomb using the magnet, and the temperature is controlled during pressurization. (C) Rapid cooling to 200 K is triggered while under pressure, when the sample is moved quickly to the bottom of the bomb. Addition of a shaft collar on the pressure bomb helps ensure proper positioning of the cell during cooling. (D) The bomb is depressurized, disconnected from the pressure intensifier, and submerged in the dry ice/ethanol bath. (E) The sample capillary is transferred to liquid nitrogen (purple) for cooling to 77 K in preparation for DEER data acquisition at 80 K. The magnetic collar is removed prior to transfer to the resonator.

Reversibility of pressure-populated changes was verified using a 57R1/132R1 sample prepared at 2 kbar, as described above. After data acquisition, the sample was thawed, re-frozen at atmospheric pressure, and DEER was performed. The distance distribution is nearly identical to that for 57R1/132R1 at 0 bar, before pressurization (Figure 4.A3B), confirming the reversibility of the observed pressure-populated conformational changes.

4.3.2 PR DEER distributions for holoMb suggest local regions of compressibility in an otherwise rigid structure. Figure 4.3 shows the background corrected dipolar evolution functions (left panel) and the corresponding distance distributions (center panel) for holoMb at

pressures in the range of 0 bar to 3 kbar (gauge pressure; 0 bar gauge is atmospheric pressure). At atmospheric pressure, the distributions (shaded gray areas) are dominated by a single distance with distribution widths of ≈3-5 Å (full-width at half maximum), except for 41R1/132R1 and 31R1/87R1, which have broader bimodal distributions which likely arise from two conformations of the protein involving the helices C and F, respectively (see section **4.4**). In all cases, the most probable distance corresponds closely to that for the R1 side chains modeled in the holoMb crystal structure (PDB ID code 2MBW (21)). As the pressure is increased, there is a slight broadening of the distance distributions, while the relative populations at different distances are unchanged for most pairs (Figure 4.3). For 12R1/132R1, 31R1/70R1, 31R1/87R1, 70R1/106R1, and 70R1/132R1 the distance distributions are nearly superimposable up to 2 kbar, and only a slight degree of broadening in the distance widths is observed at 3 kbar (Figure 4.3), reflecting the incompressibility of holoMb.

Although the distance distributions for most pairs are nearly pressure-independent, the distributions for 57R1/132R1 and 41R1/132R1 exhibited a shift in populations toward longer distances at 2 kbar, but without the appearance of additional populations; at 3 kbar, an additional population appears in 41R1/132R1 at ≈36 Å (Figure 4.3C and D).

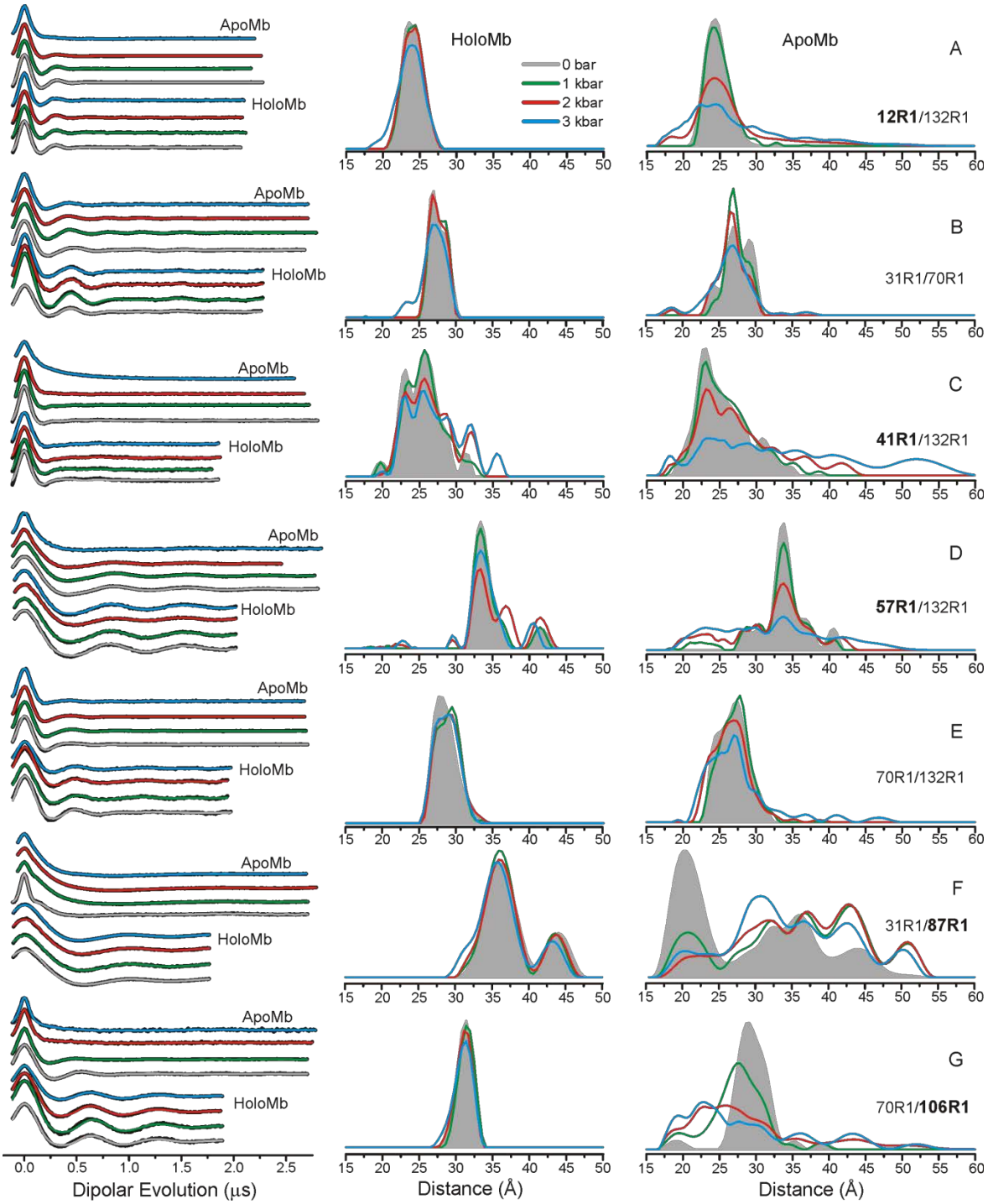

Figure 4.3 PR DEER distance distributions for holoMb and apoMb at pH 6. Background-corrected dipolar evolutions are shown in the left-hand column in black, with fits to the data (section **4.6**) overlaid and color coded by pressure. The area-normalized distance distributions are shown in the center (holoMb) and right-hand (apoMb) columns for (A) 12R1/132R1, (B) 31R1/70R1, (C) 41R1/132R1, (D) 57R1/132R1, (E) 70R1/132R1, (F) 31R1/87R1, and (G) 70R1/106R1. An inset indicates the color-coding of the distance distributions and fits to the dipolar evolutions. Dipolar evolutions are vertically offset for clarity. Bold labels indicate sites in each mutant in which structural motion as a function of pressure is attributed.

4.3.3 ApoMb structure exhibits strong and non-uniform pressure dependence. Removal of the heme to form apoMb produces structural changes relative to holoMb at atmospheric pressure (right column, Figure 4.3) sensed by inter-spin distance distributions. In all cases except for 12R1/132R1, the distributions are broadened and modified in shape relative to holoMb. The increase in distribution width reflects heterogeneity in the population relative to holoMb, which in turn mirrors increased flexibility and structural fluctuations at ambient temperature. In the case of the 31R1/87R1 the effect is extreme, with a dominant population appearing at a 15 Å shorter distance and the full distribution extending over a 25 Å range. This result is consistent with the dynamic disorder in helix F, where 87R1 resides, deduced from both NMR and SDSL in apoMb (11, 19).

For the purposes of the work presented in this chapter, the effect of pressure at 2 kbar on apoMb is the most interesting, because this is the pressure at which the putative MG state is populated, as inferred from extreme broadening in the HSQC NMR spectrum (9) and the appearance of multiple components in the EPR spectra of R1. Although there are detectable changes in the distance distributions for all R1 pairs at 2 kbar, the effect is small for 70R1/132R1, and the most probable distance for 31R1/70R1 is unchanged, although there is a shift in relative populations. Moreover, the distance distributions for 31R1/70R1 and 70R1/132R1 display a total width of ≈10 Å, which is substantially narrower than for any other spin pair in apoMb reported here at high pressure. Based on these data, residues 31R1, 70R1, and 132R1 are assigned as reference sites located in helical segments that apparently do not substantially change position as a function of pressure up to at least 3 kbar (right panel, Figure 4.3). These are reference sites not in the sense that they lack conformational flexibility, but that they are spatially restricted on the angstrom length scale. With this tentative assignment and the

fact that the helical content of apoMb is unchanged up to 2.4 kbar, the inter-spin distance distributions can be discussed in terms of rigid body movement of helical segments relative to the reference sites.

In the context of the above model, helices B, E, and H (in which the reference sites reside) remain relatively localized at 2 kbar compared to atmospheric pressure, i.e., additional states with substantial populations and different structures do not appear. Helix A, monitored by 12R1 relative to the 132R1 reference, is not displaced at 2 kbar but has an increased spatial disorder indicated by the breadth of the distance distribution (Figure 4.3A). Helix F, monitored by 87R1 relative to the 31R1 reference, shows a dramatic shift in population from the main 20 Å peak at atmospheric pressure to a broad distribution of states spread from ≈20 to 50 Å at 2 kbar, with only small additional changes at 3 kbar. Residue 41R1 relative to the 132R1 reference monitors the position of helix C. At 2 kbar, the most probable distance at 23 Å remains unchanged, and though additional distances appear at 36 and 42 Å, they have relatively small populations. Helices D and G, monitored by 57R1 and 106R1 relative to references 132R1 and 70R1, respectively (Figure 4.3D and G), show striking displacements to shorter distances with broad distributions at high pressure. Collectively, the data show that the high-pressure state of apoMb at pH 6 is spatially disordered, but not uniformly so, relative to that at atmospheric pressure. Interestingly, the distance distributions at high pressure also contain the discrete populations present at atmospheric pressure, suggesting that the high-pressure ensemble includes a population corresponding to the native apoMb structure. A structural model of the high-pressure state consistent with these changes will be presented in section **4.4**.

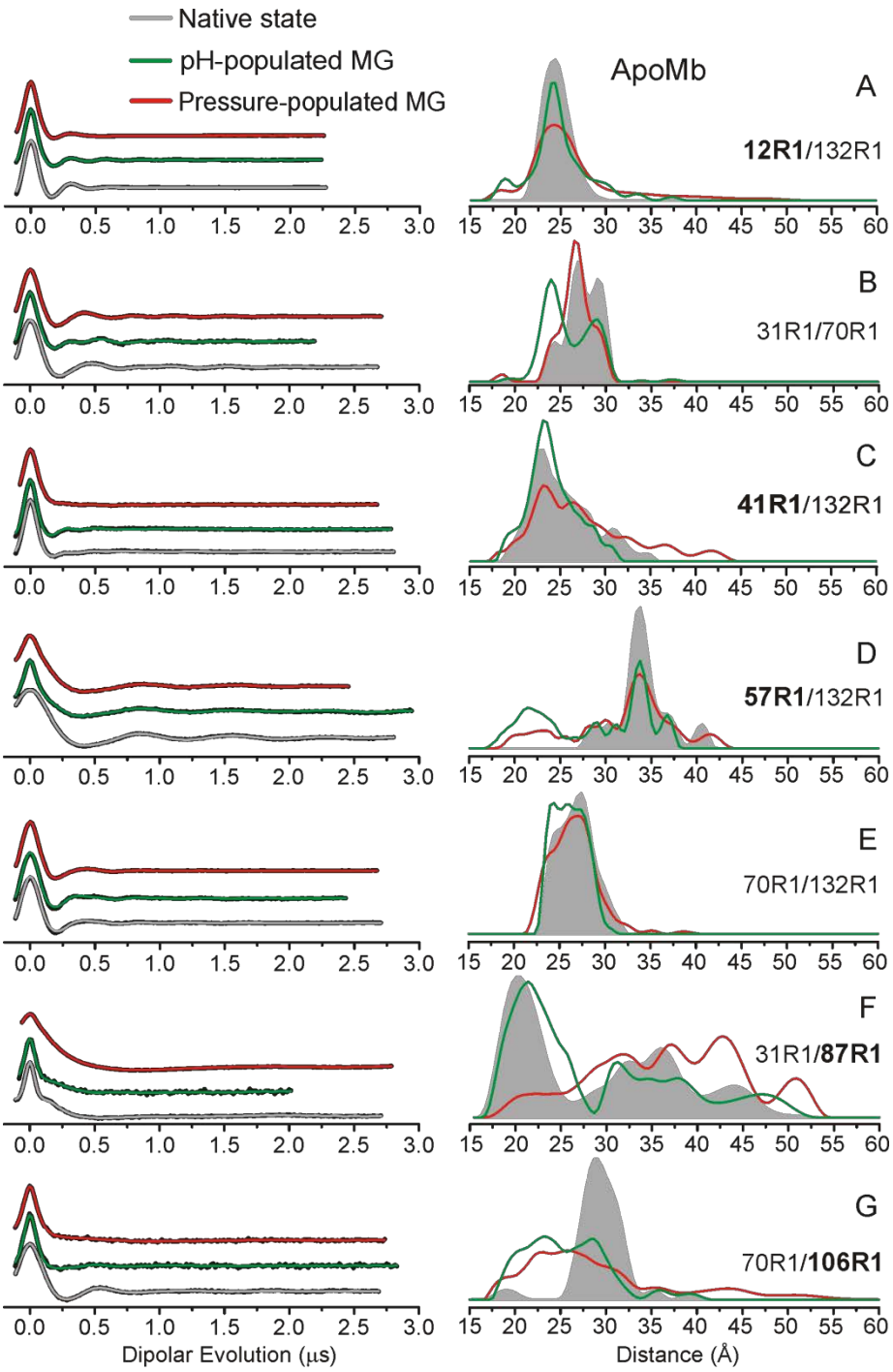

Figure 4.4 DEER distance distributions for the conformational ensemble of apoMb in the native state at 0 bar and pH 6, the pH-populated MG at 0 bar and pH 4.1, and the pressure-populated MG at 2 kbar and pH 6. Background-corrected dipolar evolutions of the indicated mutants are shown in the left-hand column in black, with fits to the data (section **4.6**) overlaid and color coded by state. The area-normalized distance distributions from are shown to the right for (A) 12R1/132R1, (B) 31R1/70R1, (C) 41R1/132R1, (D) 57R1/132R1, (E) 70R1/132R1, (F) 31R1/87R1, and (G) 70R1/106R1. An inset indicates the color-coding of the distance distributions and fits to the dipolar evolutions. Dipolar evolutions are vertically offset for clarity. Bold labels indicate sites in each mutant in which structural motion as a function of pressure is attributed.

4.3.4 Comparison of pressure- and pH-populated MG states of apoMb. As reviewed in section **4.2**, the NMR ^{1}H-^{15}N HSQC spectrum was well resolved in the pH-populated MG, and analysis showed local unfolding in the C, D, E, and F helices as well as the N-terminal half of helix B (20, 33). On the other hand, the pressure-populated MG state showed extreme broadening of cross peaks in the ^{1}H-^{15}N HSQC spectrum (9), and CD and SDSL showed that this state maintains the full helical content of the native state. Thus, the two states cannot be identical, and their structural relationship is revealed in the DEER distance distributions for the two states shown in Figure 4.4. Despite the differences in secondary structure and dynamics exposed by the above studies, the DEER data show a surprising similarity in the topology of the two MG states, except for the location of helix F in the structure. In the pH populated MG state, the distance distribution resembles that of native apoMb, while the dominant population at 20 Å is largely depleted in the high-pressure state, being shifted to a broad distribution centered at greater distances (Figure 4.4F). Although similar, there are interesting differences in the distributions of particular pairs. For example, for 12R1/132R1, 41R1/132R1, and 70R1/106R1, the overall distribution widths are greater for the pressure-populated MG, reflecting greater spatial disorder. For 31R1/70R1, the same discrete distances are present in the two states, but high pressure favors the longer distances.

Removal of the heme moiety from holoMb to form apoMb generates a large cavity, and pressure populates distances which are consistent with insertion of the R1 side chain in or near this central cavity for several spin pairs in apoMb (see section **4.4**). It should be considered whether the interaction of the R1 side chain with the protein contributes favorably to this interaction, or whether native protein motion is fully responsible for the distance changes

observed. Recently a case was reported of the R1 side chain filling a hydrophobic cavity in a cavity-creating mutant of T4 lysozyme (34), and the acetamidoproxyl (AP) side chain was used as a comparison with R1 to evaluate the energetic contribution of the spin label to the observed structural changes in the protein. AP contains an amide in its linkage to the protein and lacks the disulfide of R1, therefore AP is a more polar label. PR DEER was performed for three of the spin pairs reported here for apoMb with the AP label (Figure 3.A4), and in all cases the 0 bar and 2 kbar distance distributions were broadly similar to those collected using the R1 label. More importantly, the changes in the distance distributions due to pressure were strikingly similar to those observed with R1, particularly for 31AP/70AP. Using both labels, the distance distributions for this spin pair are narrow and trimodal, and pressurization to 2 kbar increases the probability of the middle distance.

It is likely that the cavity in apoMb left by heme removal is hydrated, and therefore the hydrophobicity of R1 is less likely to produce significantly favorable interaction energy. Nonetheless, the comparability of the distance distributions generated from these two labels is sufficient to conclude that the spin label side chain provides negligible contribution to the pressure-populated changes observed here.

4.4 Discussion

One aim of the work presented in this chapter was to develop a methodology to kinetically trap high-pressure conformational ensembles of proteins by flash-freezing, such that DEER distance measurements may be employed to determine structure and structural heterogeneity in the ensemble. If successful, the unique advantage of DEER in this context is to provide global distance constraints and analytical distance distributions that directly reveal structural heterogeneity and the amplitude of the corresponding fluctuations that are presumed to

occur at ambient temperatures (14). The success of this approach relies on the ability to kinetically trap the high-pressure conformational equilibrium by flash-freezing to 200 K in the presence of glycerol as a cryoprotectant.

There are two questions relevant in evaluating the method. First, is conformational exchange slow enough at 200 K so that thermal and pressure equilibration does not occur following depressurization during the time required to cool the sample below the glass transition temperature (150 K)? Second, is the cooling time to 200 K sufficiently short compared to the characteristic relaxation time for conformational movement so that the ensemble trapped is representative of the one at ambient temperature?

Regarding the first question, it is of interest to consider the environment of the protein at 200 K. At the cooling rates achieved here (Figure 4.A1), the amount of ice crystal formation will be much less than that computed from the equilibrium phase diagram of the two- component glycerol-water mixture at atmospheric pressure (35). If the system were at thermal equilibrium during cooling, ≈80% of the water would be ice crystal as predicted by the phase diagram, thereby concentrating the protein by a factor of ≈3 in a super-cooled water-glycerol mixture. Analysis of the exponential background in the DEER data gives a total spin concentration similar to that of the starting solution (≈300-400 μM) (36, 37), demonstrating that such concentration does not occur, either at atmospheric pressure or at high pressure. Thus, the bulk of the sample is assumed to be a super-cooled solution, whose viscosity at 200 K can be estimated as ≥3000 cP at atmospheric pressure (32) and presumably higher under pressure. In the context of Kramer's theory (38), rate constants for conformational exchange scale as $\eta^{-1}e^{-Ea/RT}$ (39). Thus, both the low thermal energy and the high viscosity conspire to dramatically slow conformational exchange at 200 K. Indeed, as delineated above, no relaxation of the distinct ensemble of apoMb

frozen under high pressure occurs at 200 K after depressurization even on a time scale of 120 minutes. Because the pressure effect is fully reversible, i.e., thawing a pressurized sample and re-freezing at atmospheric pressure gives the native-like ensemble, this result shows that conformational movements are very slow at 200 K. Because the sample is cooled below the glass transition temperature within ≈3 min after depressurization, it is tentatively concluded that the high-pressure conformational ensemble has been effectively trapped. On the other hand, small side chain motions can occur above the glass transition temperature on the time scale of seconds, and it is likely that side chain rotamers will equilibrate with respect to both temperature and pressure at 200 K (40). If this is the case, the rotamer population of R1 in the PR DEER experiment is unchanged from that at atmospheric pressure. Under any circumstance, the pressure independence of CW spectra for R1 in holoMb to 2 kbar strongly suggests that rotameric equilibria of R1 are not pressure sensitive in the pressure range investigated.

In regard to the second question above, the cooling time to reach 200 K is, in general, long compared to the characteristic relaxation time for conformational motions at ambient temperature. However, the large temperature coefficient for the viscosity of glycerol/water mixtures (32), and, in some cases, large enthalpies of activation, likely slow the exchange rates sufficiently during cooling to result in kinetic entrapment. This is a basic assumption in all published DEER experiments, and considerable empirical evidence is available to justify the assumption (14, 24-31). In addition, distance distributions between spin pairs in T4 lysozyme were found to be only weakly dependent on cooling rates (22). Typically, DEER samples are frozen in liquid nitrogen, which is in fact slower to ≈223 K compared to the dry ice/ethanol used here (Figure 4.A1), and the same body of evidence as conventional DEER is relied on here to justify kinetic entrapment during the cooling phase. For relatively unstable MG states, one must

consider the possibility of cold denaturation of the protein during the early stages of the freezing process. The few studies of the rate of cold denaturation that have been published found the process to be extremely slow, on the order of minutes to hours (41-43). Although no measurements have been made for the MG state of apoMb, it is tentatively assumed that the rate of cold denaturation, as for conformational exchange, is sufficiently slow that this process does not occur during the freezing to 200 K.

In addition to the cryoprotective function mentioned above, glycerol is a stabilizing osmolyte which favors folded states of proteins (44-47) and the effect of glycerol on the structure and conformational equilibria of Mb must be considered. A systematic SDSL EPR study of the osmolyte effect on holoMb, apoMb, and the MG state of apoMb has been carried out for each of the R1 labeled sites used in the present experiments with sucrose as the osmolyte. In each case, addition of osmolyte had observable effects only where multicomponent EPR spectra signaled the existence of conformational equilibria. The effects were a simple shift in the equilibrium and were relatively small; for example, the largest effects were observed for equilibria involving order-disorder equilibria in helix F, where 30% wt/wt sucrose resulted in a stabilization of the ordered state by ≈-0.3 kcal/mol (48). Glycerol is considerably weaker than sucrose as a stabilizing osmolyte (49-51), and in general the perturbation of 25% vol/vol glycerol on conformational equilibria should be even smaller and acceptable in exchange for the cryoprotective function.

Collectively, the data presented here provide a tentative empirical validation of the methodology for trapping high-pressure states of proteins for exploration with PR DEER spectroscopy. At the same time as providing validation, the data add another dimension to the characterization of the pressure-populated MG state of apoMb, namely the amplitude of

structural changes, and allow a comparison with the extensively characterized pH-populated MG state. The results of the experiments, beginning with holoMb, and a comparison with expectations from other methods are discussed below, leading to a model for the high-pressure state ensemble of apoMb.

4.4.1 The apparent compressibility of holoMb is non-uniform in the structure. Five of the seven mutants in holoMb reported here exhibit minimal changes in distance distributions as a function of pressure (Figure 4.3), consistent with previous studies that showed holoMb to be a highly ordered and well-packed protein (11, 20, 21) with minimal pressure sensitivity at pH 6 and in the pressure range used here (52). The only cases of significant pressure-dependent changes in holoMb are the mutants with R1 in the short helices C and D, which show a shift in population toward longer distances at high pressure. Crystallographic and SDSL studies found a relatively high degree of flexibility in these two helices (11, 53, 54), and the most attractive model consistent with the data is that the alternative packing modes of the structure around helices C and D, identified by the discrete populations in the PR DEER distance distributions, have different molar volumes. The population shift at high pressure reflects local protein compressibility. Interestingly, compression does not result in a decrease in the total width of the distributions as one might expect for simple compaction, but rather drives a slight increase in the distribution widths. The mechanism may be, for example, hydration of packing imperfections which lowers the partial molar volume, but enables alternative packing arrangements of the local core (55).

4.4.2 PR DEER reveals the structural diversity of the pressure-populated MG state. Unlike the relatively pressure-insensitive structure of holoMb, pressurizing apoMb to 2 kbar results in extremely broad distance distributions in particular mutants, covering >25 Å in 5 of the

7 spin pairs studied here. The increased widths reflect the increase of conformational heterogeneity in the protein. The distance distributions include discrete states corresponding to native apoMb, indicating that the excited state ensemble includes the native conformation. As in all cases, the static distributions resolved with PR DEER are taken to reflect conformational fluctuations at ambient temperature. Considering that the high-pressure state has the full helical content of the native protein, it can be concluded that the fluctuations are comprised of nanometer-scale rigid body motions of helices or helical segments (with the exception of F, which is locally unfolded in the native state). A tentative model for the structural origins of conformational fluctuations involving helices D, F, and G in the pressure-populated MG of apoMb is presented in Figure 4.5 and discussed below. The model builds on earlier data showing that the helical content of the pressure-populated MG is the same as native apoMb. Since there are no secondary structural changes, the simple models of Figure 4.5 assume that the distance changes monitored by a single site in a helix reflect motion of the entire helix. In reality, independent segmental motions within individual helices are clearly possible, but the sparse data set presented here does not permit this level of interpretation.

In the native state of apoMb, NMR, and SDSL-DEER data showed that the sequence corresponding to helix F undergoes conformational exchange involving non-helical states that probably occupy the otherwise empty heme pocket (11, 19). The extremely broad distribution of 87R1 (helix F) with respect to the reference site 31R1 in apoMb reflects a conformational ensemble that involves motions of approximately 25 Å, consistent with conformational exchange events of this amplitude at ambient temperature. Moreover, the dominant 20 Å peak in the distance distribution requires a 15 Å displacement of 87R1 toward 31R1 from its position in holoMb (Figure 4.3F), a motion that would place 87R1 into the heme cavity. At high pressure,

the 20 Å peak sharply diminishes, while multiple populations at longer distances grow in a broad distribution, indicating a movement of 87R1 out of the heme pocket at high pressure (Figure 4.5A); forming a distribution more similar to that for holoMb.

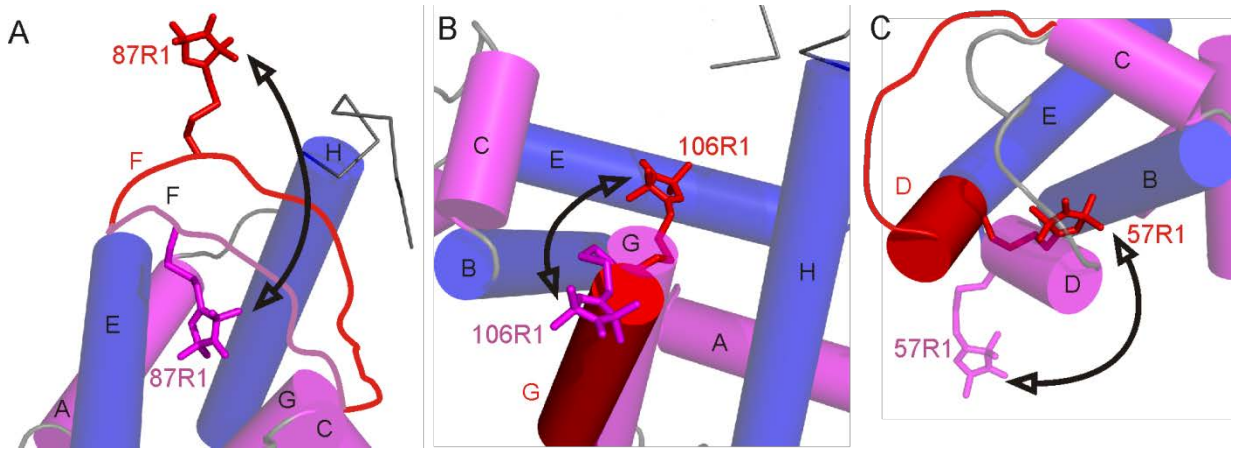

Figure 4.5 Models for the conformational changes of selected sequences in the transition to the pressure-populated MG of apoMb at 2 kbar, pH 6. Panels A, B, and C show the proposed changes relative to the native structure in particular regions. In each panel, the model of the native state is based on the crystal structure of holomyoglobin (PDB ID code 2MBW (21)), except for the contiguous sequence of the F helix and N-terminus of G, which is locally unfolded in the native state of apoMb and is drawn in as a disordered loop in panel A; this sequence is omitted from panel B for clarity (56). Helices are shown in cylinder representation; helices that contain reference sites are colored blue, and helices that contain sites that undergo large amplitude motions in the pressure-populated MG are in magenta. Models for a dominant conformation in the pressure-populated MG based on PR DEER data at 2 kbar are superimposed and shown in red. Arrows indicate a trajectory of motion followed by each segment in the pressure-populated native-to-MG transition. (A) The sequence of helix F moves out of the heme pocket. The native state position of the F helix is modeled to satisfy the most probable distance (20 Å) of 31R1/87R1 in apoMb at 0 bar. (B) Helix G fluctuates between the native state and a twist/tilt which inserts R1 into the heme pocket; alternatively, additional fraying of the N-terminal end of helix G at high pressure could result in the disordered sequence containing 106R1 rearranging in a number of distinct conformations which insert the nitroxide into the heme pocket. (C) Helix D fuses with the E helix in a motion that involves a concurrent rotation placing the 57R1 side chain near helix B.

At the N-terminus of helix G, the distribution of 106R1 relative to 70R1 at atmospheric pressure is broader compared to holoMb (6 Å *vs* 3 Å width at half-maximum; Figure 4.3G), mirroring the disorder in the N-terminal segment of the G helix identified by NMR (19, 56, 57). High pressure produces a dramatic increase in overall breadth of the distribution, to over 35 Å. The most dominant populations are now centered at shorter distances, revealing a displacement of 106R1 by ≈5 Å toward 70R1, which would require 106R1 to be located in the heme cavity. The model shown in Figure 4.5B to account for this shift in the distribution is a twisting motion

of the N-terminal segment of helix G. Since 106R1 is near the end of the helical portion of G at atmospheric pressure, it is possible that the sequence is disordered in the pressure-populated MG, such that many other specific configurations could place 106R1 in the cavity. In both the 31R1/87R1 and 70R1/106R1 distributions, there are populations corresponding to native apoMb at atmospheric pressure, suggesting that the F and G helix segments fluctuate between positions in and out of the heme cavity.

The distance of 57R1 relative to 132R1 monitors the position of helix D. In native apoMb, the distance distribution is broader than that for holoMb due to the appearance of additional populations, reflecting the flexibility of this short helical segment in the native apoMb state. The striking increase in width of the distribution at 2 kbar identifies conformational disorder involving fluctuations of this helix with an amplitude of ≈20 Å (Figure 4.3D). The shorter distances in the distribution suggest a large rotation of helix D to place the nitroxide of 57R1 closer to 132R1. A model was previously reported for the pH-populated MG state of apoMb wherein the D helix sequence fuses with the end of E to form a transient helical structure (19, 58); this structural rearrangement is consistent with the 22 Å distance in the high-pressure state, and is tentatively proposed for one conformer of the pressure-populated MG ensemble.

4.4.3 Structural similarity of the pH- and pressure-populated MG states of apoMb. Overall, the pH- and pressure-populated MG states are more similar than different as assessed by distance mapping. The major difference lies in the spatial distribution of the F helix segment, which is located outside the heme cavity in the high-pressure state but dominated by an intra-cavity conformation similar to that in native apoMb in the pH-populated MG. However, the N-terminus of the G helix still occupies part of that cavity in a location similar to that in the pressure-populated MG, indicating that either the F and G segments occupy unique sites within

the cavity, or the two segments alternate between collapsed and native-like conformations out of phase with one another.

The differences between the pH- and pressure-populated MG states identified by NMR, CD, and SDSL may appear to be at odds with the obvious global similarity of the two MGs as viewed by DEER distance mapping. For example, NMR describes local unfolding in the non-core C, D, and E helices with dynamic disorder on the ns time scale in the pH-populated MG, while CD shows the helical content of the high-pressure state to be the same as the native apoMb. Based on these data, one might expect the distance distributions in the pH-populated MG between sites in helices found to undergo unfolding by NMR to be broader than those in the pressure-populated state. This expectation is rooted in a model for partial unfolding of helices identified by NMR in which the entire helix collectively fluctuates between a folded and unfolded conformation. However, this model is incompatible with the DEER data, shown in Figure 4.4, where the distance distributions between residues in the C, D, and E helices and stable references are similar in the two MGs. An alternative interpretation consistent with the DEER results is that dynamic disorder revealed by NMR and SDSL is not necessarily correlated with large amplitude motions. Partial unfolding of secondary structure elements as deduced by NMR $^{13}C\alpha$ shifts may involve relatively small amplitude local distortions that migrate along helical sequences, fluctuating on a ns-μs time scale, that do not contribute to a large amplitude motion that would be observed in the DEER distance distributions.

4.4.4 Structural transitions responsible for the reduction of volume at high pressure. Typically, pressure effects are attributed primarily to the elimination of internal cavities through hydration (59, 60), leading to local, and eventually global, unfolding (9). Based on the similar helical content of native apoMb and the pressure-populated MG state, it was suggested that

pressure populates alternative packing arrangements of the helical core rather than producing local unfolding in order to reduce internal cavity volume, consistent with recent studies showing that pressure shifts helix-coil equilibria towards the helical conformation rather than an unfolded state (61, 62). The PR DEER data adds the amplitude of conformational rearrangements involved to this model. The large degree of heterogeneity reported by the PR DEER distance distributions, along with the long distances populated (40-50 Å in some cases), suggest that perhaps some helices have lost close packing entirely in the MG state due to solvent insertion between native hydrophobic contacts (63).

4.5 Conclusions

Hydrostatic pressure is expected to access protein excited states of higher configurational entropy than the ground state. NMR and CW SDSL EPR spectroscopy can identify sites undergoing conformational fluctuations in proteins under pressure and identify a time scale, but they do not provide a length scale for the motion or resolve the individual members in an ensemble. The results presented here establish the feasibility of kinetically trapping high-pressure conformational equilibria of spin-labeled proteins for analysis by conventional DEER instrumentation operated at atmospheric pressure. High-pressure EPR sample cells are not required, and pressures of 6.2 kbar can be explored with PR DEER using standard high-pressure equipment. The important feature of PR DEER is that the distance distributions directly reveal the structural heterogeneity of the excited states populated by pressure and provide a length scale for structural fluctuations. The initial results from application to the pressure-populated MG of apoMb both serve to validate the methodology and reveal fluctuations of helices or segments thereof with amplitudes as large as 25 Å. Although the data set presented is sparse and the model of Figure 4.5 highly schematic, systematic application of the method with judiciously selected

spin pairs can increase the resolution. The method should be general, and serve to map structure and structural heterogeneity in pressure-populated excited states in proteins of any degree of complexity, including membrane proteins.

4.6 Methods

4.6.1 Mb preparation. The plasmid pET17b (EMD Millipore) containing WT sperm whale Mb gene was generously provided by Steven Boxer (Stanford University). Double cysteine mutants were generated in the WT background using the QuickChange Method (Agilent) and confirmed by DNA sequencing. Four of the seven mutants reported here are previously published (H12C/N132C, R31C/T70C, R31C/K87C, and A57C/N132C) (11). The mutant plasmids were transformed into and expressed in *E. coli* BL21(DE3) cells, then purified from inclusion bodies, spin-labeled with (1-oxyl-2,2,5,5-tetramethylpyrroline-3-methyl) methanethiosulfonate (MTSL) reagent, gel-filtered (apoMb), and heme-reconstituted (holoMb) as previously described (11). Samples spin-labeled with 3-(2-iodoacetamido)-proxyl (Sigma) instead of MTSL were prepared according to the same protocol. The samples were concentrated to ≈250 μM for apoMb or ≈360 μM for holoMb and switched into a buffer containing 20 mM MES, pH 6.0 using Amicon ultra concentrators (10 kDa MWCO; Millipore) for DEER experiments. The pH-populated MG state was prepared by switching the apomygoglobin into a buffer containing 10 mM sodium acetate, pH 4.1, using Amicon ultra concentrators. Protein concentration was measured via absorption spectroscopy at 280 nm (ε_{280} = 15,400 $L*mol^{-1}*cm^{-1}$) for apoMb and 409 nm (ε_{409} = 157,000 $L*mol^{-1}*cm^{-1}$) for holoMb. Finally, glycerol was added to a final concentration of 25% vol/vol just prior to DEER studies. The typical volume of DEER samples was 12-16 μL.

4.6.2 Pressurization and freezing of DEER samples. Silicone pistons were made using a two-part encapsulant (Sylgard 184, Dow Corning), prepared according to manufacturer's instructions and allowed to cure inside clean quartz capillaries (1.4 mm ID X 1.7 mm OD, VitroCom Inc.). The capillaries were broken open to release the silicone after curing, which was then cut into ≈3 mm long pistons. PR DEER samples were loaded into the same size capillary tube as that used for silicone piston preparation. A silicone piston was loaded into the capillary and pushed into place just above the sample, minimizing air bubbles between the sample and the piston. Ethanol was used to wash the inside of the capillary above the piston, and then fresh ethanol was used to fill the capillary. A custom-built magnetic collar (416 stainless steel) was glued onto the outside of the capillary near the top end to allow external control of the sample position within the pressure bomb using a neodymium-iron-boron ring magnet on the outside of the bomb. The loaded capillary was sealed inside a pressure bomb (60-HM6-12, High Pressure Equipment Company) connected to a pressure intensifier (HUB440, Pressure BioSciences Inc.). The pressurization fluid inside the bomb was ethanol, while water was used in the rest of the high-pressure system.

The sample capillary was positioned at the top of the bomb using the magnet. The bottom portion of the bomb was submerged in a dry ice/ethanol bath for 2 min to cool the lower half of the bomb and pressurization fluid to 200 K, while the upper half of the bomb was maintained at room temperature using a heat gun (the temperature setting and placement of the heat gun was calibrated using a mock setup of the pressure bomb and cooling bath, with a thermocouple in place of the capillary). The bomb was pressurized, and the sample was allowed to equilibrate for 30 s prior to freezing. The sample was rapidly moved to the cooled portion of the pressure bomb

using the magnet. After 30 s, the bomb was depressurized, disconnected from the pressure intensifier, and fully submerged in the dry ice/ethanol bath for 2 min.

The capillary was removed from the pressure bomb, and the portion of the capillary containing the sample was kept immersed in the dry ice/ethanol bath while the ethanol above the piston was removed with a syringe. The capillary was removed from the dry ice ethanol bath, and immediately submerged in liquid nitrogen to cool the sample from 200 K to 77 K. Finally, the magnetic collar was cut and the sample tube was loaded into the resonator for data acquisition.

4.6.3 Q-band DEER. DEER measurements were performed on a Bruker ELEXSYS 580 spectrometer equipped with a SuperQFT Q-band bridge and a 10W AmpQ Q-band amplifier. An ER 5107 D 2 Q-Band resonator (Bruker Biospin) was used for all data acquisition. The cryostat temperature was maintained at 80 K using liquid nitrogen and Oxford ITC503S temperature controller (Oxford Instruments). The standard 4-pulse DEER sequence: $(\pi/2)_{\upsilon,obs}$ - τ_1 - $(\pi)_{\upsilon,obs}$ - T - $(\pi)_{\upsilon,pump}$ - τ_2 - $(\pi)_{\upsilon,obs}$ – τ_2 - echo, where υ,obs and υ,pump indicate the observe and the pump frequency, respectively, was used. The pulse durations of the $(\pi/2)_{\upsilon,obs}$, $(\pi)_{\upsilon,obs}$, and $(\pi)_{\upsilon,pump}$ pulses were 16 ns, 32 ns, and 36 ns, respectively. The τ_1 was selected to be 200 ns, while τ_2 varies from 2 to 3.2 μs depending on the sample with a constant step size of 16 ns. Interval T was set to 100 ns in order to collect a dead-time free DEER trace. A two-step phase cycling (+x, -x) was carried out on the first ($\pi/2$) pulse. The microwave frequency for all measurements was in the range of 33.4-33.8 GHz, depending on coupling conditions. The pump pulse frequency was always adjusted to be consistent with the maximum peak of the Q-band absorption spectrum of the nitroxide labels, and the observe pulses were always applied at ≈50 MHz lower than the pump frequency. Typical signal acquisition time was 30-60 minutes

depending on sample concentration. All DEER data were analyzed using the program LongDistances, written in LabVIEW and available at www.chemistry.ucla.edu/directory/hubbell-wayne-l.

4.7 Appendix

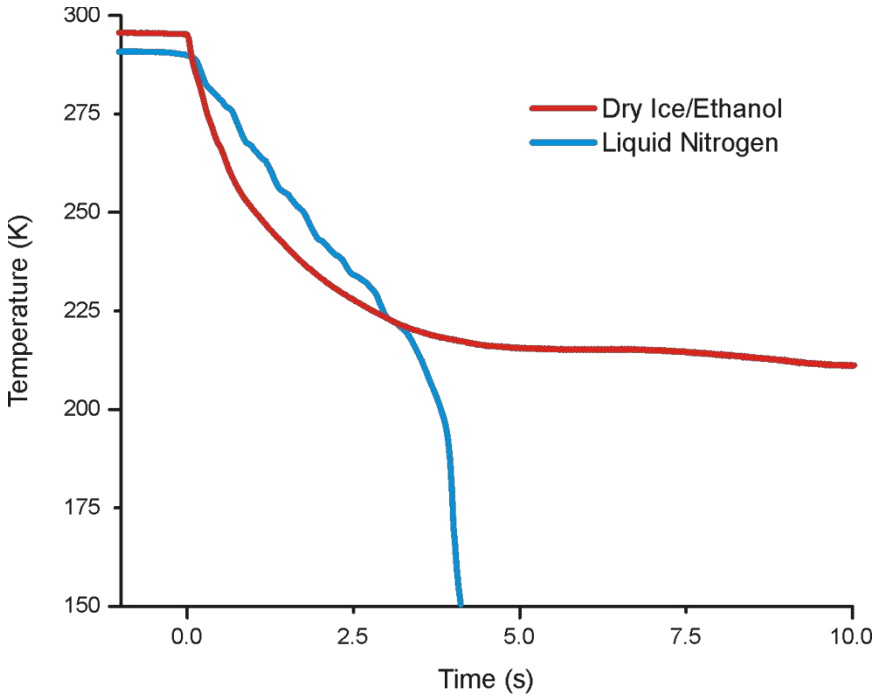

Figure 4.A1 Freezing rates in dry ice/ethanol and liquid nitrogen. A borosilicate DEER capillary was loaded with ≈20 μL 25% vol/vol glycerol in water, and a silicone piston was placed above the solution. A thermocouple (Omega COCO-001) with ≈2 ms response time was used to monitor the temperature of the solution as the capillary was frozen in dry ice/ethanol or liquid nitrogen. For the dry ice/ethanol test, the pressure bomb was filled with ethanol and pre-cooled in the dry ice bath, and the capillary was plunged into the cooled bomb exactly as in the PR DEER experiments reported in this dissertation. The initial temperature in the dry ice/ethanol test was 295 K, while the initial temperature in the liquid nitrogen test was 290 K. Upon plunging the capillary into the cooling baths, dry ice/ethanol has a faster cooling rate. To 273 K, dry ice takes ≈300 ms and liquid nitrogen takes ≈700 ms. A crossover occurs at 223 K at ≈3 seconds; after this time, liquid nitrogen cools the sample to a lower temperature at equivalent time points. The temperature in the dry ice/ethanol test stabilizes after ≈16 seconds at 208 K, according to the thermocouple reading. The thermocouple accuracy is limited at low temperature, and it is assumed that the true final temperature is that known for dry ice/ethanol at atmospheric pressure, 200 K.

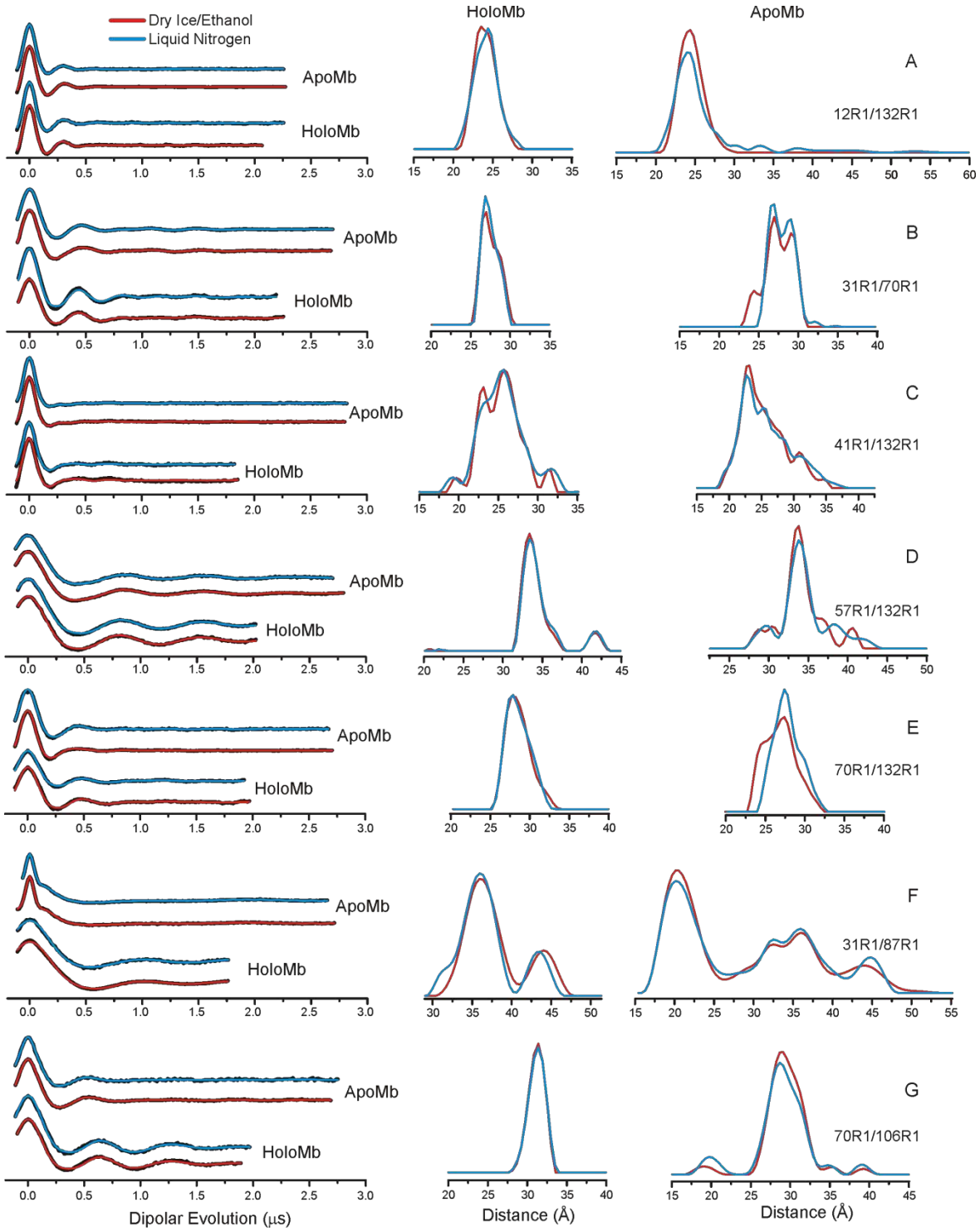

Figure 4.A2 DEER distance distributions for native apoMb and holoMb at 0 bar, pH 6, generated from samples prepared using dry ice/ethanol and liquid nitrogen. Background-corrected dipolar evolutions of the indicated mutants are shown in the left-hand column in black, with fits to the data (section **4.6**) color coded according to freezing method used. The area-normalized distance distributions are shown at the center (holoMb) and right (apoMb) for (A) 12R1/132R1, (B) 31R1/70R1, (C) 41R1/132R1, (D) 57R1/132R1, (E)70R1/132R1, (F) 31R1/87R1, and (G) 70R1/106R1. An inset indicates the color-coding of the distance distributions and fits to the dipolar evolutions. Dipolar evolutions are vertically offset for clarity.

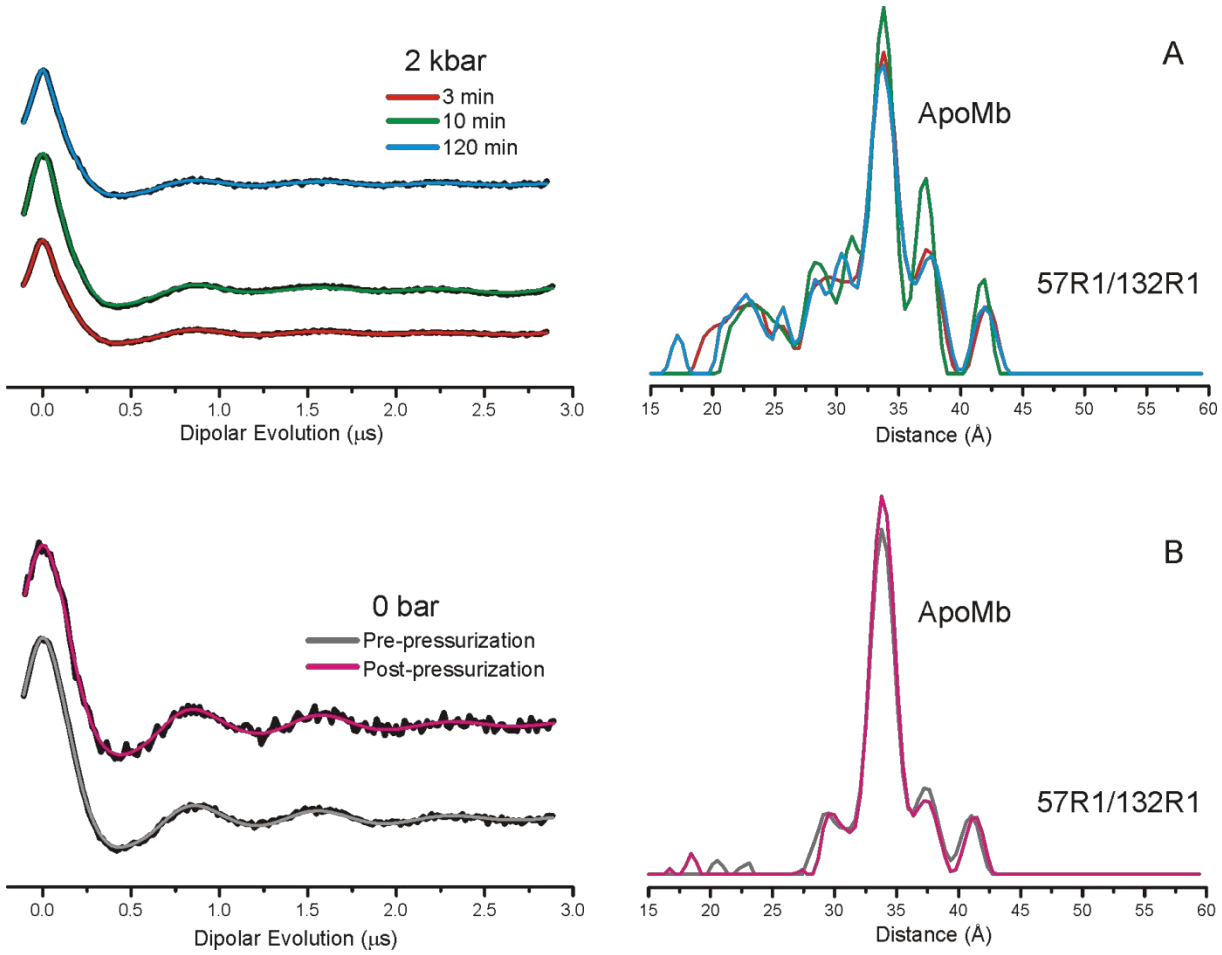

Figure 4.A3 Reversibility of pressure-populated changes in apoMb and evaluation of conformational relaxation at 200 K. Background-corrected dipolar evolutions are shown to the left in black, with fits to the data (section **4.6**) color coded as indicated by an inset. The area-normalized distance distributions are shown to the right for apoMb 57R1/132R1 in (A) the pressure-populated MG at 2 kbar, pH 6, for samples held at 200 K for variable time after depressurization of the frozen sample, prior to further cooling in liquid nitrogen to 77 K for data acquisition, and (B) the native state at 0 bar, pH 6, pre- and post-pressurization to 2 kbar. Dipolar evolutions are vertically offset for clarity. An inset indicates the color-coding of the dipolar evolutions and fits to the data for each panel.

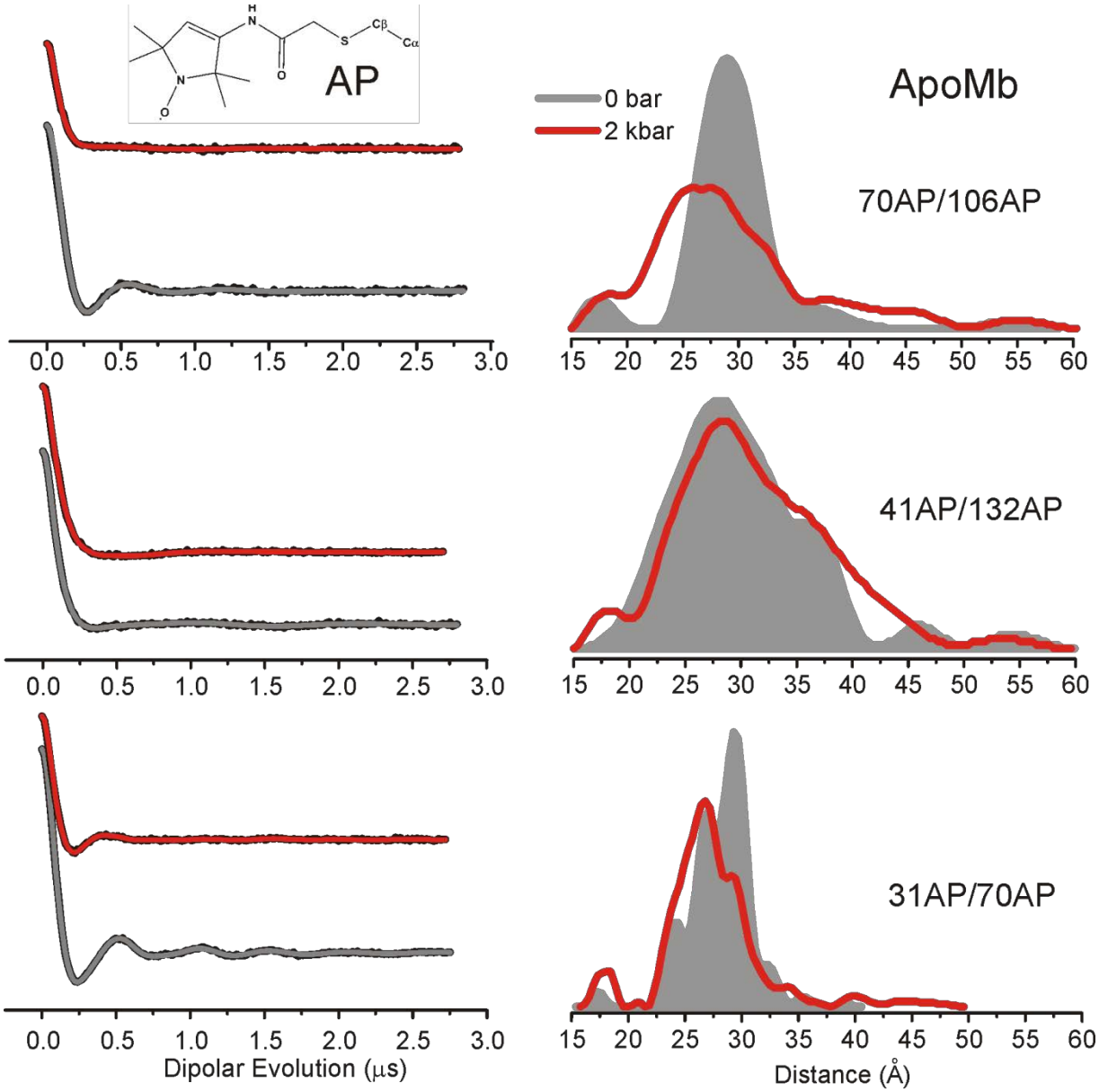

Figure 4.A4 PR DEER distance distributions for apoMb at pH 6 labeled with AP. Background-corrected dipolar evolutions are shown in the left-hand column in black, with fits to the data (section **4.6**) overlaid and color coded by pressure. The area-normalized distance distributions are shown in the right-hand column for 70AP/109AP (top panel), 41AP/132AP (middle panel), and 31AP/70AP (lower panel). Insets indicate the color-coding of the distance distributions and fits to the dipolar evolutions, and the structure of the AP side chain. Dipolar evolutions are vertically offset for clarity.

4.8 References

1. Akasaka K, Kitahara R, & Kamatari YO (2013) Exploring the folding energy landscape with pressure. *Arch Biochem Biophys* 531(1-2):110-115.
2. Fourme R, Girard E, & Akasaka K (2012) High-pressure macromolecular crystallography and NMR: status, achievements and prospects. *Curr Opin Struct Biol* 22(5):636-642.
3. Leopold PE, Montal M, & Onuchic JN (1992) Protein Folding Funnels - a Kinetic Approach to the Sequence Structure Relationship. *Proceedings of the National Academy of Sciences of the United States of America* 89(18):8721-8725.
4. Onuchic JN, Luthey-Schulten Z, & Wolynes PG (1997) Theory of protein folding: the energy landscape perspective. *Annu Rev Phys Chem* 48:545-600.
5. Henzler-Wildman K & Kern D (2007) Dynamic personalities of proteins. *Nature* 450(7172):964-972.
6. Frauenfelder H, Sligar SG, & Wolynes PG (1991) The energy landscapes and motions of proteins. *Science* 254(5038):1598-1603.
7. Akasaka K (2006) Probing conformational fluctuation of proteins by pressure perturbation. *Chem Rev* 106(5):1814-1835.
8. Kitahara R, Hata K, Li H, Williamson MP, & Akasaka K (2013) Pressure-induced chemical shifts as probes for conformational fluctuations in proteins. *Prog Nucl Magn Reson Spectrosc* 71(0):35-58.
9. Kitahara R, Yamada H, Akasaka K, & Wright PE (2002) High pressure NMR reveals that apomyoglobin is an equilibrium mixture from the native to the unfolded. *J Mol Biol* 320(2):311-319.

10. Bridges MD, Hideg K, & Hubbell WL (2010) Resolving conformational and rotameric exchange in spin-labeled proteins using saturation recovery EPR. *Appl Magn Reson* 37(1-4):363.

11. López CJ, Oga S, & Hubbell WL (2012) Mapping molecular flexibility of proteins with site-directed spin labeling: a case study of myoglobin. *Biochemistry* 51(33):6568-6583.

12. Milov AD, Ponomarev AB, & Tsvetkov YD (1984) Electron-electron double resonance in electron spin echo: model biradical systems and the sensitized photolysis of decalin. *Chem Phys Lett* 110(1):67-72.

13. Pannier M, Veit S, Godt A, Jeschke G, & Spiess HW (2000) Dead-time free measurement of dipole-dipole interactions between electron spins. *J Magn Reson* 142(2):331-340.

14. Mchaourab HS, Steed PR, & Kazmier K (2011) Toward the fourth dimension of membrane protein structure: insight into dynamics from spin-labeling EPR spectroscopy. *Structure* 19(11):1549-1561.

15. Jeschke G (2012) DEER distance measurements on proteins. *Annu Rev Phys Chem* 63:419-446.

16. Yang Z, *et al.* (2012) Pulsed ESR dipolar spectroscopy for distance measurements in immobilized spin labeled proteins in liquid solution. *J Amer Chem Soc* 134(24):9950-9952.

17. Eliezer D, Jennings PA, Dyson HJ, & Wright PE (1997) Populating the equilibrium molten globule state of apomyoglobin under conditions suitable for structural characterization by NMR. *FEBS Lett* 417(1):92-96.

18. Jennings PA & Wright PE (1993) Formation of a molten globule intermediate early in the kinetic folding pathway of apomyoglobin. *Science* 262(5135):892-896.

19. Meinhold DW & Wright PE (2011) Measurement of protein unfolding/refolding kinetics and structural characterization of hidden intermediates by NMR relaxation dispersion. *Proc Natl Acad Sci USA* 108(22):9078-9083.

20. Eliezer D, Yao J, Dyson HJ, & Wright PE (1998) Structural and dynamic characterization of partially folded states of apomyoglobin and implications for protein folding. *Nat Struct Biol* 5(2):148-155.

21. Brucker EA, Olson JS, Phillips GN, Jr., Dou Y, & Ikeda-Saito M (1996) High resolution crystal structures of the deoxy, oxy, and aquomet forms of cobalt myoglobin. *J Biol Chem* 271(41):25419-25422.

22. Georgieva ER, *et al.* (2012) Effect of freezing conditions on distances and their distributions derived from double electron electron resonance (DEER): a study of doubly-spin-labeled T4 lysozyme. *J Magn Reson* 216(0):69-77.

23. de Vera IMS, Blackburn ME, Galiano L, & Fanucci GE (2013) Pulsed EPR distance measurements in soluble proteins by site-directed spin labeling (SDSL). *Curr Protoc Protein Sci* 74:17.17.1-17.17.29.

24. Altenbach C, Kusnetzow AK, Ernst OP, Hofmann KP, & Hubbell WL (2008) High-resolution distance mapping in rhodopsin reveals the pattern of helix movement due to activation. *Proc Natl Acad Sci USA* 105(21):7439-7444.

25. Dawidowski D & Cafiso DS (2013) Allosteric control of syntaxin 1a by munc18-1: characterization of the open and closed conformations of syntaxin. *Biophys J* 104(7):1585-1594.

26. de Vera IMS, *et al.* (2013) Elucidating a relationship between conformational sampling and drug resistance in HIV-1 protease. *Biochemistry* 52(19):3278-3288.

27. Dockter C, *et al.* (2012) Rigid core and flexible terminus: structure of solubilized light-harvesting chlorophyll a/b complex (LHCII) measured by epr. *J Biol Chem* 287(4):2915-2925.

28. Georgieva ER, Borbat PP, Ginter C, Freed JH, & Boudker O (2013) Conformational ensemble of the sodium-coupled aspartate transporter. *Nat Struct Mol Biol* 20(2):215-221.

29. Krishnamani V, Hegde BG, Langen R, & Lanyi JK (2012) Secondary and tertiary structure of bacteriorhodopsin in the SDS denatured state. *Biochemistry* 51(6):1051-1060.

30. Sattig T, Rickert C, Bamberg E, Steinhoff HJ, & Bamann C (2013) Light-induced movement of the transmembrane helix B in channelrhodopsin-2. *Angew Chem, Int Ed* 52(37):9705-9708.

31. Van Eps N, *et al.* (2011) Interaction of a G protein with an activated receptor opens the interdomain interface in the alpha subunit. *Proc Natl Acad Sci USA* 108(23):9420-9424.

32. González JAT, Longinotti MP, & Corti HR (2011) The viscosity of glycerol-water mixtures including the supercooled region. *J Chem Eng Data* 56(4):1397-1406.

33. Uzawa T, *et al.* (2008) Hierarchical folding mechanism of apomyoglobin revealed by ultra-fast H/D exchange coupled with 2D NMR. *Proc Natl Acad Sci USA* 105(37):13859-13864.

34. López CJ, Yang Z, Altenbach C, & Hubbell WL (2013) Conformational selection and adaptation to ligand binding in T4 lysozyme cavity mutants. *Proc Natl Acad Sci USA* 110(46):E4306-E4315.

35. Morris GJ, Goodrich M, Acton E, & Fonseca F (2006) The high viscosity encountered during freezing in glycerol solutions: effects on cryopreservation. *Cryobiology* 52(3):323-334.

36. Raitsimring AM, Salikhov KM, Umanskii BA, & Tsvetkov YD (1974) Instantaneous diffusion in electron-spin echo of paramagnetic centers stabilized in solid matrices. *Fizika Tverdogo Tela* 16(3):756-766.

37. Ruthstein S, *et al.* (2009) Distribution of guest molecules in pluronic micelles studied by double electron electron spin resonance and small angle X-ray scattering. *Phys Chem Chem Phys* 11(1):148-160.

38. Kramers HA (1940) Brownian motion in a field of force and the diffusion model of chemical reactions. *Physica* 7(4):284-304.

39. Ramos CH, Weisbuch S, & Jamin M (2007) Diffusive motions control the folding and unfolding kinetics of the apomyoglobin pH 4 molten globule intermediate. *Biochemistry* 46(14):4379-4389.

40. Nienhaus GU, Muller JD, McMahon BH, & Frauenfelder H (1997) Exploring the conformational energy landscape of proteins. *Physica D* 107(2-4):297-311.

41. Romero-Romero ML, Inglés-Prieto A, Ibarra-Molero B, & Sanchez-Ruiz JM (2011) Highly anomalous energetics of protein cold denaturation linked to folding-unfolding kinetics. *PloS ONE* 6(7): e23050.

42. Cho KC & Chan KK (1984) Kinetics of cold-induced denaturation of metmyoglobin. *Biochim Biophys Acta* 786(1-2):103-108.

43. Chen BL, Baase WA, & Schellman JA (1989) Low-temperature unfolding of a mutant of phage-T4 lysozyme. 2. Kinetic investigations. *Biochemistry* 28(2):691-699.

44. Gekko K & Timasheff SN (1981) Mechanism of protein stabilization by glycerol - preferential hydration in glycerol-water mixtures. *Biochemistry* 20(16):4667-4676.

45. Saunders AJ, Davis-Searles PR, Allen DL, Pielak GJ, & Erie DA (2000) Osmolyte-induced changes in protein conformation equilibria. *Biopolymers* 53(4):293-307.

46. Jiménez RHF, Do Cao MA, Kim M, & Cafiso DS (2010) Osmolytes modulate conformational exchange in solvent-exposed regions of membrane proteins. *Protein Sci* 19(2):269-278.

47. Lee JC & Timasheff SN (1981) The stabilization of proteins by sucrose. *J Biol Chem* 256(14):7193-7201.

48. López CJ, Fleissner MR, Guo ZF, Kusnetzow AK, & Hubbell WL (2009) Osmolyte perturbation reveals conformational equilibria in spin-labeled proteins. *Protein Sci* 18(8):1637-1652.

49. Auton M, Rosgen J, Sinev M, Holthauzen LMF, & Bolen DW (2011) Osmolyte effects on protein stability and solubility: a balancing act between backbone and side-chains. *Biophys Chem* 159(1):90-99.

50. Street TO, Bolen DW, & Rose GD (2006) A molecular mechanism for osmolyte-induced protein stability. *Proc Natl Acad Sci USA* 103(45):17064-17064.

51. Silvers TR & Myers JK (2013) Osmolyte effects on the self-association of concanavalin A: testing theoretical models. *Biochemistry* 52(51):9367-9374.

52. Zipp A & Kauzmann W (1973) Pressure denaturation of metmyoglobin. *Biochemistry* 12(21):4217-4228.

53. Phillips GN, Jr. (1990) Comparison of the dynamics of myoglobin in different crystal forms. *Biophys J* 57(2):381-383.

54. Frauenfelder H, *et al.* (1987) Thermal expansion of a protein. *Biochemistry* 26(1):254-261.

55. Baldwin RL & Rose GD (2013) Molten globules, entropy-driven conformational change and protein folding. *Curr Opin Struct Biol* 23(1):4-10.

56. Eliezer D & Wright PE (1996) Is apomyoglobin a molten globule? Structural characterization by NMR. *J Mol Biol* 263(4):531-538.

57. Lecomte JTJ, Sukits SF, Bhattacharya S, & Falzone CJ (1999) Conformational properties of native sperm whale apomyoglobin in solution. *Protein Sci* 8(7):1484-1491.

58. Yao J, Chung J, Eliezer D, Wright PE, & Dyson HJ (2001) NMR structural and dynamic characterization of the acid-unfolded state of apomyoglobin provides insights into the early events in protein folding. *Biochemistry* 40(12):3561-3571.

59. Kamatari YO, Smith LJ, Dobson CM, & Akasaka K (2011) Cavity hydration as a gateway to unfolding: an NMR study of hen lysozyme at high pressure and low temperature. *Biophys Chem* 156(1):24-30.

60. Roche J, *et al.* (2012) Cavities determine the pressure unfolding of proteins. *Proc Natl Acad Sci USA* 109(18):6945-6950.

61. Neumaier S, Buttner M, Bachmann A, & Kiefhaber T (2013) Transition state and ground state properties of the helix-coil transition in peptides deduced from high-pressure studies. *Proc Natl Acad Sci USA* 110(52):20988-20993.

62. Imamura H & Kato M (2009) Effect of pressure on helix-coil transition of an alanine-based peptide: an FTIR study. *Proteins: Struct, Funct, Bioinfor* 75(4):911-918.

63. Hummer G, Garde S, Garcia AE, Paulaitis ME, & Pratt LR (1998) The pressure dependence of hydrophobic interactions is consistent with the observed pressure denaturation of proteins. *Proc Natl Acad Sci USA* 95(4):1552-1555.

Chapter 5: A structure-relaxation mechanism for the response of T4 lysozyme cavity mutants to hydrostatic pressure

5.1 Summary

High pressure has emerged as a powerful tool for exploring the energy landscape of proteins, but structural origins of the pressure response remain controversial. A current view is that the volume reduction at high pressure is dominated by elimination of voids or cavities in the protein interior *via* cavity hydration, although an alternative mechanism wherein cavities are filled with protein side chains resulting from a structure relaxation has been suggested (1). In this chapter, mechanisms for elimination of cavities under high pressure are investigated in the L99A cavity mutant of T4 lysozyme and derivatives thereof using site-directed spin labeling together with variable-pressure electron paramagnetic resonance and pressure-resolved double electron-electron resonance, as well as high-pressure circular dichroism spectroscopy. In the L99A mutant, the ground state is in equilibrium with an excited state of only ≈3% of the population in which the cavity is filled by a protein side chain (2). Here, the results show that in L99A the native ground state is the dominant conformation to pressures of 3 kbar, with cavity hydration apparently taking place in the range of 2-3 kbar. However, in the presence of additional mutations which lower the free energy of the excited state, pressure strongly populates the excited state thereby eliminating the cavity with a native side chain rather than solvent. Thus, both cavity hydration and structure-relaxation are mechanisms for cavity elimination under pressure, and which is dominant is determined by details of the energy landscape. Importantly, the results highlight the capability of the instrumentation and methodologies introduced in this dissertation to explore the structural and dynamical features of the protein conformational ensemble under pressure.

5.2 Introduction

Pressure shifts equilibria in a direction to reduce the total volume of the system. The current view is that the volume reduction that accompanies pressure-modulated transitions in proteins, including formation of the denatured state, is dominated by the elimination of voids or cavities in protein interior (3-7) *via* hydration, although other factors contribute (8-12). For many proteins the “pressure-denatured” state this state retains a relatively compact fold, at least near neutral pH and in the absence of denaturants, and is thus distinct from the unfolded states produced thermally or by chemical denaturants wherein both secondary and tertiary structure are largely lost (3, 8, 13-17). The pressure-denatured state is often labeled as “unfolded state” (18), but here the term “unfolded” is reserved to describe a state with little tertiary or secondary structure.

In the present communication attention is focused on moderate pressures (<4 kbar) that shift conformational equilibria rather than leading to a pressure-denatured state. In the equilibrium between two folded conformations, ground state (**G)** ↔ excited state **(E)** for example, an alternative "structure-relaxation" mechanism may play a role in the pressure response. In this model, voids are eliminated by pressure due to an increase in the population of an alternative packing arrangement of the core in which cavities are filled with native side chains rather than solvent. This model has been suggested to play a role in certain proteins at high pressure (1, 19, 20), although to the author’s knowledge direct observation of structure relaxation under pressure has not been reported.

That a structure-relaxation mechanism may play a role in the pressure response is suggested by recent studies of cavity-creating mutants in T4 lysozyme (T4L) at atmospheric pressure (1). Although the crystal structures of the cavity mutants are nearly identical to those of the WT protein (21-24), in solution there are multiple conformations in equilibrium (1, 25). For

example, in the T4L cavity mutants L121A/L133A, L133G, and W138A, two conformations of similar free energy were identified in solution (1). Perhaps the most extensively investigated cavity-forming mutation is T4L L99A that enlarges a pre-existing cavity in the rigid four helix bundle of the protein. In this mutant, a minor conformation (**E**) in equilibrium with the ground state (**G**) was detected that accounted for ≈3% of the population (25, 26). Remarkably, in each of the above cavity-creating mutants, one member of the conformational ensemble corresponds to a structural rearrangement that fills the cavity with a side chain; for L99A it is Phe114 that occupies the engineered cavity (2). Such conformations in which cavities are absent or reduced are expected to have a lower molar volume, and thus may be populated by pressure.

The pressure dependence of the L99A mutant was recently studied with NMR methods by Nucci et al. (11) and independently by Maeno et al. (20). In the study of Maeno et al. (20), the disappearance of cross-peaks in a ^{1}H-^{13}C HSQC NMR experiment at pressures up to 3 kbar was interpreted to reflect an increase in population of the **E** conformation with Phe114 occupying the cavity, consistent with a structure-relaxation mechanism rather than cavity hydration or unfolding. However, based on ^{1}H-^{15}N HSQC NMR studies on the same protein, Nucci et al. (11) concluded that cavity hydration and unfolding occurred at pressures less than 2.5 kbar rather than populating the **E** conformation. Commentaries on these conflicting interpretations were recently published (27, 28).

In this chapter, the pressure dependence of T4L WT*, L99A, and L99A containing the additional mutations G113A and G113A/R119P is investigated. Both G113A and G113A/R119P have been shown to lower the free energy of the **E** conformation and hence increase the equilibrium population (2). The experimental approach is based on site-directed spin labeling EPR (SDSL EPR) and the technologies of high-pressure continuous wave (CW) EPR

spectroscopy for SDSL (29), pressure-resolved double electron-electron resonance (PR DEER) spectroscopy, and high-pressure circular dichroism (HP CD), described in the preceding chapters.

The results reported below indicate that at pressures up to 2.4 kbar the secondary structure content of T4L L99A is unchanged, eliminating the possibility of global or sub-global unfolding of the helical C domain, in agreement with the results of Maeno et al. (20). Collectively, the data do not support a large-scale shift to the **E** conformation of T4L L99A under high pressure, but rather cavity hydration and finally transition to a partially disordered state at pressures of 4 kbar. On the other hand, pressure strongly shifts the **G** ↔ **E** equilibrium towards **E** in the presence of the additional G113A and R119P mutations that lower the energy of the **E** conformation, thus demonstrating a structure-relaxation mechanism for the pressure response. Moreover, ligand binding to the engineered cavity strongly stabilizes the **G** conformation. Taken together, the results show that both cavity hydration and structure relaxation are valid models for the pressure dependence in proteins, and which prevails depends on the details of the energy landscape.

5.3 Results

5.3.1 Experimental strategy. An objective of this study is to monitor the structure and dynamics of T4L cavity mutants under pressure using SDSL EPR methods, and to determine whether the **E** conformation is populated as opposed to local or global unfolding. The structure of the **E** state of T4L L99A at atmospheric pressure and pH 5.5 determined by NMR and Rosetta modeling is shown in Figure 5.1 where it is compared with the WT*, or **G** state (2).

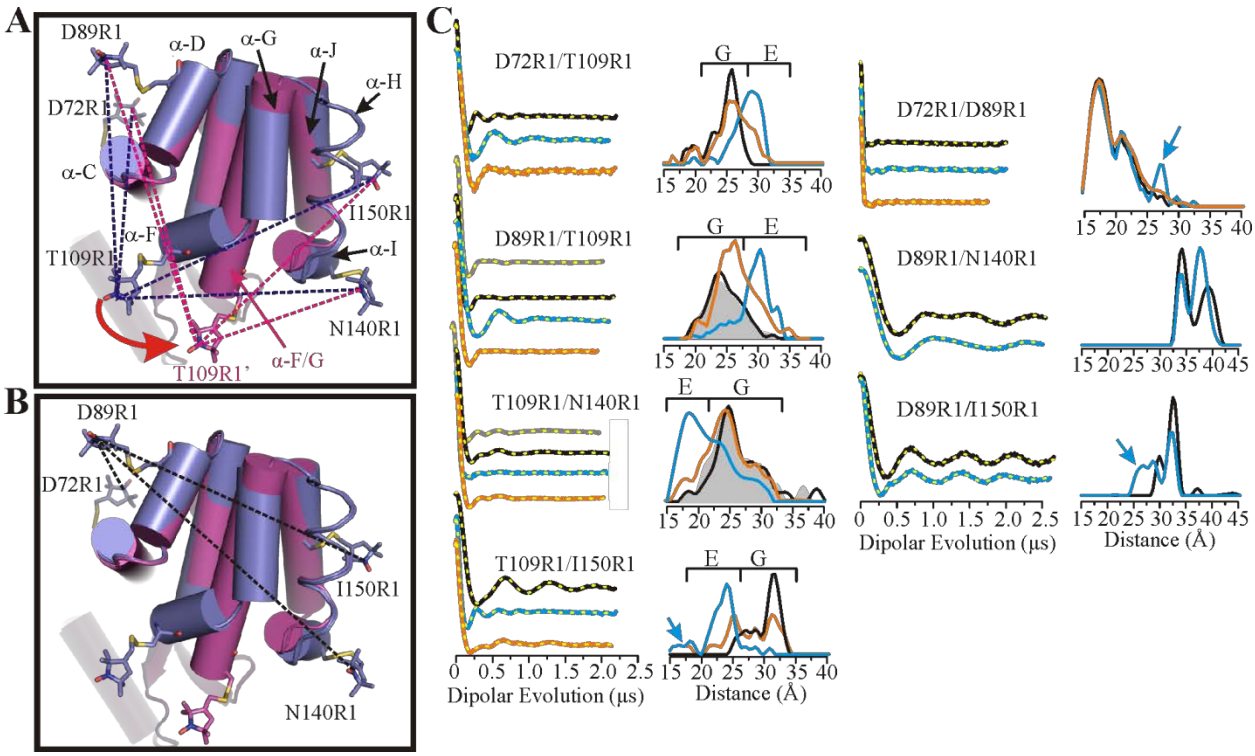

Figure 5.1 Distance mapping of the **G** and **E** conformations at atmospheric pressure and pH 5.5 with DEER spectroscopy. (A) An overlay in cylinder representation of the **G** (PDB ID code 3DMV (30)) and **E** (PDB ID code 2LC9 (2)**)** conformations of L99A in blue and magenta, respectively. Models of the R1 side chain are shown in stick representation; helix H is rendered in ribbon form to show the I150R1 side chain and its parent helix J. The direction of movemnt of helix F in the **G→E** structural transition is indicated by a red arrow. The dashed lines show the distances measured involving residue T109R1 with respect to an R1 reference for the G state (blue) and **E** state (magenta). (B) Cylinder diagram showing the interspin distances measured between the indicated reference sites in the **G** and **E** conformations. (C) DEFs, model-free fits of the DEFs (dashed yellow traces), and corresponding distance distributions for the indicated spin-labeled mutants in the WT* (black), L99A (gray), and L99A/G113A/R119P (blue) backgrounds in buffer consisting of 50 mM phosphate, 25 mM NaCl, 20% vol/vol glycerol at pH 5.5. The DEFs and distance distributions after addition of benzene to mutants in the L99A/G113A/R119P background are shown in orange. The blue arrows identify distances only observed in the E conformation. The range of distances corresponding to the **G** and **E** conformations are indicated by brackets above the distributions.

In the context of these models, the major structural rearrangement in the **G** to **E** transition involves dramatic rigid body motions of helices F and G to form a single helix, with only minor changes elsewhere in the structure. The motion of helices F and G place Phe114 in the cavity created by the L99A mutation. An R1 nitroxide side chain (31, 32) placed at position 109 in helix F (T109R1) is well-suited to monitor changes in the position of the F helix, and hence to identify the **E** conformation. For example, the change in environment that accompanies helix F

movement would in general lead to changes in the mobility of T109R1, and hence the EPR spectral line shape. More importantly, T109R1 would move toward helices I and J, but further from helices C and D. These changes can be monitored experimentally using DEER spectroscopy to measure the distance between T109R1 and a second R1 residue placed at a reference site in a helix that shows comparably little or no movement. For this purpose, residues D72R1 (helix C), D89R1 (helix D), N140R1 (helix I), and I150R1 (helix J) were selected (Figure 5.1A and 1B). Residues D72R1, D89R1, and I150R1 are in helices for which NMR showed essentially no change in structure between **G** and **E**; residue N140R1 in helix I is displaced in **E** relative to **G**, but the magnitude is relatively small (≈2 Å) compared to that involving helix F. Thus, these sites are suitable for monitoring the position of T109R1 in the structure and consequently for identifying the **E** conformation. This simple strategy assumes the veracity of the NMR-based model of **E**, an assumption that can be checked by a quantitative comparison between measured and modeled distances, including distances between the references themselves, which should remain relatively constant independent of the position of T109R1.

To evaluate these ideas, and confirm the structure of the **E** conformation, the additional mutants G113A and G113A/R119P are employed in the L99A background. These mutations were shown to strongly shift the **G** ↔ **E** equilibrium toward **E**, resulting in large equilibrium populations of **E** (34% and 96% respectively, at 274 K)(2). Thus, these additional mutations enable a direct characterization of the **E** conformation at atmospheric pressure using SDSL technology. Armed with SDSL-based metrics for identifying the **E** conformation, it is then possible to ask whether or not this conformation is populated by pressure in L99A, and to study the pressure dependence of the **G** ↔ **E** equilibrium in the G113A and G113A/R119P variants.

The results, described below, provide new insight into mechanisms regarding the response of proteins to pressure.

5.3.2 Characterization of the G and E states of T4 lysozyme with SDSL. To quantitatively characterize the **G** and **E** conformations at atmospheric pressure, interspin distance distributions were measured between seven pairs of R1 residues in the WT*, L99A, and/or L99A/G113A/R119P backgrounds using DEER spectroscopy. Additionally, one of the pairs was also engineered in the L99A/G113A background. Four of the R1 pairs measure interspin distances between residue T109R1 in helix F and a reference at D72R1, D89R1, N140R1, or I150R1 (Figure 5.1A), while three pairs measure distances between the reference sites themselves (Figure 5.1B).

Figure 5.1C (left panel) shows the dipolar evolution functions (DEFs), the model free fits to the DEFs, and the corresponding distance distributions for T109R1 paired with each of the reference R1 residues in the WT*, L99A, and L99A/G113A/R119P backgrounds. The distance measurements in the WT* background provide a means for assigning distances corresponding to the pure **G** state for each spin pair. The distance distributions in the WT* and L99A backgrounds are nearly identical for the sites investigated, as expected due to the low population of the **E** state in the L99A background. Addition of the G113A/R119P mutations drives the **G** ↔ **E** equilibrium strongly towards the **E** state; therefore the distances corresponding to the **E** state for each spin pair may be easily identified in the L99A/G113A/R119P background. Indeed, changes in the most probable distance are observed for all pairs involving residue T109R1 in L99A/G113A/R119P relative to WT* and/or L99A (Figure 5.1C). Distributions for these pairs reveal that in the **E** state, residue T109R1 moves away from residues D72R1 and D89R1, and closer to N140R1 and I150R1. The direction and magnitude of changes are in reasonable

agreement with the rotation and translation of helix F reported by NMR for the **G** to **E** transition (Table 5.A1). The T109R1/I150R1 pair that measures the position of helix F relative to J was also engineered in the L99A/G113A background. Compared to the same pair in L99A/G113A/R119P, the population of the **G** conformation is substantially increased, further demonstrating qualitative consistency with NMR relaxation dispersion measurements (Figure 5.A1A) (2). Interestingly, for the T109R1/I150R1 pair in the L99A/G113A/R119P and L99A/G113A backgrounds, there is a minor population at ≈18 Å that does not correspond to the **G** or **E** states (Figure 5.1C, 5.A1A). The possible origins of this minor population will be discussed below.

Previous DEER studies have shown that analysis of complex distance distributions using a multiple-Gaussian model provides a means to estimate equilibrium constants and relative energies between states in equilibrium (33). To obtain the fractional populations of the **G** and **E** states from the distance distributions, the DEFs were fit to a multiple-Gaussian model for the distance distribution which was found to be equivalent to the model-free analysis in reproducing the details of the distance distributions (Figure 5.A2 and A3). Based on this metric, the energy difference at 295 K between the **G** and **E** ($\Delta G_{G\leftrightarrow E}$) for D89R1/T109R1 and T109R1/I150R1 in the L99A/G113A/R119P background is ≈1 kcal/mol. For D72R1/T109R1 and T109R1/N140R1 the states are nearly iso-energetic (left panel, Figure 5.A2). The differences in the equilibrium constant and derived free energy among the four doubles investigated likely arises from a population bias due to site-specific attractive or repulsive interactions of the spin label with the local protein environment. This inevitable consequence of labeling methodology has been previously discussed in detail, and does not influence the overall conclusions regarding shifts in the equilibrium due to other factors (1).

The interspin distance distributions between reference pairs D72R1/D89R1, D89R1/I150R1, and D89R1/N140R1 in the WT* and L99A/G113A/R119P backgrounds are shown in Figure 5.1C (right panel). For D72R1/D89R1and D89R1/I150R1 the distance distributions characteristic of the **G** conformation are preserved in **E**, but with the appearance of small new populations at ≈27 Å that are not observed in **G** (arrows, right panel, Figure 5.1C), suggesting the presence of a conformational sub-state in the cavity mutant that is not represented in the structural models of Figure 5.1. The potential significance of this population will be discussed below. As anticipated from the models, there are small differences in the interspin distance distributions between the **G** and **E** conformations for reference pair D89R1/N140R1, corresponding to the small displacement of helix I (N140R1) in the structural models of Figure 5.1. Under any condition, the differences in the distance distributions between the reference residues are small compared to those involving T109R1 and a reference residue, validating their use as reference sites. The origin of the strongly bimodal distribution in D89R1/N140R1 could arise from positional heterogeneity of the flexible helix I or rotamers of R1, as discussed previously (1).

CW EPR spectra of residue T109R1 in the WT*, L99A, and L99A/G113A/R119P backgrounds (Figure 5.2) support the changes of helix F position documented by DEER. For example, the CW spectra are essentially identical for WT* and L99A, and show two relatively mobile components, the possible origins of which have been previously discussed (34). However, in the L99A/G113A/R119P background in which the **E** state is stabilized, the spectrum becomes highly ordered showing restricted mobility of the R1 side chain, which confirms a change in the environment around R1 when helix F rotates and translates to a new position. Modeling suggests that an interaction of the nitroxide with a nearby carboxylate

(residue E108) may be responsible for the ordering (Figure 5.A1B). Interaction of nitroxides with carboxylates has been previously identified (35, 36).

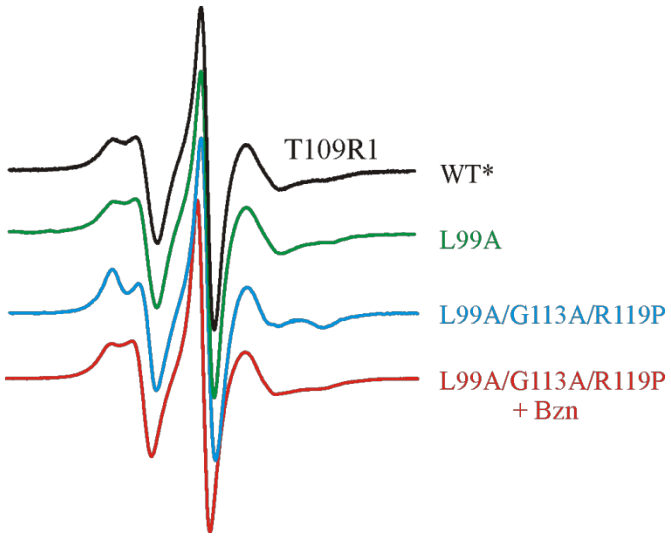

Figure 5.2 CW EPR spectra of T109R1 in the indicated genetic background. Spectra were recorded in 30% wt/wt sucrose at pH 6.8.

5.3.3 Shifting the G ↔ E equilibrium at atmospheric pressure with ligand binding and pH change. The L99A cavity mutant binds benzene with sub-millimolar affinity (21, 37-39). Structurally, the ligand-bound state is similar to the **G** state (21, 25, 37), thus addition of benzene to the **E**-stabilized mutant (L99A/G113A/R119P) should shift the equilibrium population towards the **G** state. Indeed, CW spectra of T109R1/L99A/G113A/R119P and DEER distance distributions for all doubles involving T109R1 show shifts in population towards the **G** state upon addition of benzene (Figure 5.1C, 2, A1A, and A2) demonstrating that the distances assigned as **G** and **E** states represent states in equilibrium. Interestingly, benzene binding to the reference pair D72R1/D89R1 in the L99A/G113A/R119P background essentially eliminates the population of the new minor state (27 Å) observed in the apo-protein (Figure 5.1C), suggesting a possible role of this minor state in ligand binding (see section **5.4**).

The equilibrium populations of **G** and **E** are not only shifted by ligand binding, but by pH as well. The data in Figure 5.1 were collected at pH 5.5, the same as in the NMR experiments

that modeled the **G** and **E** states (2). At this pH, the population is strongly biased towards **E** in the L99A/G113A/R119P background (Figure 5.1C). As will be shown below, pressure further populates the **E** state in this mutant, and in order to quantitatively investigate the pressure dependence of the **G** ↔ **E** equilibrium, experimental conditions are desired where the populations of **G** and **E** are similar so that shifts in equilibrium are readily detectable. The equilibrium population of the **G** state can be conveniently increased in the L99A/G113A/R119P background by an increase in the pH from 5.5 to 6.8, as assayed by the changes in distance distributions for all doubly labeled mutants involving T109R1 (Figure 5.A2). For D72R1/T109R1, D89R1/T109R1, and T109R1/N140R1 the **G** population is increased by 16 ± 4% at pH 6.8 relative to pH 5.5. For T109R1/I150R1, the equilibrium is still biased towards **E** (**E** 61%, **G** 21%) even at pH 6.8. The population of **G** is increased to 48% in the L99A/G113A background (without the R119P mutation), as qualitatively expected from Bouvignies et al. (2).

In the following sections, experiments designed to monitor pressure-dependent shifts in the **G** ↔ **E** equilibrium for L99A/G113A/R119P or L99A/G113A were carried out at pH 6.8 for the reason outlined above. Experiments designed to monitor the pressure dependence of WT* or L99A alone were done under the same conditions used in the NMR studies that led to the models of Figure 5.1, i.e., pH 5.5.

5.3.4 Far-UV circular dichroism measurements of global secondary structure at high pressure. Recent development of a modified high-pressure optical cell suitable for use in far-UV CD allowed for monitoring global secondary structure in the range of 0-2.4 kbar (gauge pressure; 0 bar gauge is atmospheric pressure). The pressure dependence for L99A and L99A/G113A/R119P was investigated to assess whether pressure affects the global secondary structure. CD spectra and secondary structure composition are shown in Figure 5.3A and 3B and

Table A2, respectively. Both mutants exhibited expected levels of helical content (≈60%) and β-sheet content (≈6%) at atmospheric pressure, corresponding to the WT* protein. The HP CD data for both indicate little change in the secondary structure content up to 2.4 kbar (≈1%), showing that for L99A at pH 5.5 the protein does not unfold in the pressure range investigated. The same conclusion applies to L99A/G113A/R119P at pH 6.8, with the addition that there is also little difference in secondary structure between the **G** and **E** conformations, in agreement with the models of Figure 5.1.

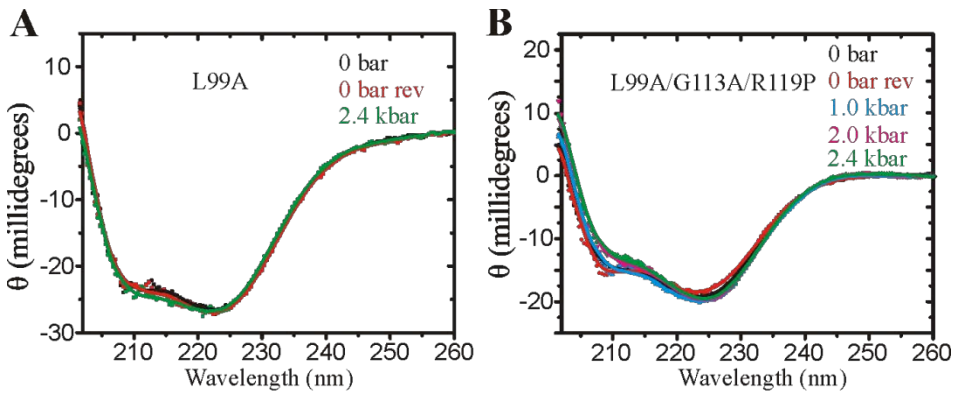

Figure 5.3 High-pressure CD of T4L mutants. (A) High-pressure far-UV CD of L99A, and (B) L99A/G113A/R119P. Both proteins contained spin labels D89R1/T109R1. CD Spectra were recorded in 5 mM MES and 2.5 mM NaCl at pH 5.5 for L99A and 10 mM MES and 25 mM NaCl at pH 6.8 at the indicated pressure. The typical protein concentration was ≈15 μM.

5.3.5 Pressure effects on conformational equilibria in WT*, L99A, L99A/G113A, and L99A/G113A/R119P. CW EPR spectra were collected from 0 to 2.5 kbar at pH 5.5 for the single R1-containing mutants D72R1 and D89R1 in the WT* and L99A backgrounds, and T109R1 in the WT*, L99A, and L99A/G113A backgrounds (Figure 5.4). Spectra of R1 at the selected sites serve to sample local backbone dynamics and conformational sub-states involving the inter-domain helix C, and helices D and F in the C-terminal domain, respectively. This pressure range corresponds to that where NMR studies reported either enhancement of fluctuations within a **G** state ensemble and an increase in the population of **E** (20) or unfolding

of the C domain of T4L L99A (11). In the WT* background, application of pressure to 2.5 kbar results in a slight reduction in nanosecond nitroxide motion as evidenced by a minor line broadening in the spectra of R1 at each site. Such effects have been previously reported and interpreted to reflect a limited compressibility of the protein in the region of the label site (29). In the L99A background, the pressure-dependent changes are of substantially larger magnitude. Indeed, for D72R1 and T109R1, pressure produces an increase in spectral intensity corresponding to partially immobilized states of the nitroxide (arrows, Figure 5.4), clearly evident at 2.5 kbar, that signals a corresponding increase in the population of conformational sub-states not detected in the WT*. Consistent with HP CD data, the CW spectra in L99A unequivocally show that the C terminal domain is not globally unfolded at 2.5 kbar; in that case the CW resonance line shape would consist of sharp resonance lines rather the reversible appearance of components corresponding to immobile states of R1 (Figure 5.A1C) (29). As shown below, the new conformational sub-states sensed by R1 in L99A at 2.5 kbar are not related to the **E** conformation, but likely reflect low amplitude structural fluctuations within the ground state ensemble of L99A (but see section **5.4**). Within the context of this model, the enhanced pressure dependence of L99A relative to WT* is interpreted to arise from an increased compressibility due to the presence of the cavity, in agreement with Maeno et al. (20).

Singular value decomposition of the variable-pressure CW spectra was performed according to the procedure described in chapter 3. Plots of the component amplitudes vs. pressure are shown in Figure 5.4 (right column), along with fits to determine values of $\Delta\overline{V}^o$ and ΔG^o where indicated.

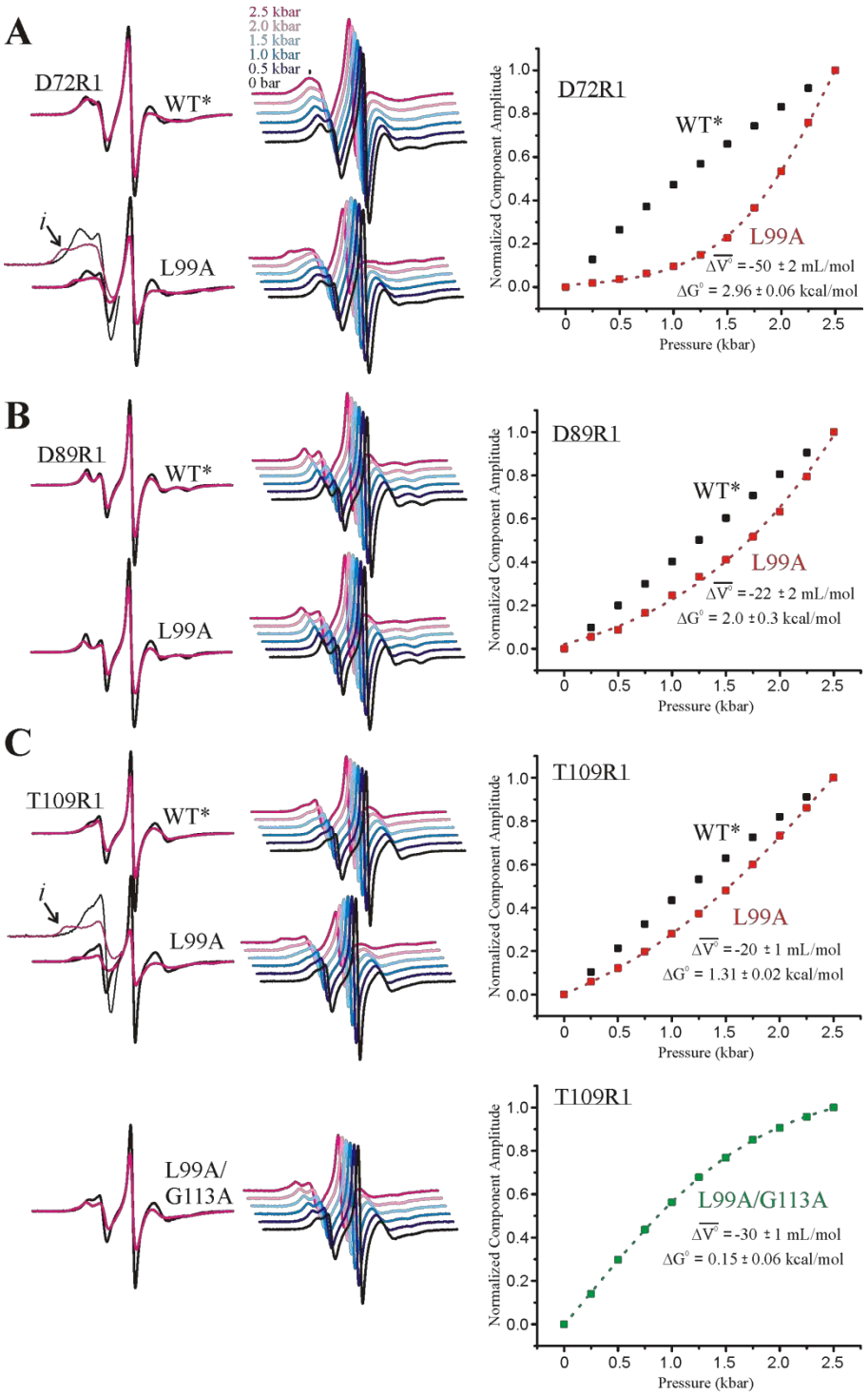

Figure 5.4 Variable-pressure CW EPR and SVD analysis of T4L mutants. EPR spectra of (A) D72R1, (B) D89R1, and (C) T109R1 in the indicated genetic background at 0 and 2.5 kbar are shown in black and magenta traces, respectively, in the left column. For clarity, the low field lines in the spectra of D72R1/L99A and T109R1/L99A are amplified. Arrows identify a new component observed at 2.5 kbar. Variable-pressure spectra are shown in the center column and are color-coded as indicated. Spectra were recorded in 25% wt/wt Ficoll-70 at pH 5.5. Plots of component amplitudes vs. pressure for the indicated mutants, with fits to a two-state equilibrium model to measure the indicated values of $\Delta\overline{V}^o$ and ΔG^o, are shown in the right column.

The amplitudes were more linear with pressure in the WT* background compared to the same site in the L99A or L99A/G113A backgrounds. However, the amplitudes of D72R1 displayed weak curvature in the WT* background (Figure 5.4A), and the possibility of a localized conformational transition involving low-amplitude structural changes cannot be ruled out. The amplitudes for all sites in the L99A background were well-fit with a two-state equilibrium model, although the values of $\Delta\overline{V}^o$ and ΔG^o varied significantly from site-to-site, indicating heterogeneity in the transition.

For T109R1 in the L99A/G113A background, the spectral lineshape at 2.5 kbar (Figure 5.4C) is very similar to that of the same residue in the L99A/G113A/R119P background at 0 bar (Figure 5.2), where the **E** state is highly populated. This supports the conclusion that the **E** state is populated by pressure, and that the local protein dynamics near residue T109R1 are relatively unchanged in the range of 0-2.5 kbar. Component amplitudes from SVD of the T109R1 spectra in the L99A/G113A background are well-fit to a two-state transition with $\Delta\overline{V}^o$ = -30 mL/mol and ΔG^o = +0.15 mL/mol (right column, Figure 5.4C). These values are consistent with an equal population of the **G** and **E** states at atmospheric pressure, as expected for the L99A/G113A background based on NMR, and predominance of the **E** at 2.5 kbar in accordance with results from PR DEER (see below).

Although the CW spectra qualitatively identify protein compression, they do not directly reveal the magnitude of structural changes with pressure. For this purpose, PR DEER is required. In this method, high-pressure states of a protein are trapped by rapid freezing in dry-ice/ethanol (200 K) (section **5.6**) and the distance and distance distributions between pairs of R1 residues introduced into the protein are measured with DEER after depressurization to atmospheric pressure. In agreement with previous work, freezing in dry-ice/ethanol and the more

conventional liquid nitrogen results in similar distance distributions for T4L doubly-labeled mutants in the WT*, L99A, and L99A/G113A/R119P backgrounds at atmospheric pressure (Figure 5.A4).

For reference, the effect of pressure on the WT* protein was investigated to 3 or 4 kbar with PR DEER and four pairs of R1 residues that sampled distances between a reference pair (D89R1/N140R1) and distances that monitored the position of T109R1 in helix F (D72R1/T109R1, T109R1/N140R1 and D89R1/T109R1). Remarkably, the distance distributions at 3 or 4 kbar were essentially identical to those at atmospheric pressure (Figure 5.A5), showing that the tertiary fold of the WT* protein throughout the broad domain sampled by the above sites (Figure 5.1A and 1B) is unchanged. Therefore, any pressure dependence observed in the L99A, L99A/G113A, and L99A/G113A/R119P backgrounds can be attributed to conformational changes in the protein due to the presence of the cavity.

The effect of pressure on L99A was explored with DEER using R1 pairs T109R1/N140R1 and D89R1/T109R1 (Figure 5.5 and 5.A7A). As shown above (Figure 5.1C) distances between R1 residues in these pairs monitor the position of helix F and are diagnostic for the formation of the **E** state. In the range of 0-3 kbar (Figure 5.5), only subtle shifts in the relative population of individual distances are observed for the two mutants. While this sparse data set is insufficient to draw global conclusions about the protein conformation, it serves to demonstrate that the **E** conformation characterized by NMR is not substantially populated with pressure up to 3 kbar. At 4 kbar, the distance distributions begin to broaden in L99A (full width >30 Å), but not in WT*, suggesting a transition to a non-native state for L99A in the regions sampled by the R1 sites. The 4 kbar conformation is not fully unfolded, because in this case the distance distribution would be far broader, as illustrated by that for the doubly-labeled T4

lysozyme mutants in the guanidine hydrochloride-unfolded state (Figure 5.A1C). Additional PR DEER data will be needed to draw conclusions regarding the global fold, but for the spin pairs investigated, discrete distances corresponding to a highly populated **E** conformation (as illustrated in Figure 5.1C) are not observed in the L99A background at any pressure, in agreement with Nucci et al. (11). The pressure response for the two mutants in the L99A was fully reversible (Figure 5.A6).

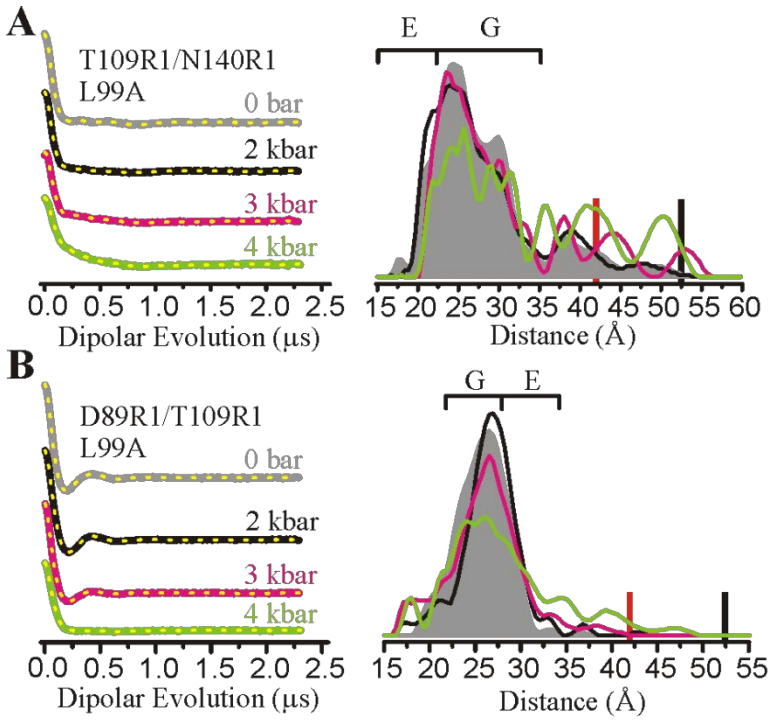

Figure 5.5 Effect of pressure on L99A monitored with DEER using spin pairs (A) T109R1/N140R1 and (B) D89R1/T109R1. DEFs and model-free fits (dashed yellow traces) (left panel) and corresponding distance distributions (right panel) are shown from 0-4 kbar. The DEFs and distance distributions are color-coded as indicated. The approximated distances corresponding to the **G** and **E** states are indicated with brackets above the distributions. PR DEER experiments were conducted in buffer consisting of 50 mM MES, 25 mM NaCl, 20% vol/vol glycerol at pH 5.5. The red and black bars indicate the upper limit of reliable shape and distance of the distribution, respectively (see section **5.6**).

Of particular interest is the effect of pressure on L99A/G113A/R119P, the mutant that lowers the free energy of the **E** state. In this mutant, the position of helix F is again monitored using spin pairs involving T109R1 and one of the reference sites D72R1, D89R1, N140R1, or I150R1 at pH 6.8. Distances between reference pairs D72R1/D89R1 and D89R1/N140R1 are

rather weakly dependent on pressure to 3 kbar, although there are small shifts in populations (Figure 5.6A) in the latter; in D72R1/D89R1 a minor population at ≈27 Å, also observed at atmospheric pressure and pH 5.5 (Figure 5.1C), is increased by pressure (arrows, Figure 5.6A). For D89R1/I150R1 populations at short distances (≈22 and 27 Å), also observed at atmospheric pressure and pH 5.5 (Figure 5.1C), are substantially enhanced (arrows, Figure 5.6A); the significance of states identified by these distances will be considered below.

The PR DEER data for D89R1/T109R1, T109R1/N140R1, and D72R1/T109R1 that define the position of helix F in the L99A/G113A/R119P background are shown in Figure 5.6B and 5.A7B. The primary effect of pressure on the distance distributions of these mutants is to shift the two-state **G** ↔ **E** equilibrium towards the **E** conformation as can be seen by comparison with the data in Figure 5.1C (note that the data in Figure 5.1 was obtained at pH 5.5, whereas those in Figure 5.6 are for pH 6.8 at which the population of the **G** conformation is increased). For the three R1 pairs, the population of the **E** state is already substantially increased at 1 kbar. In all cases, pressures up to 3 kbar shift the equilibrium without populating new states, and the widths of individual populations in the distributions do not increase. A similar result was observed for T109R1/I150R1 in the L99A/G113A background, where the distance distribution shows a nearly complete shift to the **E** conformation at 2 kbar (Figure 5.A7C).

For D72R1/T109R1, D89R1/T109R1, and T109R1/N140R1, the distance distributions remain narrow up to 4 kbar, showing that introduction of the G113A/R119P mutations in L99A dramatically stabilizes the protein against the pressure-dependent structure changes seen in L99A alone. Remarkably, distributions for D72R1/T109R1 and D89R1/T109R1 remain narrow even to 6 kbar, with only T109R1/N140R1 showing an increased breadth, likely due to local structural changes in the short helix I in which N140R1 resides (Figure 5.A7) (see section **5.4**).

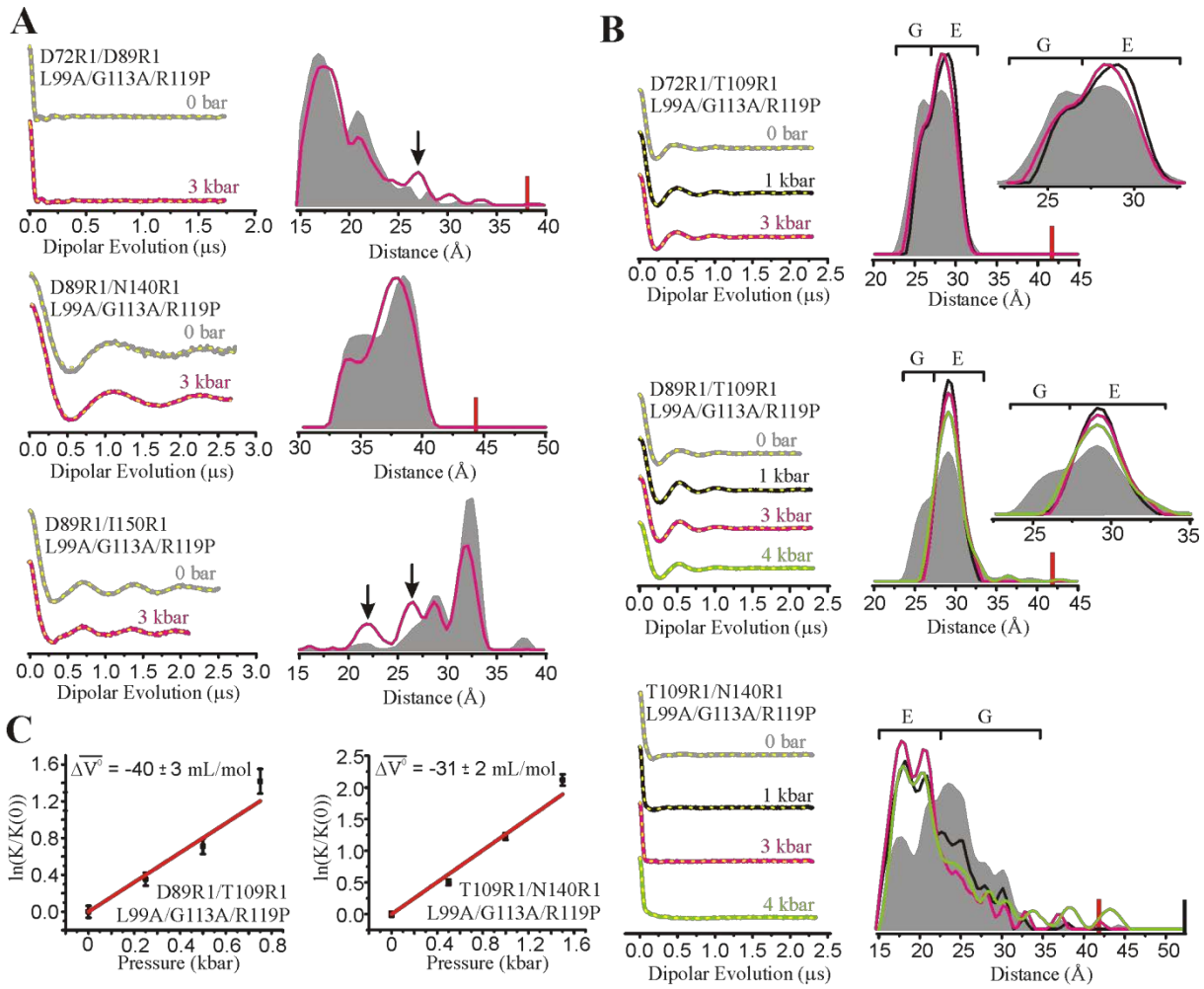

Figure 5.6 The effect of pressure on the **G** ↔ **E** equilibrium in L99A/G113A/R119P. PR DEER was used to map distance changes between (A) indicated reference sites and (B) between T109R1 and selected references to monitor the position of helix F. DEFs, model-free fits of the DEFs (dashed yellow traces), and corresponding distance distributions are shown at various pressures between 0 and 4 kbar. DEFs and distance distributions are color-coded as indicated. The black arrows identify populations in reference pairs increased by pressure. The approximate distance ranges corresponding to **G** and **E** are indicated by brackets above the distributions. PR DEER data were collected for the protein in buffer consisting of 50 mM MOPS, 25 mM NaCl, 20% vol/vol glycerol at pH 6.8. The red and black bars indicate the upper limit of reliable shape and distance of the distribution, respectively (see section **5.6**). (C) Plots of ln(K/K(0)) vs. pressure for the indicated mutants, and fits (red trace) using a two-state model to measure $\Delta\overline{V}^{o}$ for the **G** → **E** transition.

The pressure dependence of the **G** ↔ **E** equilibrium constant (K) was determined using fits of the DEF to multiple-Gaussian distance distributions as described in section **5.6**. Figure 5.A8A and A8B contain a subset of the fits and associated multiple-Gaussian distance distributions along with their model-free counterparts, highlighting the similar goodness-of-fit for the two methods. Plots of ln(K/K(0)) vs. pressure (P) for T109R1/N140R1 and

D89R1/T109R1 in the L99A/G113A/R119P background (Figure 5.6C) and T109R1/I150R1 in the L99A/G113A background (Figure 5.A8C) were fit to determine the change in partial molar volume ($\Delta\overline{V}^o$) for the **G** to **E** transition as described in section **5.6**. Values of $\Delta\overline{V}^o$ were -31, -40, and -29 mL/mol, respectively. It is noted that for this analysis, the data set was fit in the low pressure range ($\leq$1.5 kbar) to eliminate contributions from compressibility of the individual states.

5.4 Discussion

The present study was undertaken to elucidate the response of T4L cavity mutants to hydrostatic pressure, with the expectation that the results will have general applicability to proteins with native cavities or packing imperfections. The structural origins of the volume changes that underlie the shift in equilibrium between folded conformations at moderate pressures are of particular interest, rather than those that lead to a pressure-denatured state (3, 8, 13-17), or to an unfolded state formed at high pressure in the presence of a chemical denaturant (4, 40). In the present study unfolding will refer to a process in which loss of tertiary and secondary structure occurs.

The interpretations of the pressure-dependent EPR data rely on the NMR/Rosetta models of the **G** and **E** conformations of T4L L99A. Collectively, all SDSL and CD data for WT*, L99A, and L99A with G113A or G113A/R119P at atmospheric pressure are in good agreement these models (Figure 5.1-3 and 5.A1; Table 5.A1 and A2). In particular, the essentially identical CD spectra as a function of pressure for the L99A and L99A/G113A/R119P mutants, which differ greatly in the populations of the **G** and **E** states, indicate that the global secondary structure of the two states is the same, as expected from the models, and any changes in intramolecular distances measured by DEER must arise from changes in tertiary structure. The

distinctive distance changes involving movement in the F helix detected by DEER distance mapping are in good agreement with the models. Thus, the models of Figure 5.1 are assumed to reliably reflect the salient features of the **G** and **E** conformations, and that the SDSL EPR data can be interpreted in the context of these models. The structural change involving the F helix, readily identified by DEER distance mapping, is used as a "fingerprint" to identify the **E** state population upon pressure application. In addition, the overall breadth of distance distributions reflects structural heterogeneity, while CW EPR spectra of single R1 residues monitor backbone dynamics and identify regions in conformational exchange on a time scale long compared to ns (41, 42). The main conclusions employing this strategy are discussed in relationship to the earlier NMR results of Maeno et al. (20) and Nucci et al. (11) in the sections to follow. It is noted that the conclusions refer only to the C-terminal domain of T4L that contains the engineered L99A cavity.

5.4.1 Pressurization of L99A drives cavity hydration and an increase in structural heterogeneity. Distance distributions in L99A that monitor the position of helix F show only subtle changes between 0 bar and 3 kbar (Figure 5.5) and HP CD reveals no secondary structure changes up to 2.4 kbar (Figure 5.3A and Table 5.A2). These data unambiguously show that the folded conformation of T4L L99A is maintained to 2.4 kbar, without loss of global secondary structure or tertiary structure in the regions sampled. This conclusion is strongly supported by the CW EPR data, which reveal no detectable dynamic disorder in the form of sharp resonance line shapes (Figure 5.A1C), but instead indicate structural fluctuations of the tertiary fold within the ground state ensemble of L99A at pressures in the range of 0-2.5 kbar (Figure 5.4). Interestingly, SVD of the variable-pressure CW spectra indicate the presence of a conformational exchange that is heterogeneous across the structure. Taken together with the HP CD and PR DEER results

on L99A, the transition identified by SVD likely corresponds to small amplitude fluctuations the position of the helices accompanying hydration of the cavity.

These fluctuations correspond to an increased compressibility in L99A relative to WT*, possibly resulting from hydration of the L99A cavity (see below). Interestingly, the structural fluctuations inferred from the line shapes of T109R1 and D72R1 must be of small amplitude because the DEER distance distributions involving these sites show only small changes in the same pressure range. This reinforces a previous conclusion that the line shapes of single R1 residues with multiple components are exquisitely sensitive to very small changes in structure due to the r^{-6}/r^{-12} dependence of attractive/repulsive interactions of the nitroxide with the local environment (41).

The above results are in general agreement with Maeno et al. (20) but apparently at odds with the conclusions of Nucci et al. (11), who interpret the responses observed for the C domain of L99A under pressure in the range of 1-2.5 kbar in terms of local unfolding of secondary structural elements. The HP CD data obtained in the present study show no significant loss of secondary structure up to 2.4 kbar, while the PR DEER show the tertiary fold to be intact.

Interestingly, large changes in tryptophan fluorescence were reported in the pressure range of 1-3 kbar at neutral pH with a midpoint at 2.4 kbar. As discussed by Ando et al. (3), these changes apparently correspond to cavity hydration. The fact that PR DEER detects no rearrangements in the tertiary fold in this pressure range shows that the putative hydrated cavity ground state ($\mathbf{G_H}$) has essentially the same conformation as that for the empty cavity (**G**), at least in the domains sampled by the spin labels. This is in accord with the previous high pressure crystallography of L99A (5) and NMR studies of the same mutant contained in inverse micelles (11), although this result might not be anticipated considering that the available conformational

space in a crystal lattice and trapped in an inverse micelle is highly limited. Overall, the fluorescence, HP CD, CW EPR, and PR DEER data are consistent with a model wherein the L99A cavity becomes hydrated in the range of 2-3 kbar, concomitant with the onset of conformational flexibility involving small-amplitude tertiary structure fluctuations without unfolding.

The PR DEER data do not show discrete distances corresponding to the **E** conformation in L99A within the detection limit of the experiment (≈10%) in the pressure range of 0-3 kbar, apparently at odds with the conclusions of Maeno et al. (20). However, the **E** state is an established member of the conformational ensemble (2) and is surely present at some level, so the differences may be quantitative rather than qualitative. Maeno et al. note that, in addition to an increase in the **E** state population, pressure-dependence of the **G** ↔ **E** exchange rates could also account for their data and this would be consistent with the PR DEER data presented here. At pressures above ca. 3 kbar, the distance distributions for D89R1/T109R1 and T109R1/N140R1 in the L99A background become markedly broadened, with a full distribution width of ≈30-35 Å at 4 kbar, reflecting the onset of significant structural heterogeneity. The relatively broad distance distributions may arise from local/global unfolding driven by internal hydration and the formation of a "wet" molten globule state, as was recently observed for apomyoglobin by PR DEER.

5.4.2 Distance mapping in L99A/G113A and L99A/G113A/R119P supports a structure-relaxation mechanism rather than cavity hydration for the pressure response. In the G113A and G113A/R119P mutations in L99A, the energy of the **E** state is lowered relative to **G** (2) and the **G** ↔ **E** equilibrium is readily resolved at atmospheric pressure using DEER distance mapping (Figure 5.1). Remarkably, the equilibrium is shifted towards the **E**

conformation with increasing pressure in the range of 0-3 kbar (Figure 5.6B), with no new states appearing as judged by the shift in position of helix F, the constancy of the CD spectra (to 2.4 kbar) (Figure 5.3B), and the lack of substantial distance change between reference sites (Figure 5.6A) (but see below). SVD of the variable-pressure EPR spectra of T109R1 in the L99A/G113A background (Figure 5.4C) reports a conformational transition with values of $\Delta\overline{V}^o$ and ΔG^o that are fully consistent with the **G** to **E** transition characterized by PR DEER, and the spectral lineshape at 2.5 kbar is similar to that observed for T109R1 in the **E** state at atmospheric pressure (Figure 5.2). Thus, the **G** and **E** structures are tentatively concluded to be essentially pressure independent at low pressures, and the primary effect of pressure is to shift the **G** ↔ **E** equilibrium. In the context of this model, the data show that the **E** conformation has a lower partial molar volume compared to **G** and they provide direct experimental evidence for a structure-relaxation mechanism as the basis for the volume reduction.

Interestingly, the $\Delta\overline{V}^o$ estimates for the **G** to **E** transition are in the range of -30 to -40 mL/mol, close to the molar volume of the Phe114 side chain that occupies the cavity in the **E** state (42 mL/mol). The $\Delta\overline{V}^o$ for the **G** to **E** transition is similar in the presence and absence of R119P (Figure 5.6C and A8C), further reinforcing that the G113A and R119P mutations shift the relative energies of **G** and **E** without significantly altering their structures. Moreover, the widths of the distance distributions for peaks corresponding to the **G** and **E** conformations are essentially pressure independent (Figure 5.6B), suggesting that the two states have similar flexibility in the structural elements sampled by the distance measurements. Viewed in combination with the results from HP CD, this indicates that, in the case of equilibria involving nearly iso-energetic states, pressure may populate a conformational state with similar backbone configurational entropy to the **G** state. For truly excited states with substantially higher energy

than the ground state, a large body of evidence suggests that the excited state has higher configurational entropy (the “volume rule” (43)).

A remaining question regarding ligand binding to L99A is the ingress/egress pathway for ligand exchange (2). The structure of the T4L L99A **G** state shows the cavity to be completely solvent inaccessible, and in the **E** state the ligand binding site is occupied by Phe114. Access to the empty cavity must then be *via* an as yet unresolved conformation, distinct from both the **G** and **E** states, as suggested by Bouvignies et al. (2). Interestingly, three of the R1 pairs (D72R1/D89R1, D89R1/I150R1, T109R1/I150R1) show populations at distances not corresponding to the **E** or **G** states in the L99A/G113A/R119P background (Figure 5.1C), and the size of those populations increases with pressure (Figure 5.6A and 5.A7C). This suggests that both pressure and the additional G113A and R119P mutations populate not only the **E** state, but also the putative ligand binding state to a small extent. For the one case investigated involving reference sites (D72R1/D89R1), the new additional distance disappears upon ligand binding. While the data are too sparse draw conclusions regarding possible structures, the third state observed may correspond to the ligand accessible conformation that must exist to enable rapid (≈ms) binding of ligands to the otherwise buried cavity (39). Because D89R1 is common to the two reference pairs that reveal the new populations and it is located at a helix (helix D) closest to the engineered cavity, it is tentatively suggested that it is helix D that moves in the new state, closer to I150R1 and further from D72R1. Such a motion could open a direct path to the cavity. Interestingly, structural analysis using Caver (44, 45) reveals putative tunnels in the interface between helices D and G that could enable ligand entry (Figure 5.A1D). This pathway is different than that identified by MD simulations for water penetration and escape from the L99A cavity (5).

5.4.3 The thermodynamic basis for hydration vs. structure-relaxation. Collectively, the above data suggest that pressure hydrates the enlarged cavity in the L99A mutant, but shifts the conformation from **G** to **E** in L99A/G113A/R119P and L99A/G113A. Why is the cavity not hydrated by pressure in these latter mutants? A likely explanation for this difference lies in details of the energy landscape. The combination of atmospheric and high-pressure data from NMR, fluorescence, X-ray crystallography, and EPR suggest an equilibrium model for L99A and L99A/G113A/R119P with at least four states in the pressure range of 0-3 kbar, namely **E**, **G**, $\mathbf{G_H}$, and **L**, where **L** is a proposed conformation where the ligand has access to the cavity, and $\mathbf{G_H}$ is a state wherein the L99A cavity is hydrated. At higher pressures, the putative molten globule state would be included. To illustrate a simple model that can account qualitatively for structure relaxation vs. cavity hydration, consider a 3-state equilibrium excluding a minor **L** state.

$$\mathbf{E} \Leftrightarrow \mathbf{G} \Leftrightarrow \mathbf{G}_H$$

Although thermodynamically distinct, the protein is structurally similar in $\mathbf{G_H}$ and **G** based on high-pressure crystallography (5), HP CD (Figure 5.3), and PR DEER at 2 kbar (Figure 5.5). To compute pressure-dependent free energy changes, values for free energy differences between states at atmospheric pressure (ΔG^o) and corresponding volume changes ($\Delta \overline{V}^o$) are needed. ΔG^o can be estimated from NMR (2, 25), fluorescence (3), and the DEER data presented above. $\Delta \overline{V}^o$ values corresponding to the transitions are obtained from the pressure dependence of the corresponding equilibria. For the $\mathbf{G} \rightarrow \mathbf{G_H}$ transition, a value of -75 mL/mol was taken because it generates landscapes that illustrate the main features of the experimental results presented above. This value is intermediate between that for complete cavity elimination (-100 mL/mol) and a value of -56 mL/mol measured from fluorescence at pH 7. The $\Delta \overline{V}^o$ for the $\mathbf{G} \rightarrow \mathbf{E}$ transition identified by PR DEER is ≈-36 mL/mol, and since the **G** and **E** states are expected

to be structurally similar in L99A, L99A/G113A/R119P, and L99A/G113A based on the evidence presented above, it is assumed that $\Delta\bar{V}^o$ is the same for all three genetic backgrounds. With these values, free energy profiles as a function of pressure can be generated and are shown in Figure 5.7 for 0 bar and 2 kbar. These landscapes are not intended to reproduce the experimental data in detail because of the neglect of other conformations and compressibility effects, but only to illustrate a concept with realistic values of ΔG^o and $\Delta\bar{V}^o$.

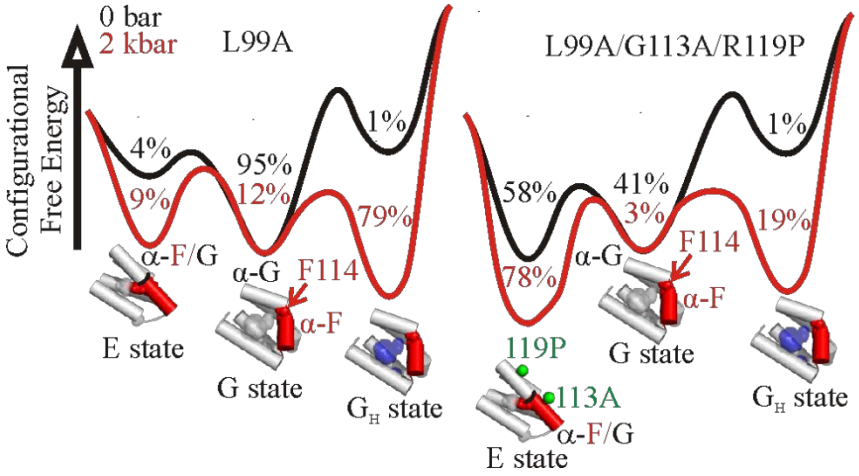

Figure 5.7 Effect of pressure on the equilibrium between the $\mathbf{G}_H$, **G**, and **E** states of T4L mutants L99A (left panel) and L99A/G113A/R119P (right panel). Relative configurational free energies (ΔG^o) are shown for 0 and 2 kbar; values for the $\mathbf{G}_H$ and **E** states are relative to **G**. Values for $\Delta\bar{V}^o$ and ΔG^o are -36 mL/mol and -0.2 kcal/mol, respectively, for the **G** to **E** transition (based on PR DEER of L99A/G113A/R119P), and -75 mL/mol and 2.5 kcal/mol, respectively, for the **G** to $\mathbf{G}_H$ transition (based on high-pressure tryptophan fluorescence of L99A (3) and the total L99A cavity volume). Populations of each state are indicated in the local minima of the landscape. Structural models for the C domain are shown below the corresponding energy minima. Helix F is shown in red. The location of Phe114 (red spheres) in the **G** and **E** states are indicated. The empty cavity is shown in gray surface representation. A blue surface is used to represent pressure-populated hydration of the cavity in the L99A mutant. Green spheres at the Cα are used to indicate the position of G113A and R119P mutants in the **E** state structure (PDB ID code 2LC9 (2)).

The volumetric contribution to stabilization of the **E** state under pressure is less than that for hydration, and pressure will drive hydration instead of repacking unless the ΔG^o for repacking is markedly smaller than ΔG^o for hydration. This is not the case for the L99A mutant, so pressure populates the $\mathbf{G_H}$ state. The addition of G113A and R119P mutations lowers ΔG^o for

formation of the **E** conformation (2) sufficiently that pressure drives the equilibrium to the **E** state in the L99A/G113A and L99A/G113A/R119P mutants.

The preference for repacking in L99A/G113A/R119P rather than hydration has important implications regarding the stability of proteins under pressure. For example, the spin pairs T109R1/N140R1 and D89R1/T109R1 have narrower distance distributions in L99A/G113A/R119P backgrounds compared to the L99A background at 4 kbar (Figure 5.5 and 6B), suggesting increased disorder in L99A but not in L99A/G113A/R119P. Thus, hydration of the cavity in L99A at intermediate pressures leads to destabilization compared to L99A/G113A/R119P, because in the **E** conformation that dominates L99A/G113A/R119P, the side chain of Phe114 occupies the cavity and must be displaced before water can penetrate the protein. Similarly, both cavity-filling mutations and ligand binding have been found to stabilize proteins against denaturation at high pressure (7, 46, 47). In the context of this model, cavities in flexible proteins that can repack are expected to be more stable to pressure than a corresponding rigid protein in which the cavity will hydrate with pressure. Indeed, repacking has been proposed to explain the stabilizing effect of proline-to-glycine mutations against pressure-denaturation observed in staphylococcal nuclease (48). In that study, the authors speculated that the increased flexibility caused by the mutations could have allowed the protein to sample alternative, more stable packing modes. Evolutionarily, mutations like G113A and R119P that modify the energy landscape to stabilize or expand the number of accessible conformations that the protein can sample within the native state ensemble may prove advantageous for adaptation to various environmental stresses such as pressure and temperature, and give rise to new functionality.

5.5 Conclusions

Collectively, the data presented here show that a protein can respond to pressure by structure relaxation to fill a cavity or by the established mechanism of cavity solvation. In principle, any cavity-containing protein can have conformational sub-states in equilibrium in which the core is rearranged to fill or partially fill the cavity with protein atoms, thus reducing the partial molar volume. If the strain energy involved in forming such a conformation is high, cavity hydration will be of lower energy. This appears to be the case for L99A in solution. If the strain energy is lower than hydration, structure relaxation will be favored over hydration. The strain energy will be low in proteins that have nearly iso-energetic conformational sub-states, at least one of which has an alternative packing mode that fills the cavity. This is the case with L99A containing the additional mutations G113A and G113A/R119P that relieve steric hindrance for forming the cavity-filled conformation (the **E** conformation) (2). Although the principles were elucidated with cavity-creating mutants, they are expected to apply to proteins with naturally occurring packing imperfections.

5.6 Methods

5.6.1 Construction, expression, and purification of T4L mutants. All the mutations designed for this study were introduced to the T4L gene (pET11a vector) using the QuikChange site-directed mutagenesis method. All of the mutants contain the pseudo wild type (WT*) mutations C54T and C97A. Mutations were verified by sequencing. Expression, purification, and spin labeling of cysteine mutants in the WT* background was done as previously described (32). All the cysteine mutants in the L99A background were purified from inclusion bodies as described in López et al. (1).

5.6.2 EPR spectroscopy. CW EPR spectra of spin-labeled proteins were recorded at X-band in a Bruker ELEXSYS 580 spectrometer at room temperature in buffer at pH 5.5 (50 mM

MES and 25 mM NaCl) or pH 6.8 (50 mM MOPS and 25 mM NaCl) containing 30% wt/wt sucrose or 25% wt/wt Ficoll-70 (Sigma). These concentrations of sucrose and Ficoll-70 cause an equivalent increase in the effective viscosity of the solution, and are thus equally effective in reducing the contribution of rotational diffusion of the protein to the spectral lineshape (29, 49, 50). Protein concentrations were in the range of 100-500 μM. For ligand binding studies, benzene was added *via* vapor diffusion as described in López et al. (1). Atmospheric pressure CW samples were loaded into glass capillaries (0.60 ID X 0.84 OD; VitroCom Inc., NJ). Variable-pressure CW EPR spectra were recorded at room temperature using ceramic sample cells and a computer-controlled pressure intensifier (HUB440-Cer and HUB440; Pressure BioSciences, Inc.) as described in chapter 3. SVD of variable-pressure EPR spectra was performed according to methods described in chapter 3, and the component amplitudes were fit to determine the reported values of $\Delta\overline{V}^{o}$ and ΔG^{o}.

Four-pulse DEER data at 80 K were obtained on a Bruker ELEXSYS 580 operated at Q-band as described in chapter 4. The protein concentration was at or below 200 μM. For DEER measurements at atmospheric pressure, samples of 12-20 μL in 50 mM phosphate and 25 mM NaCl at pH 5.5 or buffer at pH 6.8 containing 20% vol/vol glycerol were loaded in a glass capillary (1.4 ID X 1.7 OD; VitroCom Inc., NJ) and flash-frozen in liquid nitrogen. A glycerol solution in the appropriate buffer was used as a stock in all cases. The materials and detailed protocol for PR DEER experiments up to 3 kbar are described in chapter 4. For PR DEER above 3 kbar, a Barocycler HUB880 pressure intensifier (Pressure BioSciences, Inc.) was used with 100,000 psi-rated pressure tubing and connectors (Maxpro Technologies) according to the same protocol. Pressures specified in this dissertation are gauge pressure, i.e., 0 bar is equal to atmospheric pressure. All pressure-resolved DEER experiments were done in buffer at pH 6.8

containing 20% vol/vol glycerol, except for mutants in the L99A background, for which the buffer used consists of 50 mM MES, 25 mM NaCl, 20% vol/vol glycerol at pH 5.5. The upper limit of reliable distance (r) and width determination (σ) for each mutant in nanometers was calculated using the following equations (51): $r_{max,\langle r\rangle} \approx 5\sqrt[3]{t_{max}/2\mu s}$; $r_{max,\langle\sigma\rangle} \approx 4\sqrt[3]{t_{max}/2\mu s}$, where t_{max} is the maximum time domain recorded for each sample. Model-free and model-based distance distributions were obtained from the raw dipolar evolution data using the program "LongDistances" available at http://www.chemistry.ucla.edu/directory/hubbell-wayne-l.

5.6.3 Model-based Gaussian fit of DEER data. Fits of the background-corrected DEER dipolar evolution functions (Figure 5.A2, A3, and A8) to a multiple-Gaussian model for the distance distribution were performed using the software LongDistances, written in LabVIEW and available for download at: http://www.chemistry.ucla.edu/directory/hubbell-wayne-l. Initial estimates for each Gaussian mean were obtained by extracting the most probable distances for each peak observed in the model-free fit with the lowest chi-square value. During the first iteration of the fitting process for atmospheric pressure data, the mean for each Gaussian was fixed and the amplitudes and widths were allowed to vary. During subsequent iterations, the mean of each Gaussian was allowed to vary up to 0.5 Å to improve the fit. In a few cases, the lowest chi-square value from Gaussian-based fit to the time domain data was obtained after further optimization of the baseline correction. The width of the Gaussians was in the range of 1.03-5.30 Å. For fitting of the high-pressure data, the mean and width of each Gaussian obtained at atmospheric pressure were kept constant and only the relative amplitudes were allowed to vary.

5.6.4 Thermodynamic analysis of the G ↔ E equilibrium. The use of multiple-Gaussians to represent DEER distance distributions and relative populations of states has been previously described (33). Fits presented here were performed using LongDistances for D89R1/T109R1 and T109R1/N140R1 in the L99A/G113A/R119P background and for T109R1/I150R1 in the L99A/G113A background in the range of 0–1.5 kbar. The data were fit as a function of pressure according to a two-state equilibrium, **G** ↔ **E**, where 1-2 individual Gaussians were used to account for each state at each pressure. The fractional population of **G** and **E** (f_G and f_E) were calculated using the sum of the integrated areas for the individual Gaussians corresponding to the given state, normalized to the total area for all Gaussians. Errors reported by LongDistances for the areas of individual Gaussians were propagated throughout the analysis. The equilibrium constant (K) is given by [5.1].

$$K = f_E/f_G \quad [5.1]$$

A first order approximation for the pressure dependence of the Gibbs free energy (ΔG), [5.2] and [5.3], was utilized due to the relatively low pressures used in this analysis.

$$\Delta G = \Delta G° + \Delta\bar{V}^o(P) \quad [5.2]$$

$$\Delta G = -RT\ln(K) \quad [5.3]$$

Combining [5.2] and [5.3] yields [5.4], where R is the gas constant and T is temperature. The temperature was set to 298 K, which was the holding temperature for all samples prior to rapid freezing for DEER.

$$\ln\left(\frac{K}{K(0)}\right) = \frac{-\Delta\bar{V}^o}{RT}(P) \quad [5.4]$$

Plots of ln(K/K(0)) vs. pressure (P) were fit to [5.4] to solve for the change in partial molar volume ($\Delta\bar{V}^o$) associated with the pressure-populated transition from **G** to **E**.

5.6.5 High-pressure far-UV CD spectroscopy. High-pressure far-UV CD was done as described in chapter 3. The sample concentration was 12-16 μM in buffer consisting of 10 mM MES, 25 mM NaCl at pH 6.8 for D89R1/T109R1/L99A/G113A/R119P and 5 mM MES, 2.5 mM NaCl at pH 5.5 for D89R1/T109R1/L99A. For both buffers, the baseline as a function of pressure was recorded and used for correction. The path length of the optical cell was 0.5 mm, the scan rate used was 50 nm/min with a response time of 1 second. The sample was allowed to equilibrate for 5 minutes at each pressure prior to data collection. Each spectrum shown is an average of 9 scans. Reversibility was verified by data collection after depressurization. The changes in secondary structure were quantitatively analyzed using the CONTIN algorithm (52, 53).

5.7 Appendix

Table 5.A1 Expected and experimentally observed changes in distances from residue T109R1 to the indicated reference in the **G → E** transition. The expected changes in distances are based on modeling the R1 side chain in **G** and **E** (Figure 5.1A).

Mutant	$\Delta r_{G \rightarrow E}$ (Å) Modeling[a]	$\Delta r_{G \rightarrow E}$ (Å) Experimental
D72R1/T109R1	+ 5.0	+ 3.5
D89R1/T109R1	+ 7.0	+ 6.5
T109R1/N140R1	- 7.5	- 6.8
T109R1/I150R1	- 5.0	- 7.0

[a]The R1 side chains at sites 72, 89, 109, and 140 were modeled using one of the most commonly observed R1 rotamers on X-ray structures of R1 in T4L that most closely match the experimentally determined distances. For site 150, the R1 rotamer modeled was that observed in the X-ray structure of I150R1 (54).

Table 5.A2 Secondary structure of indicated T4L mutants as a function of pressure determined from CD.

Mutant	Pressure (kbar)	α-Helix*	β-Sheet	Turn	Unordered
D89R1/T109R1/L99A	0	.58	.09	.14	.19
	2.4	.59	.08	.14	.19
D89R1/T109R1/ L99A/G113A/R119P	0	.57	.06	.14	.23
	2.4	.59	.05	.15	.21
L99A†	N/A	.62	.07		
L99A/G113A/R119P‡	N/A	.59	.07		

† and ‡: Values for α-helix and β-sheets obtained from deposited PDB structures 1L90 (55) and 2LC9 (2).

* Fraction of secondary structure at each pressure was estimated using the CONTIN algorithm (52, 53).

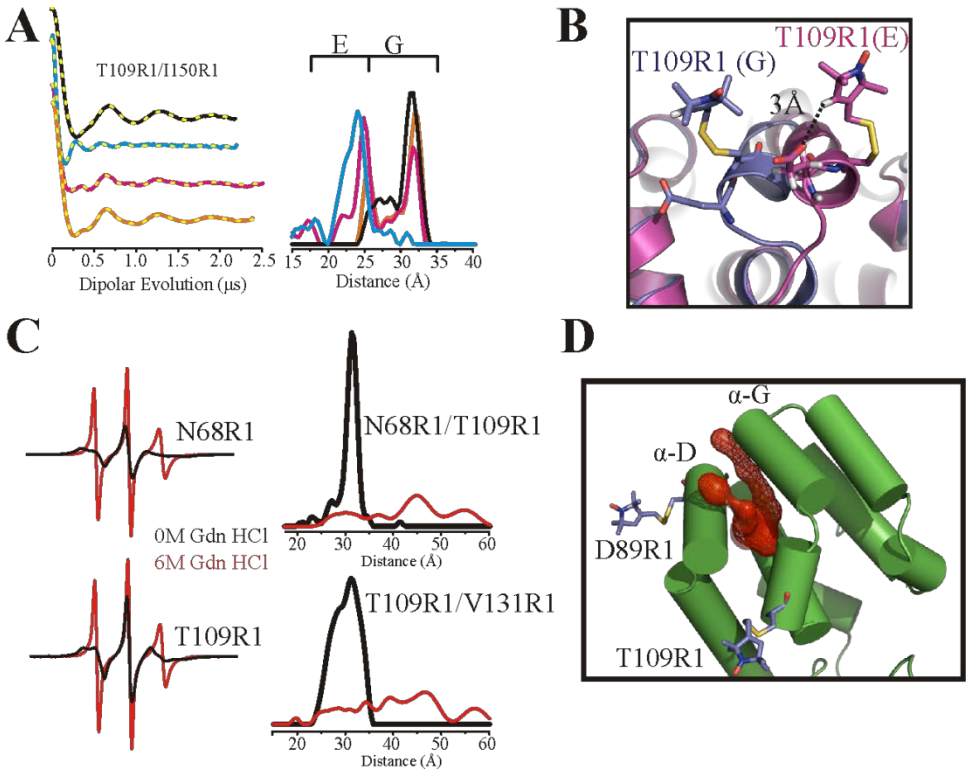

Figure 5.A1 DEER distance distributions for T109R1/I150R1 in different genetic backgrounds at atmospheric pressure, models of T109R1 side chain structure, characteristic CW spectra and DEER distance distributions of a fully unfolded protein, and putative tunnels in T4L L99A that could allow ligand access. (A) DEFs and corresponding distance distributions for T109R1/I150R1 in the WT* (black), L99A/G113A/R119P (blue), L99A/G113A (magenta), and L99A/G113A with benzene (orange). The data show that the shift to the **E** conformation is smaller in L99A/G113A compared to L99A/G113A/R119P. (B) Model of T109R1 in the **G** and **E** states showing possible non-classical H-bonding interaction of the 4-H in the R1 nitroxide ring with E108 in the **E** conformation; the distance of the 4-H to E108 is too long for interaction in the **G** conformation. (C) Examples of CW EPR spectra (left panel) and DEER distance distributions (right panel) for fully folded (black) and unfolded T4L WT* in 6 M GdnHCl (red). (D) Ribbon diagram of T4L L99A structure showing two putative tunnels to the cavity identified by Caver analysis (44, 45) in the interface between helices D and G. The tunnels are shown in red surface representation.

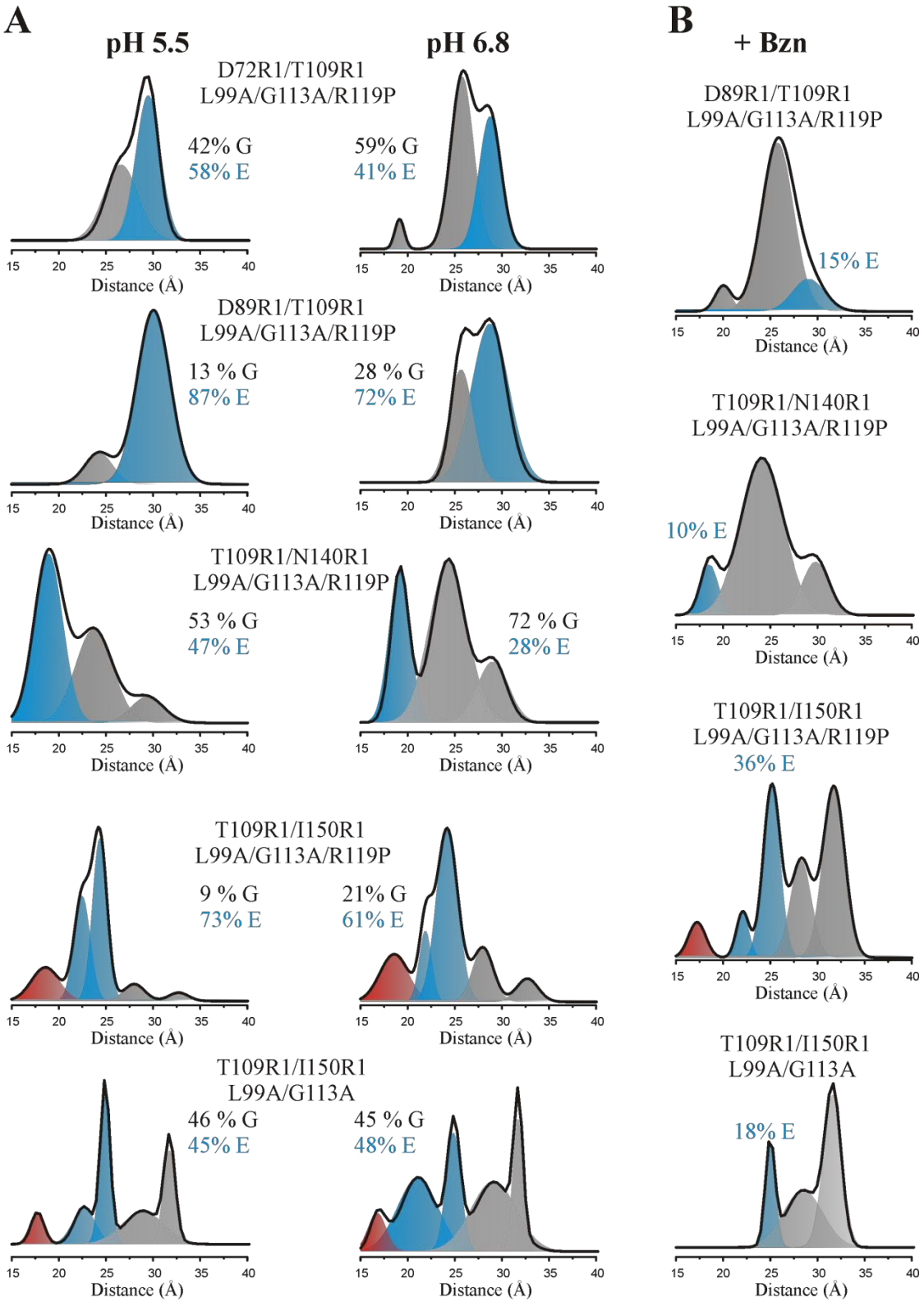

Figure 5.A2 Multiple Gaussian distance distributions of the indicated mutants. (A) Distance distributions of the indicated mutants at pH values of 5.5 and 6.8. (B) Distance distributions in the presence of benzene at pH 6.8. The black line is the overall distance distribution based on Gaussian fits. The Gaussians representing distances of **G** and **E** and a third state are shown in gray, blue, and red, respectively.

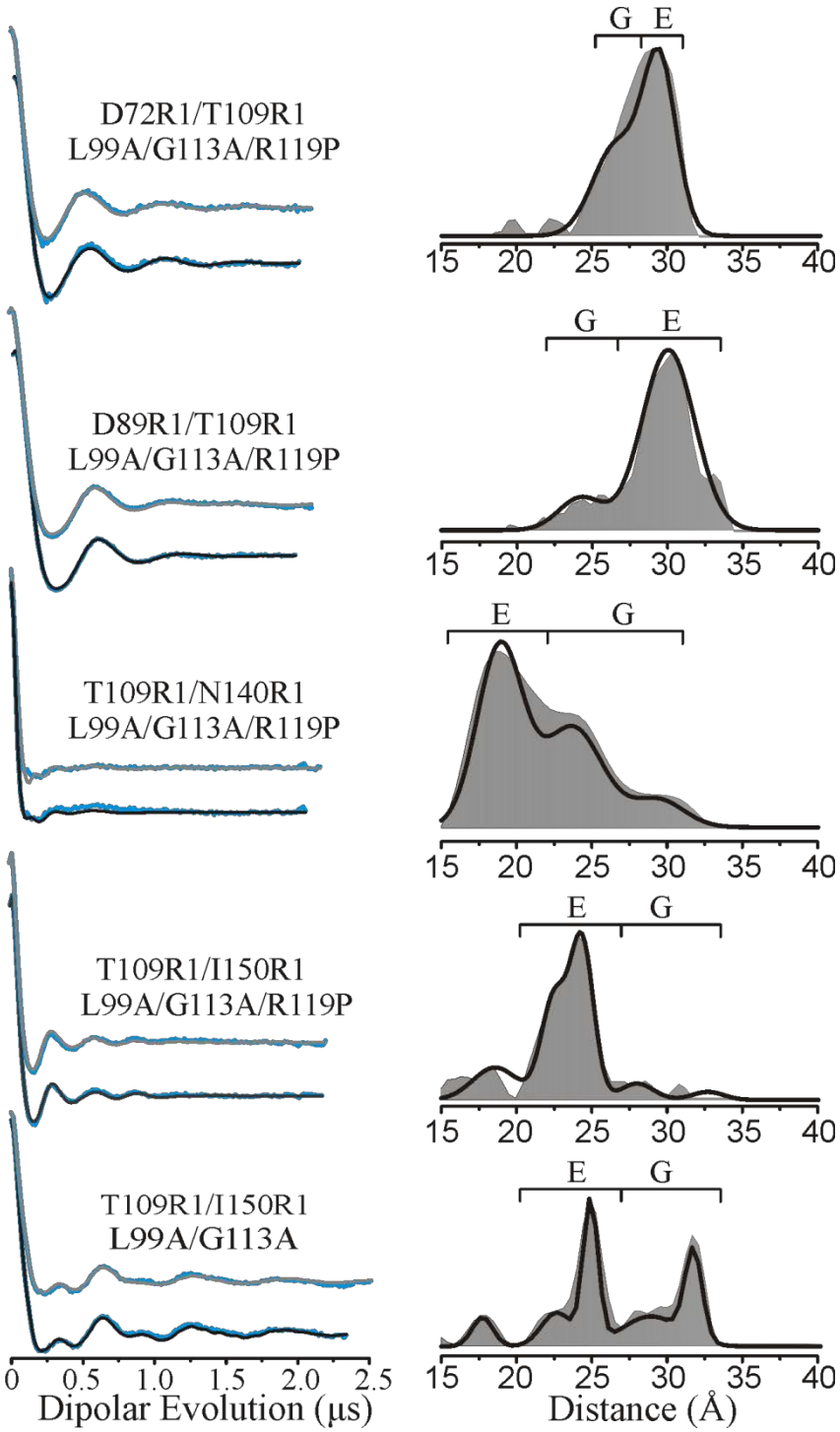

Figure 5.A3 Comparison of model-free and multiple Gaussian fits in the indicated mutants. Left Panel: Model-free fits (gray) and multiple Gaussian fits (black) to the DEFs (blue) of the indicated mutants. Right panel: Corresponding distance distributions based on model-free fit (shaded) and multiple Gaussian fit (black trace) of the indicated mutants.

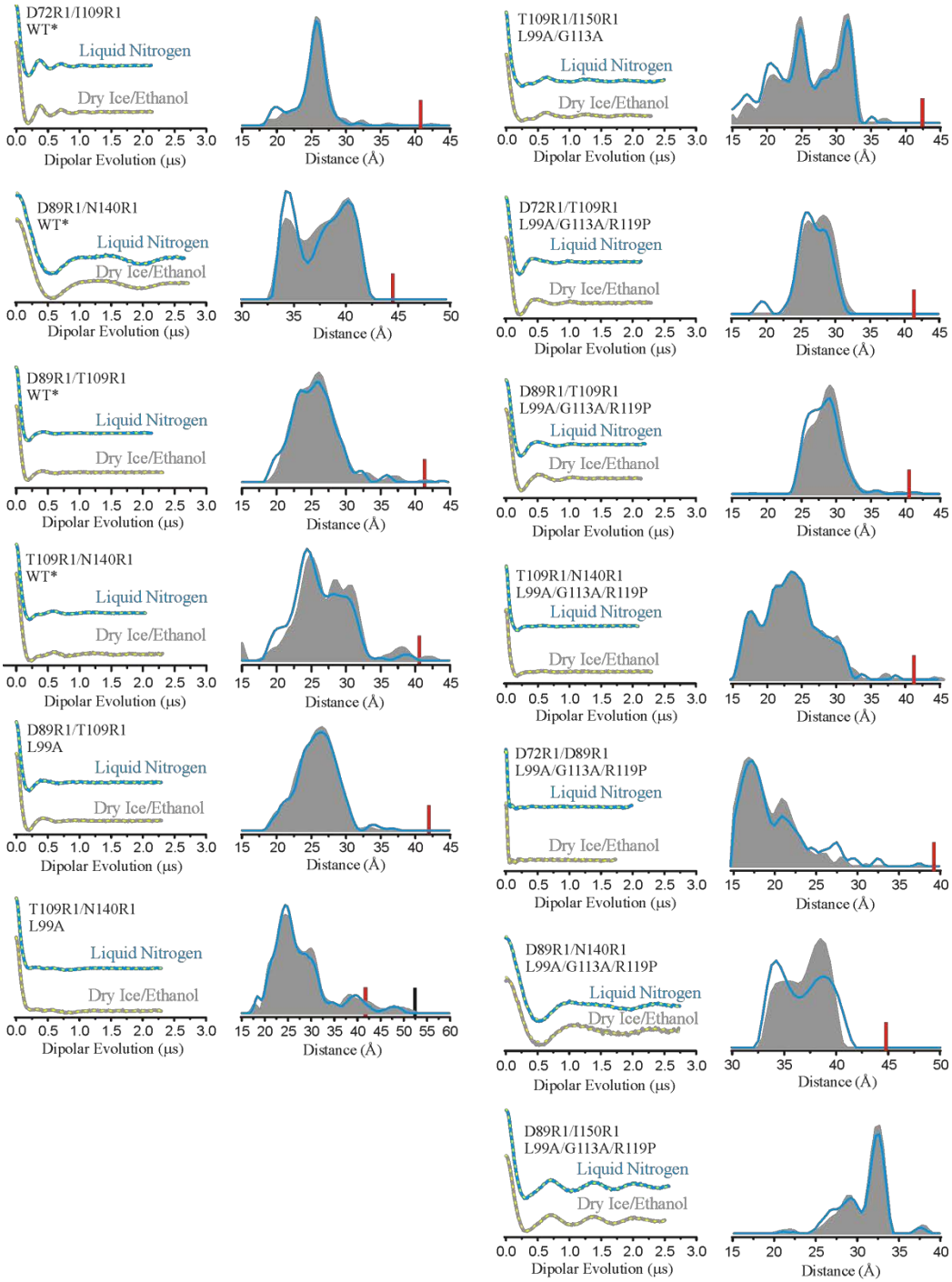

Figure 5.A4 Comparison of dry ice/ethanol and liquid nitrogen freezing prior to DEER. DEFs, model-free fits of the DEFs (dashed yellow traces), and corresponding distance distributions are shown for the indicated mutants prepared using dry ice/ethanol and liquid nitrogen at atmospheric pressure. The DEFs and distance distributions are color-coded as indicated. The red and black bars indicate the upper limit of reliable shape and distance of the distribution, respectively (see section **5.6**).

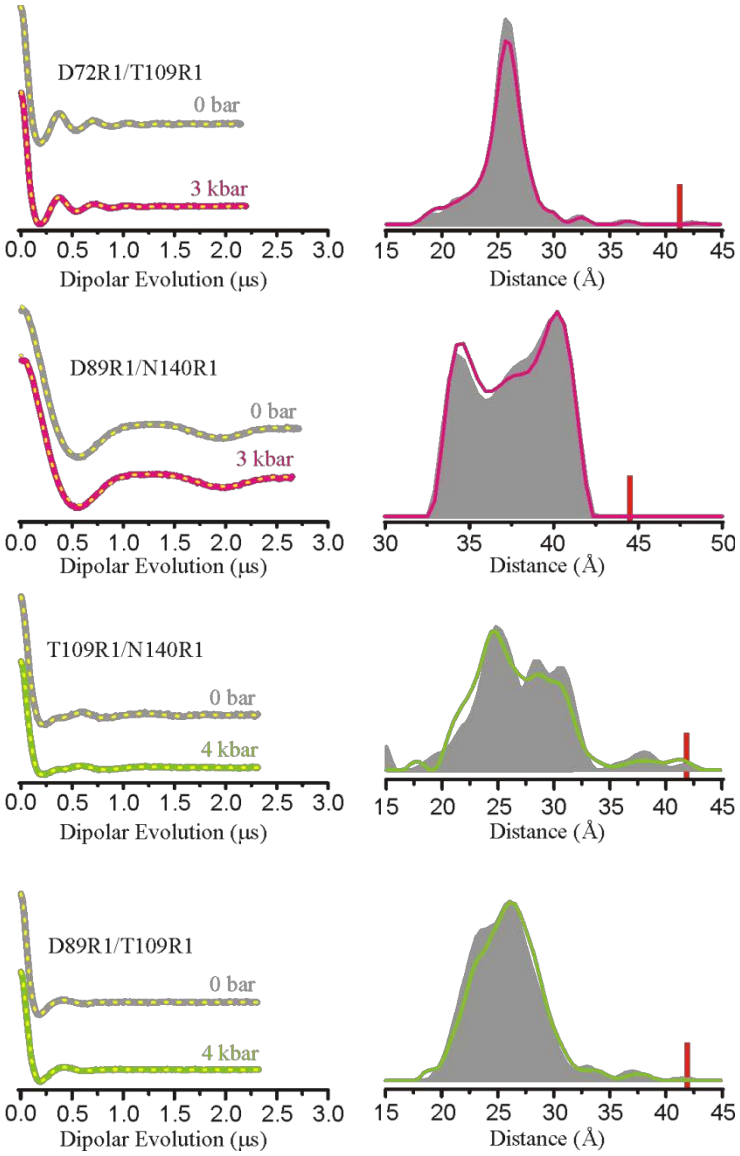

Figure 5.A5 PR DEER in the WT* background. DEFs, model-free fits of the DEFs (dashed yellow traces), and corresponding distance distributions are shown for the indicated doubles in the WT* background. The DEFs and distance distributions are color-coded as indicated. The red bar indicates the upper limit of reliable shape of the distribution (see section **5.6**).

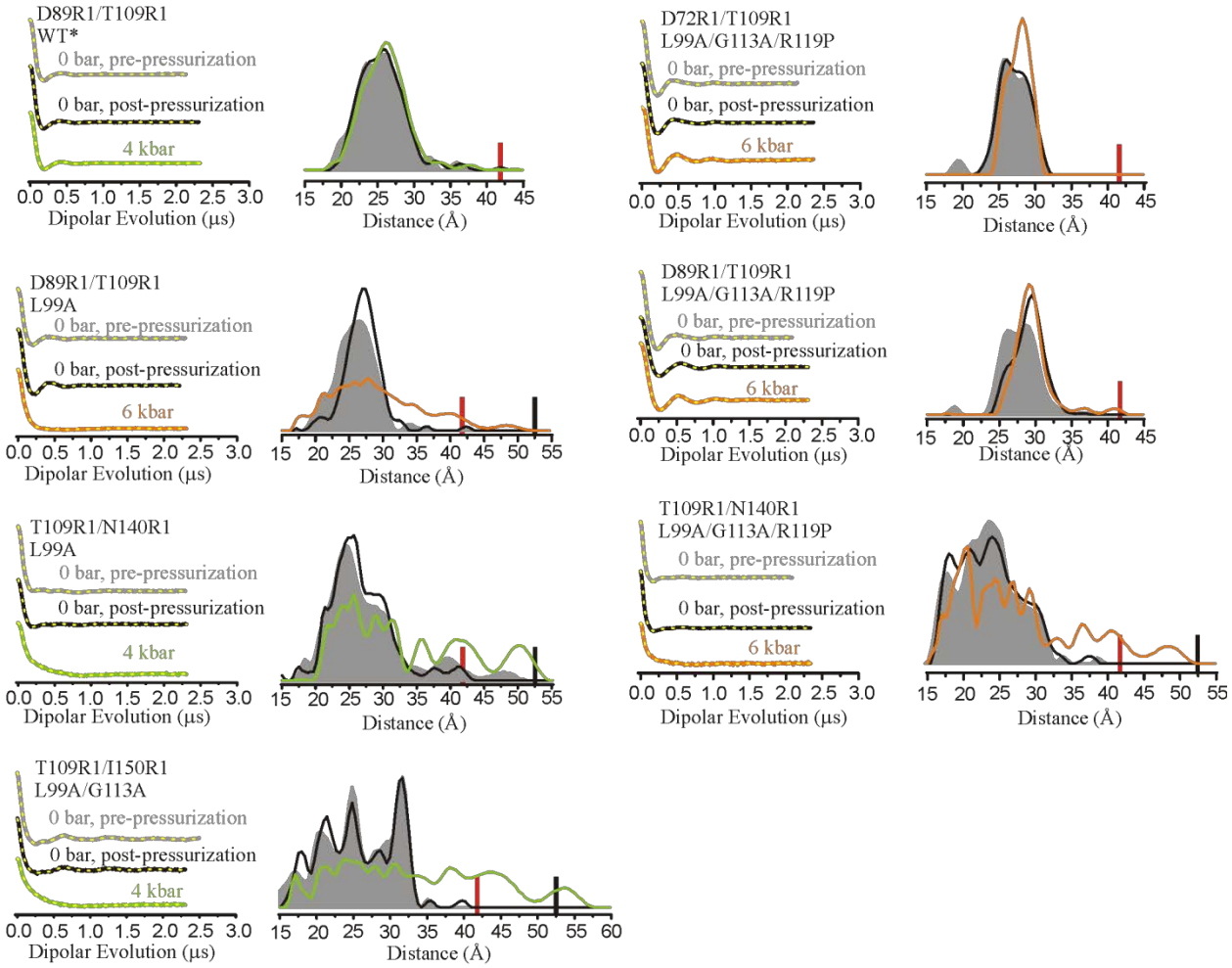

Figure 5.A6 Reversibility of changes observed with PR DEER. DEFs, model-free fits of the DEFs (dashed yellow traces), and corresponding distance distributions are shown for the indicated mutants at 0 bar pre- and postpressurization (data for each mutant at either 4 or 6 kbar is shown for comparison). Excellent reversibility is observed for all mutants except D89R1/T109R1 in the L99A and L99A/G113A/R119P backgrounds, which are only partially reversible after pressurization to 6 kbar. The DEFs and distance distributions are color-coded as indicated. The red and black bars indicate the upper limit of reliable shape and distance of the distribution, respectively (see section **5.6**).

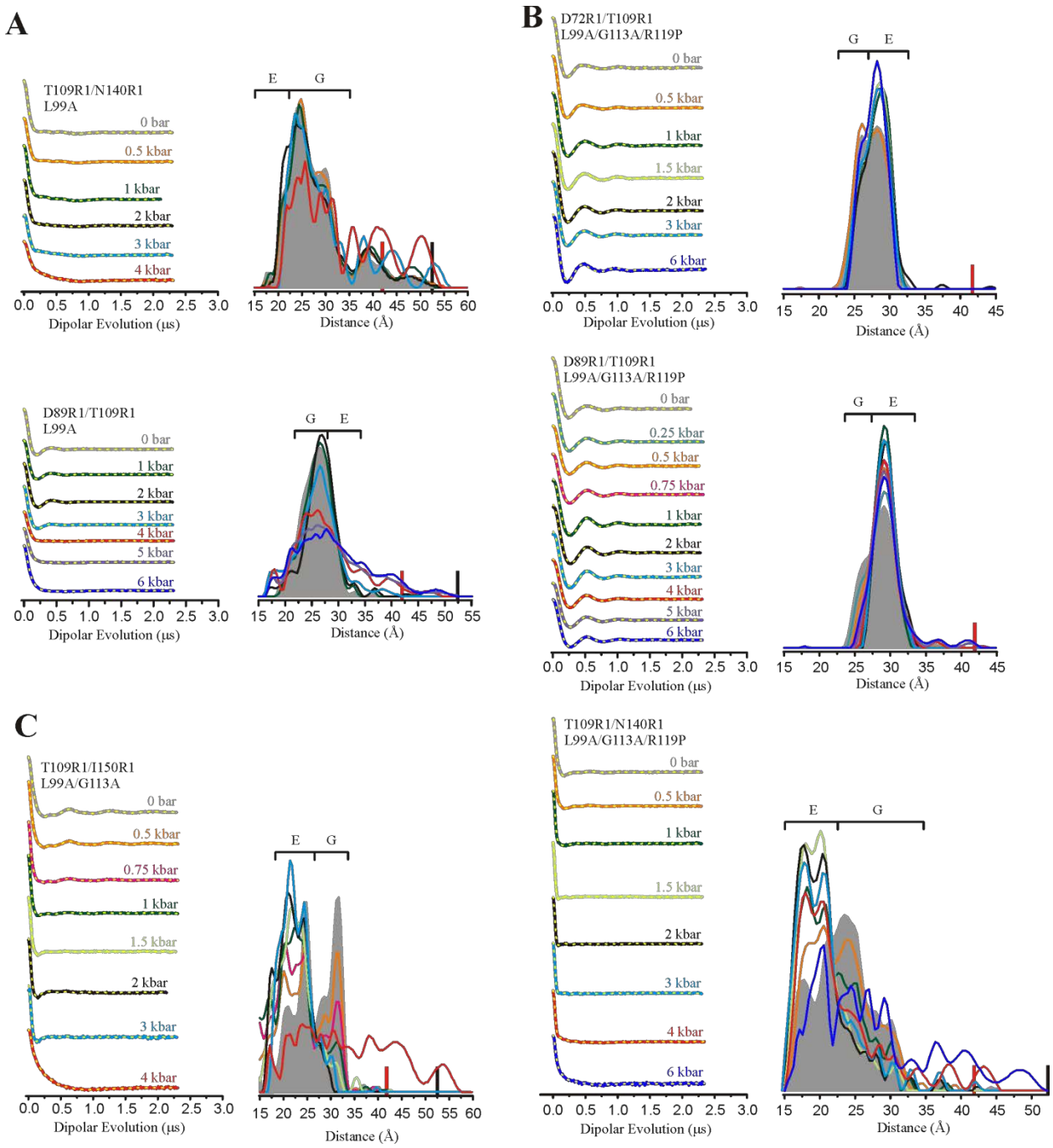

Figure 5.A7 PR DEER in the (A) L99A, (B) L99A/G113A/R119P, and (C) L99A/G113A backgrounds. DEFs, model-free fits of the DEFs (dashed yellow traces), and corresponding distance distributions are shown for the indicated doubles. The DEFs and distance distributions are color-coded as indicated. The red and black bars indicate the upper limit of reliable shape and distance of the distribution, respectively (see section **5.6**).

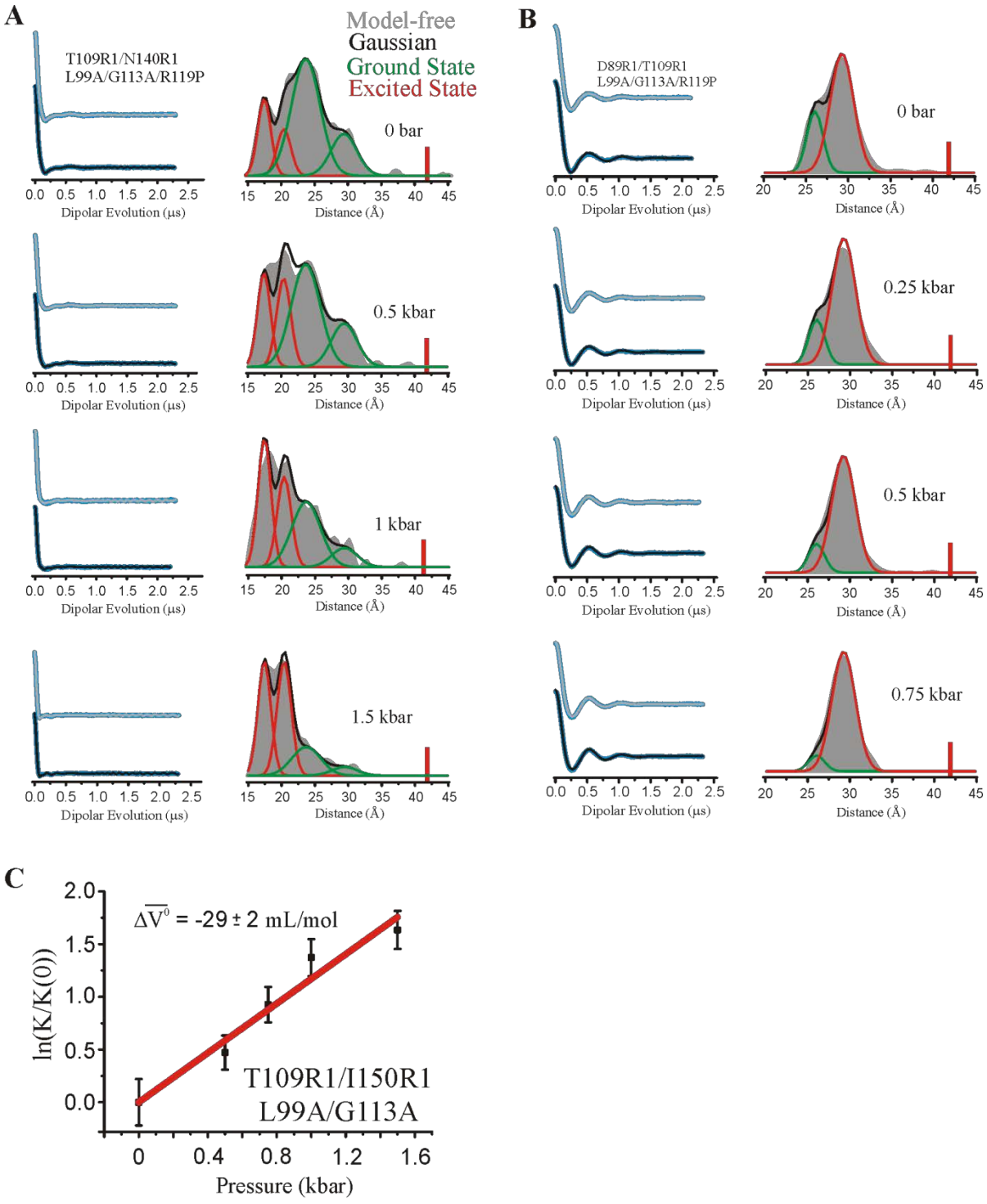

Figure 5.A8 Comparison of model-free and multiple Gaussian fits of the DEF from PR DEER. Model-free fits (gray) and multiple Gaussian fits (black) to the DEF (blue) of (A) T109R1/N140R1/L99A/G113A/R119P and (B) D89R1/T109R1/L99A/G113A/R119P are shown for the indicated pressures. Corresponding distance distributions are overlaid to the right of the DEF, and are color-coded according to the inset. The red bar indicates the upper limit of reliable shape of the distribution (see section **5.6**). (C) Plot of ln(K/K(0)) vs. pressure for the indicated mutant, and fit (red trace) using a two-state model to measure $\Delta\bar{V}^{o}$ for the **G** → **E** transition.

5.8 References

1. López CJ, Yang Z, Altenbach C, & Hubbell WL (2013) Conformational selection and adaptation to ligand binding in T4 lysozyme cavity mutants. *Proc Natl Acad Sci USA* 110(46):E4306-4315.
2. Bouvignies G, *et al.* (2011) Solution structure of a minor and transiently formed state of a T4 lysozyme mutant. *Nature* 477(7362):111-114.
3. Ando N, *et al.* (2008) Structural and thermodynamic characterization of T4 lysozyme mutants and the contribution of internal cavities to pressure denaturation. *Biochemistry* 47(42):11097-11109.
4. Roche J, *et al.* (2012) Cavities determine the pressure unfolding of proteins. *Proc Natl Acad Sci USA* 109(18):6945-6950.
5. Collins MD, Hummer G, Quillin ML, Matthews BW, & Gruner SM (2005) Cooperative water filling of a nonpolar protein cavity observed by high-pressure crystallography and simulation. *Proc Natl Acad Sci USA* 102(46):16668-16671.
6. Kamatari YO, Smith LJ, Dobson CM, & Akasaka K (2011) Cavity hydration as a gateway to unfolding: an NMR study of hen lysozyme at high pressure and low temperature. *Biophys Chem* 156(1):24-30.
7. Lassalle MW, *et al.* (2001) Filling a cavity dramatically increases pressure stability of the c-Myb R2 subdomain. *Proteins* 45(1):96-101.
8. Chalikian TV & Macgregor Jr RB (2009) Origins of pressure-induced protein transitions. *J Mol Biol* 394(5):834-842.

9. Hummer G, Garde S, García AE, Paulaitis ME, & Pratt LR (1998) The pressure dependence of hydrophobic interactions is consistent with the observed pressure denaturation of proteins. *Proc Natl Acad Sci USA* 95(4):1552-1555.

10. Rouget J-B, *et al.* (2011) Size and sequence and the volume change of protein folding. *J Amer Chem Soc* 133(15):6020-6027.

11. Nucci NV, Fuglestad B, Athanasoula EA, & Wand AJ (2014) Role of cavities and hydration in the pressure unfolding of T-4 lysozyme. *Proc Natl Acad Sci USA* 111(38):13846-13851.

12. Voloshin VP, Medvedev NN, Smolin N, Geiger A, & Winter R (2015) Exploring volume, compressibility and hydration changes of folded proteins upon compression. *Phys Chem Chem Phys* 17(13):8499-8508.

13. Zhang J, Peng X, Jonas A, & Jonas J (1995) NMR study of the cold, heat, and pressure unfolding of ribonuclease A. *Biochemistry* 34(27):8631-8641.

14. Smeller L (2002) Pressure–temperature phase diagrams of biomolecules. *Biochim Biophys Acta, Protein Struct Mol Enzymol* 1595(1–2):11-29.

15. Chryssomallis GS, Torgerson PM, Drickamer HG, & Weber G (1981) Effect of hydrostatic pressure on lysozyme and chymotrypsinogen detected by fluorescence polarization. *Biochemistry* 20(14):3955-3959.

16. Meersman F, *et al.* (2013) High-pressure biochemistry and biophysics. *Rev Mineral Geochem* 75(1):607-648.

17. Meersman F, Smeller L, & Heremans K (2002) Comparative fourier transform infrared spectroscopy study of cold-, pressure-, and heat-induced unfolding and aggregation of myoglobin. *Biophys J* 82(5):2635-2644.

18. Akasaka K (2006) Probing conformational fluctuation of proteins by pressure perturbation. *Chem Rev* 106(5):1814-1835.

19. Vidugiris GJA, Truckses DM, Markley JL, & Royer CA (1996) High-pressure denaturation of staphylococcal nuclease proline-to-glycine substitution mutants. *Biochemistry* 35(12):3857-3864.

20. Maeno A, *et al.* (2015) Cavity as a source of conformational fluctuation and high-energy state: high-pressure NMR study of a cavity-enlarged mutant of T4Lysozyme. *Biophys J* 108(1):133-145.

21. Morton A & Matthews BW (1995) Specificity of ligand binding in a buried nonpolar cavity of T4 lysozyme: linkage of dynamics and structural plasticity. *Biochemistry* 34(27):8576-8588.

22. Eriksson AE, *et al.* (1992) Response of a protein structure to cavity-creating mutations and its relation to the hydrophobic effect. *Science* 255(5041):178-183.

23. Baldwin E, Baase WA, Zhang X, Feher V, & Matthews BW (1998) Generation of ligand binding sites in T4 lysozyme by deficiency-creating substitutions. *J Mol Biol* 277(2):467-485.

24. Xu J, Baase WA, Baldwin E, & Matthews BW (1998) The response of T4 lysozyme to large-to-small substitutions within the core and its relation to the hydrophobic effect. *Protein Sci* 7(1):158-177.

25. Mulder FA, Hon B, Muhandiram DR, Dahlquist FW, & Kay LE (2000) Flexibility and ligand exchange in a buried cavity mutant of T4 lysozyme studied by multinuclear NMR. *Biochemistry* 39(41):12614-12622.

26. Mulder FA, Mittermaier A, Hon B, Dahlquist FW, & Kay LE (2001) Studying excited states of proteins by NMR spectroscopy. *Nat Struct Biol* 8(11):932-935.

27. Kitahara R & Mulder FAA (2015) Is pressure-induced signal loss in NMR spectra for the Leu99Ala cavity mutant of T4 lysozyme due to unfolding? *Proc Natl Acad Sci USA* 112(3):E923.

28. Wand AJ & Nucci NV (2015) Reply to Kitahara and Mulder: An ensemble view of protein stability best explains pressure effects in a T4 lysozyme cavity mutant. *Proc Natl Acad Sci USA* 112(3):E924.

29. McCoy J & Hubbell WL (2011) High-pressure EPR reveals conformational equilibria and volumetric properties of spin-labeled proteins. *Proc Natl Acad Sci USA* 108(4):1331-1336.

30. Liu L, Baase WA, & Matthews BW (2009) Halogenated benzenes bound within a non-polar cavity in T4 lysozyme provide examples of I···S and I···Se halogen-bonding. *J Mol Biol* 385(2):595-605.

31. Fleissner MR, Cascio D, & Hubbell WL (2009) Structural origin of weakly ordered nitroxide motion in spin-labeled proteins. *Protein Sci* 18(5):893-908.

32. Mchaourab HS, Lietzow MA, Hideg K, & Hubbell WL (1996) Motion of spin-labeled side chains in T4 lysozyme. correlation with protein structure and dynamics. *Biochemistry* 35(24):7692-7704.

33. Georgieva ER, Borbat PP, Ginter C, Freed JH, & Boudker O (2013) Conformational ensemble of the sodium-coupled aspartate transporter. *Nat Struct Mol Biol* 20(2):215-221.

34. Bridges MD, Hideg K, & Hubbell WL (2010) Resolving conformational and rotameric exchange in spin-labeled proteins using saturation recovery EPR. *Appl Magn Reson* 37(1-4):363.

35. Lietzow MA & Hubbell WL (2004) Motion of spin label side chains in cellular retinol-binding protein: correlation with structure and nearest-neighbor interactions in an antiparallel β-sheet. *Biochemistry* 43(11):3137-3151.

36. Guo Z, Cascio D, Hideg K, & Hubbell WL (2008) Structural determinants of nitroxide motion in spin-labeled proteins: solvent-exposed sites in helix B of T4 lysozyme. *Protein Sci* 17(2):228-239.

37. Eriksson AE, Baase WA, Wozniak JA, & Matthews BW (1992) A cavity-containing mutant of T4 lysozyme is stabilized by buried benzene. *Nature* 355(6358):371-373.

38. Morton A, Baase WA, & Matthews BW (1995) Energetic origins of specificity of ligand binding in an interior nonpolar cavity of T4 lysozyme. *Biochemistry* 34(27):8564-8575.

39. Feher VA, Baldwin EP, & Dahlquist FW (1996) Access of ligands to cavities within the core of a protein is rapid. *Nat Struct Mol Biol* 3(6):516-521.

40. Roche J, *et al.* (2012) Remodeling of the folding free energy landscape of staphylococcal nuclease by cavity-creating mutations. *Biochemistry* 51(47):9535-9546.

41. López CJ, Oga S, & Hubbell WL (2012) Mapping molecular flexibility of proteins with site-directed spin labeling: a case study of myoglobin. *Biochemistry* 51(33):6568-6583.

42. Columbus L & Hubbell WL (2004) Mapping backbone dynamics in solution with site-directed spin labeling: GCN4−58 bZip free and bound to DNA. *Biochemistry* 43(23):7273-7287.

43. Fourme R, Girard E, & Akasaka K (2012) High-pressure macromolecular crystallography and NMR: status, achievements and prospects. *Curr Opin Struct Biol* 22(5):636-642.

44. Kozlikova B, *et al.* (2014) CAVER Analyst 1.0: graphic tool for interactive visualization and analysis of tunnels and channels in protein structures. *Bioinformatics* 30(18):2684-2685.

45. Chovancova E, *et al.* (2012) CAVER 3.0: A tool for the analysis of transport pathways in dynamic protein structures. *PLoS Comput Biol* 8(10):e1002708.

46. Toleikis Z, Cimmperman P, Petrauskas V, & Matulis D (2011) Determination of the volume changes induced by ligand binding to heat shock protein 90 using high-pressure denaturation. *Anal Biochem* 413(2):171-178.

47. Toleikis Z, Cimmperman P, Petrauskas V, & Matulis D (2012) Serum albumin ligand binding volumes using high pressure denaturation. *J Chem Thermodyn* 52(0):24-29.

48. Royer CA, *et al.* (1993) Effects of amino-acid substitutions on the pressure denaturation of staphylococcal nuclease as monitored by fluorescence and nuclear-magnetic-resonance spectroscopy. *Biochemistry* 32(19):5222-5232.

49. Zhang Z, *et al.* (2010) Multifrequency electron spin resonance study of the dynamics of spin labeled T4 lysozyme. *J Phys Chem B* 114(16):5503-5521.

50. López CJ, Fleissner MR, Guo Z, Kusnetzow AK, & Hubbell WL (2009) Osmolyte perturbation reveals conformational equilibria in spin-labeled proteins. *Protein Sci* 18(8):1637-1652.

51. Jeschke G (2012) DEER distance measurements on proteins. *Annu Rev Phys Chem* 63(1):419-446.

52. Fasman GD (1996) *Circular dichroism and the conformational analysis of biomolecules* (Plenum, New York, NY).

53. Sreerama N & Woody RW (2000) Estimation of protein secondary structure from circular dichroism spectra: comparison of CONTIN, SELCON, and CDSSTR methods with an expanded reference set. *Anal Biochem* 287(2):252-260.

54. Fleissner MR (2007) X-ray structures of nitroxide side chains in proteins: a basis for interpreting distance measurements and dynamic studies by electron paramagnetic resonance. Dissertation (University of California, Los Angeles, Los Angeles, CA).

55. Eriksson AE, Baase WA, & Matthews BW (1993) Similar hydrophobic replacements of leu99 and phe153 within the core of T4 lysozyme have different structural and thermodynamic consequences. *J Mol Biol* 229(3):747-769.